

AIRFOIL SELF-NOISE

INVESTIGATION WITH PARTICLE IMAGE VELOCIMETRY

AIRFOIL SELF-NOISE

INVESTIGATION WITH PARTICLE IMAGE VELOCIMETRY

Proefschrift

ter verkrijging van de graad van doctor
aan de Technische Universiteit Delft,
op gezag van de Rector Magnificus prof. ir. K. C. A. M. Luyben,
voorzitter van het College voor Promoties,
in het openbaar te verdedigen op donderdag 1 oktober 2015 om 10:00 uur

door

Stefan PRÖBSTING

ingenieur lucht- en ruimtevaart
geboren te Kamp-Lintfort, Duitsland.

Dit proefschrift is goedgekeurd door de promotor:

Prof. Dr.-Ing. F. Scarano

Samenstelling promotiecommissie:

Rector Magnificus, voorzitter
Prof. Dr.-Ing. F. Scarano, Technische Universiteit Delft, promotor

Onafhankelijke leden
Prof. Dr.-Ing. G. Eitelberg, Technische Universiteit Delft
Prof. Dr. S. C. Morris, University of Notre Dame
Prof. Dr. C. Schram, Von Karman Institute for Fluid Dynamics
Prof. Dr. S. Yarusevych, University of Waterloo
Dr. M. Kotsonis, Technische Universiteit Delft
Ir. M. Tuinstra, Nationaal Lucht- en Ruimtevaartlaboratorium
Prof. Dr.-Ing. S. Hickel, Technische Universiteit Delft, reservelid



Printed by: Ipskamp Drukkers

Copyright © 2015 by S. Pröbsting

Part of this research was supported by the European Research Council through the AFDAR project (ERC grant 265695).

ISBN 978-94-6186-523-6

An electronic version of this dissertation is available at <http://repository.tudelft.nl/>. The online version has been revised with respect to the print version.

PREFACE

GRATITUDE for his continued support I would like to express to Fulvio Scarano, who has been my supervisor for most of my academic life. It has been a challenging and rewarding experience. I would also like to thank my other supervisors during the years as a graduate student in Delft and at the Von Karman Institute, namely Christophe Schram, Patrick Rambaud, and Lilla Koloszar for their introduction to aeroacoustics, and Sina Ghaemi for sharing his wisdom on PIV. Thanks to the members of the thesis committee for finding the time to read this work.

During the past four years, I have had the chance and pleasure to work with aeroacoustic groups in Europe and overseas. I would like to thank Scott Morris for the good collaboration and providing the opportunity to visit the University of Notre Dame, Mike Bilka for helping further when nothing else did, and Yaoyi Guan for his welcoming, professional attitude and friendship. Thanks to the former and present members of the aeroacoustics group at the NLR, namely Marthijn Tuinstra, Pieter Sijtsma, and Stefan Oerlemans for the collaboration and sharing of experience and advise. I would also like to thank Stéphane Moreau and Prateek Jaiswal from the University of Sherbrooke for their interest in my work and the resulting collaboration.

I am grateful to Serhiy Yarusevych from the University of Waterloo and Marios Kotsonis for their pointers in the right direction; to Serhiy for insightful discussions on the genesis of vortical structures and beyond. Carlos Arce, Daniele Ragni, Francesco Avallone, Wouter van der Velden: I enjoyed our discussions and continuous scientific discourse. Thanks, Wouter, for the translation.

I feel indebted to our technicians, namely Nico van Beek, Stefan Bernardy, Frits Donker-Duyvis, Peter Duyndam, Eric de Keizer, Leo Molenwijk, and Henk-Jan Siemer. Experiments do not happen without you. Stefan and Leo, thanks for sharing the LSL.

Thanks to all my colleagues - especially to those from HSL 1.01 and those who moved beyond in the meantime - in particular Andrea, Beppe, Jan, Kyle, Matteo, Mustafa, Peppe, Qinqinq, Shuanghou, Theo, Vahid, Valeria, Zhengzhong, and my former student, colleague, friend, and paranymph Jacopo Serpieri. To all the other students, who I had the pleasure to (co-)supervise or whose paths crossed mine for other reasons: Abhineet, Jigar, Maarten, Martina, Mudit, Ram, Stefano, Thibault, Umer, Xueqing, and those I did not mention. Without you, I would have learned less!

Thanks to the ones who distracted my mind from studies and research; especially Christina, Fredy, Jannis, Jules, Marc, Moritz, Othaniel, and Thorsten.

Zu guter Letzt gebührt meiner Familie Dank für ihre fortwährende und liebevolle Unterstützung, insbesondere meinen Eltern, meinem Bruder Sebastian und meiner Großmutter Sophia. Auf euch ist immer Verlass. 谢谢你, 文璟.

*Stefan Pröbsting
Delft, August 2015*

CONTENTS

Summary	1
Samenvatting	3
Prologue	5
1 Introduction	7
1.1 Aerodynamically generated sound and noise	8
1.2 Airfoil self-noise	8
1.3 Present challenges and research efforts	12
1.4 Source diagnostics and acoustic measurements	14
1.4.1 Acoustic measurement techniques	14
1.4.2 Flow measurement techniques	15
1.4.3 Particle Image Velocimetry	16
1.5 Motivation and objectives	18
1.6 Outline of the thesis	19
2 Airfoil self-noise	21
2.1 Trailing edge noise	22
2.1.1 A brief history	22
2.1.2 Influence of trailing edge flow and geometry	24
2.1.3 Methods for trailing edge noise prediction	28
2.2 Diffraction at the trailing edge	31
2.2.1 Incident pressure gust	31
2.2.2 Unsteady surface pressure field	32
2.2.3 Solution for the semi-infinite half-plane	37
2.2.4 Extended solution	39
2.2.5 Trailing edge bluntness noise	42
2.3 Laminar boundary layer instability noise	44
2.3.1 Characteristics of acoustic spectrum	44
2.3.2 Concept of acoustic feedback	47
2.3.3 Role of boundary layer separation	50
2.3.4 Overview of previous studies	52
3 Estimation of sound and surface pressure	57
3.1 Particle Image Velocimetry	58
3.2 PIV based noise prediction	60
3.2.1 Turbulent boundary layer trailing edge noise	60
3.2.2 Trailing edge bluntness noise	64

3.3	Unsteady surface pressure reconstruction	64
3.3.1	Estimation of material derivative	65
3.3.2	Discretization of fluid parcel trajectory reconstruction.	66
3.3.3	Least squares estimate	67
3.3.4	Boundary conditions for pressure reconstruction	67
3.3.5	Error estimation	68
3.4	Unsteady surface pressure measurements	70
I	Laminar boundary layer instability noise	73
4	Tonal noise and related flow structure	75
4.1	Introductory remarks	76
4.2	Description of experiments	77
4.2.1	Acoustic measurements	78
4.2.2	Flow field measurements	78
4.2.3	Effective angle of attack	79
4.3	Results and discussion	80
4.3.1	Noise generated by smooth airfoil	80
4.3.2	Noise generated under forced transition	84
4.3.3	Regimes of tonal noise generation	90
4.3.4	Flow structure and relation to different regimes	96
4.3.5	Characteristics of secondary tones.	98
4.3.6	A perspective view on previous studies.	101
4.4	Conclusion	105
5	Amplitude modulation of amplified instability waves	107
5.1	Introductory remarks	108
5.2	Description of experiments	108
5.2.1	Acoustic measurements	108
5.2.2	Flow field measurements	109
5.3	Results and discussion	110
5.3.1	Periodic amplitude modulation of acoustic pressure.	110
5.3.2	Flow structure and topology	112
5.3.3	Amplification of instability waves	115
5.3.4	Temporal evolution of instability waves	118
5.3.5	Periodic amplitude modulation of instability waves	124
5.4	Conclusion	129
6	Effect of tonal noise on separation bubble dynamics	131
6.1	Introductory remarks	132
6.2	Description of experiments	132
6.3	Results and discussion	135
6.3.1	Overview of flow development and tone generation	135
6.3.2	Effect of acoustic excitation on separation bubble	141
6.3.3	Temporal evolution of unstable disturbances	146
6.3.4	Summary of feedback effect	152
6.4	Conclusion	153

II	Turbulent boundary layer trailing edge interaction	155
7	Pressure reconstruction in a turbulent boundary layer	157
7.1	Introductory remarks	158
7.2	Description of experiments	159
7.2.1	Planar flow field measurements	159
7.2.2	Volumetric flow field measurements	160
7.2.3	Surface pressure fluctuations	161
7.2.4	Direct Numerical Simulation.	161
7.3	Results and discussion	162
7.3.1	Characterization of boundary layer	162
7.3.2	Turbulence characteristics	166
7.3.3	Unsteady surface pressure	168
7.3.4	Estimation of correlation length	172
7.4	Conclusion	174
8	PIV based estimation of trailing edge noise	177
8.1	Introductory remarks	178
8.2	Description of experiments	178
8.2.1	Acoustic measurements	179
8.2.2	Flow field measurements	182
8.3	Results and discussion	186
8.3.1	Flow characteristics	186
8.3.2	Noise emission.	192
8.3.3	Surface pressure fluctuations	194
8.3.4	Application of diffraction theory	201
8.4	Conclusion	203
III	Trailing edge bluntness noise	207
9	Prediction of trailing edge bluntness noise	209
9.1	Introductory remarks	210
9.2	Description of experiments	211
9.2.1	Acoustic measurements	211
9.2.2	Flow field measurements	213
9.3	Results and discussion	215
9.3.1	Flow field	215
9.3.2	Acoustic emission	224
9.4	Conclusion	225
	Epilogue	227
10	Conclusion	229
10.1	Laminar boundary layer instability noise	229
10.2	Turbulent boundary layer trailing edge noise	231
10.3	Trailing edge bluntness noise	231
	References	233

Appendix	251
A Fundamental definitions of acoustics	253
B Schwarzschild solution	255
C Acoustic transfer function	257
D Basic relations for application of PIV	259
E Statistical data analysis	261
F Amplitude modulation	269
Curriculum Vitae	273
List of Publications	275

SUMMARY

AIRFOIL SELF-NOISE is a nuisance present in the world of today. In particular, it is of major concern for the wind energy industry, where strict noise regulations are often in conflict with other requirements for the placement of on-shore wind turbines. In its many manifestations, it can be of broadband type, narrowband type, and even tonal in nature. Broadband noise can be caused, for instance, by the interaction of the turbulent boundary layer with a sharp trailing edge, narrowband noise by large scale vortex shedding behind a blunt trailing edge, and particularly disharmonious and unpleasant tones by the development of instabilities in a laminar boundary layer and their interaction with the trailing edge. Prediction of the radiated sound, understanding of the underlying source, and ultimately noise control are the objectives of present day research.

This thesis is concerned with all of the aforementioned mechanisms of noise generation on an airfoil, with the objective to apply recently developed and advanced Particle Image Velocimetry (PIV) methods for noise prediction and source analysis.

The tonal noise mechanism on an airfoil at low to moderate Reynolds numbers is investigated by means of combined time-resolved PIV and acoustic measurements. In addition, the noise emission is characterized over a wide parameter space, including Reynolds number, angle of attack, and the placement of roughness elements on the surface of the airfoil to induce transition. In particular for the NACA 0012 airfoil profile at incidence, tonal noise emission at low Reynolds numbers is found to be dominated by events on the suction side of the airfoil. Instead, at high Reynolds number, tonal noise emission is dominated by pressure side events. At intermediate Reynolds numbers, interaction between the events on the two sides is relevant and can be of acoustic and hydrodynamic nature. This division of tonal noise regimes is related to the mean flow structure and topology; a separation bubble or separated shear layer in the vicinity of and upstream of the trailing edge, promotes the amplifications of instability waves that scatter at the trailing edge. By non-stationary spectral analysis, the presence of multiple tones in the acoustic spectrum is related to a near periodic amplitude modulation of the acoustic pressure. Instability waves in the source region near the trailing edge show a similar amplitude modulation. The latter does not require a secondary feedback loop with strong interaction between events on pressure and suction side, but can also be sustained by the events on a single side of the airfoil only. Further, the effect of the tonal noise emission on the separation bubble development and vortex shedding thereof is investigated in detail. With tonal excitation, the vortex shedding is rendered substantially more coherent, providing strong evidence for a self-excited aeroacoustic feedback loop as frequency selection mechanism.

High-speed tomographic PIV is employed to examine the interaction of the turbulent boundary layer with the trailing edge. The broadband type distribution of scales and turbulent state of the boundary layer, requires a time-resolved and volumetric data for the resolution of the aeroacoustic source. Statistics of the unsteady surface pres-

sure field and related to the far field sound radiation by diffraction theory. The unsteady surface pressure field is thus reconstructed from the velocity field data obtained with tomographic PIV and the statistics are compared to surface pressure measurements and to the solution of a Direct Numerical Simulation. After application of diffraction theory, the predicted sound radiation is compared to reference acoustic measurements. Over the range of well resolved frequencies, the results show good agreement. It is thus demonstrated that tomographic PIV in combination with pressure reconstruction methods can provide a useful tool for the analysis of the trailing edge noise mechanism.

A similar approach is followed to predict bluntness noise due to vortex shedding behind a beveled trailing edge. An additional wake model relates the wake vortex shedding to a surface pressure distribution. Therefore, a measurement configuration including high-speed stereoscopic PIV is used to determine the relevant statistics of the upwash velocity in the near-wake. In contrast to earlier studies on blunt trailing edges, comparison with reference acoustic measurements shows a large overestimation of sound radiation in this case. The results imply that the simplified wake model is not appropriate and applicable for an arbitrary trailing edge geometry.

SAMENVATTING

GELUID afkomstig van en geproduceerd door vleugelprofielen is een hinderlijk probleem in de wereld dezer dagen. Met name in de wind energie sector speelt het een grote rol, waar strenge geluidsnormen vaak conflicten kunnen opleveren voor het plaatsen van windturbines op land. Geluid komende van windturbines kan vele verschillende verschijnselen aannemen; het kan breedband, korte band of zelfs tonaal geluid zijn. Het breedband geluid kan bijvoorbeeld veroorzaakt zijn door de interactie van de turbulente grenslaag met een scherpe achterrand, het korte band geluid bijvoorbeeld door het op grote schaal afscheiden van wervelingen achter een stompe achterrand, en tenslotte het met name on-harmonieuze en onaangename tonale geluid door de ontwikkeling van instabiliteit in een laminaire grenslaag en de interactie met de achterrand. Een voorstelling van het uitgestraalde geluid, het inzicht in de onderliggende bron en uiteindelijk, de controle van het onderdrukken van het geluid zijn de doelen van het huidige onderzoek.

Dit proefschrift heeft betrekking op alle bovengenoemde geluid producerende mechanismen op een vleugelprofiel, met als doel het recent ontwikkelende en geavanceerde Particle Image Velocimetry (PIV) te gebruiken voor de voorspelling van het geluid en het analyseren van de geluidsbronnen.

Tonaal geluid afkomstig van een vleugelprofiel in stroming van lage tot middelmatige Reynolds getallen is bestudeerd middels een combinatie van tijd opgeloste PIV en akoestische metingen. De emissie van geluid is gekarakteriseerd over een breed scala aan parameterruimtes, inclusief Reynolds getal, invalshoek, en de plaatsing van ruwheid elementen op het oppervlak van het vleugelprofiel om transitie te induceren. Met name het NACA 0012 vleugelprofiel onder invalshoek produceert een dominant tonaal geluid bij lage Reynolds getallen door gebeurtenissen aan de zuigzijde van het profiel. Aan de ander kant, bij hoge Reynolds getallen is het dominante tonale geluid afkomstig van gebeurtenissen aan de drukzijde. Bij tussenliggende Reynolds getallen is de interactie tussen beide gebeurtenissen aan weerszijden interessant en kan zowel van akoestische of hydrodynamische aard zijn. Deze verdeling van het tonale geluid is gerelateerd aan de gemiddelde stroming en topologie; een loslatingsbubbel of geïsoleerde schuif laag in de nabijheid van en voor de achterrand bevordert de versterking van de instabiliteitsgolven die weerkaatst worden bij de achterrand. Bij gebruik van niet-stationaire spectrale analyse is aangetoond dat de aanwezigheid van meerdere tonen in het geluidsspectrum gerelateerd is aan een bijna periodieke amplitude modulatie van de akoestische druk. De instabiliteitsgolven in het brongebied dicht bij de achterrand tonen een vergelijkbare amplitude modulatie. Dit laatste heeft geen secundaire terugkoppeling met sterke wisselwerking tussen de gebeurtenissen op de druk- en zuigzijde maar kunnen worden toegewezen aan de gebeurtenissen op een enkele kant van het vleugelprofiel. Ook is het effect van de emissie van het tonale geluid op de ontwikkeling van de loslatingsbubbel en wervel afscheiding in detail verder bestudeerd. Door middel van het bekrachtigen van

tonale tonen kan wervel afscheiding aanzienlijk samenhangender worden gemaakt, wat een sterke aanwijzing oplevert voor een zelf aangeslagen terugkoppeling als frequentie specifieke selectie mechanisme.

Hoge snelheid tomografisch PIV is gebruikt om de interactie tussen de turbulente grenslaag met de achterrand te onderzoeken. Het breedband type geluid en turbulente toestand van de grenslaag vereist tijdsopgeloste en volumetrische data voor het verkrijgen van de aëroakoestische bron. De statistieken van de tijd opgeloste druk op de wand zijn gerelateerd aan de radiatie van het akoestische verre veld door middel van diffractie theorie. De oppervlakte drukken worden geconstrueerd uit het snelheidsveld wat is verkregen met tomografisch PIV en vergeleken met oppervlakte drukmetingen en resultaten van een directe numerieke oplossing. Na de toepassing van de diffractie theorie kan de voorspelde geluidsafstraling worden vergeleken met akoestische metingen. De resultaten vertonen goede overeenkomsten binnen de met zekerheid opgeloste frequenties. Er kan dus derhalve worden aangetoond dat tomografisch PIV gecombineerd met druk reconstructie technieken een nuttig hulpmiddel kan zijn voor de analyse van achterrand geluid mechanisme.

Een soortgelijke aanpak is gevolgd voor het bepalen van geluid van een stompe achterrand door het afscheiden van wervels. Een additioneel zog model relateert de wervel afscheiding aan de druk distributie op de wand. Hiervoor wordt een meting uitgevoerd met een hoge snelheid stereoscopische PIV setup om zo de relevante data van de opstromings snelheid in het nabije zog te bepalen. In tegenstelling tot eerdere studies die uitgevoerd zijn op stompe achterranden, geeft een vergelijking met akoestische referentie data aan dat er een grote overschatting van geluidsniveau is geobserveerd. De resultaten impliceren dat het vereenvoudigde zog model niet geschikt is voor toepassing op een willekeurig achterrand model.

PROLOGUE

1

INTRODUCTION

What one did hear quite clearly was an odd sort of chattering, clattering sound from the crossed chains which drove the two long-bladed air-screws. And there was also a penetrating whistling sound from the air-screws themselves. The net result was a mingled whistling, chattering hum which, once heard, could never be forgotten.

British journalist Harry Harper on the Wright Flyer [1]

The "swish-swish-swish" aerodynamic noise from three-bladed rotors is a common wind turbine sound. These sounds may not be objectionable, but they are detectable. The whir of the compressor in a refrigerator is audible, for example, but few find the sound objectionable. Some have compared this situation to that of a leaky faucet. Once recognized, the noise is hard to ignore.

Paul Gipe, *Wind Energy Comes of Age* [2]

Aeroacoustics of lifting surfaces has experienced increased attention in recent years due to stricter noise regulations, for instance in the aviation and wind energy sector. Particle Image Velocimetry (PIV) has matured and become a tool for aeroacoustic research. This chapter provides background on the aerodynamic source of noise on airfoils, recent developments in PIV, and its relevance and perspective for research in aeroacoustics.

1.1. AERODYNAMICALLY GENERATED SOUND AND NOISE

NOISE, unpleasant, unwanted, or loud sound, is encountered in many engineering applications in today's society and environment. We can recall the swishing noise of a wind turbine on a windy day, that present in a car with the windows open while driving, and the jet roaring of an aircraft on the apron or during flight. Some of these sources involve turbulent airflows or the interaction of an airflow with a structure. In such cases we refer to *aerodynamically* generated sound [3] and the scientific discipline concerned with its analysis is called *aeroacoustics* [4]. Aerodynamically generated noise is addressed in fields as diverse as the automotive or aerospace industry and architecture. Two fields of engineering, which have received ample attention in aeroacoustics include the aviation [4, 5] and, especially in recent years, the wind energy industry [6, 7].

Firstly, ever increasing demand for transportation of goods and travelers leads to an annual increase in the number of flights and therefore aircraft movements around airports. Many of these transportation hubs, especially within densely populated regions, are located in the vicinity of a metropolitan areas and thus the increasing number of take-offs and landings effects a large number of people. Low flights level during take-off and landing further increase the perceived noise level on the ground. With reduction of engine noise to levels similar to that generated by the airframe, noise sources previously categorized as secondary become increasingly important. These airframe noise sources include the interaction of the turbulent boundary layer with the trailing edge of wing or flap, unsteady wing tip vortices, vortex shedding in the slat cavity, and the complex flow interaction with the landing gear [5].

Secondly, noise is an important consideration in the design and approval of wind energy parks and individual wind turbines in the vicinity of homes and urban areas [8]. The familiar *swishing noise*, produced by the cyclic motion of the blades through the air, can be particularly displeasing and can have detrimental effects on health [7]. The source of this *swishing noise* is related to interaction of turbulent boundary layers on the wind turbine blades with the trailing edge [6]. Scarcity of suitable, uninhabited sites for onshore wind farms especially in Europe and the need to be connected to an existing power grid drives wind turbine manufacturers to invest in research and development to find practical engineering solutions for aeroacoustic noise attenuation. Part of this effort focuses the modification of the blade and trailing edge geometries [9], porous materials, or brushes in order to eliminate noise at its source [10].

Our society is thus aware of noise in our environment and the effect that it can have on the human well-being [11]. In order to understand noise the underlying generation mechanisms and to be able to efficiently predict noise emission and design attenuation strategies, research focuses on advances in source diagnostics for aeroacoustics [12].

Sources of noise on aircraft or wind turbines can be manifold. However, both examples share one element: three-dimensional lifting surfaces, or airfoils, in the form of a wing on an aircraft or a blade on a wind turbine, respectively.

1.2. AIRFOIL SELF-NOISE

What are the mechanisms for noise generation on the isolated blade of a wind turbine and on the wings of an aircraft? To answer this question, we zoom in on the airfoil itself

and consider the different flow conditions that it might encounter. These flow conditions include the angle of attack, the free-stream velocity, and the degree of inflow turbulence.

According to Brooks *et al.* [13] airfoil self-noise is the “[...] total noise produced when an airfoil encounters smooth non[-]turbulent flow [...]”. Here, non-turbulent flow refers to a flow with low free-stream turbulence intensity (TI) as commonly encountered during free flight or in quiet wind tunnels ($TI < 1\%$). Below, the main mechanisms for airfoil self-noise are addressed. Figure 1.1 illustrates these principal mechanisms.

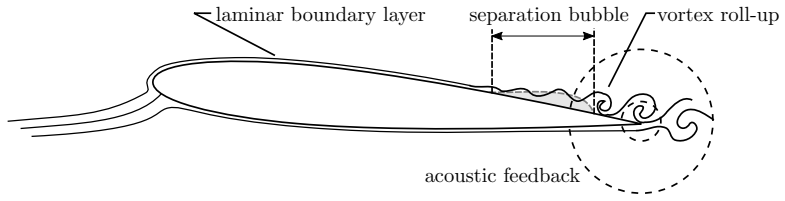
- **Laminar boundary layer instability noise** (figure 1.1a)

Tonal noise, i.e. well-defined peaks about 30dB above background noise in the acoustic pressure spectrum, is often perceived in low-speed flows and/or for small airfoils (low Reynolds number) as found on glider and model airplanes, submarines, cooling fans, ventilators, and compressors. Other relevant applications, experiencing increased interest in recent years, include small wind turbines and small unmanned air vehicles [14, 15]. Nash *et al.* [16] even attributed the observation of a penetrating source of noise on the Wright Flyer, commented on by the British journalist Harry Harper in 1908, to this phenomenon (see citation at beginning of this chapter).

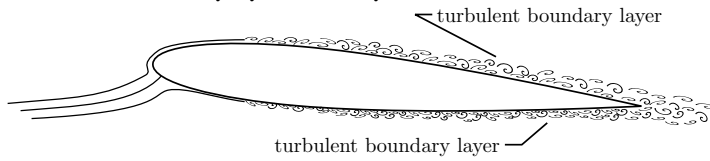
The flow over an airfoil creates a boundary layer due to the presence of viscous shear forces acting on the fluid and surface. Initially, this boundary remains laminar, i.e. no fluctuations are present. At low to moderate Reynolds numbers (about 50,000 to 500,000), small perturbations in a laminar boundary layer are often amplified coherently over a laminar separation bubble or separated shear layer in proximity of the trailing edge through an instability mechanism. These amplified instability waves, which eventually roll up into vortical structures, pass the trailing edge. During this interaction with the trailing edge, acoustic waves are scattered [17, 18]. The acoustic waves propagate upstream and trigger the development of new instability waves. This intrinsic acoustic excitation renders the vortex shedding process periodic in nature and thus narrowband in frequency. Noise generated due to such periodic vortex shedding is perceived as *tones*. Moreover, instability waves in the laminar boundary layer are often characterized by large spanwise correlation, which results in a high intensity of the tonal emission [18].

- **Turbulent boundary layer trailing edge interaction noise** (figure 1.1b)

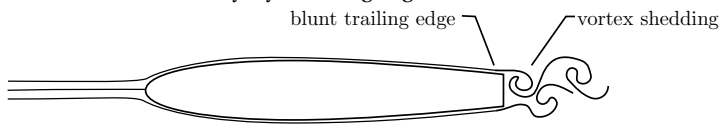
At higher Reynolds number due to earlier transition, the boundary layer attains a more random or turbulent state with a large range of scales being present at the trailing edge. This is the case on most large scale wind turbines and aircraft. Under such conditions, discrete and periodic flow events are no longer encountered at the trailing edge. Instead, the vortical structures in the turbulent boundary layer are to a large extent randomly arranged and its motion can best be described in a statistical manner. A well-known example is the *swish* noise produced by a wind turbine at the blade passing frequency. The underlying source mechanism in this case is believed to be the interaction of the turbulent boundary layer with the trailing edge, while the receiver on the ground experiences an additional low frequency



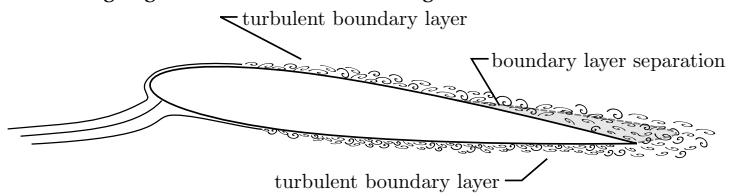
(a) Laminar boundary layer instability noise.



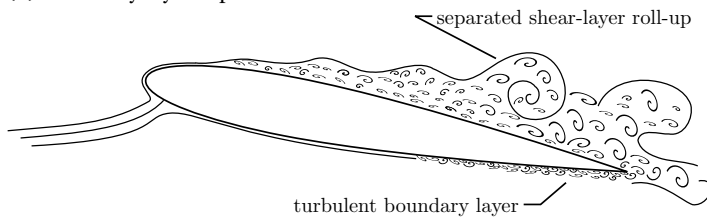
(b) Turbulent boundary layer trailing edge interaction noise.



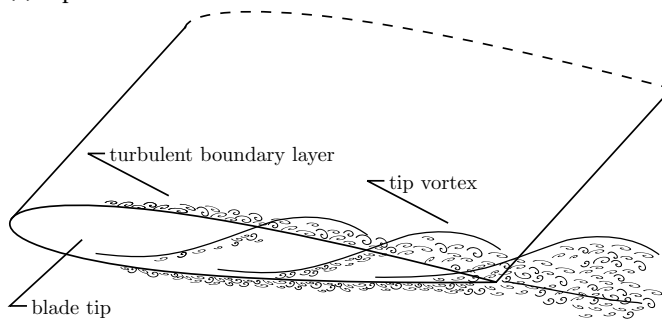
(c) Trailing edge bluntness vortex shedding noise.



(d) Boundary layer separation noise.



(e) Separation stall noise.



(f) Tip noise.

Figure 1.1: Categories of airfoil self-noise. Figures partially adapted from Brooks *et al.* [13].

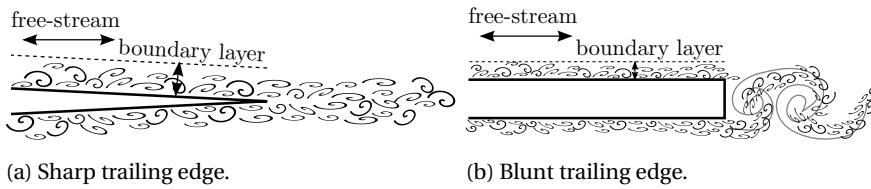


Figure 1.2: Difference between sharp and blunt trailing edge flow.

amplitude modulation of the sound due to directivity and convective amplification [6].

However, the principal mechanism of noise radiation at the trailing edge is similar to that of laminar boundary layer instability noise: the sudden change in boundary condition in combination with the differences in pressure forces acting on pressure and suction side, induced by the turbulent boundary layer, lead to the radiation of acoustic waves. An important difference is that the small scale, less organized turbulent boundary layer results in broadband type acoustic emission. Due to the broadband type character of the noise emission and small correlation of the flow along the span, acoustic feedback is not relevant in this case.

- **Trailing edge bluntness noise** (figure 1.1b)

While laminar boundary layer instability and turbulent boundary layer trailing edge interaction noise are usually prevalent for *sharp* trailing edges, this is not the case for the class of *blunt* trailing edges. Figure 1.2 illustrates the difference between these two conditions. At the sharp trailing edge turbulence originating upstream convects to a large extent unaltered past the discontinuity (figure 1.2a). This behavior is fundamentally different at the blunt trailing edge, which gives rise to large scale vortex shedding (figure 1.2b) over a region of recirculating flow. In contrast to the turbulent boundary layer, vorticity is not shed from the boundary layer over the trailing edge into the wake, but created due to a roll-up process in the near-wake. Due to the fixed length scale (trailing edge thickness or bluntness) and free-stream velocity, this vortex shedding is restricted to a narrow band of frequencies. Such flows involving vortex shedding possess a large spanwise correlation length [19]. The larger correlation for the vortex shedding component often causes bluntness vortex shedding noise to prevail over the turbulent boundary layer trailing edge noise over the associated band of frequencies. In cases where the vortex shedding process is very periodic and of narrowband nature in frequency, the process can even result in tonal noise being emitted.

- **Separation and stall noise** (figures 1.1d and 1.1e)

At non-zero incidence, flow can separate on the suction side and produce noise due to shedding of vorticity. At high angle of attack airfoils often encounter a condition of deep stall, i.e. a separated shear layer forms far upstream on the suction side of the airfoil. As a result of this large scale separation, large scale vortex shedding might occur and due to the comparatively large length scale lead to low-

frequency noise [13]. An extreme example is a flat plate perpendicular to the flow direction. Although not present at optimal operation, separation and stall noise can be encountered on wind turbine blades under certain conditions.

- **Tip noise** (figure 1.1f)

All of the above mechanism can be encountered on infinite aspect ratio airfoils with spanwise homogeneous mean flow condition. An additional mechanism, that is only encountered for finite wings, is related to the formation of a wing tip vortex. Wing tip vortices can be highly turbulent and unsteady and thus generate noise. Additionally, a steady wing tip vortex can lead to convection of fluctuations within the turbulent boundary layer past the wing tip edge and thus act as a noise mechanism similar to that of turbulent boundary layer trailing edge noise (figure 1.1b). This latter is believed to be one of the aerodynamic sources of sound on a modern wind turbine [6].

Further sources of noise generated on airfoils have been investigated in the recent years, such as roughness noise and noise due to the turbulent boundary layer convecting over the airfoil prior to encountering the trailing edge. Often, these sources are weak when compared to trailing edge noise and thus not discussed here. However, the aforementioned definition of airfoil self-noise excludes another important mechanism for the generation of noise on airfoils, namely *vortex-structure interaction noise*.

- **Vortex-structure interaction noise**

Vorticity in the free-stream encountering the airfoil is swept past the surface and causes changes in circulation and unsteady loading, thus resulting in the generation of noise [20]. Noise generated on the rotor of a helicopter when one blade cuts the vortex shed from the tip of another one *blade-vortex interaction noise*, which is typically encountered at descending forward flight condition [21], is an example for this category. Vortex-structure interaction noise is also important in applications where the airfoil is positioned in the wake of another object. The blades of a wind turbine interact often with high levels of atmospheric turbulence (*leading-edge interaction noise*) or the flow perturbed by the supporting structure (*blade-tower interaction noise*) [6].

1.3. PRESENT CHALLENGES AND RESEARCH EFFORTS

It becomes clear from the discussion in the previous section that airfoil self-noise is of concern in particular for the wind turbine industry. Legislation introduced in several countries during the past decade has led to an acceleration in construction and deployment of wind turbines and parks, and as a result rapid growth of wind power generation. Two examples include Germany's Renewable Energy Act (Erneuerbare-Energien-Gesetz, 2000) and the Ontario's Green Energy Act (GEA, 2009). Along comes the need to place an increasing number of wind turbines in the proximity of urban areas. Even in less densely populated areas, required access to the power grid and existing infrastructure results in the construction of wind turbines close to homes (figure 1.3).



Figure 1.3: Wind turbines in Catalonia, Spain. Image provided courtesy of C. Arce Leon.

Moreover, it has been shown that wind turbine noise is perceived more annoying than other forms of industrial noise at the same level of intensity [22]. Control of aerodynamic sources of sound on wind turbines and in particular airfoil self-noise is thus of paramount importance for the wind turbine industry. Thus, research and development efforts have been directed towards effective source identification and elimination. A comparatively complex and expensive approach to noise reduction is shape optimization of the wind turbine blade [9, 23, 24]. A less invasive method are trailing edge add-on solution, for instance serrations, which have become popular in recent years and find application on industrial wind turbines. Howe [25, 26] investigated such trailing edge geometries analytically and concluded that they possess a large potential for noise attenuation. Examples in nature, such as the plumage of a silent flier like the owl, provide further inspiration for the design of such devices [27, 28].

Initially, serrations have been used for the reduction of turbulent boundary layer trailing edge interaction noise [9, 29]. Chong and co-workers [30, 31] also applied serrated trailing edges in research on laminar boundary layer instability noise. Acoustic measurement prove the effectiveness of such noise reduction devices, but do not assist to understand the underlying mechanism, which are not yet fully understood. Thus, source diagnostics is important to assess their working principle. Therefore, recent research efforts with PIV are directed towards the use of advanced flow diagnostics in noise abatement related research [32].

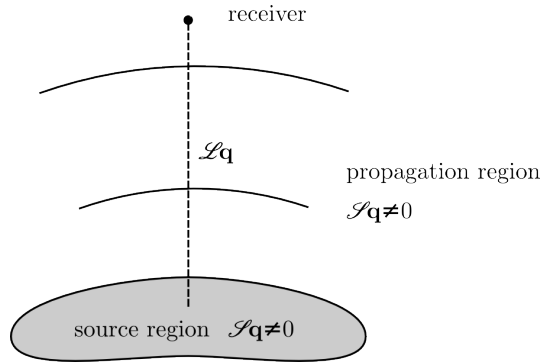


Figure 1.4: Application of acoustic analogy with division of domain in source and propagation region.

1.4. SOURCE DIAGNOSTICS AND ACOUSTIC MEASUREMENTS

Flows generating noise aerodynamically, which have been addressed in section 1.2, can be modeled mathematically. In general, a flow solution written in terms of a state vector \mathbf{q} , containing velocity and thermodynamic variables, fulfills a set of compressible flow equations $\mathcal{N}\mathbf{q} = \mathbf{0}$, where \mathcal{N} is a non-linear operator [33]. \mathbf{q} contains both the hydrodynamic and the acoustic part of the solution. An *acoustic analogy* provides a decomposition of \mathcal{N} into a wave propagation operator \mathcal{L} , which is usually linear and models the propagation of sound, and a non-linear source operator \mathcal{S} . The analogy is then written as $\mathcal{L}\mathbf{q} = \mathcal{S}\mathbf{q}$. If the domain can be divided into a source region, where $\mathcal{S}\mathbf{q}$ is known by simulation or experiment and otherwise zero, and a propagation region and that \mathcal{L} can be inverted, the acoustic part of the solution in the propagation domain \mathbf{q} can be recovered. Such acoustic analogies are at the basis of aeroacoustic research and are useful to obtain insight into the source (analysis of \mathcal{S}) as well as for prediction and modeling of acoustic emission. On the downside, full evaluation of $\mathcal{S}\mathbf{q}$ requires a wealth of information on the flow in the source region; in general volumetric data with sufficient temporal and spatial resolution. Figure 1.4 illustrates this application of the acoustic analogy.

Historically, experimental methods for the investigation of aeroacoustic noise generation include microphone measurements, surface pressure probes, and flow measurement techniques, such as hot-wire anemometry and Laser Doppler Velocimetry (LDV). More recently, PIV measurements have found entry to aeroacoustic research and gain importance with advance in the measurement and processing techniques. Specifically for trailing edge noise, Bahr [34] extensively reviewed the application of flow and acoustic measurement techniques. Below, a short overview of these experimental techniques is given.

1.4.1. ACOUSTIC MEASUREMENT TECHNIQUES

In anechoic wind tunnel facilities, microphone measurements are often used to quantify sound radiation and directivity in terms of the auto-spectral density of the acoustic pressure or integral quantities such as the Sound Pressure Level (SPL). Such techniques have been applied from the early stages of experimental research in aeroacoustics [35].

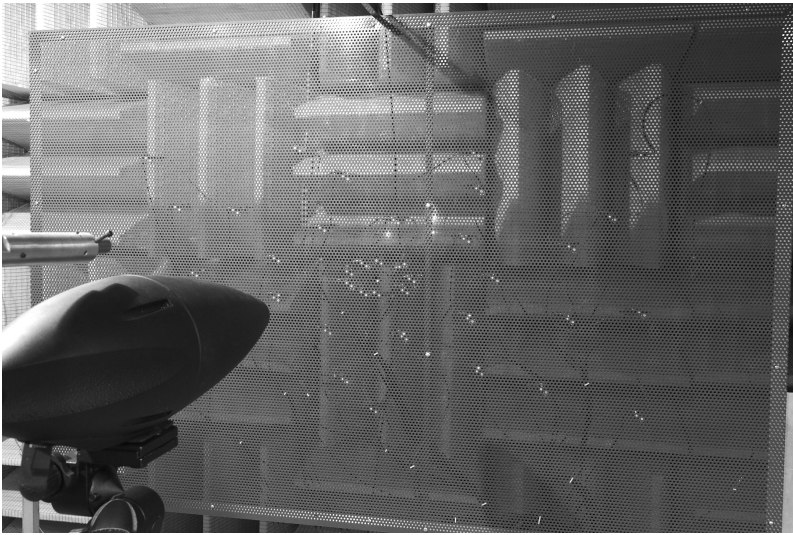


Figure 1.5: Microphone array in the anechoic wind tunnel facility at the University of Notre Dame.

When translated around the source of interest, a single microphone can be used to characterize the directivity of a source, i.e. the intensity of noise emission as a function of direction. Multiple microphones can facilitate such directivity measurements. Multiple microphones have also been used to filter the incoherent part of an acoustic signal and thus to focus on a part of the source region in an attempt to eliminate *parasitic noise*¹ [36, 37]. Directional microphone arrangements, such as the use of acoustic mirrors [38], were introduced for the purpose of source localization.

Today, arrays with several dozen of microphones (acoustic phased arrays) are frequently used in aeroacoustic source diagnostics. They find application in dedicated anechoic facilities, aerodynamic wind tunnels with open and closed test section, but also in field tests [39, 40]. Processing the data collected by acoustic phased arrays with so-called beamforming algorithms allows to obtain a mapping of the source distribution. Figure 1.5 shows an example of a microphone array. Field measurements on wind turbines are relevant to characterize sound radiation and evaluate the effectiveness of noise reduction measures on blades under realistic conditions [41, 42].

1.4.2. FLOW MEASUREMENT TECHNIQUES

Flow visualization has been a classical and readily available tool for the qualitative description of aeroacoustic sources. Flow measurement techniques have found application for the qualitative and quantitative description of the flow field constituting the source region. Figure 1.6 shows an example of the smoke visualization technique, imaging the vortex shedding behind two rounded trailing edge. Another example is the application of shadowgraphy by Yu and Tam [43].

Point measurement techniques, such as hot-wire and Laser Doppler Velocimetry

¹parasitic noise in an acoustic measurement originates from noise sources other than the one of interest



Figure 1.6: Smoke visualization of wake flow behind a beveled trailing edge. Images provided courtesy of S.C. Morris, University of Notre Dame.

(LDV), are commonly applied tools in experimental aeroacoustics, providing high resolution in both space and time. For instance, Nash *et al.* [16] and McAlpine *et al.* [44] used LDV to describe the flow structure on an airfoil, characterizing the development of laminar boundary layer instability waves.

In many aeroacoustic problems involving surfaces, characterization of the unsteady surface pressure field is of interest. For this purpose, surface mounted microphones have found application since the early days of experimental aeroacoustics [35, 45].

1.4.3. PARTICLE IMAGE VELOCIMETRY

In recent years, Particle Image Velocimetry (PIV) flow measurements have been applied for source analysis in experimental aeroacoustics. The aeroacoustic source is in most cases distributed in space and therefore the main incentive for the use of PIV in aeroacoustic source diagnostics is its qualification as a flow field measurement technique. Developments such as high-speed PIV and tomographic PIV even provide the capability to resolve the flow field evolution over time and obtain measurements in a volume. In a comprehensive review article, Morris [12] has provided an overview of PIV in aeroacoustics research. The publication of this review article coincided with the start of this thesis project. On the state of PIV application in this field at the time of writing Morris [12] commented:

“The sound sources can be represented statistically through a double convolution of a Green’s function with the time-dependent two-point correlation of the Lighthill stress tensor. This type of information is never completely available in an experiment, and thus most PIV results are still used as a qualitative description of the acoustic sources.”

An example of such *qualitative* source description is the detailed analysis of the vortex shedding process at a rounded trailing edge geometry by Shannon and Morris [46].

PIV results were phase-averaged to reveal the structure of the flow field during different stages of the vortex shedding process. Nakano *et al.* [47] conducted similar experiments to capture the flow structure around the trailing edge of an airfoil with a transitional boundary layer at the trailing edge. Within the work of the present thesis, the latter flow case has been revisited with planar high-speed PIV [48–52]. The work of Henning and co-workers [53–55] focuses on the integration of information obtained from simultaneous microphone and PIV measurements through correlation analysis (*causality correlation*) for advanced source diagnostics. Breakey *et al.* [56] extended this analysis to application with high-speed PIV systems.

In recent years, high-speed PIV systems have been used for aeroacoustic source diagnostics. Since high-speed systems assess also temporal derivatives, they can provide an enhanced *quantitative* source description and estimation of sound radiation. Schröder *et al.* [57] presented an early feasibility study on the use of planar high-speed PIV for the estimation of turbulent boundary layer trailing edge interaction noise. However, a comparison between predicted and measured acoustic levels was not shown or feasible at this early stage of development, likely due to missing information on the third spatial dimension due to limitations of planar PIV. Haigermoser *et al.* [58] with stereoscopic and tomographic PIV and both de Jong *et al.* [59] and Koschätzky *et al.* [60] with high-speed planar PIV investigated cavity flows and the related flow-induced resonance phenomena. In the latter study, the authors estimated acoustic emissions with time-resolved planar PIV data. Another example is the estimation of vortex-structure interaction from an airfoil mounted in the wake of a cylinder [61, 62]. Schram *et al.* [63] employed stroboscopic PIV measurements in order to analyse the pseudo-time-resolved evolution of vortex pairing and related acoustic sources in a jet. By means of time-resolved tomographic PIV Violato and Scarano [64] characterized jet core breakdown and the quantified the source term identified by an acoustic analogy.

In the studies of Koschätzky *et al.* [60] and Lorenzoni *et al.* [62] high-speed planar PIV systems were used to measure the relevant flow quantities in the source region. The relevant source terms were identified through application of an acoustic analogy. In both cases discrete and periodic vortex shedding events were present, which are highly correlated along the spanwise dimension. The large spanwise correlation essentially reduces the problem of tonal noise estimation to the measurement of a 2D flow close to the shedding frequency, which can conveniently be measured using planar PIV. However, the broadband component cannot be approximated in such way and thus deviations with respect to directly measured acoustic spectra were observed in both studies. In order to relax the constraints imposed by the 2D assumption, both experiment and analysis have to be extended to 3D. Tomographic PIV has been developed and applied for measurement of all velocity components in a volume and is thus one of few flow measurement techniques capable of providing the required information.

Within the work of the present thesis, the extension to 3D velocity field measurements was suggested to solve the issues related to incomplete 2D source description [65]. Recently, the feasibility of the high-speed tomographic PIV approach for prediction of acoustic emissions for trailing edge noise has been demonstrated [66].

The European Project Advanced Flow Diagnostics for Aeronautical Research (AFDAR [67]) has been set up with the aim to accelerate application of and enhance advanced

flow measurement techniques for the analysis of aerodynamic systems. AFDAR contains a component on aeroacoustic source diagnostics with such advanced flow measurement techniques - namely high-speed and tomographic PIV. The work conducted within the present thesis is set within the framework of AFDAR and aims at application of such advanced PIV methods in aeroacoustic research.

Anticipating these recent developments, Morris [12] concluded:

“New advanced PIV methods may have a substantial impact on the study of acoustic sources in the near future. Two examples are tomographic and time-resolved PIV. Continuing improvements in these technologies will provide more complete information about sound production.”

1.5. MOTIVATION AND OBJECTIVES

Advanced PIV techniques, such as high-speed and tomographic PIV have become available for practical application during the past decade. High-speed PIV, being a field measurement technique, can provide a wealth of information on the spatio-temporal structure of an aerodynamic source of sound. In conjunction with acoustic measurements, this information can reveal the underlying mechanism and provide both qualitative and quantitative insight. The general objective of this thesis is to investigate and demonstrate how novel PIV techniques contribute to research in aeroacoustics. Application is centered on airfoil self-noise, which relates to actual noise sources on wind turbines in particular and is therefore considered of relevance to society.

The research questions addressed in this thesis are twofold. On one hand, this thesis is concerned with question in how far complementary PIV measurements can contribute to a better understanding of source mechanisms, in particular for airfoil self-noise (research question I). Direct measurement of the aeroacoustic source may provide new insights and a qualitative description of these underlying mechanisms. On the other hand, it is asked whether novel PIV techniques are suitable to quantitatively predict broadband noise emission on airfoils (II). The capability to obtain noise predictions from flow measurements may provide an alternative to microphone measurements in echoic environments and to isolate sound emitted from a particular region of interest.

To provide answers to these research questions, studies have been performed on a number of selected test cases, focusing on laminar boundary layer instability noise (I), turbulent boundary layer trailing edge interaction noise (II), and vortex shedding noise (I and II).

Laminar boundary layer instability noise has received ample attention in the past, but still questions with regard to the details of the noise generation mechanism remain unanswered. In combination with microphone measurements for far-field and unsteady surface pressure, the high-speed PIV may allow for relating the unsteady flow structure to the generation of tonal noise and in particular for answering the following questions:

- Experimental analysis of the laminar boundary layer instability noise mechanism
 - What flow events are responsible for noise generation?
 - What is the cause of the presence of multiple tones in the acoustic spectrum?

- How does the strong tonal noise generated at the trailing edge influence upstream events in the flow over the airfoil?

Noise due to the interaction of a turbulent boundary layer interaction with the trailing edge is selected as a test case for a quantitative source description of broadband noise. High-speed tomographic PIV is applied to further complement and extend the limits of the flow measurements for a case where volumetric and time-resolved information on the source field is required in order to obtain an accurate estimate. In particular, the studies presented in this thesis focus on the following aspects:

- Experimental deduction of pressure field quantities for trailing edge aeroacoustics
 - What are relevant source quantities for trailing edge noise?
 - Can these quantities be measured using advanced PIV methods?
- Quantitative estimation of turbulent boundary layer trailing edge interaction noise based on high-speed tomographic PIV
 - How can PIV be applied for the estimation of broadband noise?
 - How does the noise estimation compare to acoustic measurements?

Trailing edge bluntness noise and the associated vortex shedding remains a subject of interest and is investigated here for a rounded trailing edge. By means of a modeling approach, the flow field parameters required for the estimation of vortex shedding noise can be reduced to those measurable in a stereoscopic PIV experiment. The vortex shedding process is described and the general applicability of such the semi-empirical prediction approach is assessed.

- Experimental validation of a semi-analytic model for vortex shedding noise
 - Is it possible to estimate the vortex shedding noise at a general trailing edge geometry by measurement of a reduced set of parameters?
 - How does the noise estimation compare to acoustic measurements?

1.6. OUTLINE OF THE THESIS

The thesis contains five parts: *Prologue*, *Laminar boundary layer instability noise (Part I)*, *Turbulent boundary layer trailing edge interaction (Part II)*, *Trailing edge bluntness noise (Part III)*, and the *Epilogue*.

The *Prologue* offers the reader an introduction to the topic and motivation, research objectives, background, and methodology. Chapter 2 provides an overview of available literature and important concepts of airfoil self-noise, in for the particular laminar boundary layer instability, turbulent boundary layer trailing edge interaction, and trailing edge bluntness noise mechanisms. In chapter 3 the measurement techniques applied in the experimental studies described in *Parts II* and *III* are introduced. In particular, relevant aspects of time-resolved and tomographic PIV for aeroacoustics are discussed. It further explains how high-speed tomographic PIV can be applied to obtain the

necessary information for trailing edge noise estimation. The PIV-based pressure reconstruction technique in turbulent boundary layers is discussed and the chapter concludes with an overview of unsteady surface pressure measurements.

Part I addresses the underlying mechanism for *laminar boundary layer instability noise* and provides a qualitative source description for this purpose. Chapter 4 examines the relevance of pressure side, suction side, and their interaction for a large range of flow conditions. Chapter 5 describes the source field as origin of the typical tonal noise observed for this type of mechanism in more detail. Concluding *Part I*, chapter 6 considers the influence of acoustic feedback on upstream events, in particular on separation bubble dynamics.

Part II is concerned with the quantitative estimation of turbulent boundary layer trailing edge interaction noise. PIV-based estimation of relevant, statistical quantities of the unsteady surface pressure field induced by a turbulent boundary layer is compared to Direct Numerical Simulation (DNS) results (chapter 7). In chapter 8, a pressure reconstruction technique is applied with tomographic PIV data and combined with the theory on diffraction noise. The PIV-based noise estimation is then compared to phased array measurements of the acoustics emissions.

Part III treats the applicability of a semi-analytical model for the estimation of trailing edge bluntness noise, in particular of the vortex shedding behind a rounded trailing edge. Combination of such a model with time-resolved stereoscopic PIV measurements is proposed and the results are compared to those obtained through phased array measurements.

The thesis concludes with the *Epilogue* (chapter 10), summarizing the conclusions of the different parts.

2

AIRFOIL SELF-NOISE

*Courage is the price that
Life exacts for granting peace.
The soul that knows it not, knows no release,
From little things;
Knows not the livid loneliness of fear,
Nor mountain heights where bitter joy can hear
The sound of wings.*

Amelia Mary Earhart, American aviator

I wanted to make noise, not study theory.

James Hetfield, lead vocalist of Metallica

Airfoil self-noise is relevant in a multitude of engineering applications. Several of the distinct mechanisms, which are labeled as airfoil self-noise, are related to trailing edge noise. This chapter provides an overview of important results related to trailing edge noise and further discusses the particularities of turbulent boundary layer trailing edge interaction, trailing edge bluntness, and laminar boundary layer instability noise.

Parts of this chapter have been published in
the Journal of Fluid Mechanics **747** (2014) [50]
the Journal of Fluid Mechanics (2015) [68]
the Journal of Fluid Mechanics (2015) [69]
the Journal of Sound and Vibration **346** (2015) [66].

2.1. TRAILING EDGE NOISE

TRAILING EDGE NOISE is fundamental to a number of the noise generating mechanisms that are categorized as airfoil self-noise (section 1.2). These include the interaction of the trailing edge with instability waves, the turbulent boundary layer, and vortex shedding due to bluntness. Thus we embark first on a very short history on important analytical developments concerning trailing edge noise, before introducing the specifics of sharp and blunt trailing edges as well as transitional boundary layers. Howe [70, 71] provided extensive reviews on the theory of trailing edge noise.

2.1.1. A BRIEF HISTORY

Lighthill [3] considered the problem of jet noise and thus investigated the generation of sound due to turbulence in an unbounded medium. He rearranged the governing flow equations in the form of a wave equation and source term (see section 1.4) and then considered a turbulent flow of length scale δ and velocity u_∞ . Based on dimensional arguments, in a medium of density ρ , and at Mach number $M_0 = u_\infty/c_0$ with speed of sound c_0 , the radiated sound intensity I (see appendix A for the definition) at receiver distance R (figure 2.1a) was found to scale with

$$I \sim \rho u_\infty^3 M_0^5 \frac{\delta^2}{R^2} \quad (2.1)$$

However, it was quickly realized that, especially for low speed flows, the presence of solid boundaries in the flow change the radiation of sound significantly. Thus, soon after the seminal contribution to aeroacoustics of Lighthill [3], Curle [20] considered the influence of solid boundaries upon the radiation of sound, namely a surface of length c . In the case of a compact source region (Helmholtz number $\text{He} = kc = 2\pi c/\lambda_a \ll 1$ with k and λ_a the acoustic wavenumber and wavelength, respectively; figure 2.1b), the propagation time of sound waves within that region is negligible with respect to the inverse of the frequency and thus the source can be replaced by a point source. By dimensional analysis it was demonstrated that the sound intensity due to an equivalent dipole, replacing the quadrupole distribution and surface, scales as

$$I \sim \rho u_\infty^3 M_0^3 \frac{c^2}{R^2} \frac{L}{c} \quad (2.2)$$

The additional factor L/c accounts for the aspect ratio of the lifting surface. Thus, the intensity or radiated sound power scales with the free-stream velocity $\sim u_\infty^6$, given $kc = \omega c/c_0 \ll 1$, where ω is the angular frequency. Further, equation 2.2 implies a dependence of $\sim \rho^2 u_\infty^4 M_0^2 = 4q_\infty^2 M_0^2$, with the free-stream dynamic pressure $q_\infty = 1/2\rho u_\infty^2$, for the spectrum of acoustic pressure. Comparison to equation 2.1 ($\sim M_0^5$) reveals that the presence of surfaces indeed leads to stronger sound emission at low Mach numbers. In the case of a compact surface with infinite span, the directivity of the source is that of a dipole (figure 2.2).

But which characteristic flow scales generate sound waves at frequencies such that $kc = \omega c/c_0 \ll 1$ holds? Consider a train of eddies of characteristic wavelength $\lambda \approx 2\delta$ that convects at velocity u_∞ and at frequency $\omega = 2\pi u_\infty/\lambda \approx \pi u_\infty/\delta$ past the trailing edge. One can then write a condition for the acoustic compactness of the surface in terms

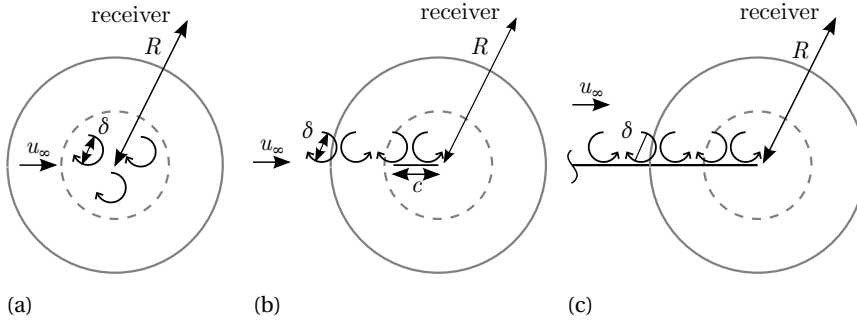


Figure 2.1: Simplified representations of noise generating flows scaling parameters: a) free-stream turbulence, b) compact surface, and c) non-compact surface.

of parameters related to the flow field $2\pi M_0(c/\lambda) \ll 1$. In contrast, for non-compact surfaces or, equivalently, comparatively high frequencies ($kc = \omega c/c_0 \gg 1$), the results of Curle [20] are difficult to interpret since the reduced dipole term cannot be estimated quantitatively by dimensional arguments [72].

Powell [73] was the first to investigate the specific problem of *edge noise* in the non-compact case analytically. The author suggested that the sound power varies with the free-stream velocity between $\sim u_\infty^4$ and $\sim u_\infty^6$. Additionally, the auto-spectral density of acoustic pressure was found to vary inversely to the cube of the frequency $\sim \omega^{-3}$.

Ffowcs Williams and Hall [72] approached the trailing edge noise problem by solving the analogy of Lighthill [3] using the analytic, tailored Green's function for a semi-infinite half-plane (figure 2.1c). The latter assumption requires that the acoustic wavelength is small with respect to the chord length. Considering turbulent eddies of characteristic size δ passing the trailing edge with span L at close distance, Ffowcs Williams and Hall [72] found the intensity of the radiated sound to scale as

$$I \sim \rho u_\infty^3 M_0^2 \frac{\delta^2 L}{R^2 \delta} \sin^2(\theta/2) \quad (2.3)$$

For eddies remote to the edge, the result of turbulence in free space (equation 2.1) was recovered. The last term in equation 2.3, $\sin^2(\theta/2)$, indicates the directivity of the source in the limit of high frequency ω , which is different from that of the compact dipole. Instead, sound radiation is biased towards the upstream direction in this case (figure 2.2). Equation 2.3 can be interpreted as a dependence of $\sim u_\infty^5$ on the free-stream velocity and δ on the characteristic scales of the flow, e.g. boundary layer thickness. Equation 2.3 also implies a dependence of $\sim \rho^2 u_\infty^4 M_0 = 4q_\infty^2 M_0$ for the spectrum of acoustic pressure. Similar works based on the analogy of Lighthill [3] include the ones of Crighton and Leppington [74], Crighton [75] and Howe [76, 77, 78]. Figure 2.2 summarizes the characteristics of the compact and non-compact cases for trailing edge sound radiation.

At the same time, Chase [79, 80], Crighton [81], Chandiramani [82] and Amiet [17] proposed the application of diffraction theory within the context of trailing edge noise. In diffraction theory a scattered pressure field deduced by requiring specific boundary

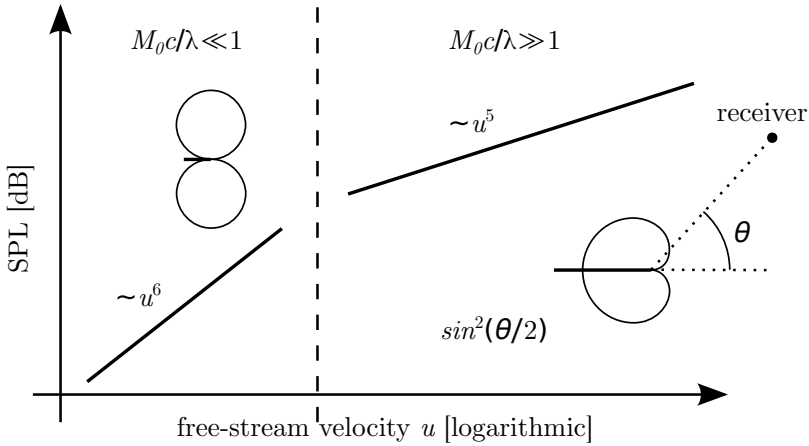


Figure 2.2: Characteristics of trailing edge noise. Figure adapted from Blake [19].

conditions for the overall pressure. This scattered pressure field is thus the result of an interaction of the incident pressure field, induced by the turbulent boundary layer, with the trailing edge. An estimation of noise emission based on the characteristics of the unsteady surface pressure field thus becomes possible. This approach has been applied and investigated in a number of experimental and numerical studies [36, 83, 84].

Later, Howe [85] considered the back-scattering effects from the leading edge on noise radiation for acoustically compact chords (relatively large wavelength). Under such conditions the assumption of the semi-infinite half-plane [17, 72] does not hold and the radiation pattern approaches that of a dipole instead of the cardioid. Roger and Moreau [83, 86] proposed similar modification to the work of Amiet [17] to account for compact chord effects. Furthermore, Roger and Moreau [86] introduced 3D gusts to infer the far-field radiation for a receiver off the mid-span plane. Roger and Moreau [87] summarized and commented on the limitations of airfoil self-noise models.

2.1.2. INFLUENCE OF TRAILING EDGE FLOW AND GEOMETRY

Apart from the radiation characteristics for the compact (equation 2.2) and non-compact case (equation 2.3), specific features of the trailing edge geometry can have a large influence on the radiated sound. In the introduction, figure 1.2 showed two different trailing edge flows around a sharp and a truncated trailing edge, respectively. These flows show a fundamentally different behavior and, consequently, the energy associated to a specific turbulence length scales δ and frequency ω differs.

Based on an empirical evidence, Blake [19] stated that a trailing edge can be considered as sharp if a bluntness parameter $T/\delta^* < 3.3$, where T is for instance the thickness of the truncated trailing edge and δ^* the displacement thickness of the boundary layer. If this condition applies, sound radiation is dominated by the contribution of the boundary layer turbulence interacting with the trailing edge. If the boundary layer is turbulent (figure 1.2a), the radiated noise is of broadband character. A special case is a boundary layer reaching the trailing edge in a transitional stage, which will be treated in section

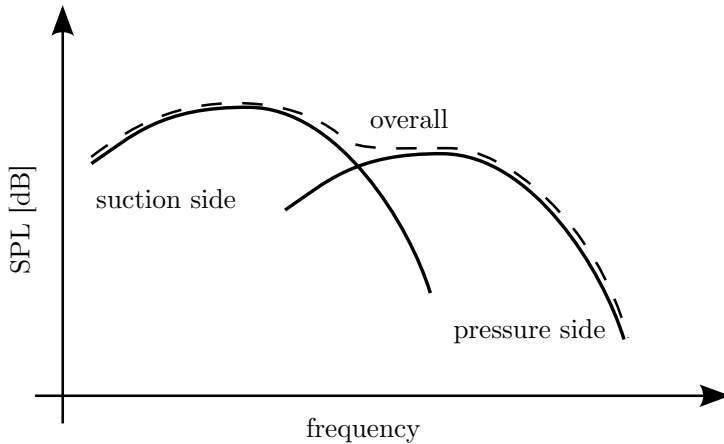


Figure 2.3: Contribution of pressure and suction side boundary layers to overall acoustic spectrum.

2.3.

For attached flow at the trailing edge, equation 2.3 allows for some considerations on the relative contribution from the pressure and suction side of an airfoil. The length scale δ of the boundary layer on the suction side is larger than that on the pressure side [13]. While the dimensional frequency associated to fixed a non-dimensional frequency $\omega\delta/u_\infty$ is thus larger for the pressure side, the intensity of the radiated sound is smaller. Figure 2.3 shows schematically the expected relative contribution of pressure and suction side to overall broadband noise generation.

For larger values of the bluntness parameter $T/\delta^* > 3.3$, vortex shedding linked to tonal noise is likely to occur (figure 1.2b). In such cases, the flow separates on the suction and pressure side, forming a region of reversed flow behind the trailing edge. The strong velocity gradients in the separated shear layers lead to the roll-up of vortices behind the trailing edge due to an instability mechanism. The frequency of this roll-up can be expressed in terms of a constant non-dimensional shedding frequency $St = f_{sh}\lambda/u_c$, where u_c is a convective velocity and depends as the length scale λ on the details of the flow geometry. For a fixed geometry and at high Reynolds number, u_c and λ are proportional to T and u_∞ , respectively. For a thick plate with non-rounded corners and large bluntness ratio, the limiting value of the shedding frequency is $St = f_{sh}T/u_\infty \approx 0.21$ [13]. Figure 2.4 schematically shows the influence of vortex shedding on the radiated sound. For a given trailing edge bluntness $T_1/\delta^* \gg 1$ a clearly defined peak due to vortex shedding is present. Decreasing the bluntness to $T_2 < T_1$ results thus in a broader peak, centered at higher frequency, and lower in intensity (equation 2.3 with $\delta = T$). In case $T \approx \delta^*$, the boundary layer thickness should be considered in addition to the bluntness of the edge, e.g. $\lambda \approx T + 2\delta^*$ [19].

Apart from sharp and sharply truncated trailing edges, situations with rounded trailing edges are common and serve as parametric representations for more general classes of trailing edges. These half-rounded trailing edges are also called beveled trailing edges (figure 2.5) and blend the mechanisms of broadband trailing edge interaction and vortex

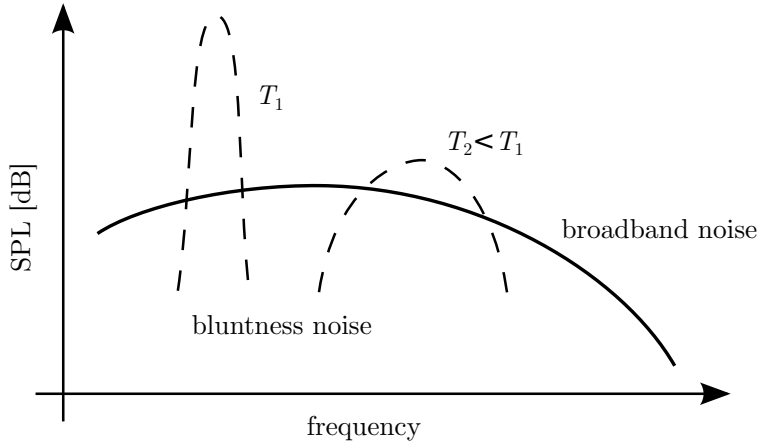


Figure 2.4: Influence of trailing edge bluntness on spectrum of radiated sound.

shedding noise. The geometry has been introduced in the work of Blake and co-workers [45, 88, 89], and is characterized by the angle θ enclosed by the surfaces at the trailing edge, and the ratio of radius of curvature over plate thickness R/T . The beveled shape results in a net camber and, hence, the upper and lower surfaces will be referred to as the *suction* and *pressure* sides, respectively.

The details of the beveled trailing edge flow field depend on the geometric parameters (θ , R/T) as well as on the flow conditions, specified by the Reynolds number ($Re = u_\infty T/\nu$ with ν the kinematic viscosity) and the bluntness parameter (T/δ^*). For larger θ a region of reverse flow extends over the trailing edge. In contrast, for larger radii of curvature R/T and Reynolds numbers Re , the extent of this region tends to be smaller since separation is delayed towards the trailing edge. An exception is the case $R/T = 0$, where the upper separation point remains fixed at the kink between the straight and slanted part of the plate. Shannon and Morris [46] investigated the structure of the wake using PIV and separated the velocity field into periodic, large scale motions related to vortex shedding and small scale turbulent motions by considering phase-averaged velocity fields. The flow separates on both the suction and pressure sides and forms a region of reversed flow. Vorticity shed from the lower boundary layer rolls up into this reverse flow region and convects coherently downstream. In contrast, vorticity in the upper shear layer was observed become more dispersed during the roll-up process.

To characterize the flow behind a blunt trailing edge, a larger set of length scales than for a sharp trailing edge is thus required. For the blunt trailing edge with vortex shedding the region over which vortex formation takes place and the characteristic size of these wake vortices are relevant parameters [19]. Following the notation of Blake [19], the *vortex formation length* is denoted by l_f and the wake thickness parameter by y_f . Blake [19] gives the definition of the wake thickness parameter y_f as the shear layer spacing (distance in y -coordinate direction between maximum streamwise velocity fluctuations $rms(u)$ of the pressure and suction side shear layers) at the end of the vortex formation zone. Gershfeld *et al.* [89] and Shannon and Morris [46] further specify that the end of

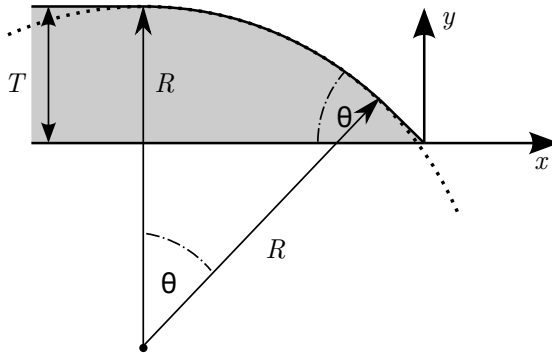


Figure 2.5: Parametric representation of beveled trailing edge.

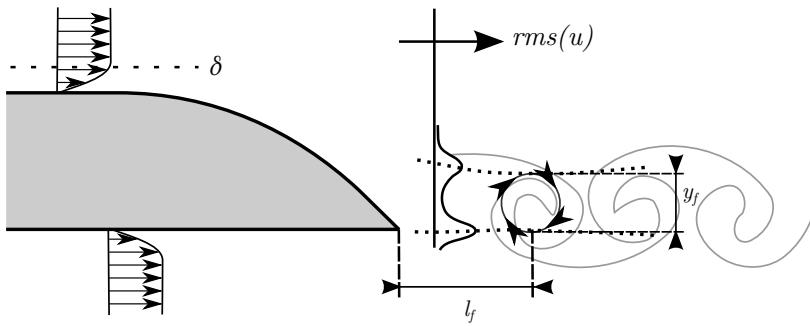


Figure 2.6: Definition of scaling parameters at blunt trailing edge. Geometry shown for $R/T = 2.5$ and $\theta = 45^\circ$.

the vortex formation zone is defined by the minimum distance between the maxima in the near wake region. A typical value for a trailing edge with $\theta = 45^\circ$ is $y_f/T \approx 0.5$ [19] and y_f replaces T in the definition of the non-dimensional frequency. The vortex formation distance l_f is then defined as the distance between the trailing edge and the end of the vortex formation zone. For $\theta = 45^\circ$ a typical value is $l_f/T \approx 1$ [19]. Figure 2.6 shows a schematic representing these definitions. It should be noted, however, that the definition of these parameters is not unique [90].

Howe [91] proposed a model for and analyzed the flow around a beveled trailing edge. He concluded that for attached flow on both sides, the finite angle θ is only relevant for sound radiation at high frequency, i.e. if the acoustic wavelength λ_a is small with respect to plate thickness T . However, flow separation on the beveled part removes turbulent eddies in the separated shear layer from the vicinity of the edge and their influence for high frequencies $\omega T/u_\infty \gg 1$ becomes negligible. The amplitude of edge-generated sound was found to decrease exponentially with increasing frequency and predicted noise levels are significantly smaller than for the semi-infinite half-plane [71]. This is corroborated in parts by the earlier analysis of the scattering from a semi-infinite half-plane by Ffowcs Williams and Hall [72], who found the radiated sound intensity to decrease with $(kr_0)^3$, where r_0 is the distance between an elementary part of the source region and the edge. Blake and coworkers [45, 88, 89] and others [46, 92–95] have investigated the flow around beveled trailing edges experimentally. Wang and coworkers [96–100] have employed such beveled edge geometries as test cases for numerical computation of trailing edge noise by coupling LES of the source field with the analytic method of Ffowcs Williams and Hall [72] for propagation to the far-field.

2.1.3. METHODS FOR TRAILING EDGE NOISE PREDICTION

With the availability of PIV and in particular high-speed systems and advanced processing algorithms, the experimental description of the aerodynamic source field reached a point where estimation of aeroacoustic emission becomes possible. Wang *et al.* [33], Colonius and Lele [101] provided comprehensive overviews for computational prediction of aerodynamically generated noise.

DIRECT APPROACHES

In direct computations, propagation to the far-field is computed simultaneously with the simulation of the aeroacoustic source by solving a set of compressible flow equations. The large ratio between hydrodynamic and acoustic length scales $\lambda/\lambda_a \sim M_0$ at low Mach number $M_0 \ll 1$ renders it difficult and expensive, however, to capture both scales within the simulation [100, 101].

The experimental equivalent to the direct computational approach are microphone measurements in an anechoic facility, which provide a free field response for the sound radiation from the isolated source of interest. However, the experimental approach also has shortcomings. In particular for trailing edge broadband noise at low Mach numbers, acoustic pressure fluctuations are low with respect to the background noise level of the wind tunnel, which is caused by parasitic noise sources, or even the self-noise of the transducer. Parasitic noise sources can be identified and often successfully eliminated by the use of microphone arrays at the expense of obtaining average results over the

aperture of the latter.

HYBRID APPROACHES

In hybrid approaches, the domain is split into a *source region* and a *propagation region* (see section 1.4). The source region usually contains the turbulent part of the flow and the surfaces that this turbulent flow interacts with. Its boundary is often placed within the near field of the aeroacoustic source. Within the propagation region, the form of the (usually linear) propagation operator for the radiated sound waves is assumed to be known. Here, the non-linear flow equations are thus replaced by a simpler set of equations (e.g. Linearized Euler Equations, wave equation). The propagation, i.e. the acoustic part of the computation, is solved using integral methods (based on Green's function) or methods based on a discrete expression of the propagation operator.

The flow in the source region is obtained from a fluid dynamic simulation with sufficient spatial and temporal resolution (DNS, LES) and the source terms (and boundary conditions) are identified through an acoustic analogy and consequently computed. Alternatively, these source terms can be estimated through a combination of a turbulence model and a lower fidelity flow simulation (RANS, URANS). As stated explicitly by Wang *et al.* [33], at low Mach number $M_0 \ll 1$ incompressible flow solutions can be adequate to approximate the source terms.

A fundamental assumption, which is often accepted when such hybrid approaches are used, is unidirectional coupling between flow and sound. Sound is generated by the turbulent flow, but does not act back upon it [33]. An example of a flow involving such acoustic feedback is that of amplified laminar boundary layer instabilities, which will be discussed in section 2.3. In a compressible simulation or in an experiment, where compressible effects within the source region are taken into account, this assumption can be relaxed.

In experimental approaches to noise estimation, flow field measurements (usually PIV) replace the simulation of the source region. PIV has been used for the measurement of turbulent flows and mapping of aeroacoustic sources [12] as well as for the prediction of sound radiation based on an acoustic analogy (e.g. Koschätzky *et al.* [60] and Lorenzoni *et al.* [62]) for cases limited to a narrow band of frequencies and wavelengths. The limited dynamic range of experimental approaches in space and/or time prevent a comprehensive approach.

Within the framework of this thesis, Tuinstra *et al.* [65] assessed two approaches for broadband trailing edge noise estimation based on time-resolved and volumetric PIV data. Application of the (tailored) Green's function for a semi-infinite half-plane following Ffowcs Williams and Hall [72] to the distributed volume source and diffraction theory [17], relating the radiated sound field to the unsteady surface pressure through a surrogate model.

Tailored Green's function Ffowcs Williams and Hall [72] considered the time-harmonic form of Lighthill's equation [3], which corresponds to an inhomogeneous Helmholtz equation. Assuming that the airfoil geometry is represented by a semi-infinite half-plane, the solution is found by solving for the acoustic pressure using an analytic, tailored Green's function. The assumption applies if the thickness of the airfoil is sub-

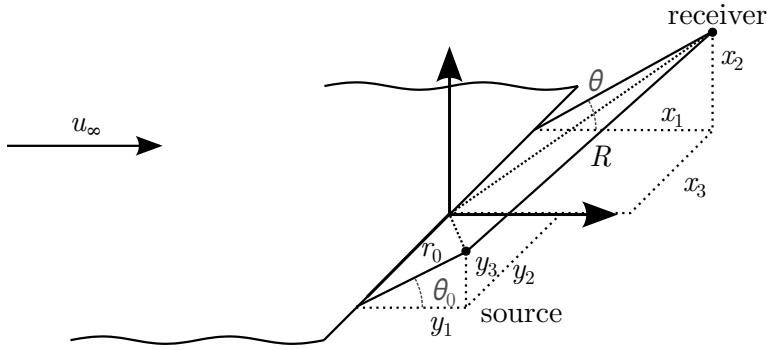


Figure 2.7: Geometry of a semi-infinite plane in a turbulent flow. The source is located at \mathbf{y} and the receiver at \mathbf{x} .

stantially smaller and the chord very large with respect to the acoustic wavelength. The Green's function solving the Helmholtz equation for this semi-infinite half-plane is known [102]. The resulting volume integral is evaluated over the quadrupole source distribution in the turbulent boundary layers on the two sides of the airfoil and in the wake. Viscous stresses are assumed to be negligible for noise generation and convection effects are neglected for low Mach numbers.

With the change of coordinate system introduced by Wang [98, 99] the integral expression for the acoustic pressure p_a is given by equation 2.4, where $R = |\mathbf{x} - \mathbf{y}|$, $\sin \Phi = R / \sqrt{R^2 + (z - z_0)^2}$ (figure 2.7), and k is the acoustic wavenumber $k = \omega / c_0$ with c_0 the speed of sound:

$$\begin{aligned} \hat{p}_a(\mathbf{x}, \omega) \approx & \rho_\infty \frac{2e^{-i\pi/4}}{\pi^{1/2}} k^2 \sin(\theta/2) \int_V \frac{e^{ikR} \sin^{1/2}(\Phi)}{4\pi R (2kr_0)^{3/2}} \\ & \times \left\{ \left[\widehat{u}_\theta^2 - \widehat{u}_r^2 \sin(\theta_0/2) \right] - 2\widehat{u}_r \widehat{u}_\theta \cos(\theta_0/2) \right\} d^3\mathbf{y} \end{aligned} \quad (2.4)$$

From equation 2.4 it is apparent that an evaluation of the far-field acoustic power requires a wealth of information on the velocity field. Not only time-resolved data for all velocity components in the 3D source region is required, but also a high accuracy and spatial resolution is needed to account correctly for phase cancellation throughout the domain. If the information is obtained experimentally, additionally the effect of measurement noise needs to be considered. Together, these requirements and limitations render the direct application of equation 2.4 at present not suitable for the use with PIV data and result in a large overprediction of the radiated sound intensity [65].

Diffraction theory A second approach for the experimental prediction of trailing edge noise is based on diffraction theory [17, 79–81, 83, 86, 87] and relates spectral characteristics of the unsteady surface pressure field to those of the far-field acoustic pressure. Amiet [17] considered Schwarzschild's solution [103] for solving the scattering problem around the trailing edge for the case of a semi-infinite half-plane (flat plate), which is

equivalent to acoustic wavelengths smaller than the chord (non-compact). The incident pressure is induced by the quadrupolar source distribution in the turbulent boundary layer and assumed to be statistically stationary near the trailing edge. Consecutively, the scattered pressure field is determined based on Schwartzschild's solution with appropriate boundary conditions. Roger and Moreau [86] derived a leading edge back-scattering correction through a two-step Schwartzschild solution for wavelengths on the order of the chord length and a correction for 3D gusts. The same authors presented an experimental validation of this approach and assessed the implications of the 3D gust solution for finite aspect ratio wings [83]. Further, they assessed the applicability of this approach in an industrial context and found it to be sufficiently accurate (on a dB scale) when applied with directly measured surface pressure statistics, but reported uncertainties of up to 10dB when source data is based on Reynolds Averaged Navier-Stokes (RANS) along with models for the unsteady surface pressure spectrum [87]. Sandberg and Sandham [104] performed DNS on a one-sided turbulent boundary layer interacting with a trailing edge and compared the simulation results to the classical theory of Amiet [17]. Specifically for trailing edge bluntness noise, Roger *et al.* [105] proposed an approach also based on diffraction theory, but reducing the required statistics to the upwash velocity in the wake instead of the incident pressure field.

2.2. DIFFRACTION AT THE TRAILING EDGE

2.2.1. INCIDENT PRESSURE GUST

Within the framework of diffraction theory following Amiet [17], the incident pressure field, which is induced by the convecting turbulent boundary layer upstream of the trailing edge, is assumed to be frozen. This means that a given surface pressure distribution convects in downstream (positive x -) direction at a *convective velocity* u_c .

If it is assumed that the airfoil is thin and the camber small ($k_y \approx 0$), the incident surface pressure can be split into Fourier components represented by $p(t, x, y, z) = p(t, x, 0, z) = p_0 e^{i(\omega t - k_x x - k_z z)}$ [17]. Figure 2.8a demonstrates the concept of a general 3D incident pressure gust, convecting in an arbitrary direction along the surface (x - z plane), which is defined by the wavenumber vector $(k_x, 0, k_z)$ and considered in the general theory on 3D pressure gusts [17, 86]. Note that the wavelength of the resulting gust is $2\pi / (k_x^2 + k_z^2)^{1/2}$.

A special case of this general representation is obtained for $k_z = 0$, e.g. a 2D gust with wavefronts parallel to the z -coordinate axis, which coincides with the trailing edge (figure 2.8b). The wavefront of such a gust can be considered to pass the trailing edge simultaneously for all z .

The velocity at which pressure fluctuations convect is in general a function of frequency and wavenumber. This velocity is also referred to as the *convective velocity* u_c . In the turbulent boundary layer and similarly in wake flows behind airfoil profiles, convection mainly occurs in the direction of free-stream velocity. The expression for the pressure gust can be rewritten as $p(t, x, 0, z) = p_0 e^{i(\omega t - k_x x - k_z z)} = p_0 e^{i(\omega / k_x t - x - k_z / k_x z) k_x}$. For a given z location, the phase remains thus constant for $\omega / k_x t - x = \text{const}$ or $dx/dt = \omega / k_x = u_c$. Thus, the convective velocity u_c represents the phase velocity in x -direction and is directly related to the maxima in the streamwise wavenumber-frequency spectrum $\Pi(\omega, k_x, 0)$ (*convective ridge*) [106].

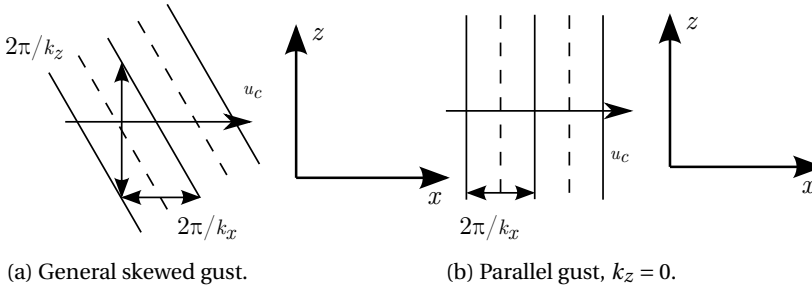


Figure 2.8: Concepts of pressure gusts convecting at velocity u_c .

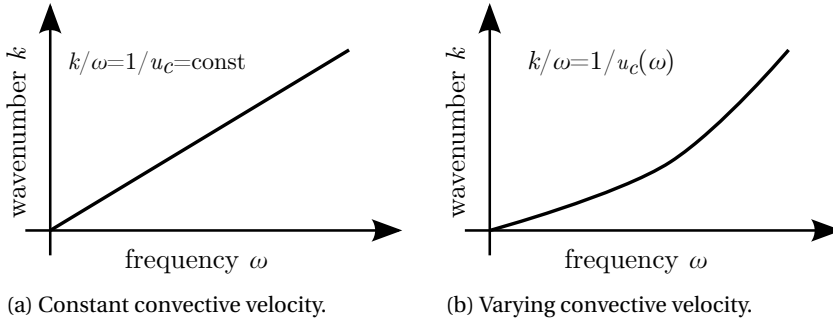


Figure 2.9: Convective velocity $u_c = \omega/k_x$ in the wavenumber frequency spectrum. Line indicates convective ridge.

Along this convective ridge the largest pressure fluctuations are encountered. For the particular case of a zero pressure gradient turbulent boundary layer the convective velocity is a weak function of frequency with $u_c/u_\infty \approx 0.6 - 0.8$ and is often assumed to be constant [17, 106] in first approximation. Figures 2.9a and 2.9b show typical wavenumber-frequency spectra for the case of constant and varying convective velocity, respectively.

2.2.2. UNSTEADY SURFACE PRESSURE FIELD

STATISTICAL DESCRIPTION

Disturbances in the boundary layer induce an incident unsteady surface pressure field. In the vicinity of the trailing edge, this incident pressure field is assumed to be statistically stationary and homogeneous in space. With the streamwise, transverse, and spanwise coordinates denoted by x , y , and z , respectively, the pressure field can be decomposed in its frequency $\omega = 2\pi f$ (where f is the ordinary frequency), streamwise wavenumber k_x , and spanwise wavenumber k_z components for the case of a flat surface ($k_y = 0$) as described in the previous section. This incident pressure field is then characterized by the wavenumber-frequency spectral density $\Pi(\omega, k_x, k_z)$, which can be written as the space-time Fourier transform of the unsteady surface pressure correlation function (see appendix E for definition of statistical quantities):

$$\Pi(\omega, k_x, k_z) = \frac{1}{(2\pi)^3} \int_{-\infty}^{\infty} \int_{-\infty}^{\infty} \int_{-\infty}^{\infty} R_{pp}(\tau, \Delta x, \Delta z) e^{i(k_x \Delta x + k_z \Delta z - \omega \tau)} d\Delta x d\Delta z d\tau \quad (2.5)$$

Evaluating the Fourier transform over time only, the wavenumber-spectral density expressed in terms of the cross-spectral density function $\Phi_{pp}(\omega, \Delta x, \Delta z)$, where Δx and Δz are the separation in streamwise and spanwise direction, is

$$\Pi(\omega, k_x, k_z) = \frac{1}{(2\pi)^2} \int_{-\infty}^{\infty} \int_{-\infty}^{\infty} \Phi_{pp}(\omega, \Delta x, \Delta z) e^{i(k_x \Delta x + k_z \Delta z)} d\Delta x d\Delta z \quad (2.6)$$

The coherence function or normalised cross-spectral density $\gamma(\omega, \Delta x, \Delta z)$ is defined as

$$\gamma(\omega, \Delta x, \Delta z) = \frac{\Phi_{pp}(\omega, \Delta x, \Delta z)}{\Phi_{pp}(\omega, 0, 0)} \quad (2.7)$$

The related spanwise magnitude square coherence $\gamma^2(\omega, \Delta x, \Delta z)$ is defined by

$$\gamma^2(\omega, \Delta x, \Delta z) = \frac{|\Phi_{pp}(\omega, \Delta x, \Delta z)|^2}{\Phi_{pp}^2(\omega, 0, 0)} \quad (2.8)$$

It was pointed out by Roger and Moreau [86] that for the case of trailing edge noise only the spanwise cross-spectral density $\Phi_{pp}(\omega, 0, \Delta z)$ and auto-spectral density of the fluctuating surface pressure $\Phi_{pp}(\omega, 0, 0)$ are relevant. Therefore, we introduce a shorter notations of the two quantities. For a given location and zero streamwise separation $\Delta x = 0$, the cross-spectral density over the span $\Phi_{pp}(\omega, \Delta z) = \Phi_{pp}(\omega, 0, \Delta z)$ is a function of frequency ω and separation Δz . For $\Delta z = 0$ one obtains the auto-spectral density, which is a function of frequency only and written as $\Phi_{pp}(\omega) = \Phi_{pp}(\omega, 0, 0)$.

Similarly, for the normalised spanwise cross-spectral density $\gamma(\omega, \Delta z)$ and spanwise coherence $\gamma^2(\omega, \Delta z)$ we write

$$\gamma(\omega, \Delta z) = \frac{\Phi_{pp}(\omega, \Delta z)}{\Phi_{pp}(\omega)} \quad (2.9)$$

and

$$\gamma^2(\omega, \Delta z) = \frac{|\Phi_{pp}(\omega, \Delta z)|^2}{\Phi_{pp}^2(\omega)} \quad (2.10)$$

In the work of Amiet [17], a spanwise correlation length scale is defined by the integral of the normalized spanwise cross-spectral density of the pressure fluctuations, $\gamma = \Phi_{pp}(\omega, \Delta z) / \Phi_{pp}(\omega, 0)$,

$$l_{zA}(\omega) = \lim_{L_z \rightarrow \infty} \int_0^{L_z} \gamma(\omega, \Delta z) d\Delta z \quad (2.11)$$

Roger and Moreau [86] extended the classical theory of Amiet [17] to include 3D gusts ($k_z \neq 0$), which are relevant to assess the noise perceived by an observer off the mid-span plane. Estimation of the acoustic pressure requires the energy associated to the wall pressure fluctuations $\Pi_0(\omega, k_z) = \int_{-\infty}^{\infty} \Pi(\omega, k_x, k_z) dk_x$ for given frequency ω and spanwise wavenumber k_z . Since $\Phi_{pp}(\omega, \Delta z) = \Phi_{pp}(\omega) \gamma(\omega, \Delta z)$ and with relation 2.6, this integral can be expressed in terms of the spanwise cross-spectral density [86]:

$$\Pi_0(\omega, k_z) = \int_{-\infty}^{\infty} \Pi(\omega, k_x, k_z) dk_x = \frac{1}{2\pi} \Phi_{pp}(\omega) \int_{-\infty}^{\infty} \gamma(\omega, \Delta z) e^{ik_z \Delta z} d\Delta z \quad (2.12)$$

For the case $k_z = 0$ and homogeneous statistics along the span ($\gamma(\omega, \Delta z) = \gamma(\omega, -\Delta z)$), the last integral in equation 2.12 corresponds to the spanwise correlation length $l_{zA}(\omega)$ defined by Amiet [17] (equation 2.11).

Roger and Moreau [86] argue that the magnitude square coherence $\gamma^2(\omega, \Delta z)$ (equation 2.10) is a quantity more accessible in experiments when compared to the complex normalised cross-spectral density function $\gamma(\omega, \Delta z)$ (equation 2.9). They introduced the *corrected correlation length* as

$$l_z(\omega, k_z) = \lim_{L_z \rightarrow \infty} \int_0^{L_z} \sqrt{\gamma^2(\omega, \Delta z) \cos(k_z \Delta z)} d\Delta z \quad (2.13)$$

Roger and Moreau [86] do not state under what assumptions equation 2.13 holds. $\gamma(\omega, \Delta z) = \gamma^*(\omega, -\Delta z)$ and in addition it is tacitly assumed $\gamma(\omega, \Delta z) = \gamma^*(\omega, \Delta z)$, or equivalently that the phase of the cross-spectral density along the span is zero. In the case of a turbulent boundary layer and a straight trailing edge this assumption is reasonable (in more general cases equation 2.12 can be considered without this simplification). For the case of small spanwise wavenumber and spanwise separations $k_z \Delta z \rightarrow 0$, $\cos(k_z \Delta z) \approx 1$ and the spanwise correlation length can be estimated by $l_z(\omega) = l_z(\omega, 0)$.

Π_0 can then be expressed as the product of unsteady surface pressure auto-spectral density $\Phi_{pp}(\omega)$ and $l_z(\omega, k_z)$ (equation 2.13):

$$\Pi_0(\omega, k_z) = \frac{1}{\pi} \Phi_{pp}(\omega) l_z(\omega, k_z) \quad (2.14)$$

MODELS FOR TURBULENT BOUNDARY LAYER

The properties of the wall pressure spectrum, especially for channel flows and zero pressure gradient boundary layers, have been investigated in the past [107]. It was pointed out that a single set of parameters does not lead to a satisfactory collapse of experimental data over the entire frequency range. This complex scaling behavior was ascribed to the dependence of the pressure field on events throughout the domain. This includes the convection and evolution of turbulent eddies with different scales. For instance, the convective velocity depends in first approximation on the distance of the eddy to the wall. A subdivision of the pressure spectrum $\Phi_{pp}(\omega)$ into four parts has been proposed [107]: the low, mid, universal, and high frequency range. Suitability of scaling rules over

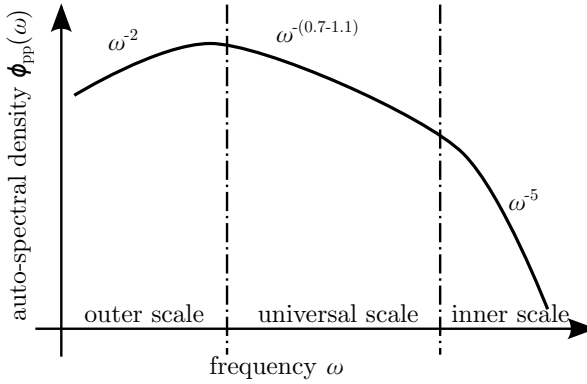


Figure 2.10: Characteristics of pressure spectrum for a zero pressure gradient turbulent boundary layer. Figure adapted from Hwang *et al.* [108].

these frequency ranges mostly depends on the Reynolds number. Hwang *et al.* [108] provided a review for the scaling of the wall pressure spectrum and empirical models (figure 2.10).

Two different scaling rules are most commonly applied and show a better collapse over the low or high frequency range, respectively. The pressure spectrum scaled using outer flow variables, namely the free-stream velocity u_∞ , displacement thickness δ^* , and dynamic pressure $q_\infty = 1/2\rho u_\infty^2$, is expressed as $\tilde{\Phi}_o(\tilde{\omega}_o) = \Phi(\tilde{\omega})u_\infty/q_\infty^2\delta^*$, where $\tilde{\omega}_o = \omega\delta^*/u_\infty$. Based on inner flow variables, namely the kinematic viscosity ν , wall shear stress $\tau_w = \rho\nu\partial u/\partial y|_{y=0}$, shear velocity $u_\tau = \sqrt{\tau_w/\rho}$, and viscous wall unit $\delta_\nu = \nu/u_\tau$, the pressure spectrum is scaled with $\tilde{\Phi}_i(\tilde{\omega}_i) = \Phi(\tilde{\omega})u_\tau^2/\tau_w^2\nu$, where $\tilde{\omega}_i = \omega\nu/u_\tau^2$ [109]. The outer scaling provides a better collapse at low frequencies, while the inner scaling applies at high frequencies.

Scientific discussion has converged on a generally accepted decay rate of ω^{-5} in the limit of high frequencies. Hwang *et al.* [108] further pointed out that the universal range, showing a decay in $\Phi(\omega)$ of approximately $\omega^{-0.7}$ between $0.6 \leq \omega\delta^*/u_\infty \leq 1.2$, is comparatively small for low Reynolds number flows. A model for the unsteady surface pressure auto-spectral density including Reynolds number dependence was proposed by Goody [109]. The Reynolds number dependence is introduced through a parameter representing the ration between outer and inner time scales $Re_T = \delta u_\tau^2/\nu u_\infty$, where δ is the boundary layer thickness. The model has been calibrated for a range of Reynolds numbers (based on the boundary layer momentum thickness θ) $1,400 < Re_\theta < 23,400$ with empirical constants $C_1 = 0.5$, $C_2 = 3$, and $C_3 = 1.1$.

$$\frac{\Phi_{pp}(\omega) u_\infty}{\tau_w^2 \delta} = \frac{C_2 \left(\frac{\omega\delta}{u_\infty}\right)^2}{\left[\left(\frac{\omega\delta}{u_\infty}\right)^{0.75} + C_1\right]^{3.7} + \left[\frac{C_3}{Re_T^{0.57}} \left(\frac{\omega\delta}{u_\infty}\right)\right]^7} \quad (2.15)$$

Schewe [110] presented experimental data for zero pressure gradient boundary layer and conditions of low Reynolds number $Re_\theta = 1,400$. The displacement thickness in

these experiments is reported to be $\delta^* = 4.6\text{mm}$, the free-stream velocity $u_\infty = 6.3\text{m/s}$ and the ratio of outer and inner boundary layer time scales is $\text{Re}_T \approx 25$.

Specifically for the estimation of trailing edge noise, Amiet [17] suggested the following empirical relation based on an outer scaling of the pressure field:

$$\frac{\Phi_{pp}(\omega) u_\infty}{(\rho u_\infty^2)^2 \delta^*} \approx \frac{1}{2} \frac{10^5}{1 + \left(\frac{\omega \delta^*}{u_\infty}\right) + 0.217 \left(\frac{\omega \delta^*}{u_\infty}\right)^2 + 0.00562 \left(\frac{\omega \delta^*}{u_\infty}\right)^4} \quad (2.16)$$

Several models for the spatial structure of the wall pressure spectrum have been proposed [111]. Corcos [112, 113] proposed a model under the assumption that the normalized cross-power spectral density $\Phi_{pp}(\omega, \Delta x, \Delta z) / \Phi_{pp}(\omega, 0, 0)$ can be represented by a function depending on two dimensionless variables $\omega \Delta x / u_c$ and $\omega \Delta z / u_c$. Assuming that separation of variables is possible, such that $\gamma(\omega, \Delta x, 0) = A(\omega \Delta x / u_c) e^{i\omega \Delta x / u_c}$ and $\gamma(\omega, 0, \Delta z) = B(\omega \Delta z / u_c)$, the normalized cross-spectral density is modeled as [86]

$$\gamma(\omega, \Delta x, \Delta z) = \Phi_{pp}(\omega, \Delta x, \Delta z) / \Phi_{pp}(\omega, 0, 0) = B\left(\frac{\omega \Delta z}{u_c}\right) A\left(\frac{\omega \Delta x}{u_c}\right) e^{i\frac{\omega \Delta x}{u_c}} \quad (2.17)$$

Experimental data suggests exponential functions provide a fair representation of the generally unknown functions A and B for turbulent boundary layers [112]. Substitution in equation 2.17 results in

$$\gamma(\omega, \Delta x, \Delta z) = e^{-\frac{\alpha_1 \omega |\Delta z|}{u_c}} e^{-\frac{\beta \omega |\Delta x|}{u_c}} e^{i\frac{\omega \Delta x}{u_c}} \quad (2.18)$$

For the spanwise correlation length ($\Delta x = 0$), the classical result for the model of the correlation length used by Amiet [17] in the context of trailing edge noise estimation, can be recovered by substitution of equation 2.18 in equation 2.11:

$$l_z(\omega) = \frac{u_c}{\alpha_1 \omega} \quad (2.19)$$

Note that for $k_z = 0$ the result is identical if equation 2.13 is used instead of equation 2.11. In the more general case $k_z \neq 0$ [86], integration based on equation 2.13 results in

$$l_z(\omega, k_z) = \frac{\alpha_1 \omega / u_c}{k_z^2 + (\alpha_1 \omega / u_c)^2} \quad (2.20)$$

Amiet [17] suggests a value of $\alpha_1 = 1/2.1$, while other literature suggests a value of $\alpha_1 = 0.77$ for an estimation of the spanwise coherence length, but slightly different values have been reported [111]. A model similar to that of Corcos [113], but including the influence of boundary layer thickness and separation of scales, was suggested by Efimtsov [114] with empirical parameters $\alpha_2 = 548$ and $\alpha_3 = 13.5$ [111]:

$$l_z(\omega) = \delta \left[\left(\frac{\alpha_1 \omega \delta}{u_c} \right)^2 + \frac{\alpha_2}{(\omega \delta / u_\tau)^2 + (\alpha_2 / \alpha_3)^2} \right]^{-1/2} \quad (2.21)$$

It should be noted that equation 2.21 converges to equation 2.19 in the limit of high frequency ω . Further, the coefficients adopted in both semi-empirical models show a considerable scatter among different experiments reported in literature [111].

2.2.3. SOLUTION FOR THE SEMI-INFINITE HALF-PLANE

In order to provide a basic understanding of the reasoning behind diffraction theory proposed for the solution of the trailing edge scattering problem by Amiet [17], the derivation of a simple case (semi-infinite half-plane) is reproduced from Roger and Moreau [86], who also included the solution for leading edge back-scattering and 3D gusts.

Consider a thin airfoil with small camber and of chord c that extends over $-c \leq x \leq 0$. Consider further an incident 2D pressure gust $p'_0(t, x, y)$ with $p'_0(t, x, 0) = e^{i(\omega t - k_x x)} = P_0(x, 0)e^{i\omega t}$ (figure 2.8b). For $x \geq 0$, P_0 is such as if the lifting surface would extend to $x \rightarrow \infty$. This incident pressure gust P_0 is canceled in the wake, accounting for the full Kutta condition by a disturbance pressure P_1 , and thus downstream of the trailing edge

$$P_0(x, 0) + P_1(x, 0) = 0 \quad x \geq 0 \quad (2.22)$$

The lifting surface upstream of the trailing edge is rigid. In the simplified problem, Amiet [17] extended this rigid wall condition infinitely far upstream in order to comply with the boundary conditions required for Schwarzschild's solution (see appendix B), thus

$$\frac{\partial P_1}{\partial y}(x, 0) = 0 \quad x < 0 \quad (2.23)$$

The disturbance pressure $p'_1(x, y, t) = P_1(x, y)e^{i\omega t}$ fulfills the convected wave equation

$$\frac{\partial^2 p'_1}{\partial x^2} + \frac{\partial^2 p'_1}{\partial y^2} - \frac{1}{c_0^2} \left(\frac{\partial}{\partial t} + u_\infty \frac{\partial}{\partial x} \right)^2 p'_1 = 0 \quad (2.24)$$

or with $k = \omega/c_0$, $\beta^2 = 1 - M_0^2$, and $M_0 = u_\infty/c_0$

$$\beta^2 \frac{\partial^2 P_1}{\partial x^2} + \frac{\partial^2 P_1}{\partial y^2} - 2ikM_0 \frac{\partial P_1}{\partial x} + k^2 P_1 = 0 \quad (2.25)$$

This is not the canonical form of the Helmholtz equation required by Scharzschild's solution (appendix B). The required form can be obtained by applying a Prandtl-Glauert coordinate transformation to equation 2.25. With the change of variables $P_1(x, y) = p_1(x, y)e^{ikM_0x/\beta^2}$ and $k_0 = \omega/u_\infty$,

$$\beta^2 \frac{\partial^2 p_1}{\partial x^2} + \frac{\partial^2 p_1}{\partial y^2} + \left(\frac{k_0 M_0}{\beta^2} \right)^2 p_1 = 0 \quad (2.26)$$

and with the coordinate transformation $X = 2x/c$, $Y = 2\beta y/c$, and $\mu = k/\beta^2 = k_0 M_0/\beta^2$, one recovers the canonical form of the Helmholtz equation

$$\frac{\partial^2 p_1}{\partial X^2} + \frac{\partial^2 p_1}{\partial Y^2} + \frac{\mu c}{2} p_1 = 0 \quad (2.27)$$

together with the transformed versions of the boundary conditions (equations 2.22 and 2.23)

$$\begin{aligned} p_1 &= -e^{-k_0 c X/2 [u_\infty/u_c + M_0^2/\beta^2]} & X \geq 0 \\ \frac{\partial p_1}{\partial Y}(X, 0) &= 0 & X < 0 \end{aligned}$$

Application of Schwarzschild's solution (appendix B) and re-substitution leads to the solution for the disturbance pressure on the negative half-plane with $k_x = \omega / u_c$ [17, 86]

$$P_1(X, 0) = e^{-ick_x X/2} [(1+i)E^* (-[ck_x/2 + (1+M_0)\mu c/2]X) - 1] \quad (2.28)$$

and the definition of $E(\xi)$ is provided in appendix C. The asterisk denotes the complex conjugate. The acoustic pressure at a receiver position $\mathbf{x}_O = [x_0, y_0, z_0]$ in the far-field due to the disturbance pressure distribution on the lifting surface can be found by evaluation of the radiation integral, where $\Delta P = 2P_1$ [86, 115] over the surface with chord c and span L as

$$p_a(\omega, \mathbf{x}_O) = \frac{-i\omega y_O}{4\pi c_0 S_0^2} \int_{-c}^0 \int_{-L/2}^{L/2} \Delta P e^{i\omega R_t/c_0} dz dx \quad (2.29)$$

and

$$\begin{aligned} R_t &= \frac{1}{\beta^2} (R_s - M_0(x_O - x)) \\ R_s &= S_0 \left(1 - \frac{x_O x + \beta^2 y_O y}{S_0^2} \right) \\ S_0^2 &= x_O^2 + \beta^2 (y_O^2 + z_O^2) \end{aligned}$$

In the 2D case, one can write $P_1 = f(x)e^{-ick_x X/2}$ (compare equation 2.28), where $f(x)$ is the complex amplitude of the source distribution. Substitution in equation 2.29 and accounting for the change of variables introduced earlier, the radiation integral becomes

$$p_a(\omega, \mathbf{x}_O) = \frac{-i\omega y_O}{2\pi c_0 S_0^2} \left(\frac{c}{2}\right)^2 \int_{-2}^0 \int_{-L/c}^{L/c} f(X) e^{-ick_x X/2} e^{-ik/\beta^2 \left[S_0 - \frac{x_O X + \beta^2 z_O Z}{S_0} \frac{c}{2} - M_0(x_O - cX/2) \right]} dZ dX \quad (2.30)$$

The integral over the spanwise coordinate Z can be evaluated readily with

$$\frac{c}{2} \int_{-L/c}^{L/c} e^{-ikcz_O Z/2S_0} dZ = L \operatorname{sinc} \left(-\frac{kLz_O}{2S_0} \right) \quad (2.31)$$

and is equal to L for an observer in the mid-span plane at $z_O = 0$. In that case

$$p_a(\omega, \mathbf{x}_O) = \frac{-i\omega y_O L c}{4\pi c_0 S_0^2} \int_{-2}^0 f(X) e^{-i(k/\beta^2)(S_0 - M_0 x_O)} e^{-ick_x X/2} e^{-i\mu c X/2 \left[M_0 - \frac{x_O}{S_0} \right]} dX \quad (2.32)$$

The remaining integral can be written as

$$\int_{-2}^0 f(X) e^{-ick_x X/2} e^{-ik/\beta^2 \left[S_0 - \frac{x_O X}{S_0} \frac{c}{2} - M_0(x_O - cX/2) \right]} dX \quad (2.33)$$

and the result of this integration is equal to the direct scattering term \mathcal{S}_1 in appendix C with $k_z = 0$ and an additional term, which balances the contribution of the incident pressure gust P_0 to sound radiation and is therefore ignored [17, 86].

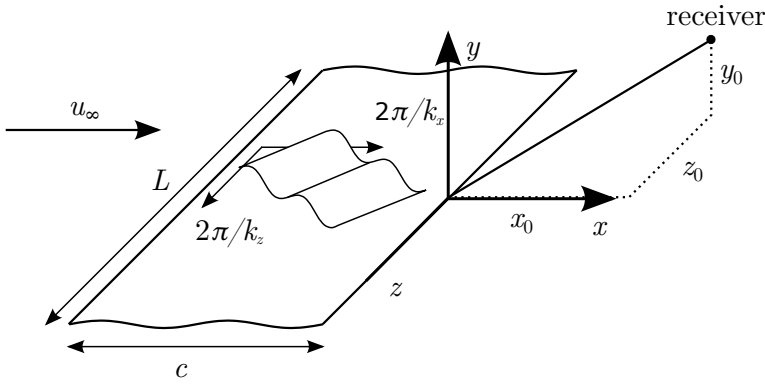


Figure 2.11: Coordinate system with finite plate in airflow with uniform velocity u_∞ and receiver located at \mathbf{x}_O .

The auto-spectral density of the far-field acoustic pressure can then be expressed as

$$\Phi_{aa}(\omega, \mathbf{x}_O) = \left(\frac{kc y_O}{4\pi S_O^2} \right)^2 2\pi L \left| \mathcal{F}_1 \left(\frac{\omega}{u_c}, 0 \right) \right|^2 \Pi_0(\omega, 0) \quad (2.34)$$

2.2.4. EXTENDED SOLUTION

In section 2.2.3, the derivation of the solution for the semi-infinite half-plane diffraction problem first described by Amiet [17] was outlined. Here, the solution including 3D pressure gusts ($k_z \neq 0$) and leading edge back-scattering is provided. For a detailed derivation the reader may refer to the study of Roger and Moreau [86].

Consider the abstract problem of an infinitely thin plate of chord c and span L placed in a turbulent stream with free-stream velocity u_∞ . The x -axis is chosen to coincide with the chord line at mid-span, the z -axis coincides with the trailing edge, and the y -axis points in the resulting surface normal direction for a right-handed coordinate system. Note that in this simplification the x -axis is also aligned with the free-stream velocity and the abstraction can thus be considered as the model for an very thin airfoil with small camber and at small angle of attack.

The wavenumber spectral density $\Pi_0(\omega, k_z)$ is related to the acoustic far-field pressure through a radiation integral, similar to the solution of the simpler problem described in the previous section. The scattering due to the boundary layer from the two sides of the plate is taken into account by assuming the full Kutta condition. An expression for the sound pressure auto-spectral density $\Phi_{aa}(\omega, \mathbf{x}_O)$ is obtained. With the observer coordinates $\mathbf{x}_O = [x_O, y_O, z_O]$, corrected observer distance $S_O = [x_O^2 + \beta^2(y_O^2 + z_O^2)]^{1/2}$ accounting for the convection of acoustic waves, $\beta^2 = 1 - M_0^2$, the acoustic wavenumber $k = \omega/c_0$, chord length c , span L , and under the assumption of large aspect ratio

$$\Phi_{aa}(\omega, \mathbf{x}_O) = \left(\frac{kc y_O}{4\pi S_O^2} \right)^2 2\pi L \left| \mathcal{F} \left(\frac{\omega}{u_c}, k \frac{z_O}{S_O} \right) \right|^2 \Pi_0 \left(\omega, k \frac{z_O}{S_O} \right) \quad (2.35)$$

$|\cdot|$ denotes the modulus or absolute value. $\mathcal{S}(\frac{\omega}{u_c}, k \frac{z_O}{S_O}) = \mathcal{S}_1(\frac{\omega}{u_c}, k \frac{z_O}{S_O}) + \mathcal{S}_2(\frac{\omega}{u_c}, k \frac{z_O}{S_O})$ represents the acoustic transfer function and defines the scatter response to an incoming pressure disturbance. Appendix C provides the full expressions for the acoustic transfer functions. \mathcal{S}_1 is the term relating to direct scattering, and \mathcal{S}_2 contains the back-scattering correction proposed by Roger and Moreau [86]. Considering only direct scattering ($\mathcal{S} = \mathcal{S}_1$) and under the assumption of 2D pressure gusts ($k_z = 0$) or equivalently an observer in the mid-span plane, the result reduces to the classical result of Amiet [17] (equation 2.34).

Equation 2.35 represents the large aspect ratio approximation, i.e. $L/c \gg 1$. Moreau and Roger [83] have investigated the applicability of this approximation and have shown that, for similar parameters as for the experiment reported in chapter 8 of this thesis, deviations for frequencies in the range $kc/\beta^2 > 5$ ($> 500\text{Hz}$) remain within 0.5dB.

To assess the implications of the infinite aspect ratio assumption, a methodology similar to the one presented by Moreau and Roger [83] is followed. Instead of restricting the analysis to an observer in the mid-span plane, the analysis is adapted to the general case of an observer at an arbitrary location. The general formulation for plate of arbitrary chord length c and thus aspect ratio is given by [83, 86]

$$\Phi_{aa}(\omega, \mathbf{x}_O) = \left(\frac{kc y_0 L}{4\pi S_O^2} \right)^2 \frac{2}{c} \int_{-\infty}^{\infty} \Pi_0(\omega, k_z) \text{sinc}^2 \left(\frac{L}{c} \left[\frac{k_z c}{2} - \frac{k z_O c}{2 S_O} \right] \right) \left| \mathcal{S} \left(\frac{\omega}{u_c}, k_z \right) \right|^2 dk_z \quad (2.36)$$

and this expression can be compared to the simpler one for the infinite aspect ratio (equation 2.35). Under the assumption of infinite aspect ratio ($L/c \rightarrow \infty$), the $\text{sinc}^2(L/c\xi)$ function behaves as a Kronecker Delta-function $\pi c/L\delta(\xi)$ [116], selecting a single span-wise wavenumber $k_z = k z_O/S_O$ depending on the observer position \mathbf{x}_O . Thus, for $L/c \rightarrow \infty$

$$\text{sinc}^2 \left\{ \frac{L}{c} \left(\frac{k_z c}{2} - \frac{k z_O c}{2 S_O} \right) \right\} \rightarrow \frac{\pi c}{L} \delta \left(k_z - \frac{k z_O}{S_O} \right) \quad (2.37)$$

Therefore, under the infinite aspect ratio assumption equation 2.36 is equivalent to equation 2.35. Amiet [17] has commented on the validity of the infinite aspect ratio assumption and gave the following two alternative criteria:

$$\frac{L}{c} \gg 1 \quad \wedge \quad k_x \frac{L}{2} \gg 1 \quad (2.38)$$

Alternatively, he remarked that effects due to the finite span are limited to within approximately a wavelength from the tips and thus the large aspect ratio assumption can also hold for cases where the acoustic wavelength is small compared to the span

$$M_0 k_x \frac{L}{2} \gg 1 \quad (2.39)$$

Moreau and Roger [83] assessed the large aspect ratio assumption numerically by considering the ratio of the finite aspect ratio solution (equation 2.36) and infinite aspect ratio solution (equation 2.35). Numerical evaluation requires the selection of a model for

the correlation length. Here, the Corcos model¹ is considered instead of experimental data for the sake of simplicity. This semi-empirical model was proposed and assessed for the fully turbulent boundary layer and thus the present analysis is restricted to the case of turbulent boundary layer trailing edge interaction. Moreau and Roger [83] assessed the effect of the infinite aspect ratio approximation for an observer in the mid-span plane ($z_O = 0$). Here, the general case ($z_O \neq 0$) is considered to assess the impact of the assumption also for an observer located near the wing tips. With the Corcos model, the expressions for the finite and infinite aspect ratio solutions read

$$\Phi_{aa}^{\infty}(\omega, \mathbf{x}_O) = \left(\frac{y_O}{2\pi S_O^2} \right)^2 Lc \left(\frac{kc}{2} \right)^2 \Phi_{pp}(\omega) \frac{(kc)/(2M_c/\alpha_1)}{(k_z c/2)^2 + (kc/2)^2/(M_c/\alpha_1)^2} \left| \mathcal{F} \left(\frac{\omega}{u_c}, \frac{kz_O}{S_O} \right) \right|^2 \quad (2.40)$$

and

$$\Phi_{aa}(\omega, \mathbf{x}_O) = \left(\frac{y_O L}{2\pi S_O^2} \right)^2 \frac{(kc/2)^3}{M_c \pi / \alpha_1} \Phi_{pp}(\omega) \int_{-\infty}^{\infty} \frac{\text{sinc}^2 \left\{ \frac{L}{c} \left(\frac{k_z c}{2} - \frac{kz_O c}{2S_O} \right) \right\}}{(k_z c/2)^2 + (kc/2)^2/(M_c/\alpha_1)^2} \left| \mathcal{F} \left(\frac{\omega}{u_c}, k_z \right) \right|^2 dk_z \quad (2.41)$$

The ratio of equations 2.40 and 2.41 becomes independent of the surface pressure auto-spectral density $\Phi_{pp}(\omega)$ and is considered as metric of comparison for the two cases. The ratio, with $M_c = u_c/c_0$, is given by

$$\frac{\Phi_{aa}}{\Phi_{aa}^{\infty}} = \frac{L}{c} \frac{kc}{2} \frac{1}{M_c \pi / \alpha_1} \int_{-\infty}^{\infty} \frac{\text{sinc}^2 \left\{ \frac{L}{c} \left(\frac{k_z c}{2} - \frac{kz_O c}{2S_O} \right) \right\}}{(k_z c/2)^2 + (kc/2)^2/(M_c/\alpha_1)^2} \frac{\left(\frac{kz_O}{2S_O} \right)^2 + (kc/2)^2/(M_c/\alpha_1)^2}{(kc/2)/(M_c/\alpha_1)} \left| \mathcal{F} \left(\frac{\omega}{u_c}, k_z \right) \right|^2 \left| \mathcal{F} \left(\frac{\omega}{u_c}, \frac{kz_O}{S_O} \right) \right|^2 dk_z \quad (2.42)$$

Note that equation 2.42 reduces to the expression given by Moreau and Roger [83] (equation 9) for the observer in the mid-span plane ($z_O = 0$). Figure 2.12 shows the result of equation 2.42 for the parameters in the study of Pröbsting *et al.* [66] ($c = 0.6m$, $M_0 = 0.03$, $x_O/c = 0$, $y_O/c = 1$, $M_c = 0.022$, see chapter 8). For $kc/\beta^2 > 1$, the difference between is less than 1dB. This confirm the alternative condition proposed by Amiet [17] (equation 2.39).

¹models for the unsteady surface pressure spectrum are discussed in section 2.2.2. Equation 2.20 describes the Corcos model for the correlation length.

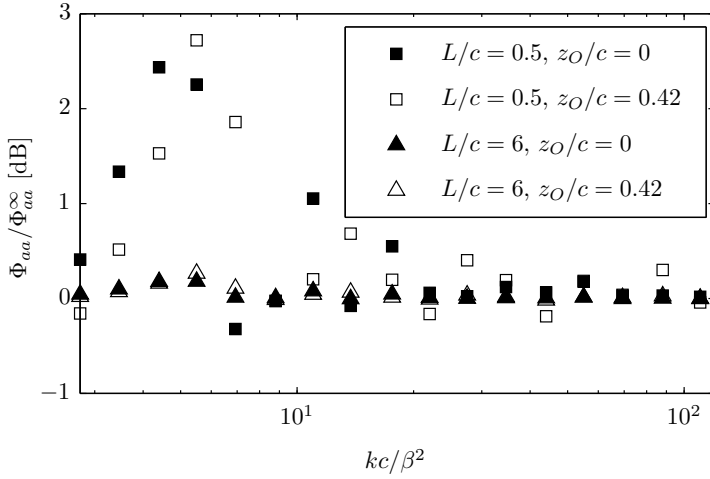


Figure 2.12: Effect of finite span $\Phi_{aa}/\Phi_{aa}^\infty$ as a function of acoustic wavenumber k , considering only the direct scattering term \mathcal{S}_1 .

2.2.5. TRAILING EDGE BLUNTNESS NOISE

The model adapted in the present study for vortex shedding noise prediction is an adaptation of the solution proposed by Amiet [115] for the estimation of noise from an airfoil in a turbulent stream. The original method estimates the pressure distribution on a flat and rigid surface induced by disturbances encountered from the turbulent flow upstream. These disturbances are represented by downstream convecting gusts of streamwise wavenumber k_x and spanwise wavenumber k_z . Consecutively, the sound power radiated to the far-field is deduced by means of a radiation integral, taking into account this pressure distribution.

An adaptation of this model for noise due to vortex shedding at the trailing edge was proposed by Roger *et al.* [105], who argued that vortex shedding can be seen as the reverse of vorticity encountering the leading edge. The disturbances are thus considered to interact with the rigid surface, giving rise to an unsteady pressure distribution. In this approach, the Kutta condition is not imposed since pressure fluctuations induced by vortex shedding are regarded to be opposite in phase on the two sides of the trailing edge [105]. In the mathematical model, the difference between the two situations described above can be expressed by an inversion of the flow velocity. Additionally, a second velocity scale is introduced: the convective velocity $u_c < u_\infty$, with u_∞ the free-stream velocity, at which the roll-up vortices are convected downstream due to the velocity deficit present in the wake.

Roger and Moreau [87], Roger *et al.* [105] provide an expression for the noise emission under the assumption of large aspect ratio. As pointed out by Amiet [17] and later by Moreau and Roger [83] this assumption also holds for high frequency noise (see previous section for discussion). Roger *et al.* [105] do not provide a back-scattering correction, which is important for surfaces with compact chord only ($kc \leq 1$, where $k = 2\pi f/c_0$ is the

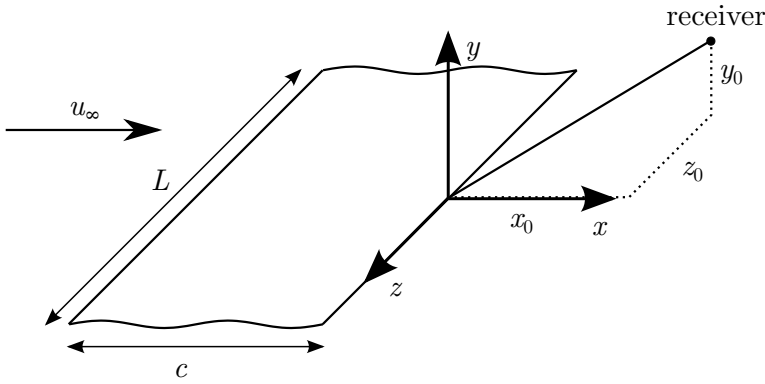


Figure 2.13: Schematic showing relevant geometric parameters of scattering surface and receiver location.

acoustic wavenumber, c the chord of the surface, f the ordinary frequency, and c_0 the speed of sound). For the experiment reported in chapter 9 of this thesis, this condition is expressed as $f \leq 150\text{Hz}$. Typically, vortex shedding at airfoil trailing edges occurs at higher frequencies and the assumption is justified.

It is further assumed that only parallel gusts contribute to the radiated sound at the observer location (spanwise wavenumber $k_z = 0$), which is strictly the case for a receiver in the mid-span plane only ($z_0 = 0$). Roger and Moreau [87] argue that vortex shedding leads to significant correlation of the upwash velocity over a larger part of the span, typically 6 or 7 times the the edge thickness, which renders the parallel gust dominant. Thus, the restriction $k_z = 0$ is justified in particular for cases, where coherent vortex shedding is dominant.

Under such assumptions, equation 2.43 provides an estimation of the acoustic pressure auto-spectral density $\Phi_{aa}(\omega, \mathbf{x}_O)$ at a receiver location $\mathbf{x}_O = [x_O, y_O, z_O]$. $\Phi_{vv}(\omega)$ is the auto-spectral density of the upwash velocity in the wake and $l_z(\omega)$ denotes the corresponding correlation length, which will be defined below. Further, ρ_0 denotes the density of the fluid, $S_0 = [x_O^2 + \beta^2(y_O^2 + z_O^2)]^{1/2}$ the convection corrected observer distance with $\beta^2 = 1 - M_0^2$, $M_0 = u_\infty/c_0$ the Mach number, and L the span of the surface (figure 2.13):

$$\Phi_{aa}(\omega, \mathbf{x}_O) = \left(\frac{\rho_0 k c y_O u_\infty}{2 S_0^2} \right)^2 \frac{L}{2} \Phi_{vv}(\omega) l_z(\omega) |\mathcal{L}_{VK}|^2 \quad (2.43)$$

Equation 2.44 provides the normalized radiation integral \mathcal{L}_{VK} that appears in equation 2.43. The bar $\bar{\cdot}$ stands for multiplication by $c/2$. Further, $k_x^* = \omega c/2u_\infty$, $\bar{K}_x = \omega c/2u_c$:

$$\mathcal{L}_{VK} = -\frac{1+i}{\pi K_x^*} \left\{ \sqrt{\frac{\Theta_1}{\Theta_1 - \Theta_2'}} E^* (2[\Theta_1 - \Theta_2']) \left(1 - \frac{\bar{K}_x - k_x^*}{\Theta_2'} \right) + (\bar{K}_x - k_x^*) \frac{e^{2i\Theta_2'}}{\Theta_2'} E^* (2\Theta_1) \right\} \quad (2.44)$$

and with $\bar{\mu} = kc/(2\beta^2)$:

$$\begin{aligned}
\Theta_1 &= \overline{K_x} + \overline{\mu}(1 + M_0) \\
\Theta_2' &= \overline{K_x} - \overline{\mu}(x_O/S_O - M_0) \\
K_x^* &= \overline{K_x} [1 - M_0^2 (1 - k_x/K_x)^2]^{1/2}
\end{aligned} \tag{2.45}$$

The spanwise correlation length $l_z(\omega)$ of the upwash velocity is defined as an integral of the coherence function $\sqrt{\gamma^2(\omega, \Delta z)}$ over the spanwise coordinate direction. For homogeneous statistics along the span, this definition can be written in terms of the distance between two points along the span Δz :

$$l_z(\omega) = \lim_{L_z \rightarrow \infty} \int_0^{L_z} \sqrt{\gamma^2(\omega, 0)} d\Delta z \tag{2.46}$$

The coherence function $\sqrt{\gamma^2(\omega, \Delta z)}$ is defined in terms of the cross-spectral density of the upwash velocity component $\Phi_{vv}(\omega, \Delta z)$ as

$$\gamma^2(\omega, \Delta z) = \frac{|\Phi_{vv}(\omega, \Delta z)|^2}{\Phi_{vv}^2(\omega)} \tag{2.47}$$

For a 45° trailing edge, Blake [19] reports an integral correlation length of $l_z/y_f = 3.5$ at the shedding frequency, where y_f is the wake thickness parameter.

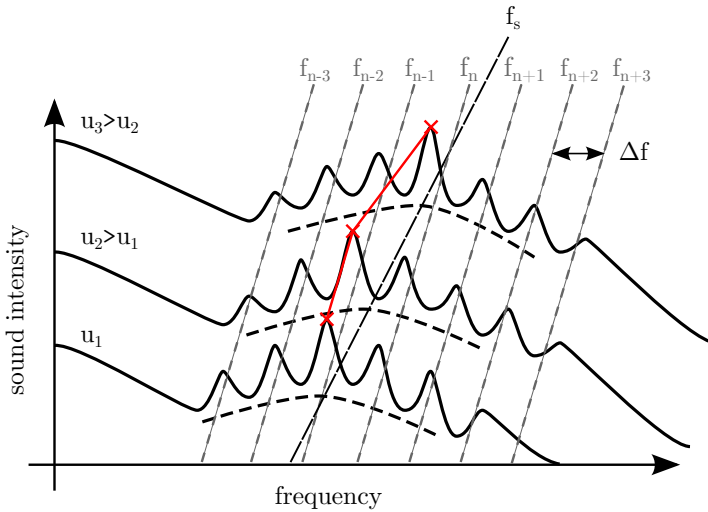
2.3. LAMINAR BOUNDARY LAYER INSTABILITY NOISE

Laminar boundary layer instability noise can be seen as trailing edge noise in the sense that the principle sound generation mechanism due to diffraction of pressure fluctuations is the identical. Disturbances introduced into the boundary layer, in this case by convecting vortical structures with a large spanwise correlation, scatter at the discontinuity posed by the trailing edge.

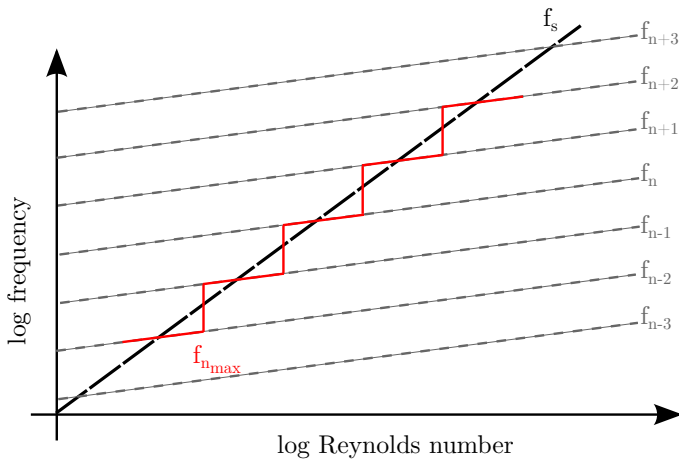
2.3.1. CHARACTERISTICS OF ACOUSTIC SPECTRUM

In an early study, Paterson *et al.* [35] dealt with the tonal noise produced by isolated airfoils and described the particular nature of the acoustic spectrum. Multiple tones (denoted by subscripts $n = 1, 2, \dots$) were present in this spectrum and their frequencies f_n were proportional to a power of the free-stream velocity $u_\infty^{0.85}$. The dominant tone $f_{n_{max}}$ (also denoted as the *primary* tone, Arcondoulis *et al.* [14]) followed this variation over a finite range of Reynolds numbers before a transition (or *jump*) to a different frequency (different index n_{max}) was observed. This particular structure of the spectrum with a primary tone $f_{n_{max}}$ and multiple side tones f_n (also denoted *secondary* tones) is called a *ladder*-type structure, where the primary tone $f_{n_{max}}$ constitutes the *rungs* of the *ladder*.

The *ladder* structure has been explained by the superposition of tones at frequencies f_n and broadband energy content in the acoustic spectrum centered at frequency f_s [18, 117]. As a consequence of this superposition, a dominant (primary) tone $f_{n_{max}}$ can be identified (figure 2.14). On average, the main tone frequency $f_{n_{max}}$ thus follows the development of the broadband center frequency f_s and is described in the work of



(a) Formation of *ladder* structure by superposition of tonal and broadband components.



(b) *Ladder* structure for frequency associated to primary tone.

Figure 2.14: Characteristics of acoustic spectrum due to laminar boundary layer instability noise.

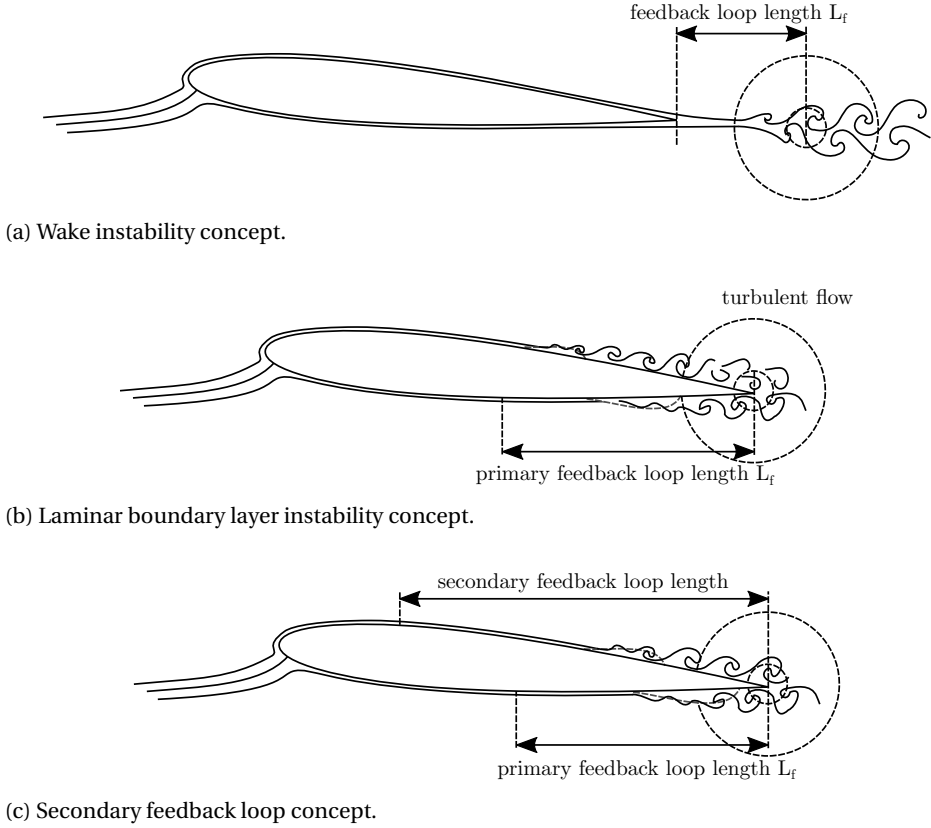


Figure 2.15: Concepts of acoustic feedback related to laminar boundary layer instability noise.

Paterson *et al.* [35] to have a dependence on velocity with $u_\infty^{1.5}$. With the airfoil chord c , kinematic viscosity ν and proportionality constant k , the expression

$$f_s^* = \frac{f_s c}{u_\infty} = k \sqrt{\frac{c u_\infty}{\nu}} = k \sqrt{Re_c} \quad (2.48)$$

describes this semi-empirical rule. Based on the data of Paterson *et al.* [35] $k = 0.011$. The dependence on the square root of the Reynolds number Re_c is reminiscent of the variation of the laminar boundary layer thickness (e.g. Blasius profile on a flat plate; Schlichting and Gersten [118]). Chong and Joseph [117] remarked that the most amplified frequency found from linear stability analysis of disturbances in the boundary layer is close to f_s and that both show good agreement with the primary tone frequency $f_{n_{max}}$.

2.3.2. CONCEPT OF ACOUSTIC FEEDBACK

With the trend of the primary tone frequency $f_{n_{max}}$ being attributed to the variation of length scales with Reynolds number, the frequency scaling of individual tones $f_n \sim u_\infty^{0.85}$ requires further explanation. Since the observation of Paterson *et al.* [35] the topic has received much attention. Recent studies indicate the sustained interest and ongoing debate [15, 50, 119] to comprehensively explain the occurrence of multiple discrete tones through the concept of a *feedback loop* as frequency selection mechanism.

Based on the observations and experimental data of Paterson *et al.* [35], the latter was initially proposed by Tam [120] as a feedback between an acoustic source in the wake due to an instability mechanism and the trailing edge (figure 2.15a), followed by Fink [121] and Wright [122]. Tam [120] stated that the total change in phase over the feedback loop has to be equal to an integral multiple of 2π , thus $n2\pi$. The length of the feedback loop is defined as the distance L_f between the point of receptivity and the noise source (denoted A and B, respectively in figure 2.15a). Assuming further a constant or time-averaged convective velocity u_c of the instability waves in the wake, the total change in phase of the latter over the feedback loop length L_f is $2\pi L_f / \lambda = 2\pi f L_f / u_c$. Similarly, the total change in phase of the upstream traveling acoustic waves is $2\pi L_f / \lambda_a = 2\pi f L_f / c_0$, where c_0 and λ_a denote the speed of sound and acoustic wavelength, respectively. Thus, according to Tam [120], the following phase condition must hold for the feedback loop:

$$2\pi f_n L_f \left(\frac{1}{u_c} + \frac{1}{c_0} \right) = n2\pi \quad (2.49)$$

Tam [120] remarked further that for a given airfoil the product $g(u_\infty, \alpha) = L_f \left(\frac{1}{u_c} + \frac{1}{c_0} \right)$ is a function of free-stream velocity u_∞ and angle of attack α , which poses a strong limitation with regard to the existence of a general scaling law. Nevertheless, in a dimensionless version equation 2.49 can be written as:

$$f_n^+ = \frac{L_f f_n}{u_\infty} = n \frac{1}{u_\infty / u_c + u_\infty / c_0} \quad (2.50)$$

Later, Arbey and Bataille [18] explained the phenomenon by the scattering of convecting surface pressure perturbations, induced by instability waves developing in the boundary layer. These instability waves are amplified through a separation bubble upstream of the trailing edge [16] (figure 2.15b). The mechanism of surface pressure perturbations passing the trailing edge and thereby generating acoustic waves was previously discussed by Amiet [17] among others (see section 2.1.3). Aizin [123] performed an analytical study, investigating the generation of noise by Tollmien-Schlichting waves. They found that the acoustic pressure at the frequency of the instability waves is proportional to the wall pressure fluctuations near the trailing edge, thus supporting the noise generation mechanism suggested by Arbey and Bataille [18]. The hypothesis is further supported by the studies of Sandberg *et al.* [124] and Jones and Sandberg [125], who performed Direct Numerical Simulations (DNS) on a series of NACA airfoils at various angles of attack and applied diffraction theory [17] to estimate the sound pressure level.

The feedback loop concept of Arbey and Bataille [18], adapting the phase condition of Tam [120] (equation 2.50), is now widely accepted. According to Arbey and Bataille [18]

$$f_n^+ = \frac{L_f f_n}{u_\infty} = \left(n + \frac{1}{2}\right) \frac{1}{u_\infty / u_c + u_\infty / (c_0 - u_\infty)} \quad (2.51)$$

describes the selection of these discrete frequencies f_n . Equation 2.51 can be obtained from the formulation of Arbey and Bataille [18] by multiplication with the normalized convective velocity of the instability waves u_c/u_∞ . In this explicit form, the feedback loop relation is simplified, since it assumes a constant convective velocity. Besides the different definition of the receptivity and source region, equation 2.51 differs from equation 2.50 in two points: Arbey and Bataille [18] found agreement with their data only by using a factor $(n+1/2)$ instead of n , which corresponds to a phase difference of π or 180° over the feedback loop. This additional phase change is due to the diffraction of instability waves at the trailing edge under consideration of the Kutta condition [18, 117, 126]. Furthermore, Arbey and Bataille [18] consider a convection correction for the propagation of sound waves $c_0 - u_\infty$. For an airfoil at zero incidence, Arbey and Bataille [18] found good agreement for their experimental data with equation 2.51 when considering the distance between the maximum velocity point and the trailing edge for the definition of the feedback loop length L_f . Later studies pointed out that the point of inception for the boundary layer instability is a more appropriate choice [117, 126].

Within the framework of hydrodynamic stability, the development and amplification of fluctuations over the separated shear layer can be seen as convective or local instability. In contrast, the feedback of acoustic disturbances to and receptivity by the boundary layer at an upstream location suggests global instability [125]. The feedback loop concept was thus further refined by Kingan and Pearse [126], who implemented linear stability analysis in the procedure to estimate the frequency of discrete tones. They modeled the amplification process of instability waves following linear stability theory, where $\Psi(x_t, x_n, t)$ is the stream function of these waves, $\Phi(x_n)$ the perturbation amplitude, α the complex wavenumber α , and t time:

$$\Psi(x_t, x_n, t) = \Phi(x_n) e^{i \int \alpha(x_t) dx_t - \omega t} \quad (2.52)$$

The phase change of the instability waves between two points $x_t = a$ and $x_t = b$ is thus related to the real part of the wavenumber α_r :

$$\int_a^b \alpha_r(x_t) dx_t \quad (2.53)$$

A refined condition for the phase condition, also considering the average free-stream velocity $\overline{u_\infty}$ between $x_t = a$ and b , is therefore written as

$$\frac{1}{2\pi} \int_a^b \alpha_r(x_t) dx_t + \frac{f_n L_f}{c_0 - \overline{u_\infty}} = n + \frac{1}{2} \quad (2.54)$$

or

$$f_n^+ = \frac{L_f f_n}{u_\infty} = \left(n + \frac{1}{2} - \frac{1}{2\pi} \int_a^b \alpha_r(x_t) dx_t\right) \frac{c_0 - \overline{u_\infty}}{u_\infty} \quad (2.55)$$

In a predictive analysis, without a priori knowledge of the selected frequencies f_n , $\alpha_r(x_t)$ is then chosen to be the real part of the wavenumber belonging to the locally most

unstable mode (largest negative imaginary part of wavenumber). Chong and Joseph [117], following the procedure of Kingan and Pearse [126], found likewise good agreement with experimental results and noted that the variation of the most amplified frequency as predicted by linear stability theory follows the same variation with free-stream velocity as $f_{n_{max}}$. It should be noted that in the above studies the local boundary layer profiles were obtained from the Falkner-Skan equation [127]. The selected boundary layer profile was such that the local shape factor of the boundary layer on the airfoil obtained from a panel method with integral boundary layer formulation (XFOIL, [128]) matched that of the Falkner-Skan solution. However, the Falkner-Skan equation does not provide a solution in case of separated flow close to the trailing edge and thus the applicability of this methodology to a number of relevant cases is questionable. Recently, de Pando *et al.* [15] assessed the global spectrum and associated modes using global stability analysis. They found that the frequency associated to the leading global modes (largest amplification rate) was in good agreement with the tonal frequencies. Furthermore, the leading global mode represented the shear layer instabilities in the aft portion of the suction side separation bubble and upstream propagation of acoustic waves. These observations thus provide evidence for the existence of an acoustic feedback loop as a frequency selection mechanism.

The difference in frequency between two tones, $\Delta f = f_{n+1} - f_n$, results in a relation for the frequency spacing:

$$\Delta f^+ = \frac{L_f \Delta f}{u_\infty} = \frac{1}{u_\infty / u_c + u_\infty / (c_0 - u_\infty)} \quad (2.56)$$

Note that, for very small values of the Mach number (i.e. $M_0 = u_\infty / c_0 \ll 1$), $u_\infty / (c_0 - u_\infty) \ll 1$ and negligible compared to the ratio u_∞ / u_c .

For a NACA 0012, Arbey and Bataille [18] proposed the following empirical relation for the frequency selection of tones present in the acoustic spectrum:

$$\Delta f^+ = \frac{L_f \Delta f}{u_\infty} \approx 0.37 M_0^{-0.15} \quad (2.57)$$

Nash *et al.* [16] suggested an alternative concept for the presence of multiple tones, namely a hydrodynamic modulation of the vortex shedding process due to interaction between events from the two sides of the airfoil. Instead of an acoustic feedback loop, the authors suggested a variation of the mean flow that extends far upstream on the airfoil and modifies the amplification behavior of instabilities. Further, Desquesnes *et al.* [129] introduced the notion of a *secondary feedback loop* that acts to modulate the main or *primary feedback loop* (figure 2.15c) and might therefore be responsible for the modulation of the primary tone amplitude.

At present questions with regard to the precise nature of the interaction between events on the two sides of the trailing edge and the aeroacoustic feedback loop remain unsolved and are subject to ongoing research. It can however be conjectured that these questions do not have a unique answer, but that the latter depends on the flow conditions encountered on a specific profile. However, the controversy highlights the need for further research on the topic.

2.3.3. ROLE OF BOUNDARY LAYER SEPARATION

The importance of the flow field topology for the amplification of instability waves has been recognized in the works of Arbey and Bataille [18], followed by Lowson *et al.* [130, 131] and Nash *et al.* [16], Nash and Lowson [132], Nash [133], who investigated the phenomenon on a NACA 0012 airfoil. They concluded that a separation sufficiently close to the trailing edge is a necessary condition for tonal noise generation. Such separation has since been observed in more recent experimental studies with PIV [50, 68, 69] and numerical simulations [125, 129].

In case the flow reattaches upstream of the trailing edge, one denotes the resulting flow topology as a *laminar separation bubble* (figure 2.17). Laminar separation bubbles often develop on airfoils operating at low Reynolds numbers ($Re_c < 5 \times 10^5$) [134–137]. At these operating conditions, laminar boundary layer separation may occur on the airfoil due to an adverse pressure gradient. Such adverse pressure gradient is in most cases equivalent to a negative gradient of the boundary layer edge velocity u_e . The resulting separated shear layer is inherently unstable and undergoes laminar-to-turbulent transition downstream of the separation location. The transition process enhances the exchange of momentum between the inner and outer parts of the wall-bounded shear layer, which can lead to flow reattachment (figure 2.17a).

The dividing streamline between separation and reattachment points separates the recirculating flow region from the separated flow. This flow topology is the defining characteristic for laminar separation bubbles. At higher angles of attack or lower Reynolds numbers, the separated shear layer fails to reattach, thus stalling the airfoil. Since laminar boundary layer separation can have a profound effect on airfoil performance, the associated key aspects of flow development, including separated shear layer transition and separation bubble topology, have been investigated in a large number of previous studies (e.g. Dovgal *et al.* [138], Burgmann and Schröder [139], Hain *et al.* [140], Jones *et al.* [141], Brinkerhoff and Yaras [142]). A detailed overview of the relevant studies on laminar separation bubbles can be found, for example, in Marxen and Henningson [143] and [144].

The results of previous investigations show that the transition process in the separated shear layer is initiated by the amplification of disturbances within a band of frequencies (e.g. Dovgal *et al.* [138], Watmuff [145], Yarusevych *et al.* [146]). The initial growth of disturbances agrees well with linear stability theory (e.g. Jones *et al.* [147], Marxen and Rist [148]), and the primary amplification mechanism is attributed primarily to an inviscid Kelvin-Helmholtz instability [144]. However, as disturbance amplitude grows, non-linear interactions ensue during the later stages of transition [149, 150]. The growing disturbances can cause the transitioning shear layer to roll up into vortices (figure 2.16). The formation of shear layer roll-up vortices in a laminar separation bubble has been observed in flows over airfoils (e.g. Burgmann and Schröder [139], Jones *et al.* [141], Burgmann *et al.* [151], Wolf *et al.* [152]) and flat plates (e.g. Watmuff [145], Lang *et al.* [149], Alam and Sandham [150], Marxen *et al.* [153]) and is depicted in figure 2.17b. The initial two-dimensional shear layer roll-up is followed by significant three-dimensional deformations of the roll-up vortices, which then break down into smaller structures. The dynamics of these structures in laminar separations bubbles as well as the underlying instability mechanisms responsible for their development are still not

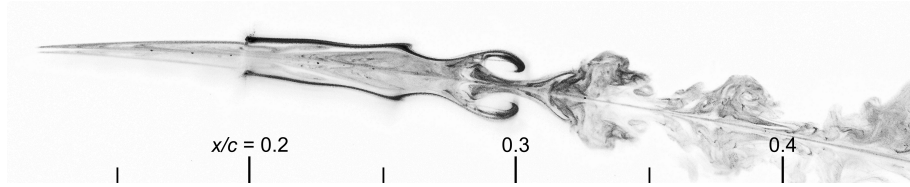


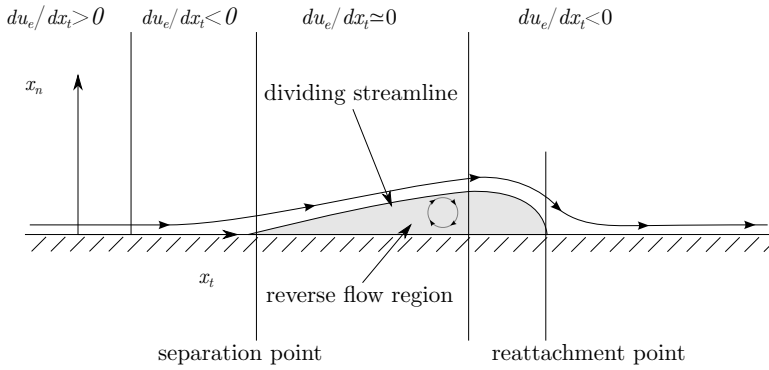
Figure 2.16: Flow visualization of the vortex shedding in the aft portion of a separation bubble on an airfoil. Image provided courtesy A. Lambert and S. Yarusevych, University of Waterloo [154].

fully understood, and are the subject of active research [153].

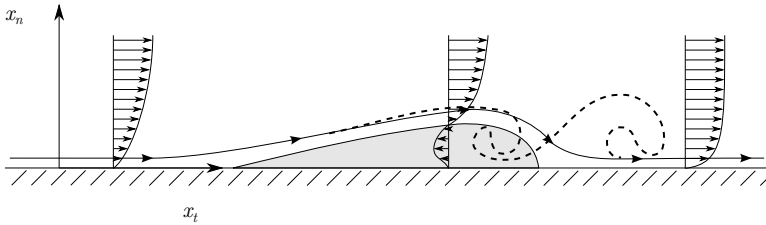
For various airfoils, McAlpine *et al.* [44] observed a separation bubble on the pressure side near the trailing edge and proposed its presence as a necessary condition for tonal noise. Furthermore, their measurements implied that the intensity of the tones is related to the extent of the separation bubble. In a related study, Nash *et al.* [16] pointed out that a region of separated flow might exist without tonal noise generation. Therefore, the conditions of Lawson *et al.* [130], requiring the presence of flow separation, may be regarded as necessary but not sufficient for discrete tones to occur.

Paterson *et al.* [35], Fink [121], Hersh and Hayden [155] performed experiments applying a tripping device to force transition on pressure and suction sides separately. By inducing transition, boundary layer separation is prevented and the turbulent boundary layer remains attached. In the aforementioned studies, forcing transition on the suction side was found to have only a small effect on the tonal noise generation, while application of the tripping device on the pressure side of the airfoil led to suppression of tonal noise. It was concluded that instability waves in the laminar boundary layer on the pressure side are essential to tonal noise generation. Thus, many studies suggest that tonal noise generation is governed by separated shear layer development on the pressure side [16, 35, 119]. Consequently, for most airfoil profiles at high Reynolds numbers, it occurs at relatively low angles of attack, when separation on the pressure side takes place upstream of the trailing edge. Experimental studies on a NACA 0012 profile show that tonal noise emissions at low Reynolds numbers can be dominated by suction side events, while emissions at higher Reynolds number relate to pressure side events [52, 156].

The origin of the amplified instability waves leading to tonal noise is often ascribed to Tollmien-Schlichting instability waves, as originally suggested by Arbey and Bataille [18]. However, Atassi [158] pointed out that since tonal noise emissions on airfoils occur in presence of boundary layer separation upstream of the trailing edge, the associated instability waves are likely to be due to a Kelvin Helmholtz instability. In fact, it can be seen from the results of recent experimental measurements [50] and numerical simulations [125, 129] that trailing edge emissions are produced by strong coherent structures, similar to roll-up vortices observed in separation bubbles and separated shear layers (figure 2.17b). While these structures may originate from small amplitude instability waves in the wall-bounded shear flow upstream of the trailing edge [50], they produce flow field fluctuations substantially exceeding those admissible for the classification of instability wave packets [118].



(a) Characteristic topology of separation bubble in relation to boundary layer edge velocity u_e .



(b) Mean velocity profiles and schematic amplification of instabilities over separated shear layer.

Figure 2.17: Schematic of separation bubble. Figure adapted from Ellsworth and Mueller [157].

2.3.4. OVERVIEW OF PREVIOUS STUDIES

A large number of experimental and numerical studies have been dedicated to the topic of laminar boundary layer instability noise. The by far largest subset of these studies, including most of the fundamental work, have concentrated on symmetric airfoil profiles and specifically on the NACA 0012.

These works cover a wide range of flow conditions defined by the parameters Reynolds number Re_c , Mach number M_0 , and angle of attack α . For experiments conducted in open or closed section wind tunnels, the geometric angle of attack α_{geo} is usually different from the effective angle of attack α_{eff} , which represent the equivalent flow condition in an infinite domain without boundaries. For the NACA 0012 a correction method has been proposed for open jet wind tunnel experiments [13] and shows the correction factor $\alpha_{eff}/\alpha_{geo}$ to be an increasing function of blockage ratio c/H , where c is the chord of the airfoil and H the jet width. Details on the correction method will be given in section 4.2.3.

Table 2.1 shows an overview of experimental studies on the topic, including the aforementioned parameters. Comparison shows that most of the previous studies have been conducted for comparatively large blockage ratios $H/c \leq 4$. This can have a considerable influence on the pressure distribution over the airfoil [159].

The topic has also been investigated numerically in a number of studies, which are listed in table 2.2. Due to the coherent nature of the instability waves observed experimentally in cases of strong tonal noise generation, the 2D flow assumption was often

accepted to be valid. The unsteady nature of the flow and acoustic feedback effects require the use of DNS or LES techniques. 2D simulations have been the preferred flow model for the past decade with few exceptions [147]. However, with increasing computational resources and the realization that turbulent breakdown upstream of the trailing edge can influence the noise generation process through reduction of the spanwise correlation length, attention will likely shift to 3D simulations in the future to provide better comparison with experiments.

It should be noted that due to the sustained interest in the topic over the past decades a large number of studies has been published and the overviews provided in tables 2.1 and 2.2 are not guaranteed to be complete.

Table 2.1: Overview of publications containing data on NACA 0012 noise generation based on experiments (not complete). Arranged chronologically from top to bottom.

Reference	c [mm]	H [mm]	$Re_c [\times 10^5]$	M_0	α_{geo}	α_{eff}
Paterson <i>et al.</i> [35]	228.6	787.4	3-29.4	0.06-0.56	$4^\circ, 6^\circ, 10^\circ$	$2.6^\circ, 3.9^\circ, 6.6^\circ$
Arbey and Bataille [18]	80, 160	150	1-7		0°	0°
Nash <i>et al.</i> [16]	300	600	1-14.5	0.01-0.2	$2^\circ, 3^\circ, 4^\circ, 5^\circ$	closed
Arcondoulis <i>et al.</i> [160]	67	75	0.5 - 1.5	0.03-0.1	$0^\circ, 5^\circ, 10^\circ$	$0^\circ, 1.6^\circ, 3.2^\circ$
Inasawa <i>et al.</i> [156]	150	600	0.48-4.3	0.01-0.1	2°	1.4°
Takagi and Konishi [161]	400	1,000	4.5	0.05	4°	2.3°
Chong and Joseph [117]	150	150	2.5-5	0.07-0.15	5°	1.4°
Plogmann <i>et al.</i> [119]	200	2,730	3.1-7.5	0.07-0.16	4°	closed
	400	2,730	15.7	0.17	$3^\circ-8^\circ$	closed

Table 2.2: Overview of publications containing data on NACA 0012 noise generation based on numerical simulations (not complete). Arranged chronologically from top to bottom).

Reference	Type	$Re_c [\times 10^5]$	M_0	α_{eff}
Desquesnes <i>et al.</i> [129]	2D DNS	2/1	0.1/0.05	$2^\circ/5^\circ$
Sandberg <i>et al.</i> [124]	2D DNS	0.5	0.4	$0^\circ/5^\circ/7^\circ$
Jones <i>et al.</i> [147]	2D/3D DNS	0.5	0.4	5°
Jones and Sandberg [125]	2D DNS	1	0.4	$0^\circ, 0.5^\circ, 1^\circ, 2^\circ$
	2D DNS	0.5	0.4	5°
Tam and Ju [162]	2D DNS	2-5	0.09-0.2	0°
Ikeda <i>et al.</i> [163]	2D DNS	0.1	0.1-0.3	0°
Golubev <i>et al.</i> [164]	2D/3D DNS	1.8	0.072	2°
de Pando <i>et al.</i> [15]	2D DNS	2	0.4	2°

3

ESTIMATION OF SOUND AND SURFACE PRESSURE

Pressure variations inevitably occur in all unsteady fluid flows. Sometimes these variations are confined to the flow itself, providing the volume forces necessary to balance fluctuations of local momentum, and sometimes they propagate away from the flow as sound. Pressure fluctuations can be recorded by the ear or with a microphone, and there is a tendency to regard all pressures sensed in this way as sound.

John "Shôn" Eirwyn Ffowcs Williams, [165]

Advances in the application and processing techniques of Particle Image Velocimetry (PIV) over the past decade have lead to a point, where it becomes possible to measure volumetric, unsteady velocity fields. Pressure reconstruction techniques allow for the statistical description of the unsteady surface pressure. This chapter describes a methodology for the deduction of this unsteady surface pressure field, induced by a turbulent boundary layer, and a novel approach for the prediction of sound produced at the trailing edge, that exclusively relies on PIV measurements.

Parts of this chapter have been published in the Journal of Sound and Vibration **346** (2015) [66].

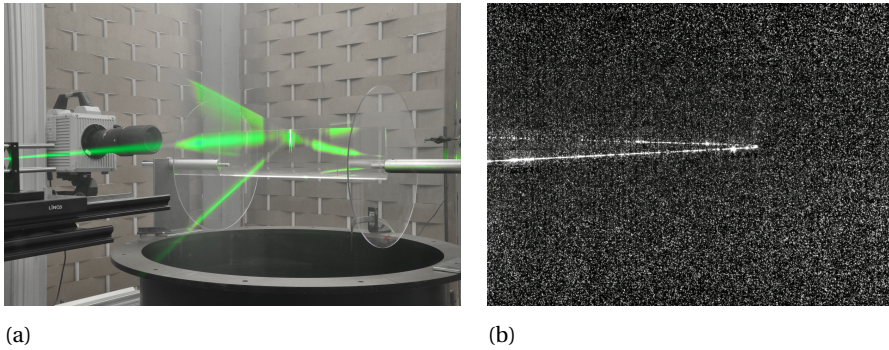


Figure 3.1: Photograph of typical planar PIV set-up for imaging the flow around a trailing edge (a) and PIV image showing tracer particles and outline of sharp trailing edge with reflections from surface (b).

3.1. PARTICLE IMAGE VELOCIMETRY

PARTICLE IMAGE VELOCIMETRY (PIV) has been treated exhaustively in a number of textbooks. Information on its principles and applications can be found for instance in Westerweel [166], Raffel *et al.* [167], and Adrian and Westerweel [168]. Here, a short introduction is provided and basic relations for experimental design can be found in appendix D.

PIV is a non-intrusive field measurement technique. In a PIV measurement so-called tracer particles are injected into the flow (*seeding of the flow*) and illuminated by a light sheet formed by an arrangement of laser and optical elements (mirrors, lenses). The light is emitted in the form of pulses with duration in the order of nanoseconds, scattered by the particles, and consequently collected on the sensor of one or multiple cameras. On one hand the tracer particles are required to follow the flow accurately, which is ensured by a small diameter or density similar to that of the fluid. On the other hand, the scattered light intensity increases with increasing diameter. At Delft University of Technology, typically a water-glycol based fog fluid solution (mean diameter $1\mu\text{m}$) is used for the seeding of low speed air-flows. Figure 3.1 shows a typical planar PIV set-up and an example of an unprocessed image, depicting the light scattered by tracer particles in the flow around a sharp trailing edge.

PIV systems can be of the low repetition rate type (low-speed) and high repetition rate type (high-speed), differing in the maximum possible sampling frequency accommodated for by illumination and acquisition hardware. With the latter systems repetition rates of up to 20kHz are possible. The relevance of unsteady flow events for the quantitative description of aeroacoustic sources suggests the application of high-speed PIV systems. The high-speed PIV system currently available at Delft University of Technology includes four Photron *FastCam SA1.1* (1024×1024 pixels (px), 12bits, pixel pitch $20\mu\text{m}$) and two Nd:YLF lasers, a Litron dual cavity laser and Quantronix *Darwin Duo* laser (2×25 mJ/pulse at 1kHz).

Images are acquired at two successive time instances, separated by the laser pulse separation Δt . In *double frame* operation, the acquisition frequency f_{acq} and pulse separation Δt are independent parameters. During *single frame* operation, the acquisition

frequency is equal to the reciprocal of the pulse separation $f_{acq} = 1/\Delta t$ and a continuous series of images is acquired. Over the pulse separation time Δt tracer particles move with the flow. The projection of these displacements on the illuminated plane finds representation in the recorded images and the displacement vector $\Delta \mathbf{x}$, required for the estimation of the velocity field, is determined by a cross-correlation of two consecutive images. Disregarding effects of aliasing, the measurements is time-resolved if $f_{acq} > 2/\tau$, where τ is characteristic period associated to the flow. In a flow mainly convecting at velocity u_c (e.g. boundary layer or wake flow), an estimation is $\tau \approx \delta/u_c$, where δ is a characteristic flow scale.

In contrast to other flow measurement techniques, such as hot-wire anemometry and Laser Doppler Velocimetry, sampling rates in high-speed PIV are currently restricted to maximum 10kHz. For aeroacoustic laboratory scale experiments, the dimensional frequency of interest increases with the square of the model scaling factor if the Reynolds number is maintained constant. Thus, higher acquisition rates through improvement in hardware are still desired. Alternative post-processing methods for enhancing the time-resolution of PIV measurements have been proposed. These *super-sampling* methods augment information measured directly by the PIV system through auxiliary models, for instance interpolation or solution of flow equations [169].

Besides spectral resolution of velocity field measurements, high-speed PIV also allows for an estimation of the acceleration. The ability to estimate temporal derivatives finds application for instance for PIV-based pressure reconstruction methods [170]. Methods for the interrogation of time-resolved image sequences have been proposed with the goal to reduce the random error on the velocity field measurement (*Multi-frame*) [171]. Recent examples of such methods include the *Pyramid Correlation* [172] and *Fluid Trajectory Correlation* (FTC) [173]. While multi-frame methods reduce the standard deviation associated to the random measurement error, the frequency response characteristics are not sufficiently understood yet. Moreover, these response characteristics also depend on the spatial resolution and type of flow. As an example, Lynch *et al.* [174] investigated the frequency response of the FTC method for a turbulent boundary layer flow. Random errors are usually reduced at frequency low with respect to the inverse of the kernel time scale, while attenuation of the signal is small in this range. At high frequency, the attenuation of the signal due to temporal filtering increases and thus a correct estimation of the auto-spectral density is not guaranteed a priori, but relies on optimization criteria. Moreover, high frequencies are associated to small length scales δ in convective flows. Thus, at high frequency the spatial resolution of the measurement becomes increasingly critical for an accurate measurement and is often the limiting factor in high-speed experiments.

Tomographic PIV is the extension of the PIV approach to volumetric measurements, providing information on all three velocity components. First applications can be found in the work of Elsinga *et al.* [175]. Scarano [176] provided a recent review of the the principles and practice of tomographic PIV. Compared to planar PIV, the set-up of a tomographic PIV involves more elements. The flow, seeded with particles, is imaged simultaneously with a minimum of three, but typically four cameras (figure 3.2a). Systems with up to 12 cameras have been implemented in the laboratory [177]. 2D images, recorded by the different cameras, are combined in a reconstruction step to yield a 3D represen-

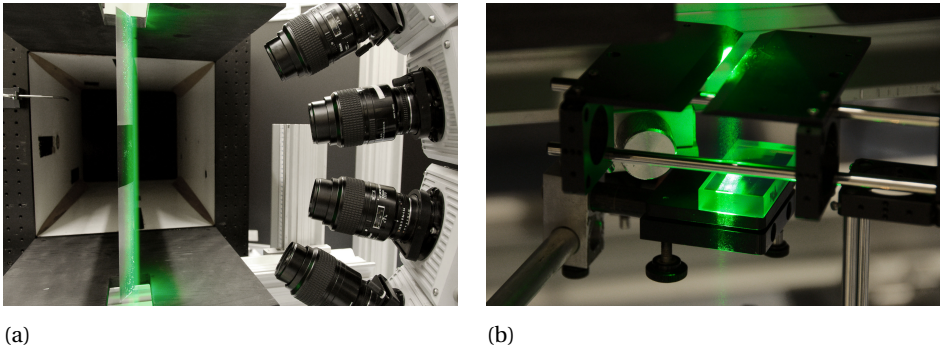


Figure 3.2: Photograph of a typical tomographic PIV set-up for imaging the flow over a trailing edge (a). Details of the multi-pass illumination arrangement (b).

tation of the intensity distribution of the light scattered by the tracer particles. Different methods for volume reconstruction are available [176]. In the work presented here, the Multiplicative Algebraic Reconstruction Technique (MART) [175] is used for volume reconstruction. For interrogation of the resulting 3D representation similar methods as in planar PIV with extension to 3D are employed.

In high-speed applications and especially in combination with tomographic PIV, the light budget imposed by the available illumination hardware and set-up is critical. In tomographic PIV, the required imaging of a measurement volumes requires a larger depth of field and thus a small aperture [178]. To alleviate this issue, Schröder *et al.* [179] and later Ghaemi and Scarano [180] employed multi-pass light amplification systems to create the measurement volume (figure 3.2b). The amplification factor achieved in the laboratory set-up was found to exceed that of a single pass system by factor seven [180].

Processing time for tomographic PIV reduced over the course of the years through availability of new hardware and more efficient implementation of reconstruction and interrogation methods. While the processing of large time-series of tomographic PIV data has posed a severe limitation at the beginning of this thesis research, it becomes more practicable with recent developments.

3.2. PIV BASED NOISE PREDICTION

3.2.1. TURBULENT BOUNDARY LAYER TRAILING EDGE NOISE

Due to limitations on the temporal and spatial dynamic range, a comprehensive approach to trailing edge noise prediction based directly on the application of an aeroacoustic analogy without further modeling is at present not possible [65] (see discussion in section 2.1.3).

Here, the approach based on diffraction theory is followed, which requires statistics of the incident pressure field as input (section 2.2.4). This approach has been applied and validated in the past through data obtained experimentally and numerically. For instance, Brooks and Hodgson [36] performed surface pressure measurements, while Christophe [84] compared predictions from Large Eddy Simulation (LES) solutions with

far-field acoustic measurements. In the first case complex instrumentation of the model was required, while in the latter case the information relating to the spanwise coherence of the pressure field was complemented by the use of semi-empirical models (section 2.2.2). An alternative to the use of surface pressure sensors is PIV based (*pressure reconstruction*). The derivation of pressure based on PIV data has received ample attention in recent years and the principle has been well established [170]. Ghaemi *et al.* [181] showed by comparison to pinhole microphone measurements that a sufficiently accurate estimation of the fluctuating surface pressure can be obtained from time-resolved tomographic high-speed PIV data. The specifics of the methodology for pressure reconstruction used in this study will be explained in section 3.3.

Using the results of section 2.2.4, in particular application of equation 2.35, requires the following statistics of the incident pressure field:

1. the auto-spectral density $\Phi_{pp}(\omega)$
2. the spanwise correlation length $l_z(\omega, \Delta z)$
3. the convective velocity u_c

Assuming near homogeneous statistics near the trailing edge and across the span, evaluation of the auto-spectral density is straightforward by sampling and analyzing the reconstructed surface pressure signal at a point upstream of the trailing edge (see appendix E for details on statistical data analysis).

ESTIMATION OF CORRELATION LENGTH

The correlation length can be obtained on the basis of its definition (equation 2.11 or 2.13) through numerical integration of the spanwise coherence. Due to convergence issues related to the finite observation period and noted by Christophe [84], the coherence does not approach zero for large separations Δz and therefore the integral in equation 2.11 is unbounded in most cases for experimental data; especially for small data sets available in tomographic experiments. Alternatively, the correlation length $l_z(\omega)$ can be estimated through a fit of the spanwise coherence to an exponential function (equation 3.1).

$$\sqrt{\gamma^2(\omega, \Delta z)} \approx e^{-\frac{|\Delta z|}{l_z}} \quad (3.1)$$

An example for its application is the work of Palumbo [182]. Other fitting models for the coherence function have been proposed. For instance, a Gaussian function was used by Roger *et al.* [105]. The latter model is physically consistent in the sense that it provides a zero derivative $\partial\gamma^2/\partial\Delta z(\omega, 0) = 0$ at $\Delta z = 0$. Equation 3.2 provides the expression, where $\lambda(\omega, \Delta z)$ is the fitting parameter. The correlation length is then given by $l_z(\omega) = \sqrt{\pi/2}\lambda(\omega)$.

$$\gamma^2(\omega, \Delta z) \approx e^{-\frac{\Delta z^2}{\lambda^2}} \quad (3.2)$$

INFLUENCE OF NOISE ON COHERENCE ESTIMATE

For the application with experimental data, it is of interest to examine the sensitivity of the coherence estimate (equations 2.9 and 2.10) to noise. To assess the latter, two signals with known coherence are generated and a white noise distribution is superimposed. Let $s_1(t)$ be the realization of a random process with a uniform probability distribution, standard deviation σ_s , and bandwidth limited to frequencies below half of the sampling frequency. Let further $s_2(t)$ be a second realization of such a process. Then signals $u(t)$ and $v(t)$ of variable coherence can be generated by summation of $(1-c)s_1(t)$ and $cs_2(t)$ with a coefficient $0 \leq c \leq 1$. To model the measurement noise, realizations of a second process with uniform probability distribution $n_1(t)$ and $n_2(t)$ (white noise) with standard deviation σ_n are superimposed on s_1 and s_2 , respectively:

$$\begin{aligned} u(t) &= s_1(t) + n_1(t) \\ v(t) &= (1-c)s_1(t) + cs_2(t) + n_2(t) \end{aligned} \quad (3.3)$$

Realizations u and v are less correlated with increasing c . Ideally, the cross-spectral density of the noise signals is identically zero $\Phi_{n_1 n_2} = 0$. On the other hand, the auto-spectral density is finite and positive $\Phi_{n_1 n_1}, \Phi_{n_2 n_2} > 0$. Thus, the noise component adds to the auto-spectral density of the signals u and v , respectively, and the coherence estimate in equation E.20 is expected to decrease with decreasing signal-to-noise ratio σ_s/σ_n .

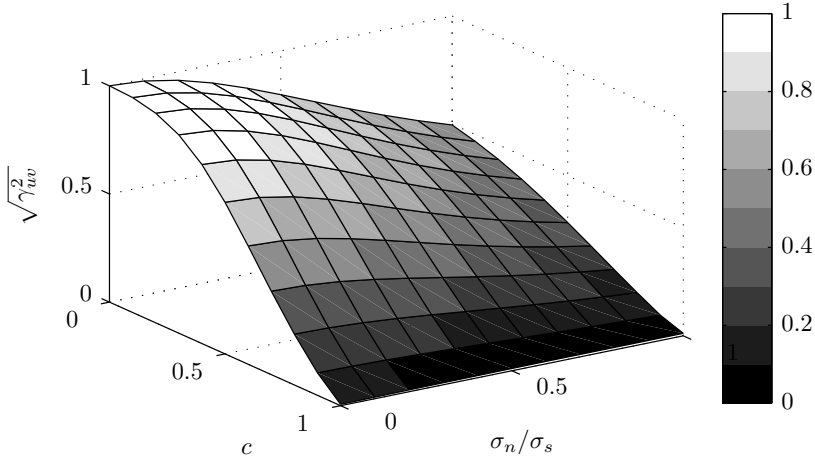
Figure 3.3 shows the magnitude square coherence γ_{uv}^2 and its positive square root for parameters of $0 \leq c \leq 1$ and $0 \leq \sigma_n/\sigma_s \leq 1$. For $c = 1$ the coherence $\gamma_{uv}^2 = 0$ since the signals u and v are uncorrelated. For $c = 0$ and $\sigma_n/\sigma_s = 0$ the signals u and v are identical and thus $\gamma_{uv}^2 = 1$. For velocity fields in PIV, the random error is typically on the order $\sigma_n/\sigma_s \approx 0.1\text{px}/10\text{px} \approx 1\%$. Figure 3.3 shows that the decrease in coherence due to measurement noise is negligible under such conditions. For reconstructed pressure spectra in boundary layers typical noise levels are $\sigma_n/\sigma_s \approx 20\%$ [181, 183] and an underestimation of the coherence by approximately 5% is expected. On a decibel scale, which is usually of interest for acoustic predictions, this underestimation is negligible ($\pm 0.2\text{dB}$).

ESTIMATION OF CONVECTIVE VELOCITY

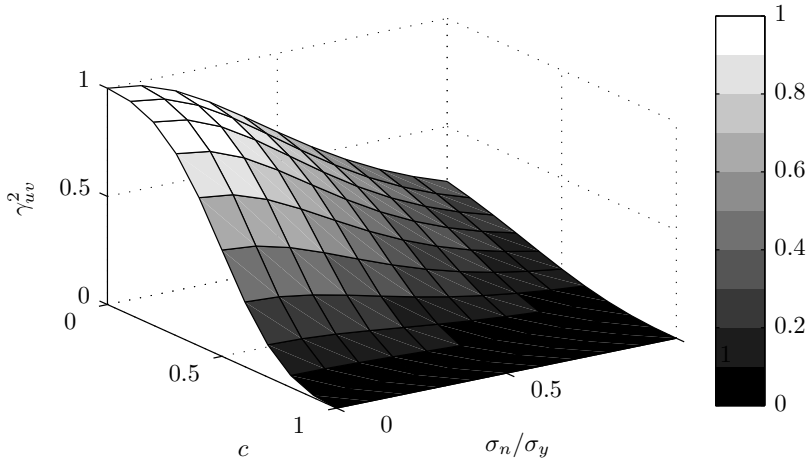
The convective velocity is often estimated using data obtained from an array of surface mounted sensors (e.g. Brooks and Hodgson [36]). This method requires complex instrumentation of the model. Assuming a constant convective velocity over all frequencies, a cross-correlation analysis between two points can provide an approximation of the convective velocity.

Alternatively, the convective velocity u_c can be estimated from the wavenumber-frequency spectrum of a flow field variable (see also section 2.2.1). It should be noted that u_c then represents an average over the spatial domain considered for the wavenumber decomposition. A convective velocity u_c is associated to a given wavelength λ (or wavenumber k_x) and frequency f , representing the maximum energy content, through the relation

$$u_c = \lambda f = \frac{2\pi f}{k_x} \quad (3.4)$$



(a) Modulus of normalised cross-spectral density.



(b) Magnitude square coherence.

Figure 3.3: Effect of random noise on coherence estimate.

An estimation of the uncertainty for the estimation can be obtained by considering the limited wavenumber δk_x and frequency resolution δf as sources of error. Assuming that the two variables are uncorrelated, the error is propagated using equation 3.5.

$$\frac{\delta u_c}{u_c} \approx \sqrt{\left(\frac{\delta f}{f}\right)^2 + \left(\frac{\delta k_x}{k_x}\right)^2} \quad (3.5)$$

Due to the short spatial domain usually available in PIV experiments, δk_x dominates this error and for the experiments in chapter 5 amounts to about 10% of the convective velocity or 5% of the free-stream velocity.

3

3.2.2. TRAILING EDGE BLUNTNESS NOISE

For the estimation of trailing edge bluntness noise, the approach described in section 2.2.5 is followed. In particular, equation 2.43 needs to be evaluated at the receiver position. This evaluation requires as input statistics of the upwash velocity at the end of the vortex formation zone, namely:

1. the auto-spectral density $\Phi_{vv}(\omega)$
2. the spanwise correlation length $l_z(\omega, \Delta z)$
3. the convective velocity u_c

For this case, the definition of $l_z(\omega)$ is given in equation 2.46. Estimation of the correlation length $l_z(\omega)$ from experimental data is based on a curve fit to an exponential function (see also section 3.2.1 for discussion).

Here, it is proposed to obtain this data by high-speed planar PIV measurements as described in the following section. In chapter 9, the method is applied and the results are compared to acoustic measurements for the case of vortex shedding behind a beveled trailing edge.

3.3. UNSTEADY SURFACE PRESSURE RECONSTRUCTION

Methods for the reconstruction of the pressure field from PIV velocity field data for incompressible flows have received much attention in recent years. van Oudheusden [170] provided a recent review of previous research on the topic. Early application of pressure reconstruction techniques is due to Liu and Katz [184]. Later studies, for instance Charonko *et al.* [185], concentrated on the assessment of the measurement accuracy and robustness of different pressure reconstruction schemes. de Kat and van Oudheusden [186] applied pressure reconstruction to flow past a square cylinder and by comparison to pressure transducer measurements obtained guidelines for the required temporal and spatial resolution of the measurements. The measurement of the unsteady surface pressure fluctuations in turbulent boundary layers based on tomographic PIV has been demonstrated in experiments reported by Ghaemi *et al.* [181] and Pröbsting *et al.* [183].

In most cases, methods for derivation of the pressure from velocity field data are based on the momentum equation 3.6, where \mathbf{u} is the velocity field vector and μ the dynamic viscosity. Here, $\partial \cdot / \partial t$ denotes a partial derivative with respect to time, ∇ the nabla operator, and $\Delta = \nabla \cdot \nabla$ the Laplace operator.

$$\rho \left(\frac{\partial \mathbf{u}}{\partial t} + (\mathbf{u} \cdot \nabla) \mathbf{u} \right) = -\nabla p + \mu \Delta \mathbf{u} \quad (3.6)$$

Applying the divergence operator and considering that the divergence of the velocity field vanishes for incompressible flows, one obtains the Poisson equation for the pressure (equation 3.7), where the material derivative is denoted by $D \cdot / Dt = \partial \cdot / \partial t + (\mathbf{u} \cdot \nabla) \cdot$.

$$\Delta p = -\rho \nabla \cdot \left(\frac{\partial \mathbf{u}}{\partial t} + (\mathbf{u} \cdot \nabla) \mathbf{u} \right) = -\rho \nabla \cdot \left(\frac{D\mathbf{u}}{Dt} \right) \quad (3.7)$$

Solution of equation 3.7 requires the definition of boundary conditions and an estimation of the material derivative based on the measured velocity fields. These items are discussed in the remainder of this section. The Poisson equation is discretized based on a second order central finite difference method and the resulting system of equations is consequently solved by a preconditioned GMRES (Generalized Minimum Residual Algorithm), as discussed by Golub and van Loan [187] among others.

3.3.1. ESTIMATION OF MATERIAL DERIVATIVE

It has been shown by Violato *et al.* [188] that Lagrangian methods, based on an approximation of the material derivative through reconstruction of the path followed by a fluid parcel, reduce the random measurement error when compared to Eulerian estimates.

This method of tracking the path followed by a fluid parcel, denoted by Γ , over time is called "pseudo-tracing" and was first introduced by Liu and Katz [184] for the estimation of the material derivative. Let $\mathbf{x}_p(t) \in \Gamma$ be the path of a fluid parcel that is located at $\mathbf{x}_p(t_0) = \mathbf{x}_0$ at time t_0 . Then the position of the fluid parcel at any time instant t can be determined by evaluating the integral expression in equation 3.8, where $\mathbf{u}_p(t) = \mathbf{u}(\mathbf{x}_p(t), t)$ denotes the velocity of the fluid parcel at a given time instant t . Note that equation 3.8 can be applied to reconstruct the path of the fluid parcel forward ($t > t_0$) or backward ($t < t_0$) in time.

$$\mathbf{x}_p(t) = \int_{t_0}^t \mathbf{u}_p(t) dt + \mathbf{x}_0 \quad (3.8)$$

Figure 3.4 shows a schematic for the evaluation of the fluid parcel's trajectory. Equation 3.8 needs to be discretized since the velocity field is only measured at discrete time instances t_i . This discretization will be explained in the following section.

Once the fluid parcel's path $\tilde{\Gamma}$ is estimated over a finite time interval, the velocity and acceleration of the fluid parcel can be evaluated. Its acceleration then provides an estimate for the material derivative.

The method originally suggested by Liu and Katz [184] relies on a finite difference approximation, considering the velocity difference at the end points of the reconstructed path $\tilde{\Gamma}$. Here, the numerical procedure is based on a least-squares regression of the fluid parcel's velocity $\mathbf{u}_p(t)$ using a first-order polynomial basis (equation 3.9) [183].

$$\mathbf{u}_p(t) = \mathbf{u}_p(t_0) + (t - t_0) \mathbf{a}_p \quad (3.9)$$

The coefficients \mathbf{a}_p are determined by solving the linear system of equations, where the velocity of the fluid parcel at varying time instances is input. Once the polynomial

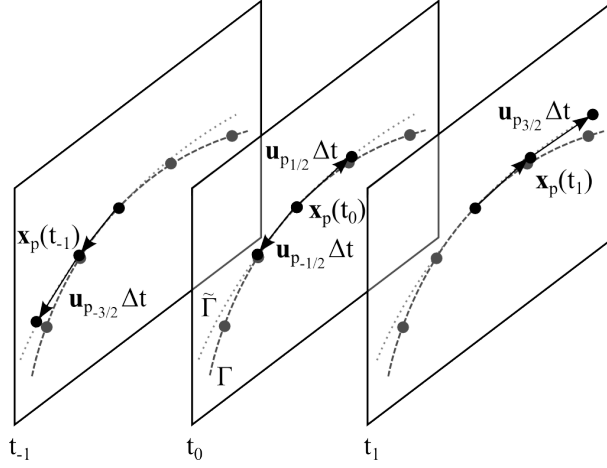


Figure 3.4: Schematic representation of path $\mathbf{x}_p(t_{\pm i})$ followed by a fluid parcel for estimation of material derivative. Approximated $\tilde{\Gamma}$ (dotted line) and real trajectory Γ (dashed).

approximation is obtained for the given fluid parcel motion, the material derivative is evaluated by analytical derivation as

$$\left. \frac{D\mathbf{u}}{Dt} \right|_{t_0} = \frac{d\mathbf{u}_p}{dt}(t_0) = \mathbf{a}_p \quad (3.10)$$

3.3.2. DISCRETIZATION OF FLUID PARCEL TRAJECTORY RECONSTRUCTION

To obtain an approximation $\tilde{\Gamma}$ of the fluid parcel's trajectory based on the measured vector fields $\mathbf{u}(\mathbf{x}, t_i)$ at discrete time instances $t_i = t_0 + i\Delta t$ equation 3.8 needs to be discretized. Typically, the discrete time intervals Δt are chosen to be the reciprocal of the sampling frequency f_{acq} . In the following, $\mathbf{x}_p(t_i)$ refers to the estimated location of the fluid parcel at time t_i , i.e. $\mathbf{x}_p(t_i) \in \tilde{\Gamma}$.

Consider a fluid parcel located at $\mathbf{x}_p(t_0) = \mathbf{x}_0$ at time t_0 . To find the location of the fluid parcel at the following time instant t_1 , the integral in equation 3.8 is discretized using a trapezoidal rule. Thus, the velocity of the fluid parcel between between t_0 and t_1 is given by the average velocity $\mathbf{u}_{p1/2} = [\mathbf{u}_p(t_0) + \hat{\mathbf{u}}_p(t_1)]/2$. $\hat{\mathbf{u}}_p(t_1)$ is the initially unknown velocity at time instant t_1 and is therefore initially approximated by $\hat{\mathbf{u}}_p(t_1) = \mathbf{u}_p(t_0)$. An approximation of the fluid parcel location at time t_1 is $\mathbf{x}_p(t_1) = \mathbf{x}_p(t_0) + \Delta t \mathbf{u}_{p1/2}$.

This initial estimate yields an improved estimate of the parcel's velocity at the following time instance $\hat{\mathbf{u}}_p(t_1) = \mathbf{u}(\mathbf{x}_p(t_1), t_1)$. The procedure is repeated until $\|\hat{\mathbf{u}}_p(t_1) - \mathbf{u}(\mathbf{x}_p(t_1), t_1)\| < \epsilon$, where $\|\cdot\|$ denotes a suitable vector norm (L^2 -norm in this case) and ϵ is a constant chosen to be small.

A general expression for evaluating the particle path is given by equation by

$$\mathbf{x}_p(t_{\pm i}) = \pm \frac{\mathbf{u}_p(t_{\pm(i-1)}) + \hat{\mathbf{u}}_p(t_{\pm i})}{2} \Delta t + \mathbf{x}_p(t_{\pm(i-1)}) \quad (3.11)$$

Here, $i = 1 \dots (N-1)/2$ and N denotes the total number of velocity fields considered

(stencil size). The subscript + applies for the evaluation of $\mathbf{x}_p(t)$ at time instances $t > t_0$ (integration forward in time) and the subscript – applies for $t < t_0$ (integration backward in time). Starting at t_0 with $\mathbf{u}_p(t_0) = \mathbf{u}(\mathbf{x}_p(t_0), t_0)$, the path of the fluid parcel is reconstructed forward and backward in time with $\Delta t = 1/f_{acq}$. In the present study the temporal stencil size is chosen as $N = 3, 5, 7, \text{ and } 9$.

3.3.3. LEAST SQUARES ESTIMATE

As result of the trajectory reconstruction described above, one obtains the velocities $\mathbf{u}_p(t_{\pm i}) = \mathbf{u}(\mathbf{x}_p(t_{\pm i}), t_{\pm i})$ along the path taken by the fluid parcel. A vector containing only the j -th velocity component over time is then given by $\mathbf{u}_{pj}(\mathbf{t})$, where the time vector \mathbf{t} has components $t_{\pm i}$.

Defining further the differences in velocity $\Delta \mathbf{u}_{pj} = \mathbf{u}_{pj}(\mathbf{t}) - \mathbf{u}_{pj}(t_0)$ and time differences $\Delta \mathbf{t} = (\mathbf{t} - t_0)$ with respect to the starting point, a linear least squares estimate of the j -th component of the material derivative approximation \mathbf{a}_{pj} is obtained as solution of equation 3.9, where the superscripts \cdot^T and \cdot^{-1} indicate the transpose and inverse, respectively:

$$\mathbf{a}_{pj} = [\Delta \mathbf{t}^T \Delta \mathbf{t}]^{-1} \Delta \mathbf{t}^T \Delta \mathbf{u}_{pj} \quad (3.12)$$

The approximation of the material derivative $D\mathbf{u}/Dt|_{t_0} \approx \mathbf{a}_p$ is obtained by evaluating equation 3.12 for each component j . The result can then be used as source term in the Poisson equation (equation 3.7).

3.3.4. BOUNDARY CONDITIONS FOR PRESSURE RECONSTRUCTION

For the solution of the Poisson equation, boundary conditions are required. Components of the pressure gradient normal to the boundary faces are derived based on the momentum equation (equation 3.6, Neumann boundary condition) and applied everywhere but at the side closest to the free-stream. At the latter boundary, a pressure $p'(\mathbf{x}, t) = p(\mathbf{x}, t) - p_\infty$ is imposed (Dirichlet boundary condition), where p is an approximation of the pressure and p_∞ is the free-stream value (figure 3.5). Ghaemi *et al.* [181] proposed the application of uniform value and showed that this boundary condition, even when imposed within the outer part of the boundary layer, has limited influence on the solution at the wall.

Here, the Dirichlet boundary conditions are applied based on a Reynolds decomposition of the flow field in a time average part $\bar{\mathbf{u}}$ and a fluctuating part \mathbf{u}' (equation 3.13) as proposed by de Kat [189].

$$p'(\mathbf{x}, t) = -\frac{\rho}{2} (\bar{\mathbf{u}}(\mathbf{x}) \cdot \bar{\mathbf{u}}(\mathbf{x}) + \mathbf{u}'(\mathbf{x}, t) \cdot \mathbf{u}'(\mathbf{x}, t) + u_\infty^2) \quad (3.13)$$

This expression can be interpreted as an extended version of the Bernoulli equation, corrected for unsteady advective perturbations. For an advecting Gaussian vortex, it was shown that the above equation corrects well for the pressure field induced at distances larger than a vortex radius (relative error < 5%) [189].

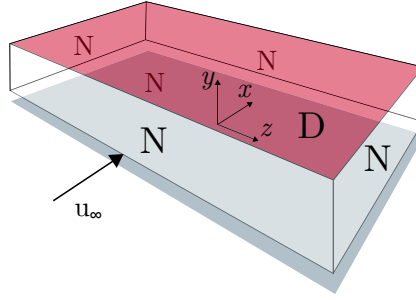


Figure 3.5: Schematic of reconstruction domain indicating the choice of Dirichlet (D) and Neumann (N) boundary conditions.

3.3.5. ERROR ESTIMATION

In studies involving tomographic PIV experiments on turbulent boundary layer flows, Ghaemi *et al.* [181] and Pröbsting *et al.* [183] have compared reconstructed surface pressure spectra to measurements of the unsteady surface pressure by pinhole microphone measurements (see 3.4). Both studies indicated a relative error of about 0.1% of the free-stream dynamic pressure or equivalently about 10% of the unsteady surface pressure fluctuation rms.

To estimate the error arising in the reconstruction of the pressure, the analysis suggested by Ghaemi *et al.* [181] is considered and adapted by accounting for an iterative approximation of the fluid parcel's path. Pröbsting *et al.* [183] reported a random error for the tomographic PIV velocity field measurement of about $0.2v_{xl}$. Thus, one obtains an expression for the random error on the velocity field $\epsilon_{u,rand}$, where S is the spatial resolution of the measurement (in v_{xl}/m) and $\Delta t = 1/f_{acq}$:

$$\epsilon_{u,rand} = 0.2v_{xl} \frac{1}{S\Delta t} \quad (3.14)$$

A systematic error (truncation error, $\epsilon_{u,sys}$) in PIV arises from the acceleration of particles between two exposures. Boillot and Prasad [190] provide an expression for this error, where an additional factor 1/2 is considered for symmetric window deformation following Ghaemi *et al.* [181]:

$$\epsilon_{u,sys} = \frac{1}{4} \Delta t \left\| \frac{D\mathbf{u}}{Dt} \right\| \quad (3.15)$$

Influence of a larger stencil on this systematic error is considered negligible, in particular for the Fluid Trajectory Correlation (FTC) [173].

Further systematic error on the PIV evaluation of the velocity field arises due to the finite spatial resolution, resulting in an attenuation of the signal for turbulent structures smaller than the window size. In convective flows, such as boundary layers and wakes, higher frequencies are associated to smaller spatial scales and the signal at high frequency is thus more attenuated than at low frequency. Lynch *et al.* [174] have investigated this effect by simulating a similar PIV experiment from DNS data of a turbulent boundary layer.

Based on these contributions to the measurement error of the velocity field, the error in the material (Lagrangian) derivative estimation ϵ_{Lag} can be approximated.

In parts, the error arises from the uncertainty of locating the fluid parcel during the trajectory reconstruction. Based on a Taylor series expansion of the particle position forward and backward in time, one can write:

$$\begin{aligned} x_p(t_0 + \Delta t) &= x_p(t_0) + u_p(t_0) \Delta t + \frac{du_p}{dt}(t_0) \frac{\Delta t^2}{2} + \mathcal{O}(\Delta t^3) \\ x_p(t_0) &= x_p(t_0 + \Delta t) - u_p(t_0 + \Delta t) \Delta t + \frac{du_p}{dt}(t_0 + \Delta t) \frac{\Delta t^2}{2} + \mathcal{O}(\Delta t^3) \end{aligned} \quad (3.16)$$

The sub-iterations in the estimation of the fluid parcel trajectory provide $[u_p(t_0) + \hat{u}_p(t_0 + \Delta t)]/2$. Assuming further that the error in the difference of the final estimate and true velocity $\hat{u}_p(t_0 + \Delta t) - u_p(t_0 + \Delta t)$ is of order $\mathcal{O}(\Delta t^2)$ one obtains an estimation for the uncertainty in locating the fluid parcel c_r (equation 3.18).

$$\begin{aligned} c_r &\approx \left| x_p(t_0 + \Delta t) - x_p(t_0) \right| - \left| \frac{u_p(t_0) + \hat{u}_p(t_0 + \Delta t)}{2} \right| \Delta t \\ &= \left| \frac{du_p}{dt}(t_0) - \frac{d\hat{u}_p}{dt}(t_0 + \Delta t) \right| \frac{\Delta t^2}{4} \end{aligned} \quad (3.17)$$

$$\lesssim \left| \frac{du_p}{dt}(t_0) \right| \frac{\Delta t^2}{2} \quad (3.18)$$

Repetitive application along the particle trajectory leads to a summation of the truncation error. Neglecting further $\mathcal{O}(\Delta t^3)$ terms due to additional error on the velocity, one obtains an estimate for the error on the Lagrangian derivative due to truncation $\epsilon_{Lag, trunc}$ (equation 3.20).

$$\epsilon_{Lag, trunc} = |n| \frac{c_r |\nabla \cdot \mathbf{u}|}{\Delta t} \quad (3.19)$$

Replacing the uncertainty on the location of the fluid parcel c_r from equation 3.18 in equation 3.19 provides the compact expression in equation 3.20.

$$\epsilon_{Lag, trunc} = \frac{n\Delta t}{2} \left\| \frac{\partial \mathbf{u}}{\partial y} \right\| \left\| \frac{D\mathbf{u}}{Dt} \right\| \quad (3.20)$$

Note that the resulting term depends on n and not on n^2 as found for single step methods by Ghaemi *et al.* [181]. Further, the truncation error depends on the nature of the velocity field. Commonly, this error can give rise to a bias on the amplitude of the pressure fluctuations due to underestimation in the curvature of the path followed by a fluid parcel. For a conservative estimation one considers $n = (N - 1)/2$.

Random error contribution in the estimation of the material derivative arises from the measurement error of the velocity field $\epsilon_{u, rand}$. Assuming that the least-squares estimate behaves similar to an average over $N - 1$ samples, one obtains an estimation of this random error (equation 3.21).

$$\epsilon_{Lag,u,rand} = \frac{\epsilon_{u,rand}}{\sqrt{N-1}\Delta t} \quad (3.21)$$

A systematic error $\epsilon_{Lag,u,sys}$ in the Lagrangian derivative is due to the systematic error in the velocity field estimation by PIV, where $\epsilon_{u,sys}$ is given in equation 3.15.

$$\epsilon_{Lag,u,sys} = \frac{\epsilon_{u,sys}}{\Delta t} \quad (3.22)$$

Assuming that solution of the Poisson equation and application of the approximate boundary condition do not add significantly to the error, equation 3.23 provides an estimate for the error components on the reconstructed pressure field, where ρ is the fluid density and h the spacing of the grid nodes used for the solution of the Poisson equation (equivalent to the vector spacing).

$$\begin{aligned} \epsilon_{p,trunc} &= \rho\epsilon_{Lag,trunc}h \\ \epsilon_{p,u,rand} &= \rho\epsilon_{Lag,u,rand}h \\ \epsilon_{p,u,sys} &= \rho\epsilon_{Lag,u,sys}h \end{aligned} \quad (3.23)$$

3.4. UNSTEADY SURFACE PRESSURE MEASUREMENTS

Unsteady surface pressure measurements are often required in research related to fluid-structure interaction, vibration, and aeroacoustics due to the significance of the wall pressure spectrum for these applications [19]. In particular, the importance for trailing edge aeroacoustics has been discussed in section 2.2.4.

To obtain a high frequency response for the measurement of the unsteady component of the surface pressure $p'(t)$ microphones are used. Typically, these microphones are of the electret condenser type¹ and mounted directly below a small pinhole orifice[181, 191] or connected through a tubing arrangement to the surface[95, 192].

Figure 3.6 shows an arrangement of the pinhole type mounting. The microphone is located in cylindrical cavity (diameter D) below the pinhole of small diameter ($d \approx 200\mu\text{m}$ in the present study). Such configuration was previously employed by Ghaemi *et al.* [181] in combination with PIV measurements. In simultaneous measurements, the pinhole was found to shield the microphones from direct exposure to and heating by the laser light, which leads to unwanted noise in the measurements. Lueptow [193] and Tsuji *et al.* [194] recommended a pinhole diameter $d/\delta_v < 20$, where δ_v is the viscous length scale of the boundary layer, in order to capture high-frequency fluctuations. Further, Shaw [195] suggested a pinhole depth $l/d \geq 2$.

The pinhole-cavity system depicted in figure 3.6 can be regarded as a Helmholtz resonator. Measurements around the resonance frequency of the system lead to a large over estimation of actual pressure fluctuations. With the speed of sound c_0 , the cross-sectional area of the pinhole $A = \pi(d/2)^2$, the volume of the cavity $V = \pi(D/2)^2H$, and the effective depth of the pinhole $h_{eff} = h + 0.85d$, the resonance frequency ω_H is estimated as follows[196]:

¹For an electret condenser type microphone the electric either the diaphragm or the back plate is permanently charged.

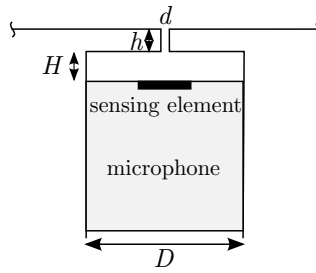


Figure 3.6: Pinhole type arrangement for unsteady surface pressure measurements with embedded microphone.

$$\omega_r = c_0 \sqrt{\frac{A}{V h_{eff}}} \quad (3.24)$$

An example for the type of microphones used for these applications is the Sonion 8010T electret condenser microphone (diameter 2.56mm, height 3mm) with a diaphragm of 0.8mm diameter. The microphones feature a built-in pre-amplifier and a flat frequency response between about 0.25 and 7.5kHz. In this case the sensitivity is -33.5dB (ref. 1V/Pa) at a frequency of 1kHz, equivalent to 0.45mV/Pa . The noise level is indicated by the manufacturer at 28dB SPL (ref. $20\mu\text{Pa}$), equivalent to 0.5mPa , and the phase shift remains within $\pm 5^\circ$. For a typical installation of this microphone with $H = d = 200\mu\text{m}$ and $h = 500\mu\text{m}$, and estimate for the resonance frequency is about $\omega_r/2\pi = 12\text{kHz}$ (equation 3.24).

For quantitative measurements calibration is required, which should be performed in situ and cover the frequency range of interest. It should include the entire data acquisition and measurement chain, i.e. pinhole, microphone, amplifier, filters, and digital-to-analogue converter. A transfer function between a known pressure signal applied over the pinhole and the sampled voltage signal is determined for this purpose. The application of a known pressure signal over the pinhole is not a trivial task to achieve in the laboratory. Therefore, if a high quality reference microphone with known calibration characteristics is available, the calibration can be performed in the following way: the reference sensor is mounted close to the pinhole above the surface (the distance depends on the frequency range of interest, typically $\approx 5\text{mm}$). Consequently, acoustic waves are generated by a loud speaker at a distance, ideally representing a white noise signal. The transfer function can be determined in the spectral domain as the ratio of cross-spectral between the signals read by the reference and pinhole mounted microphone and auto-spectral density of the pinhole mounted microphone.

I

LAMINAR BOUNDARY LAYER INSTABILITY NOISE

4

TONAL NOISE AND RELATED FLOW STRUCTURE

*The rung of a ladder was never meant to rest upon,
but only to hold a man's foot long enough
to enable him to put the other somewhat higher.*

Thomas Henry Huxley, *Life and letters of Thomas Henry Huxley*

This chapter surveys the regimes of tonal noise generation for low to moderate chord-based Reynolds number between $Re_c = 0.3 \times 10^5$ and 2.3×10^5 and effective angle of attack between 0° and 6.3° for the NACA 0012 airfoil profile. Extensive acoustic measurements of the emissions with smooth surface and with forced transition are reported. Results show that, at non-zero angle of attack, tonal noise generation is dominated by suction-side events at low Reynolds number and by pressure-side events at high Reynolds number. At smaller angle of attack interaction between events on the two sides becomes increasingly important.

PIV measurements complete the information on the flow field structure in the source region around the trailing edge. The influences of both angle of attack and Reynolds number on tonal noise generation are explained by changes in the mean flow topology, namely the presence and location of reverse flow regions on the two sides. Data gathered from experimental and numerical studies in the literature are reviewed and interpreted in view of the different regimes.

Parts of this chapter have been published in the Journal of Fluid Mechanics (2015) [69].

4.1. INTRODUCTORY REMARKS

TONAL NOISE generated by airfoils at low to moderate Reynolds number was recognized in the early stages of the development of aeroacoustics. It bears significance for a large number of applications, e.g. small-scale wind turbines, fans and - especially in recent years - unmanned aerial vehicles [14]. Compared to broadband noise, tonal components are particularly displeasing and unwanted. An improved understanding of the noise generation mechanism can lead to effective control strategies for noise elimination or abatement.

For a discussion of the principle noise mechanism at low to moderate Reynolds numbers, where the flow remains in a transitional state at the location of the trailing edge, the reader is referred to section 2.3.

Recent studies gathered further evidence of the upstream effect of acoustic scattering (e.g. Chong and Joseph [31], Pröbsting and Yarusevych [51], Takagi and Konishi [161], Arcondoulis *et al.* [197]). Takagi and Konishi [161] demonstrated the effect of tonal noise emission on the vortex shedding from the laminar separation bubble by installing a splitter plate. The absence of such stimulation resulted in a broadening of the energy content in unsteady surface pressure spectra. Further evidence for the presence of an acoustic feedback loop was presented in the recent studies of Schumacher *et al.* [198, 199], who investigated an airfoil profile with an embedded cavity, where instability waves at tonal frequency were detected only downstream of the cavity. The frequency spacing Δf was found to be inversely proportional to the distance L_f between the cavity and the trailing edge, as described by the model (equation 2.56) and empirical relation (equation 2.57) for the feedback loop. By modification of L_f , the study thus provided strong support for the feedback hypothesis. While the effects of acoustic stimulation on upstream events have been demonstrated experimentally in the above studies, an open point of discussion is whether the existence of a feedback loop is a necessary condition for the occurrence of tonal noise. For instance, Nash *et al.* [16] proposed that large-scale hydrodynamic fluctuations could provide an alternative explanation for low-frequency variations of the vortex shedding and thus also provide an alternative explanation for the presence of multiple tones, not depending on an acoustic feedback loop.

The above-noted principal features have been acknowledged and described in a large number of studies. However, differences in the details of the *ladder* structure observed in different studies have also been pointed out [50, 162]. For instance, differences have been shown in the factor k in equation 2.48, and also in the range of Reynolds numbers associated with a primary tone $f_{n_{max}}$ without undergoing transition to a different tone (different n). Further discussion has focused on the question whether pressure-side events, suction-side events, or their interaction are responsible for noise generation [50, 129].

Various researchers (e.g. Paterson *et al.* [35], Pröbsting *et al.* [50], Plogmann *et al.* [119], Inasawa *et al.* [156]) have applied tripping devices inducing bypass transition for the investigation of the phenomenon. For instance, Paterson *et al.* [35] reported that tripping of the suction-side boundary layer had no effect, while application on the pressure side induced a reduction or elimination of the tonal noise. They concluded that tonal noise emission was associated with flow instabilities on the pressure side of the airfoil. In contrast, a study of Jones and Sandberg [125] concludes that flow events on the suction

side dominate noise emission. Based on flow visualization and acoustic measurements for an airfoil at 2° Inasawa *et al.* [156] suggested that suction-side events are most important for the feedback loop at Reynolds numbers up to 2.1×10^5 . The above observations suggest the possible existence of different *regimes of tonal noise generation*, which are dominated by either pressure-side events, suction-side events, or their interaction. No previous study has focused on the conditions determining the dominant regime and the importance of possible interaction between events on the two sides. For further understanding and to clarify the differences in previous observations, it is therefore important to identify and categorize the regimes of tonal noise generation, which may bear significance for the underlying dynamical mechanism.

In most studies, especially with numerical simulations, the investigations are limited to a restricted range of flow conditions. This does not allow for a discussion about the influence of Reynolds number and angle of attack, although both parameters have a strong influence on the location and extent of separated flow regions and therefore also on flow separation and therefore on the amplification mechanism of instability waves [137]. To improve understanding of the differences in the observation of tonal noise emission due to laminar boundary layer instabilities at low to moderate Reynolds numbers, a survey of the acoustic and flow field characteristics over an extended range of flow conditions is thus required.

Most works focused on the NACA 0012 airfoil, on which most data were available. A review on the topic of laminar boundary layer instability noise, specifically for the NACA 0012, has been presented by Arcondoulis *et al.* [14]. A number of factors still hamper an unambiguous comparison in the low to moderate Reynolds number regime. In particular, the use of wind tunnels with open test sections makes the effective angle of incidence largely uncertain and a small blockage ratio is required to limit this effect. Experiments conducted in closed test sections experience resonance modes associated with the dimensions of the test section. This is problematic since the selection of tones through the feedback loop is influenced and tends to lock onto the tunnel resonance frequencies. The results of these facility-dependent effects are discrete tones, whose frequencies are independent of the reference velocity [16, 200]. Recent research efforts also focus on the effect of other installation effects, e.g. free-stream turbulence [201].

The experiment described below surveys the regimes of tonal noise generation in the low to moderate Reynolds number regime (between $Re_c = 0.3 \times 10^5$ and 2.3×10^5), in particular for the NACA 0012 profile. The parametric study includes Reynolds number and incidence effects and identifies flow events on the pressure side and suction side, and their contribution to overall noise generation. Extensive acoustic measurements were performed in an anechoic wind tunnel facility for geometric angles of attack between 0° and 8° . In conjunction with analysis of the flow field through PIV experiments, this investigation complements the picture of noise generation on isolated airfoils. Moreover, the results presented here help to interpret results from past research and provide a database for selecting flow conditions for future experiments and simulations.

4.2. DESCRIPTION OF EXPERIMENTS

The airfoil model was produced from acrylic glass to perform simultaneous PIV measurements on both sides. The chord was $c = 100\text{mm}$ and the span $L = 400\text{mm}$. Acous-

tic measurements were carried out in the Anechoic Wind Tunnel facility (AWT) at the University of Notre Dame, while PIV flow measurements were conducted in the Vertical-Tunnel facility (VT) at Delft University of Technology.

4.2.1. ACOUSTIC MEASUREMENTS

The AWT is an open jet wind tunnel facility (area of exit nozzle $0.61 \times 0.61\text{m}^2$). The walls of the room containing the test section are covered with anechoic foam wedges, rated to absorb 99% of the acoustic power above 100Hz. The inlet turbulence intensity has been measured and was found to be approximately 0.04% [202]. The model was mounted vertically between side plates with its quarter-chord point located 475mm downstream of the exit nozzle figure 4.1. The quarter-chord point also constitutes the axis of rotation.

An ACO Pacific 7016 microphone with pre-amplifier was located in the mid-span plane at a distance of 2m perpendicular to the chord at the streamwise position of the trailing edge with the airfoil at zero incidence. The analogue signal was amplified, high-pass-filtered (cut-off frequency 30Hz) and sampled at a frequency of 40kHz. A B&K 4228 piston phone was used for calibration at a single frequency. Measurements were performed over a range of angles of attack ($\alpha_{geo} = 0^\circ - 8^\circ \pm 0.15^\circ$) and velocities between $u_\infty = 5$ and 35m/s, resulting in chord-based Reynolds numbers between about $Re_c = 0.3 \times 10^5$ and 2.3×10^5 and Mach numbers between $M_0 = 0.015$ and 0.1. The increments in free-stream velocity between the measurements were approximately 0.35m/s. At each measurement point (combination of angle of attack and velocity) data were acquired over a measurement period of 30s. Between two measurement points a period of 15s was allowed for adaptation of the airflow. Additionally, measurements without the model installed were taken to determine the background noise at all flow velocities.

Spectral analysis was conducted based on the modified periodogram method [203] with segments of 16,384 samples, windowed using a Hamming window, and an overlap of 50%. The procedure results in spectra with a frequency resolution of $\delta_f = 2.44\text{Hz}$ and the average is evaluated over 145 segments. The auto-spectral density of acoustic pressure is denoted by $\Phi_{aa}(f)$ and the corresponding narrowband sound pressure spectra by $\delta_f \Phi_{aa}(f)$. If not stated otherwise, background noise spectra are subtracted.

Laminar to turbulent transition of the boundary layer is forced in some cases by means of randomly distributed three-dimensional (3D) roughness elements (carborundum, nominal grain size 0.58mm) on a 10mm wide strip attached to the airfoil at chord position $x/c = 0.25$. Measurements were performed with roughness elements on the pressure side only (denoted *p.s. tripped*), suction side only (*s.s. tripped*), both sides (*both tripped*), and with a smooth surface (*smooth*).

4.2.2. FLOW FIELD MEASUREMENTS

Planar, two-component PIV measurements were performed in the VT, a low speed, open jet facility (test section diameter 0.6m). Results are presented here for four geometric angles of attack ($\alpha_{geo} = 0^\circ, 1^\circ, 2^\circ$, and 4°) and the free-stream velocity u_∞ varying between 20 and 32m/s. The flow was restricted by side plates installed at both sides of the airfoil.

The measurement system consisted of a Litron Nd:YLF laser (dual cavity) and a Photron *Fastcam SA 1.1* ($20\mu\text{m}$ pixel pitch, 5.4kHz at $1,024 \times 1,024\text{px}$) equipped with a Nikon Micro-Nikkor 200mm objective. The light sheet was positioned in the mid-span plane,

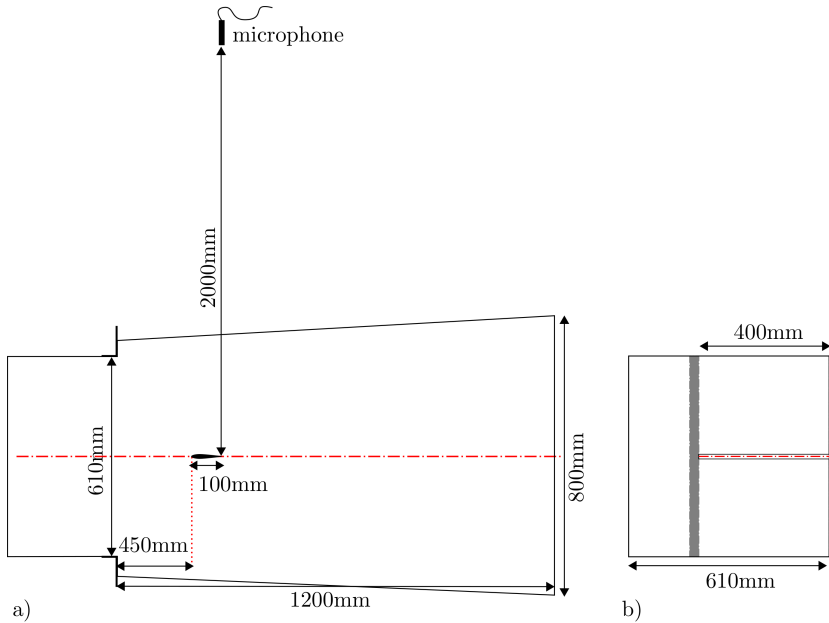


Figure 4.1: Schematic of acoustic measurements set-up. Side view (a) and back view (b). Some elements are not drawn to scale.

illuminating the field of view from one side of the airfoil. The field of view entailed an area of $32\text{mm} \times 16\text{mm}$ around the trailing edge and a sequence of 6,970 images were obtained with a digital imaging resolution of $32\text{px}/\text{mm}$ at an acquisition frequency of 6kHz. The free-stream displacement of the tracer particles was approximately 15px. The particle images were correlated using the LaVision *DaVis* software package. A final interrogation window size of $16 \times 16\text{px}$ results in a window size of $0.5 \times 0.5\text{mm}^2$ and an overlap of 75% between neighboring windows yields a vector spacing of 0.125mm. Further details of the experiment can be found in section 5.2.2 or in Pröbsting *et al.* [50]. Figure 4.2 shows a schematic of the experimental set-up.

The coordinate system is chosen such that the x coordinate indicates the free-stream flow direction, the y coordinate indicates the transverse flow direction and the z coordinate indicates the spanwise (PIV out-of-plane) direction. The origin remains fixed to the trailing edge of the airfoil.

4.2.3. EFFECTIVE ANGLE OF ATTACK

A lift-generating airfoil placed in an open jet induces a deflection of the open jet boundaries, which is representative of an infinite domain or free flight conditions. The conditions to neglect this boundary interference involve a small blockage ratio [204]. An effective angle of attack can be defined by matching the lift coefficients found for experimental conditions in the wind tunnel to their infinite-domain equivalents: the angle for which in free flight conditions the same lift coefficient is obtained as in the experiment for a given geometric angle of attack α_{geo} (also denoted α here) is said to be the effective

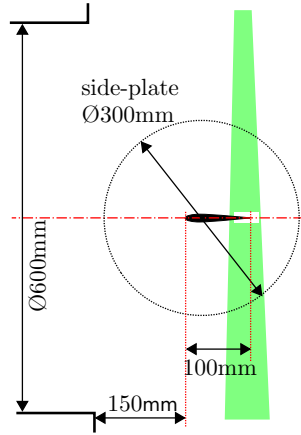


Figure 4.2: Schematic of PIV experimental set-up.

angle of attack α_{eff} . Based on lifting surface theory, Brooks *et al.* [204] proposed a semi-empirical relationship between the effective and geometric angles of attack as a function of the ratio of airfoil chord c and height of the open jet H , with $\sigma = (\pi^2/48)(c/H)^2$:

$$\alpha_{eff} = \frac{\alpha_{geo}}{(1 + 2\sigma)^2 + \sqrt{12\sigma}} \quad (4.1)$$

For the case of a NACA 0012, the same authors have shown that this relationship leads to acceptable results. Figure 4.3 shows the effective angle of attack for the 100mm chord NACA 0012 in the two open jet wind tunnels employed in the present study. For the round test section in the PIV experiments, the linear dimension has been computed from the area over the central 400mm covered by the span of the airfoil. The relatively large ratio $H/c \approx 6$ in the present experiments results in a moderate correction ($\alpha_{eff}/\alpha_{geo} \approx 0.78$) when compared to many previous studies [16, 117, 160].

It should be noted that the same lift coefficient can be the result of a set of different pressure distributions over the airfoil's surface. For cases where tonal noise emission is related to the transition process through a separation region, the details of the pressure distributions are important. Moreau and Henner [159] numerically investigated this influence for a number of profiles and commented that the pressure distribution in the case of the NACA 0012 matched that of the infinite domain at the effective angle of attack comparatively closely. This was not the case for other airfoil profiles. The above correction (equation 4.1) has been applied before, for instance in the studies of Arcondoulis *et al.* [160] and Chong and Joseph [117], but not in earlier ones, for instance Paterson *et al.* [35].

4.3. RESULTS AND DISCUSSION

4.3.1. NOISE GENERATED BY SMOOTH AIRFOIL

Figure 4.4 shows contour plots of the narrowband sound pressure level (SPL) as functions of free-stream velocity and angle of attack. Both parameters have a substantial

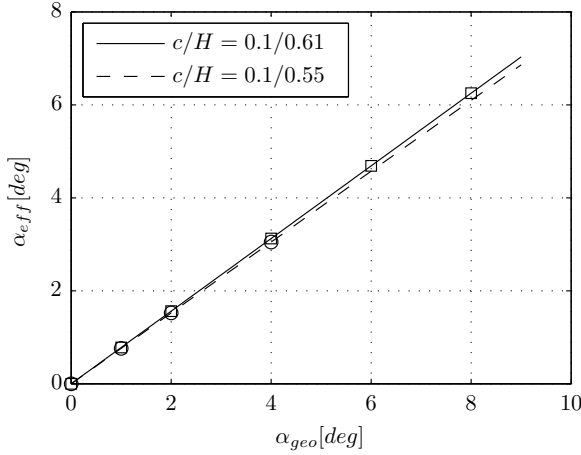


Figure 4.3: Estimated effective angle of attack based on equation 4.1 for AWT (solid line) and Vertical-Tunnel (dashed). The symbols indicated the discrete values of the angle of attack in the experiments.

influence on noise emission.

At $\alpha = 0^\circ$ (figure 4.4a) a strong primary tone at frequency $f_{n_{max}}$ with upper harmonics is present, similar to the results of the simulation results by Tam and Ju [162]. With free-stream velocity (about $u_\infty > 15\text{m/s}$) side tones appear at a frequency spacing Δf above and below the primary tone frequency, but one order lower than the latter. In contrast to the higher-Reynolds-number results of Arbey and Bataille [18], a clear ladder structure including transitions of the primary tone is not observed at $\alpha = 0^\circ$. The reader should note that the condition of geometric angle of attack $\alpha = 0^\circ$ is sensitive to asymmetry in the experimental set-up and finite accuracy of $\pm 0.15^\circ$.

At $\alpha = 1^\circ$ (figure 4.4b) the spectrum is still similar to the one at $\alpha = 0^\circ$ for $u_\infty < 15\text{m/s}$ ($Re_c < 1 \times 10^5$). For $u_\infty > 20\text{m/s}$, side tones become comparatively more pronounced and transition of the maximum intensity from one tone to another is observed (different n).

At $\alpha = 2^\circ$ (figure 4.4c), the side tone structure is particularly pronounced between 10m/s and 24m/s ($Re_c = 0.7 \times 10^5 - 1.6 \times 10^5$). Here, side tones are of similar intensity when compared to the primary tone. Their intensity is highest for the frequency band between the fundamental frequency and first harmonic of the primary tone at $\alpha = 0^\circ$ (figure 4.4a). Such pronounced side tone structure has been associated with periodic amplitude modulation with a frequency equal to the frequency spacing Δf [50, 129]. The spectrum changes markedly with further increase in Reynolds number ($u_\infty > 24\text{m/s}$, $Re_c > 1.6 \times 10^5$): a strong primary tone with weaker side tones replaces the pronounced side tone structure. The frequency of the primary tone is then close to that of the first harmonic of the primary tone at zero incidence (figure 4.4a). Side tones at frequency lower than that of the primary tone are stronger than those at higher frequencies. Compared to lower velocity ($u_\infty < 24\text{m/s}$), the rate of increase of the tonal frequency f_n with free-stream velocity is smaller.

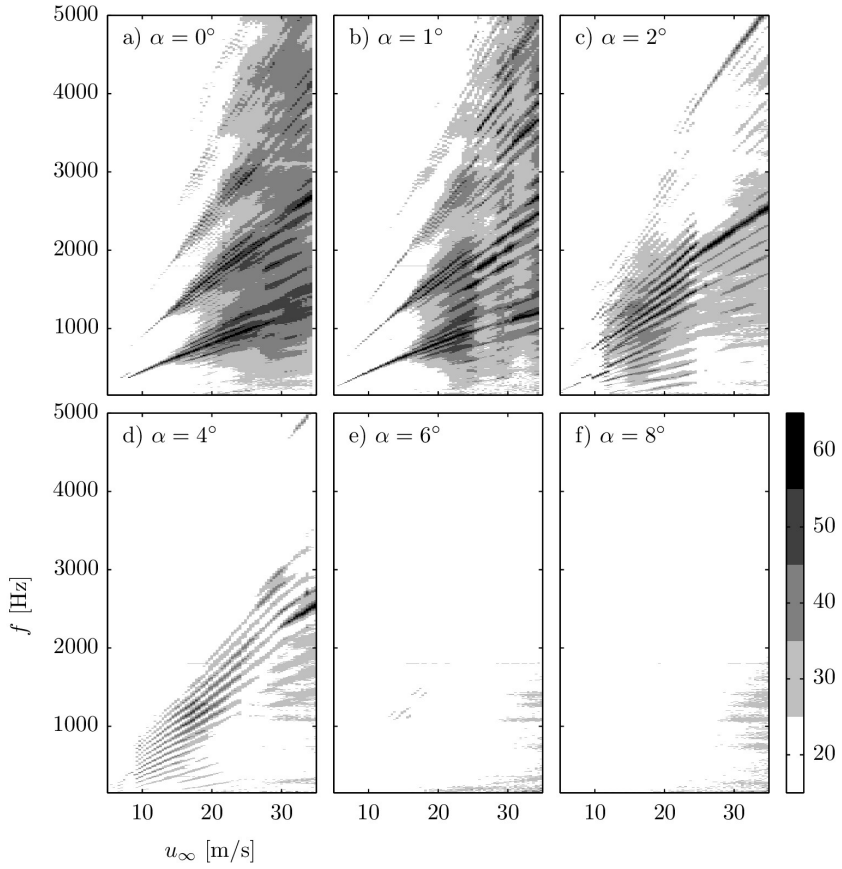


Figure 4.4: Narrowband SPL (in dB, reference $20\mu\text{Pa}$) in dependence on free-stream velocity and frequency for varying angle of attack (smooth airfoil).

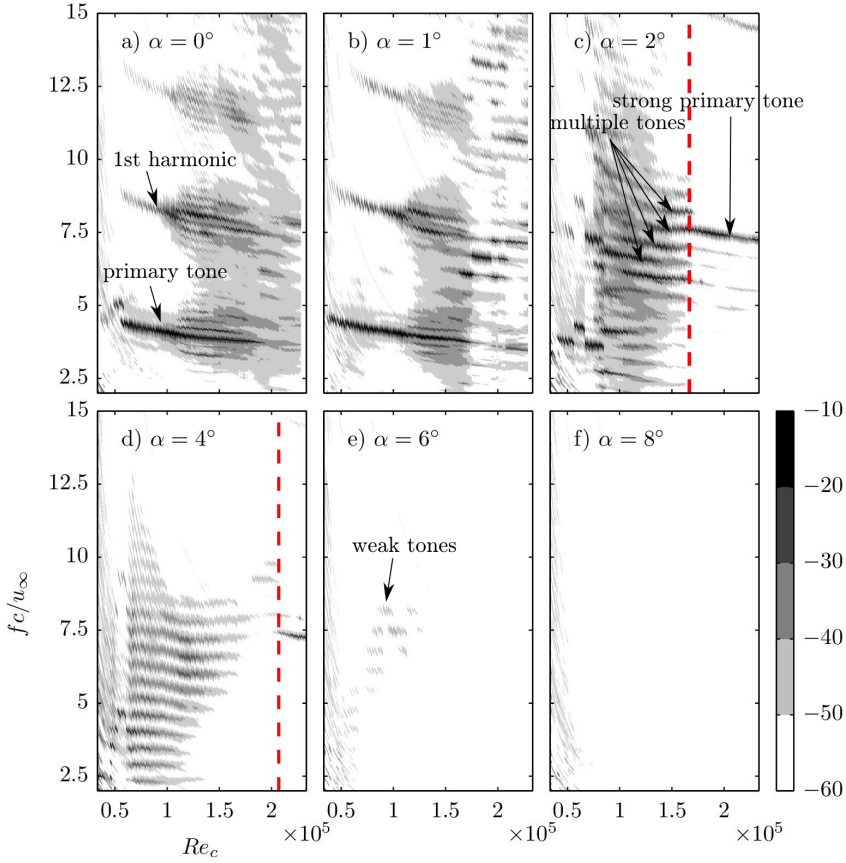


Figure 4.5: Non-dimensional auto-spectral density of acoustic pressure $10 \times \log_{10}[\Phi_{aa}/(\rho/2u_\infty^2)^2 (cs/r^2) u_\infty/c/M_0^2]$ as a function of Re_c and fc/u_∞ (smooth airfoil). Dashed line indicates transition of tonal noise regimes.

A similar division of the velocity domain is observed at higher angle of attack ($\alpha = 4^\circ$, 4.4d). Here, the marked change occurs at higher velocity ($u_\infty = 30\text{m/s}$) and as for $\alpha = 2^\circ$ the rate of increase of f_n changes compared to $u_\infty < 30\text{m/s}$.

At $\alpha = 6^\circ$ (figure 4.4e), only weak traces of the tone pattern remain, approximately 30dB below the maximum power at $\alpha = 2^\circ$, over a restricted range $10\text{m/s} < u_\infty < 20\text{m/s}$. A primary tone at higher Reynolds numbers is not observed here. However, tones are likely to occur at higher Reynolds numbers at $\alpha_{eff} = 4.7^\circ$, as data available in the literature suggests [35, 119, 130]. In combination with these previous studies, the observations here suggest that, for an intermediate range of Reynolds numbers, no tones are generated, while this may well be the case at above and below this range. Measurements at $\alpha = 8^\circ$ (figure 4.4f) show no indications of tones.

Figure 4.5 introduces a non-dimensional representation of the acoustic spectra (figure 4.4) as a function of Reynolds number Re_c and dimensionless frequency fc/u_∞ . The measured far-field auto-spectral density of the acoustic pressure Φ_{aa} is normalized and scaled by means of the free-stream dynamic pressure ($\rho/2u_\infty^2$), frequency (u_∞/c), a term accounting for the airfoil span L , and the distance between the trailing edge and the microphone r (cL/r^2). Additionally, a factor $1/M_0^2$ accounts for the radiation efficiency of a compact dipole. The vertical lines drawn in the figures for the cases of $\alpha = 2^\circ$ (figure 4.5c) and 4° (figure 4.5d) indicate the transition between the two regimes discussed above.

In conclusion, tones are present in spectra for angles of attack $\alpha \leq 6^\circ$. Striking changes within the spectra, occurring over narrow ranges of Reynolds numbers at $\alpha = 2^\circ$ and 4° , suggest that fundamental differences exist in the noise generation at the respective flow conditions. Additionally, weak tones are observed at 6° and have not been reported in experiments at such large incidence and low Reynolds number.

4.3.2. NOISE GENERATED UNDER FORCED TRANSITION

A tripping device on the airfoil promotes transition to turbulence and leads to a turbulent boundary layer reaching the trailing edge. Noise emitted due to a turbulent boundary layer is of broadband nature and tones are suppressed. Forcing transition on either of the two sides is an expedient to reveal the contribution of events on the other side, respectively, to overall noise generation. Provided that events on the two sides of the smooth airfoil are sufficiently uncorrelated, superposition of the individually tripped cases is expected to compare well to the smooth airfoil. Otherwise, interaction or coupling between events on the two sides of the smooth airfoil substantially influences noise emission. For instance, Paterson *et al.* [35] and Nash *et al.* [16] followed a similar procedure and came to the conclusion that pressure-side events are responsible for tonal noise generation. In contrast, Inasawa *et al.* [156] emphasized the importance of suction-side events for a NACA 0012 at $\alpha = 2^\circ$ and $Re_c < 1.6 \times 10^5$.

Figures 4.6 and 4.7 show the auto-spectral density of acoustic pressure for angles of attack $\alpha = 0^\circ$ through 8° with the pressure side tripped (left column), the suction side tripped (center), and both sides tripped (right). These spectra can be compared to those for the smooth airfoil in figure 4.4. In addition, figures 4.8 and 4.9 show a comparison of the narrowband SPL of the smooth and single-sided tripped cases for selected Reynolds numbers at $\alpha = 2^\circ$ and 4° , respectively.

With both sides tripped (figures 4.6 and 4.7, right column) no tones are observed

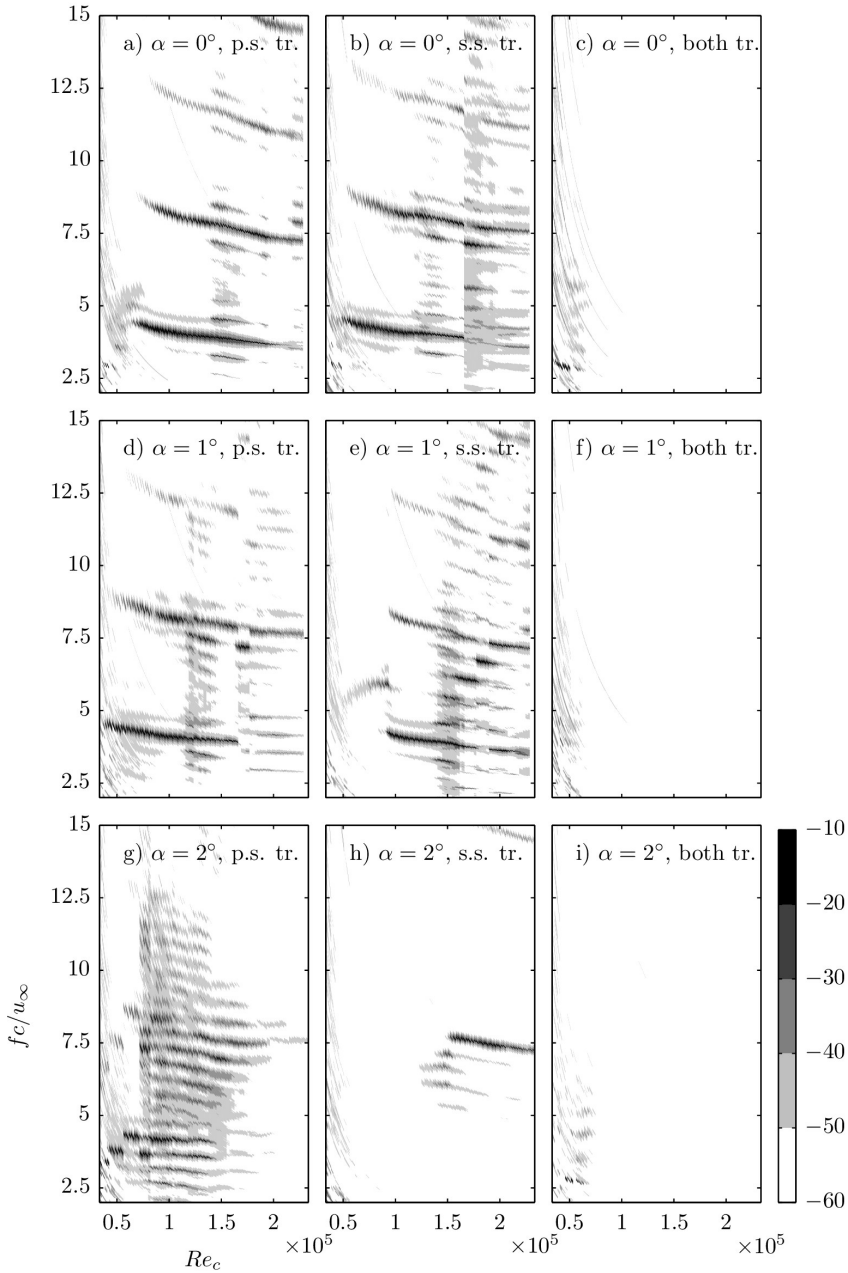


Figure 4.6: Non-dimensional auto-spectral density of acoustic pressure $10 \times \log_{10}[\Phi_{aa} / (\rho/2u_\infty^2)^2 (cL/r^2) u_\infty / c / M_0^2]$ as a function of Re_c and $f c / u_\infty$ for geometric angles of attack $\alpha = 0^\circ, 1^\circ$, and 2° with the pressure side tripped (left), the suction side tripped (center), and both sides tripped (right).

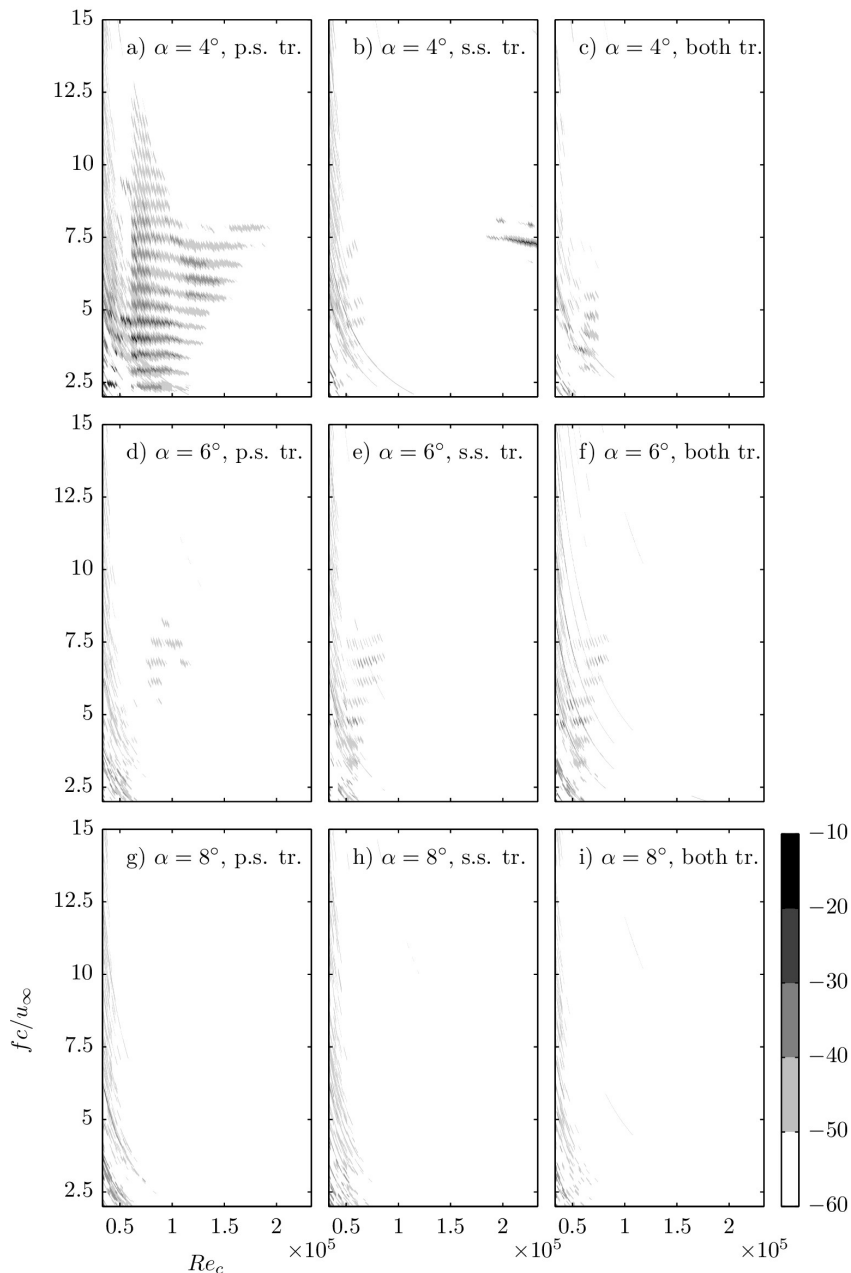


Figure 4.7: Non-dimensional auto-spectral density of acoustic pressure $10 \times \log_{10}[\Phi_{aa}/(\rho/2u_\infty^2)^2(cL/r^2)u_\infty/c/M_0^2]$ as a function of Re_c and fc/u_∞ for geometric angles of attack $\alpha = 5^\circ, 6^\circ$, and 8° with the pressure side tripped (left), the suction side tripped (center), and both sides tripped (right).

for $Re_c > 0.7 \times 10^5$, confirming the effectiveness of the applied tripping device over this range. The tripping device on the suction side is not consistently effective for $Re_c < 0.7 \times 10^5$, probably due to early separation.

At $\alpha = 0^\circ$, the spectra for the two tripped cases (figures 4.6a,b) are similar, yet not identical as expected for a symmetric airfoil profile. The onset of tones, primary tone frequency and the frequency spacing of side tones show good agreement. The differences are due to asymmetry in the experimental conditions or finite accuracy in adjusting the angle of attack ($\pm 0.15^\circ$). Side tones are better defined and the broadband noise level is lower compared to the smooth configuration (figure 4.5a), which is probably related to interaction or coupling of the events on the two sides of the smooth airfoil.

At 1° , with the pressure side tripped (figures 4.6d), the onset of the primary tone is found at a distinctly lower Reynolds number ($Re_c < 0.5 \times 10^5$) when compared to the smooth airfoil case (figure 4.5b) and that with the suction side tripped (figures 4.6d). In the latter case, this onset is delayed to $Re_c \approx 1 \times 10^5$.

At higher angle of attack ($\alpha = 2^\circ$, figure 4.6g,h), the difference between the two tripped cases becomes more apparent. With forced transition on the pressure side (figure 4.6g), multiple closely spaced tones are present. This pattern is almost identical to that found for the smooth airfoil at low Reynolds number (figure 4.5c, to the left of dashed line). The strong primary tone observed for the smooth airfoil at high Reynolds number (figure 4.5c, to the right of dashed line) appears when transition is forced on the suction side (figure 4.6h).

Figure 4.8 illustrates this transition from suction- to pressure-side-dominated tonal noise emission. Figure 4.8a and 4.8b show suction-side-dominated cases and the tonal frequencies agree closely for the pressure-side-tripped case and for the smooth airfoil. Figure 4.8d shows a pressure-side-dominated case and close agreement of the tonal frequencies is found for the suction side tripped case and for the smooth airfoil. A special case is found at intermediate Reynolds number in figure 4.8c, where the overall spectral shape with a multitude tones suggests a suction-side-dominated case, but close inspection reveals that the primary and secondary tone frequencies are determined by pressure-side events. This small shift in frequency might be evidence of acoustic interaction through a secondary feedback loop [129].

Similarly, the spectra for the tripped cases at $\alpha = 4^\circ$ (figures 4.7a,b) combine to that for the smooth airfoil (figure 4.5d). Figure 4.9 shows detailed spectra for several Reynolds numbers and in contrast to $\alpha = 2^\circ$, transition to a pressure-side-dominated case is only observed at the highest Reynolds number.

The division in pressure- and suction-side-dominated regimes continues with higher angle of attack (6° , figures 4.7d,e). With the pressure side tripped, tones for the range of Reynolds numbers investigated here are almost identical to those found for the smooth airfoil (figure 4.5e). Extrapolating the trends observed for 2° and 4° with tripped suction side (figures 4.6h and 4.7b), the onset of a strong primary tone is expected at higher Reynolds number, which is corroborated by previous studies at such conditions [16, 35, 119]. As for the smooth airfoil, no tones are present for the tripped cases at $\alpha = 8^\circ$ (figures 4.7g,h).

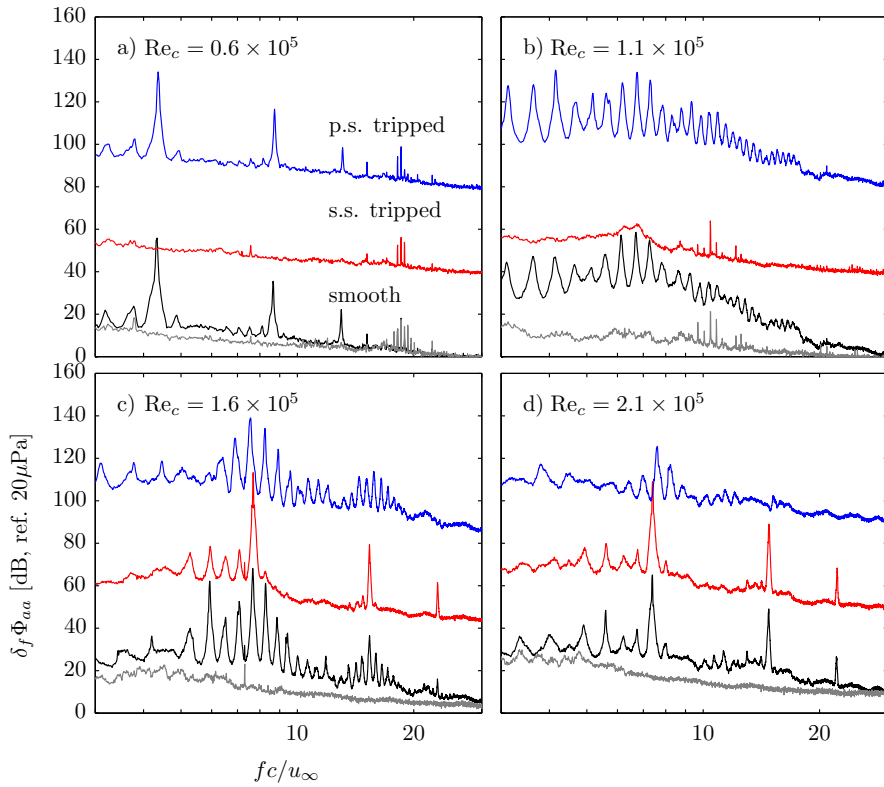


Figure 4.8: Narrowband SPL $\delta_f \Phi_{aa}$ [dB, reference $20\mu\text{Pa}$], $\alpha = 2^\circ$. Spectra with the suction and pressure side tripped are offset by 40dB and 80dB, respectively.

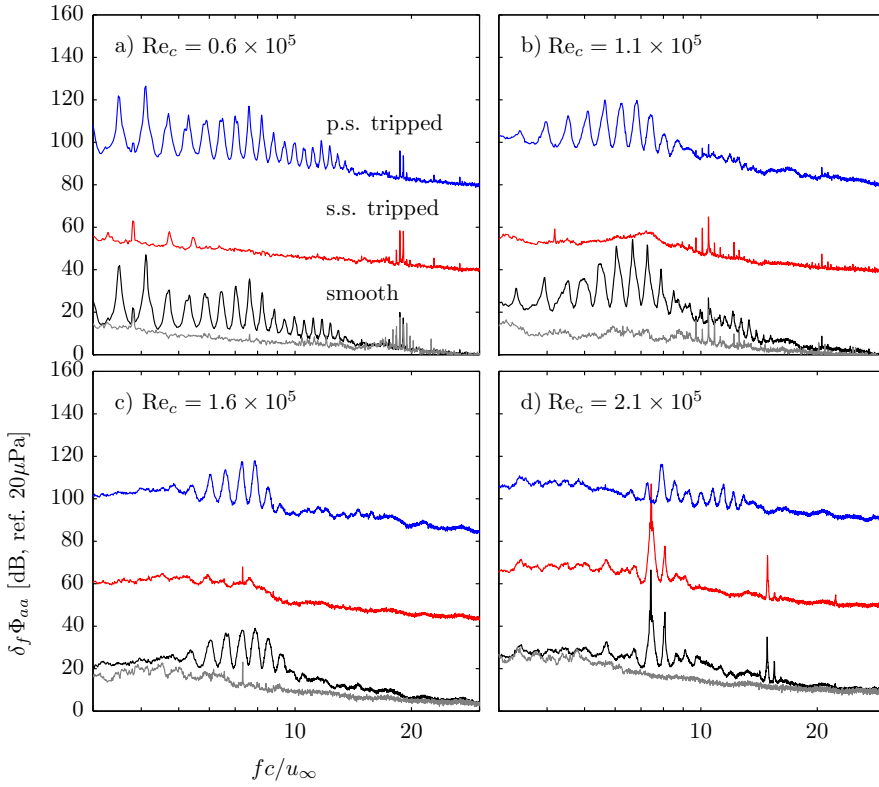


Figure 4.9: Narrowband SPL $\delta_f \Phi_{aa}$ [dB, reference $20 \mu\text{Pa}$], $\alpha = 4^\circ$. Spectra with the suction- and pressure side tripped are offset by 40dB and 80dB, respectively.

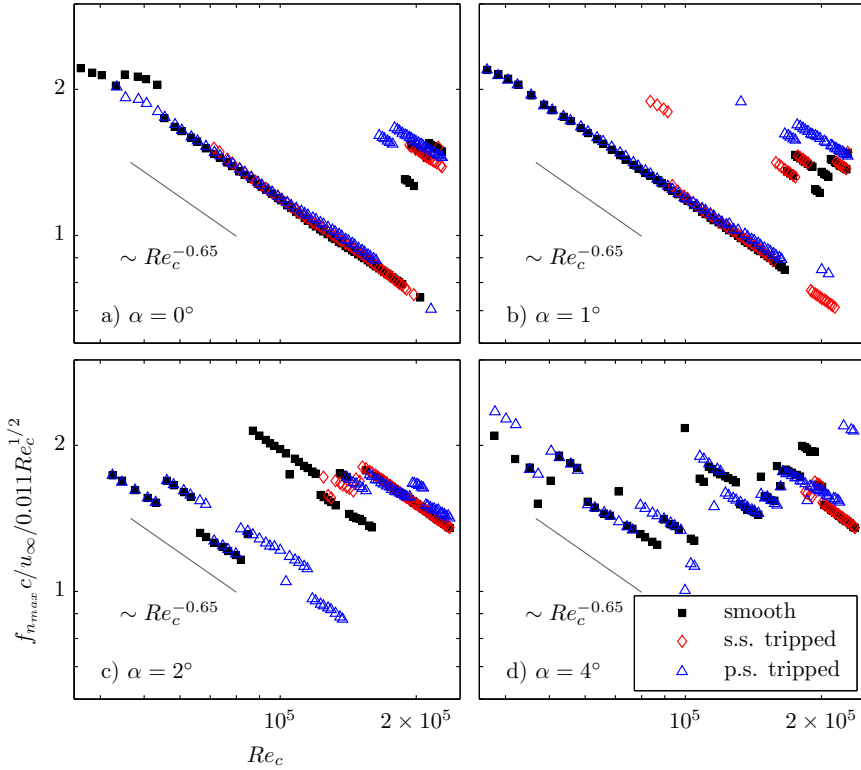


Figure 4.10: Non-dimensional primary tone frequency against Reynolds number for geometric angles of attack $\alpha = 0^\circ$ (a), 1° (b), 2° (c), and 4° (d).

4.3.3. REGIMES OF TONAL NOISE GENERATION

As discussed before (figure 4.4), the acoustic spectrum is dominated by a primary tone over significant ranges of Reynolds numbers and angles of attack. Figure 4.10 depicts this primary tone frequency $f_{n_{max}}$, which is identified by the maximum auto-spectral density Φ_{aa} at least 15dB above background noise level. $f_{n_{max}}$ is normalized by the expression for f_s given in equation 2.48, i.e. by the average development of the primary tone frequency proposed by Paterson *et al.* [35]. In this representation, unity indicates the mean trend of the primary tone frequency, scaling with $u_\infty^{1.5}$. The slope corresponding to the frequency scaling of individual tonal components with u_∞^m and $m = 0.85$ ($\sim Re_c^{-0.65}$) is indicated by the solid line. Exponents in the range $0.8 < m < 0.85$ have been reported previously [18, 35, 117, 160].

At zero incidence ($\alpha = 0^\circ$, figure 4.10a) and low Reynolds number ($Re_c < 10^5$) the primary tone frequency follows the variation with $Re_c^{-0.65}$. For the airfoil with the suction side tripped, this scaling can also be found at higher angle of attack (figures 4.10b-d) and at high Reynolds number. In contrast, the airfoil with the pressure side tripped shows a

significantly different scaling behavior with increasing angle of attack, approaching u_∞^1 ($\sim \text{Re}_c^{-0.5}$) at $\alpha = 4^\circ$ (figure 4.10d). For the smooth airfoil, the frequency scaling adapts to that of the pressure- and suction side tripped cases at low and high Reynolds numbers, respectively.

For the smooth airfoil and at all angles of incidences (figures 4.10a-d) at least one transition can be identified that can be interpreted as a *rung* of a *ladder* structure. At $\alpha = 0^\circ$ this transition at $\text{Re}_c = 2 \times 10^5$ corresponds almost to a doubling in frequency (transition to upper harmonic). The airfoil at larger angle of attack ($\alpha = 2^\circ$, figure 4.10c) shows multiple transitions. The most pronounced *ladder*-like variation is found at $\alpha = 4^\circ$ (figure 4.10d), where the trend of the primary tone frequency follows that ($u_\infty^{1.5}$) observed by Paterson *et al.* [35] comparatively closely, and as a result multiple transitions are present. Data in previous reports suggest that the *ladder* structure is primarily associated with higher Reynolds number [18, 35, 117] and thus pressure-side-dominated cases. However, other studies claim that no such *ladder* structure exists even at high Reynolds number [16]. In any case, a fine *ladder* structure is not evident for low Reynolds number at low angle of attack as figure 4.10 shows.

Figure 4.11 shows the auto-spectral density Φ_{max} corresponding to the primary tone frequencies (figure 4.10). Good agreement of Φ_{max} at low Reynolds number for the smooth and suction-side tripped airfoil give further evidence that suction-side events dominate tonal noise emission at low Reynolds number. At $\alpha = 1^\circ$ (figure 4.11b) this transition is found at about $\text{Re}_c \approx 10^5$ and shifts towards higher Reynolds number with increasing angle of attack. For instance, at $\alpha = 2^\circ$ (figure 4.11c) and $\alpha = 4^\circ$ (figure 4.11d) the transition is found at about $\text{Re}_c = 1.5 \times 10^5$ and $\text{Re}_c = 1.8 \times 10^5$, respectively. In agreement with this value for $\alpha = 2^\circ$, the data reported by Inasawa *et al.* [156] indicate that transition between suction- and pressure-side-dominated regimes occurs between $\text{Re}_c = 1.3 \times 10^5$ and $\text{Re}_c = 2.1 \times 10^5$. After transition, the SPL associated with the primary tone for the smooth and the suction-side tripped cases shows better agreement. Thus, regimes exist where events on a single side of the airfoil dominate tonal noise generation.

The comparison here suggests the definition of a characteristic Reynolds number Re_{ch} separating two regimes: the Reynolds number at which the auto-spectral density related to the isolated pressure side (observed for airfoil with the suction side tripped) supersedes that associated with suction-side events (pressure side tripped). In summary, one can thus define a *suction-side-dominated* and a *pressure-side-dominated* regimes based on a characteristic Reynolds number Re_{ch} . For $\text{Re}_c < \text{Re}_{ch}$ tonal noise emission is primarily influenced by suction-side events, while for $\text{Re}_c > \text{Re}_{ch}$, instead, tonal noise emission is dominated by pressure-side events. The value of Re_{ch} is strongly dependent on the angle of attack. There is evidence of an intermediate regime, where the primary tone frequency can deviate from that of the isolated cases.

Figure 4.11 shows that the difference in narrowband SPL of the acoustic pressure for tones generated by pressure-side events increases rapidly for $\text{Re}_c > \text{Re}_{ch}$. This rapid increase is due to the different rates at which the SPL for the pressure- and the suction-side tripped cases change. With larger angle of attack, the difference in the rate of change becomes larger and, as a result, the transition from the suction- to the pressure-side-dominated regime occurs over a smaller range of Reynolds numbers. In other words, the overlap region between the two regimes becomes smaller. To illustrate the latter,

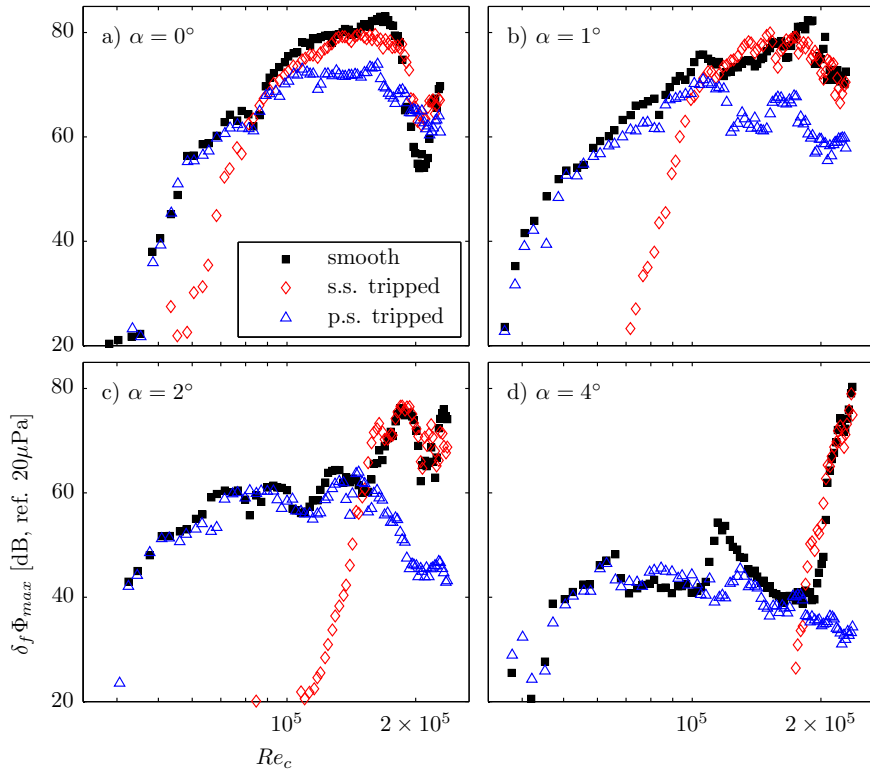


Figure 4.11: Narrowband SPL of primary tone (at frequency $f_{n_{max}}$, figure 4.10) against velocity for geometric angles of attack 0° (a), 1° (b), 2° (c), and 4° (d).

Table 4.1: Characteristic Reynolds number Re_{ch} and limits over overlap region, Re_l and Re_u .

α	0°	1°	2°	4°
$Re_l [\times 10^5]$	0.71	0.94	1.4	1.81
$Re_u [\times 10^5]$	1.73	1.2	1.55	1.86
$Re_{ch} [\times 10^5]$	0.91	1.06	1.52	1.81

figure 4.12 shows the difference in narrowband SPL $\Delta\Phi_{max}$ associated with the primary tone in the pressure- and suction-side tripped cases. As defined above, the characteristic Reynolds Re_{ch} number is the Reynolds number where this difference approaches zero (indicated by vertical line). This characteristic Reynolds number increases with angle of attack from $Re_{ch} = 1 \times 10^5$ at $\alpha = 1^\circ$ (figure 4.12b) to $Re_{ch} = 1.8 \times 10^5$ at $\alpha = 4^\circ$ (figure 4.12d). The range of Reynolds numbers, where this difference is within ± 10 dB, is bound by a lower limit Re_l and an upper limit Re_u (hatched region, dashed horizontal lines). Table 4.1 lists the characteristic Reynolds number Re_{ch} together with the limits Re_l and Re_u . The difference between the limits $\Delta Re = Re_u - Re_l$ provides a measure for the extent of the overlap of the two regimes. This overlap decreases with increasing angle of attack from $\Delta Re = 0.26 \times 10^5$ at $\alpha = 1^\circ$ (figure 4.12b) to $\Delta Re = 0.05 \times 10^5$ at $\alpha = 4^\circ$ (figure 4.12d). Thus, at higher angle of attack interaction or coupling between events on the two sides of the airfoil is confined to a smaller range of Reynolds numbers.

The reader should note that the case $\alpha = 0^\circ$ has been left out of the above discussion. Potential asymmetries in the experimental set-up and finite accuracy in setting the geometric angle of attack $\alpha = 0 \pm 0.15^\circ$ are probably the cause of the finite overlap region observed in figure 4.12a). Ideally, for a symmetric airfoil, the overlap region should extend over the entire tonal noise regime in such a symmetric condition.

Figure 4.13 shows the two regimes of tonal noise generation relative to the effective angle of attack α_{eff} (equation 4.1) and Reynolds number Re_c . Measurements acquired in the present study are depicted for tonal (filled symbols) and non-tonal (open symbols) cases. Tonal cases are identified as such if the background subtracted narrowband SPL $\delta_f\Phi_{aa}$ of the primary tone exceeds 25dB (figure 4.11). This typically coincides with a sharp rise in noise level. Lowson *et al.* [130] suggested a limit of tonal noise generation, compiled from experimental data of Paterson *et al.* [35] (high-Reynolds-number limit) and Brooks *et al.* [13] (low-Reynolds-number limit). However, it appears that Lowson *et al.* [130] considered the geometric angle of attack, at least for the data of Paterson *et al.* [35]. Therefore, the angle of attack correction (equation 4.1) with the data of Paterson *et al.* [35] is also applied to the envelope (grey, solid line). The simply hatched regions indicate the two regimes of suction- and pressure-side-dominated noise generation, respectively, where the high-Reynolds-number limit of the pressure-side-dominated regime is inferred from the envelope of Lowson *et al.* [130]. The overlap region has been defined in table 4.1 and is represented in figure 4.13 by the cross-hatched region. It is interesting to note the divergence of suction- and pressure-side-dominated regimes at higher angles of attack ($\alpha_{eff} = 4^\circ$), which allows for the existence of an intermediate non-tonal regime.

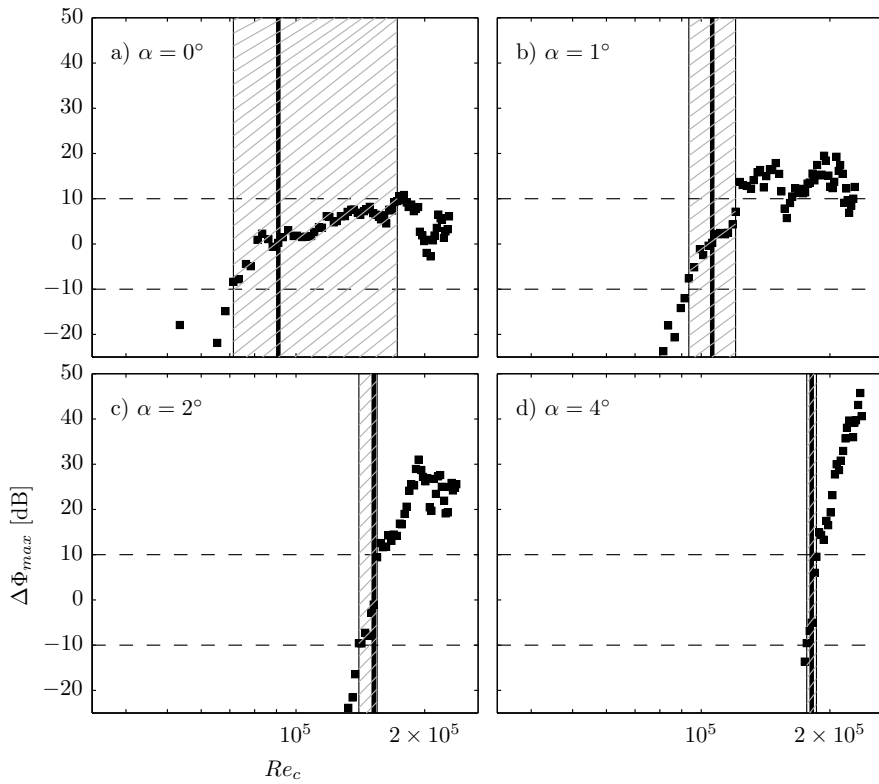


Figure 4.12: Difference of narrowband SPL at frequency at primary tone frequency between cases with the pressure and suction side tripped. The characteristic Reynolds number (vertical line) and overlap region (hatched) are indicated.

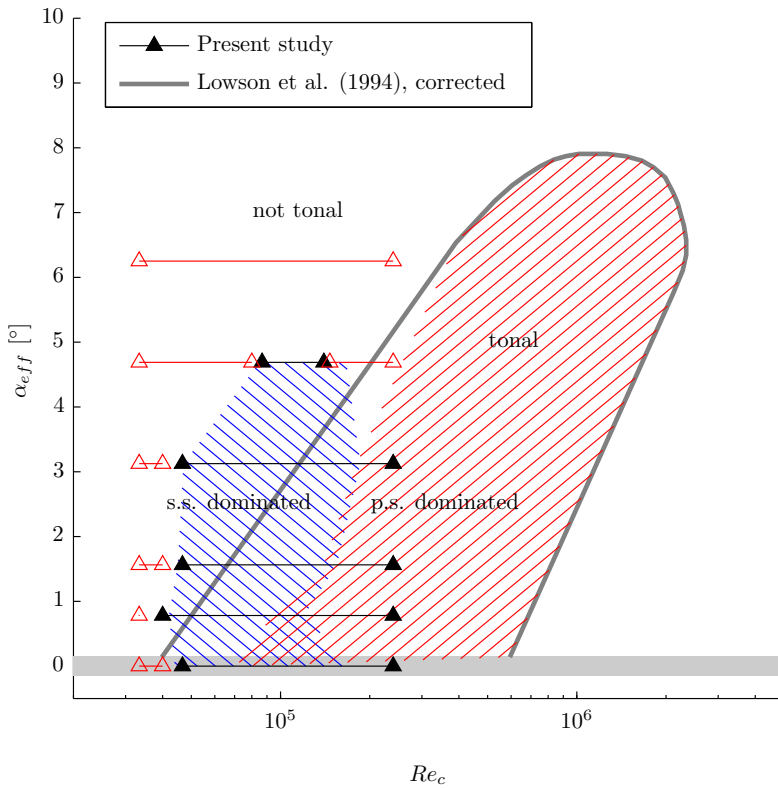


Figure 4.13: Regimes of tonal noise generation on a NACA 0012: the solid line shows limit of tonal noise generation on pressure side (adapted from Lawson *et al.* [130]). Suction (blue, hatched) and pressure-side-dominated regimes (red, hatched). Experiments showing tonal (solid symbols) and non-tonal noise (open symbols) for the present study.

4.3.4. FLOW STRUCTURE AND RELATION TO DIFFERENT REGIMES

To understand the origin of tonal noise and its relation to the different flow regimes, the structure of the flow field in the proximity of the trailing edge needs to be considered. Figure 4.14 shows an instantaneous realization of the spanwise vorticity component around the trailing edge of the smooth airfoil for $\alpha = 0^\circ$ - 4° and Reynolds numbers between $Re_c = 1.3 \times 10^5$ and 2.1×10^5 . In addition, the reverse flow region is indicated (identified by $u/u_\infty = 0$, solid line) on both pressure and suction sides, and marks the position of the separation bubble or separated shear layer. Nash *et al.* [16] postulated that the existence of a separation bubble close to the trailing edge is a necessary condition for the generation of tonal noise. Here, a separation bubble or separated shear layer is observed in all cases. For a given Reynolds number, separation on the suction side is expected to shift upstream with increasing angle of attack due to an increasingly adverse pressure gradient. For the pressure side the opposite holds true and the separation point moves downstream. For a given angle of attack the separation bubble becomes smaller and shorter with increasing Reynolds number [137].

The instantaneous flow structure shows a marked dependence upon Reynolds number and an even stronger dependence on angle of attack. At near zero incidence ($\alpha = 0^\circ$, figure 4.14, top left), the flow pattern is comparatively, yet not perfectly, symmetric, with roll-up vortices of comparable magnitude reaching the trailing edge on the two sides. These coherent vortical structures are the result of amplified unstable waves in the laminar boundary layer and roll-up over the separated shear layer. Acoustic feedback locks the shedding frequency of these structures on the frequency of the primary tone [50], which in turn induces periodic unsteady surface pressure fluctuations. Amiet [17] related the acoustic pressure in the far-field to the statistics of the unsteady surface pressure field near the trailing edge. The periodic nature of these fluctuations thus results in the strong characteristic tones. Along with a shift of reattachment to an upstream location, the amplification of instability waves and roll-up of vortical structures occurs further upstream with increasing Reynolds number.

Changing the angle of attack to $\alpha = 1^\circ$ (figure 4.14, top right) introduces a distinct change in the instantaneous flow structure. Instability waves on the suction side amplify further upstream, while on the pressure side a shift downstream is observed. These shifts are related to changes of separation and reattachment location with angle of attack. While at low Reynolds number ($Re_c = 1.3 \times 10^5$) the structures on both sides are similarly coherent near the trailing edge, early amplification and eventual 3D breakdown cause a reduction in coherence on the suction side at high Reynolds number ($Re_c = 2.1 \times 10^5$). Amplification on the pressure side is delayed and occurs closer to the trailing edge, thus strongly coherent pressure-side events will start to dominate the tonal noise generation process.

The asymmetry between the events on the two sides becomes larger with increasing angle of attack ($\alpha = 2^\circ$, figure 4.14, bottom left). At low Reynolds number ($Re_c = 1.3 \times 10^5$), strongly coherent events on the suction side are visible and, as discussed before (figure 4.13), dominate tonal noise generation under these conditions. Increasing Reynolds number ($Re_c = 1.6 \times 10^5$) implies earlier amplification on the pressure side and further progress of transition on the suction side. As a result, the strength of roll-up vortices at the trailing edge becomes comparable; a situation that is encountered close to char-

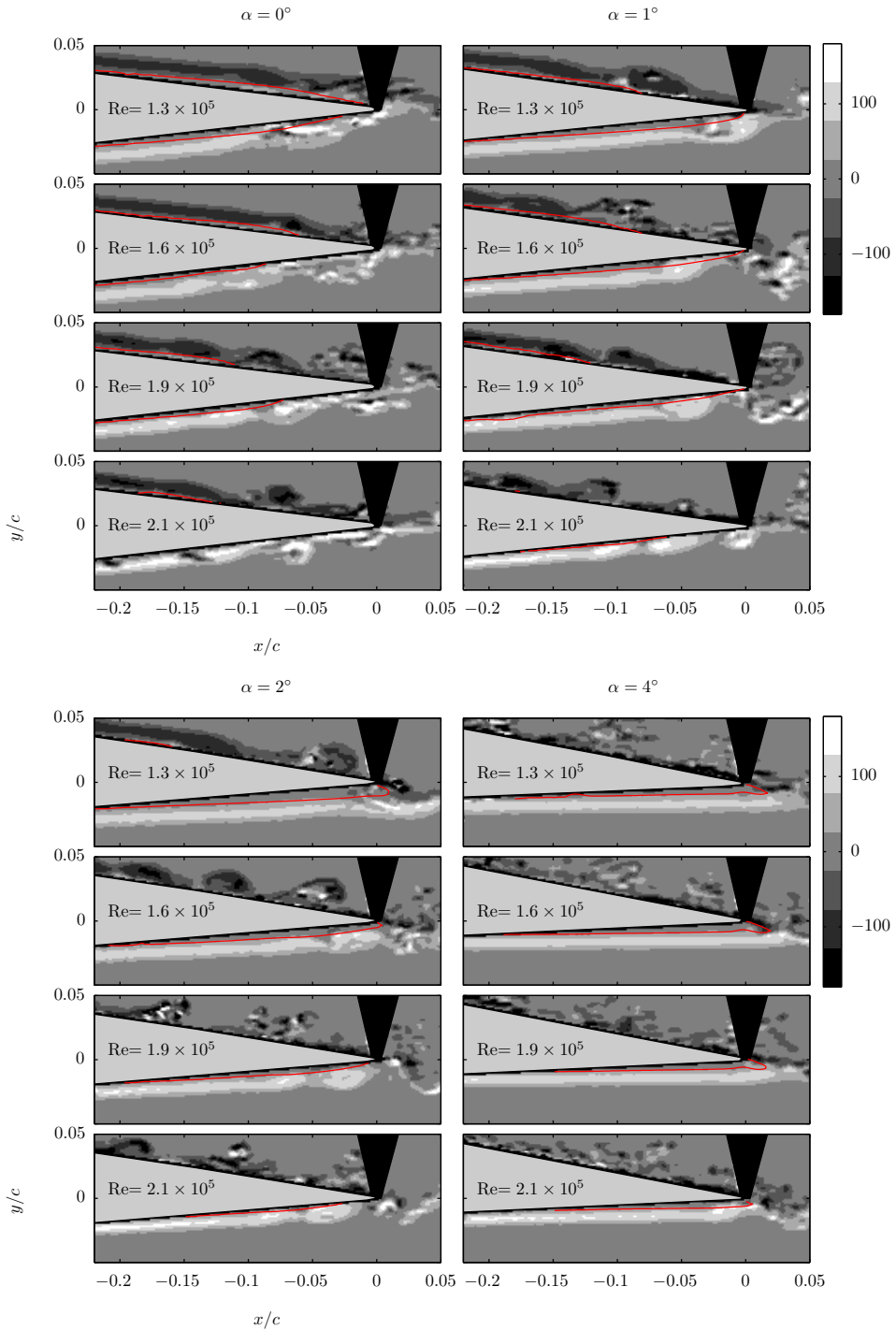


Figure 4.14: Spanwise vorticity component $(\omega_z c / u_\infty)$ and indication of reversed flow region (line at $u/u_\infty = 0$) for several angles of attack and Reynolds numbers. Smooth airfoil.

acteristic Reynolds number Re_{ch} and pertains to an overlap between the suction- and pressure-side-dominated regimes. For even larger $Re_c > Re_{ch}$ a clear loss in coherence on the suction side is observed. This loss of coherence is the result of the 3D breakdown encountered in the later stages of transition. Consequently, pressure-side events dominate tonal noise generation due to this asymmetry in flow conditions on the two sides, while the suction side primarily contributes to broadband noise emission. Inasawa *et al.* [156] described a similar Reynolds-number dependence for the particular case of $\alpha = 2^\circ$.

At $\alpha = 4^\circ$ (figure 4.14, bottom right) these changes in flow structure and the asymmetry are more emphasized. The comparatively low intensity of tones at low Reynolds numbers (compare figure 4.11) can be explained by the progressively increasing coherence loss on the suction side with increasing angle of attack. Upstream of the trailing edge, strong amplification of pressure-side instability waves is only observed at higher Reynolds number ($Re_c > 1.9 \times 10^5$) when compared to $\alpha = 2^\circ$. Thus, transition to the pressure-side-dominated regime for tonal noise generation is delayed to a higher characteristic Reynolds number (compare table 4.1).

The transition location is typically defined by a marked change in shape factor or by a steep increase of the velocity fluctuation level. Figure 4.15 shows the root-mean-square (rms) value of the corresponding y -velocity fluctuations with respect to the mean flow. For the airfoil at non-zero angle of attack (for instance $\alpha = 1^\circ$, figure 4.15, top right), the transition point based on the gradient criterion occurs upstream of the reattachment point (compare figure 4.14) and consequently earlier on the suction side than on the pressure side. The difference becomes larger with increasing angle of attack ($\alpha = 4^\circ$, figure 4.15, bottom right).

In summary, at low Reynolds number transition on the pressure side, where a separated shear layer often even extends into the wake, occurs late or even downstream of the trailing edge. On the suction side, earlier separation causes amplification of instability waves and coherent roll-up vortices to convect past the trailing edge. As a result of the shorter separation bubble length with increasing Reynolds number (figure 4.14), the transition point moves upstream on both sides of the airfoil (figures 4.14 and 4.15), leading to coherent vortical structures on the pressure side and initial stages of 3D turbulent breakdown on the suction side. This behavior causes a shift of the contribution to overall tonal noise generation from events on the suction side towards those on the pressure side. Increasing the Reynolds number even further amplifies this effect and the boundary layer on the suction side reaches a turbulent state upstream of the trailing edge. Therefore, the strong tonal noise emission is dominated by pressure-side events for $Re_c > Re_{ch}$. The existence of a separated shear layer on either the pressure or suction side sufficiently close to the trailing edge is thus confirmed to be a necessary condition for the generation of tonal noise [16].

4.3.5. CHARACTERISTICS OF SECONDARY TONES

Figure 4.5 showed that for most flow conditions multiple tones are present. Desquesnes *et al.* [129] ascribed this to periodic amplitude modulation of the primary tone. Thus, the primary tone can be interpreted as a carrier signal and the difference between the frequency of the primary tone and symmetric side tones can be interpreted as a modulation at frequency Δf and multiples thereof.

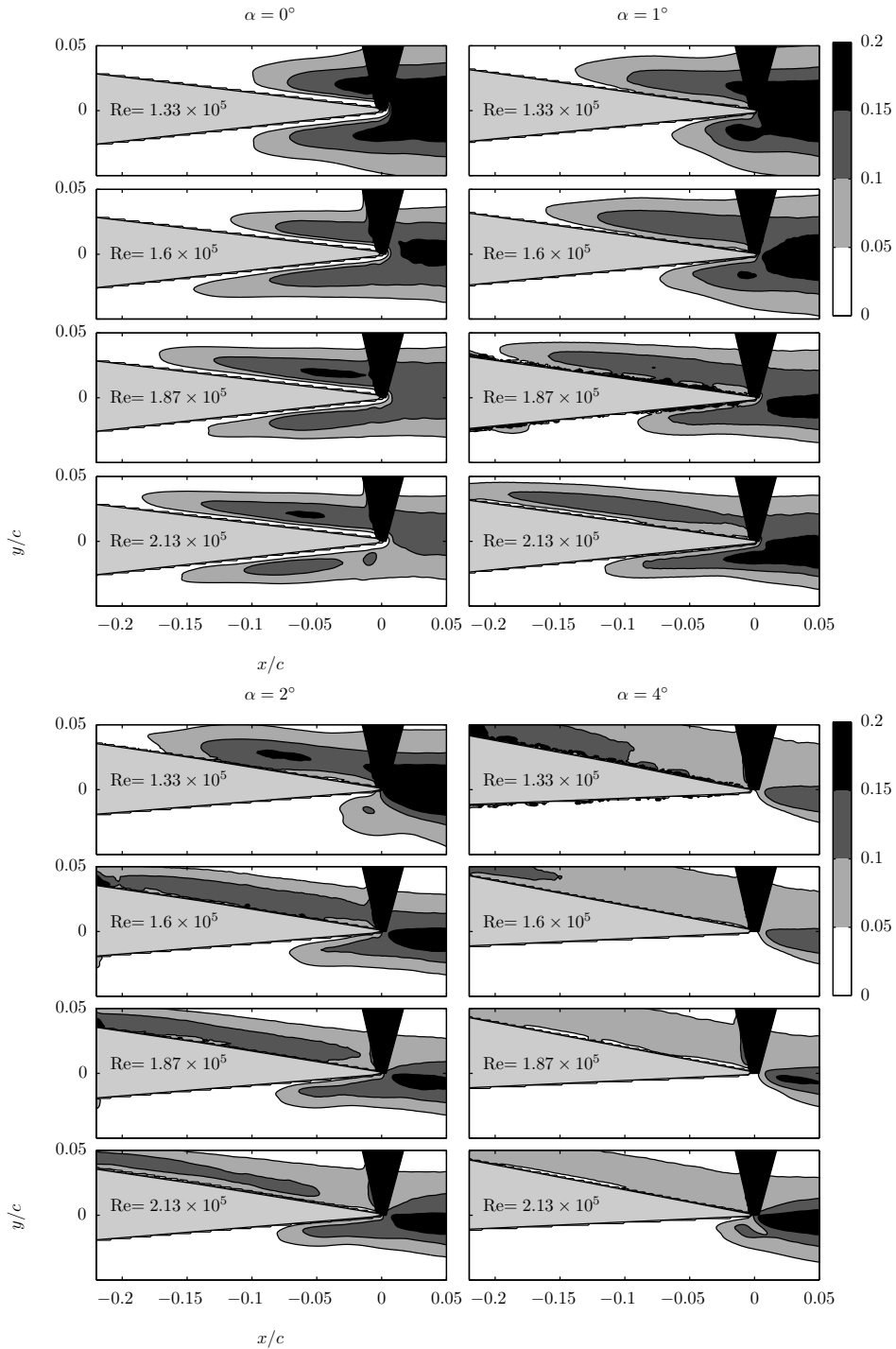


Figure 4.15: rms of fluctuating y-velocity component $rms(v^y)/u_\infty$ for different angles of attack and Reynolds numbers. Smooth airfoil.

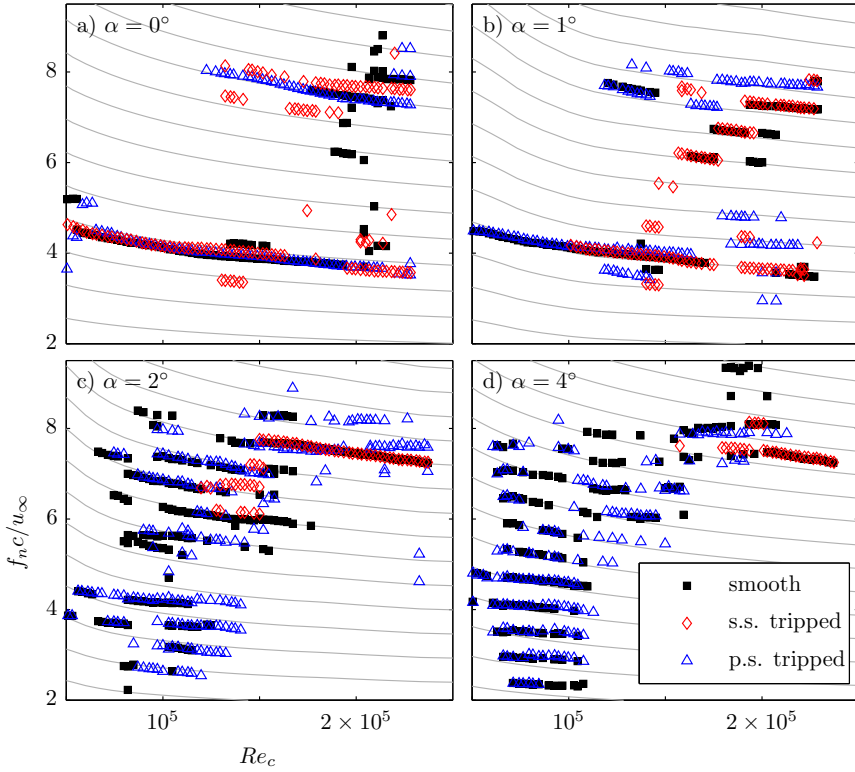


Figure 4.16: Frequencies f_n of primary and side tones (symbols). Empirical estimation based on equations 2.51 and 2.57 with $K = 0.365$ for suction side (lines).

Figure 4.16 shows the frequencies of the primary and side tones at least 30dB above the background noise level and at most 15dB below the intensity of the primary tone. Data are shown for the smooth and tripped cases (markers). In addition, the empirical estimation of the tone frequencies f_n for the suction side of the smooth airfoil is indicated (equations 2.51 and 2.57 with $K = 0.365$, lines). The latter requires an estimation of the feedback loop length scale L_f , which is considered as the distance between the maximum velocity point and the trailing edge as originally suggested by Arbey and Bataille [18]. This distance has been computed using XFOIL [128] for every combination of Reynolds number and angle of attack.

[18] suggested the empirical estimation (equation 2.57) for a NACA 0012 at near zero incidence ($\alpha = 0^\circ$). Near zero incidence, figures 4.16a) and 4.16b) indeed shows good agreement between the measured and predicted tonal frequencies for the smooth airfoil and pressure-side-tripped case ($\Delta f c / u_\infty \approx 0.65$). In particular, the increase in side tone spacing at low Reynolds number, which is described by the empirical relation, is confirmed by the measurements. Interestingly, the modulation frequency for the smooth

airfoil and Reynolds numbers $Re_c < 1.5 \times 10^5$ is substantially lower ($\Delta f c / u_\infty \approx 0.3$) over a small range of intermediate Reynolds numbers (about $Re_c \approx 1.5 \times 10^5$). To the authors' knowledge this halving of modulation frequency has not been reported before and might be a distinct feature for an airfoil at near zero incidence over a restricted range of Reynolds number.

With increasing angle of attack the predicted modulation frequency Δf decreases on the suction side as a result of an increase in feedback loop length on the suction. At $\alpha = 2^\circ$ (figure 4.16c) and $\alpha = 4^\circ$ (figure 4.16d) and for $Re_c < Re_{ch}$ the tone frequencies f_n for the smooth airfoil and that associated with the suction side are in good agreement and both configurations show a very similar side tone structure. In contrast, for $Re_c > Re_{ch}$ the frequencies for the smooth airfoil adapt to those found for the case with the suction side tripped.

For their numerical simulation, Desquesnes *et al.* [129] ascribed the periodic amplitude modulation of acoustic pressure to acoustic feedback on both the pressure and suction sides. Recently, Pröbsting *et al.* [50] reported similar periodic amplitude modulation of the acoustic pressure signal and showed that it is related to periodic amplitude modulation of the instability waves and roll-up vortices near the trailing edge. Moreover, it was demonstrated that pressure-side events can sustain such periodic amplitude modulation, while the boundary layer on the suction side is turbulent. Such an explanation does not require a strong coupling or interaction between the two sides and can explain the presence of multiple side tones.

For the present study, figure 4.16 shows that the marked side tone structure at $Re_c < Re_{ch}$ is ascribed to suction-side events. Pröbsting *et al.* [50] used wavelet analysis based on the Morlet wavelet to identify the time-dependent spectral characteristics of the corresponding signal [205]. Figure 4.17 shows the normalized magnitude of the wavelet coefficients, indicating the time-varying amplitude of acoustic pressure, for the airfoil at $\alpha = 2^\circ$ and Reynolds numbers of $Re_c = 1.1 \times 10^5$, $Re_c = 1.6 \times 10^5$, and 2.1×10^5 . At the lowest Reynolds number ($Re_c = 1.1 \times 10^5$, figure 4.17a), amplitude modulation is observed for the smooth case and is even more pronounced when the pressure side is tripped. The causality of the main modulation relating to suction-side events is more apparent at $Re_c = 1.6 \times 10^5$ (figure 4.17b). Close inspection of the smooth case reveals a secondary peak, which is not present when the pressure side is tripped. This distinct difference might point to a modification of the noise emission by a secondary feedback loop [129]. For $Re_c > Re_{ch}$, the side tone structure is substantially less emphasized (compare figure 4.16). Such a case is represented here by $Re_c = 2.1 \times 10^5$ (figure 4.17c). Clearly, the signal emitted by the smooth airfoil is pressure-side-dominated in this case and does not show strong periodic amplitude modulation when compared to cases with $Re_c < Re_{ch}$.

4.3.6. A PERSPECTIVE VIEW ON PREVIOUS STUDIES

In the past a large number of experimental and numerical studies relating to tonal noise generation on the NACA 0012 profile have been published. Arcondoulis *et al.* [160] performed extensive acoustic measurements on a NACA 0012 in a similar low to moderate Reynolds number range (0.5×10^5 to 1.5×10^5) as investigated in the present study. Their data are presented together with other experimental and numerical results discussed below in figure 4.18. The comparison suggests that Arcondoulis *et al.* [160] mainly con-

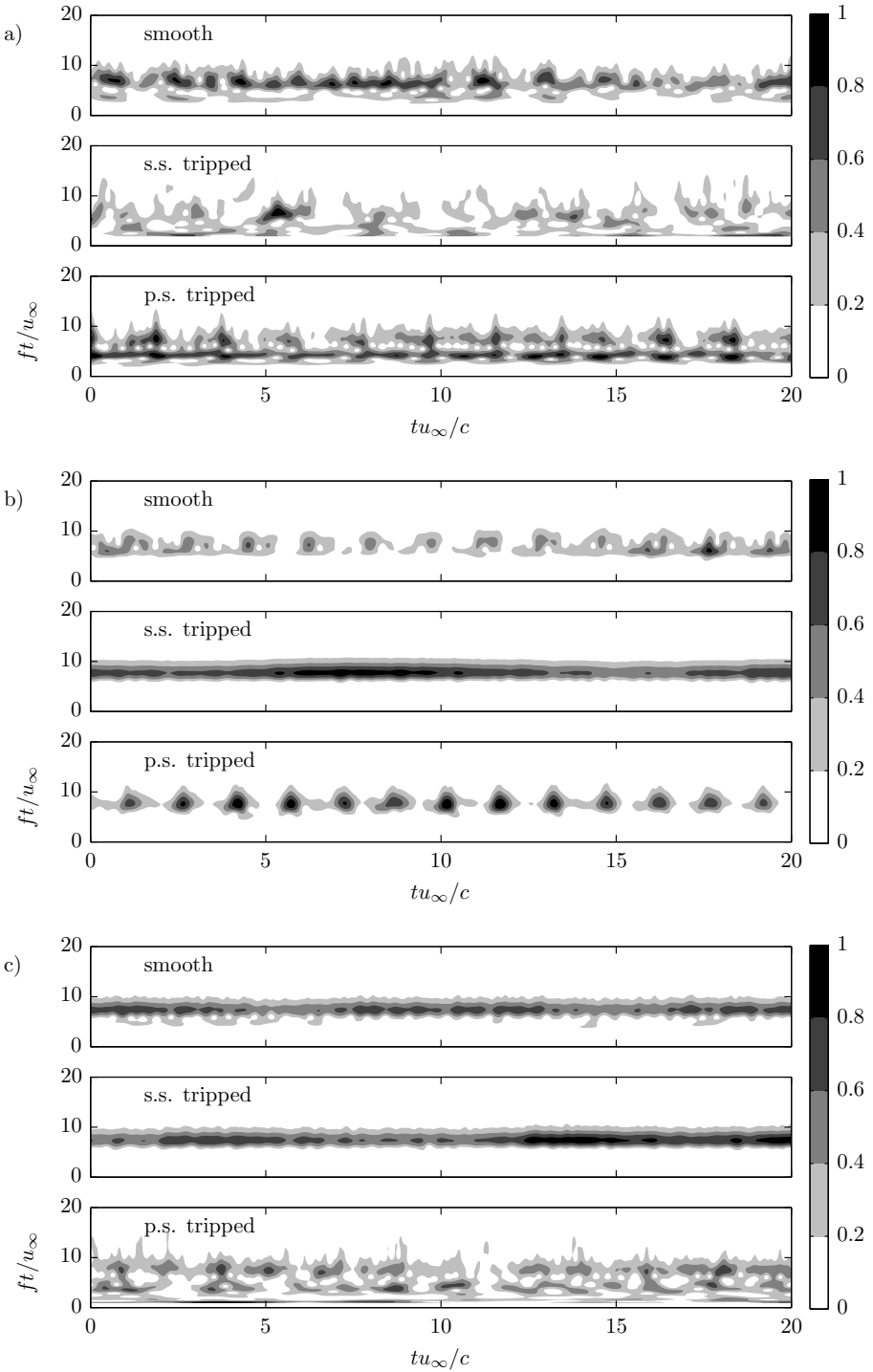


Figure 4.17: Magnitude of wavelet coefficients of acoustic pressure (normalized by maximum value) against pseudo-frequency and time for $\alpha = 2^\circ$ and $Re_c = 1.1 \times 10^5$, 1.6×10^5 , and 2.1×10^5 .

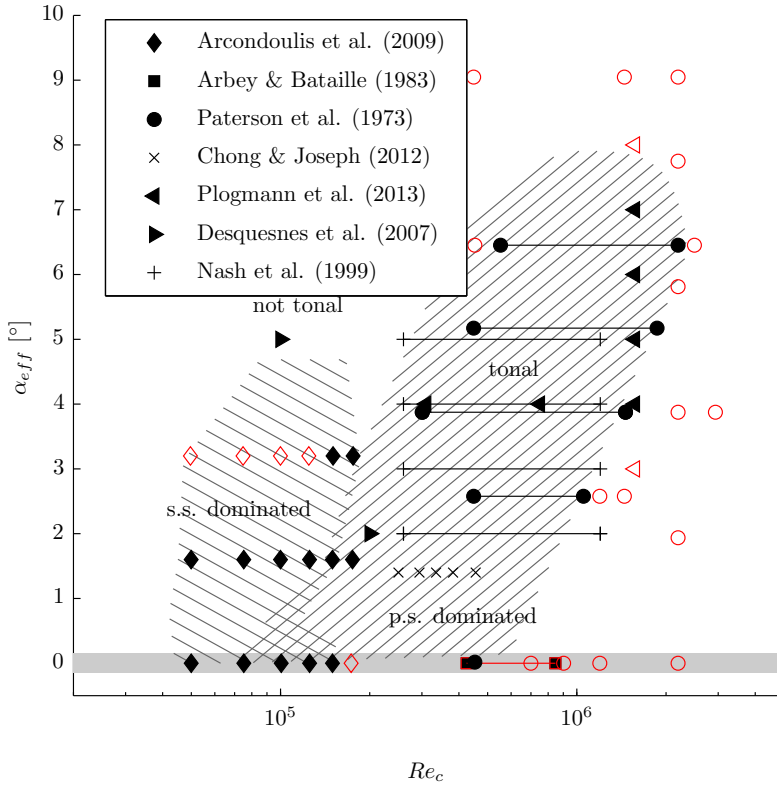


Figure 4.18: Experiments showing tonal (solid symbols) and non-tonal noise (open symbols). Suction (hatched, top left to bottom right) and pressure-side-dominated regimes (hatched, bottom left to top right). For the results of Plogmann *et al.* [119] and Nash *et al.* [16] the geometric angle of attack is reported. The grey bar around $\alpha_{eff} = 0^\circ$ indicates the uncertainty in angle of attack for the present study.

sidered suction-side-dominated cases or those constituting the overlap region. They observed no tones at their largest investigated angle of attack ($\alpha_{geo} = 10^\circ$, $\alpha_{eff} = 3.2^\circ$). The reason for the discrepancy with the results of the present study is not clear, but might be related to the comparatively large blockage ratio in the study of Arcondoulis *et al.* [160]. This might have led to a substantially different pressure distribution and renders the simple angle-of-attack correction by equation 4.1 questionable.

The study of Paterson *et al.* [35] constitutes the classical reference for boundary layer instability noise and, as evident from figure 4.18, was exclusively concerned with pressure-side-dominated cases for non-zero angle of attack. Their statement that tripping of the boundary layer on the suction side had no effect on the tonal noise emission corroborates this conclusion.

Plogmann *et al.* [119] covered a similar range of Reynolds numbers and identified a *ladder* structure with tonal emission in the range $3.1 \leq Re_c \leq 7.5 \times 10^5$ at $\alpha = 4^\circ$ (compare figure 4 of Plogmann *et al.* [119]). At fixed Reynolds number $Re_c = 1.57 \times 10^6$, they they

reported tones between $4^\circ \leq \alpha \leq 7^\circ$ (compare figure 3 of Plogmann *et al.* [119]). They also tripped the boundary layer on the pressure side, which eliminated tonal noise. It should be noted that these experiments were performed in a closed section wind tunnel and the geometric angle of attack is given. In contrast to an open jet set-up, the effective angle of attack is thus expected to be larger than the geometric one. A good match with the (corrected) tonal envelope of Lowson *et al.* [130] is found and, clearly, noise emission was pressure-side-dominated, as stated by the authors in their conclusion. However, they also concluded that a secondary feedback loop due to suction-side events is not relevant for tonal noise emission. This conclusion should be put into perspective: Desquesnes *et al.* [129], who originally proposed the secondary feedback loop, considered a case close to the interaction regime (see figure 4.18) and the results of Plogmann *et al.* [119] do not necessarily apply to this case. Nevertheless, Pröbsting *et al.* [50] showed that a secondary feedback loop is also not a necessary condition for periodic amplitude modulation of the roll-up vortices within this interaction regime.

Nash *et al.* [16] considered a NACA 0012 with 300mm chord at angles of attack between $\alpha = 2^\circ$ and 5° ($2.6 \times 10^5 < Re_c < 1.2 \times 10^6$) in a closed test section (quasi-anechoic) wind tunnel. The high Reynolds-number range suggests that tonal noise generation was pressure-side-dominated, exclusively. The authors remarked that no *ladder* structure was observed (compare figure 5 of Nash *et al.* [16]). Indeed, for $\alpha = 2^\circ$ and 3° the data show evidence of transitions (jumps) at intermediate Reynolds numbers, while this is not the case for higher angles of attack, where the primary tone frequency varies continuously with $u_\infty^{0.8}$. These transitions without clear ladder structure, albeit at different Reynolds number, are similar to the observations in the present study (figure 4.10c,d).

Chong and Joseph [117] presented results on an airfoil at effective angle of attack $\alpha_{eff} = 1.4^\circ$ for the pressure-side-dominated range of Reynolds numbers between $Re_c = 2.5 \times 10^5$ and 5×10^5 . Their results (compare figure 3 of Chong and Joseph [117]) show a similar asymmetric shape of the side tones with respect to the primary tones as in the present study (figure 4.4), which was attributed to a relative shift of broadband and tonal contributions.

Two-dimensional (2D) large-eddy simulation and direct numerical simulation (DNS) studies have been a popular tool for the investigation of the tonal noise phenomenon [15, 124, 125, 129, 162–164, 201]. Desquesnes *et al.* [129] interpreted the results of their 2D DNS such that, for a NACA 0012 at 5° and Reynolds number 1×10^5 , only broadband noise is present, while tones occurred at 2° and 2×10^5 , respectively. Their results show coherent vortical structures on both pressure and suction sides for this case (compare figure 4 of Desquesnes *et al.* [129]) and evidence of tonal noise (compare figure 7 of Desquesnes *et al.* [129]), which was in agreement with the envelope of Lowson *et al.* [130]. Observing periodic amplitude modulation of far-field acoustic pressure and vortical structures on both sides of the airfoil, the authors suggested a concept including two feedback loops to explain such modulation. In view of the results presented here, this concept can be considered for the overlap region of the two regimes. However, within the pressure- and suction-side-dominated regimes such interaction has little effect, as discussed above.

de Pando *et al.* [15] recently performed another 2D DNS simulation at similar Reynolds number (2×10^5) and angle of incidence (2°), which suggests a suction-side-dominated

case. It should be noted that in both simulations suction-side events appear to be more coherent than for the experimental results under similar conditions (figure 4.14). This is probably related to the physics of 2D flow, which fundamentally differs in the nature of the energy cascade from its 3D counterpart. Thus the interaction between the events on the two sides is likely to be overestimated for 2D simulations under such conditions. This can lead to discrepancies in the results for 2D simulations when compared to experimental studies: in order to capture the entire physics of the problem, the 2D assumption is not appropriate, which has been acknowledged by some authors by stating that, at higher angles of attack or Reynolds numbers, one of the boundary layers would become turbulent, thus leading to broadband noise emission [129]. Furthermore, owing to the comparatively low-Reynolds-numbers (suction-side-dominated) cases often targeted in numerical simulations, comparison with higher-Reynolds-number experimental data (for pressure-side-dominated cases) needs to be interpreted carefully.

A particular point of debate has been the noise emission at zero incidence. The acoustic measurements of Arcondoulis *et al.* [160] for Reynolds number between 0.75×10^5 and 1.5×10^5 show a primary tone and weak secondary tones (20dB lower). In the same study, the authors reported that the spectral content became significantly more broadband at higher Reynolds number ($Re_c > 1.8 \times 10^5$). These observations agree with the present study (figure 4.5) and the broadening at higher Reynolds numbers is related to earlier transition (figure 4.14). However, these experimental results are in conflict with the 2D DNS results of Tam and Ju [162], who found a single primary tone at a frequency scaling with f_s (equation 2.48) at even higher Reynolds number (between $Re_c = 2 \times 10^5$ and 5×10^5), but for zero inflow turbulence. Also the flow structure presented by Tam and Ju [162] shows a fundamental difference: the boundary layer remains laminar up to the trailing edge and tonal noise generation is attributed to a wake instability, which contrasts the convection and scattering of amplified instability waves at the trailing edge as suggested in the present and previous studies [18]. According to Tam and Ju [162] differences may be ascribed to the turbulence level ($\leq 0.1\%$ in the present study, [202]). A point of attention on the experimental side are asymmetries in the set-up, in particular for the adjustment of the angle of attack ($\pm 0.15^\circ$ in the present study, indicated by grey area in figure 4.18). Owing to the high sensitivity of the flow regimes to angle-of-attack changes near zero incidence, the experimental results should be considered carefully. However, it is not expected that the case of zero incidence $\alpha = 0^\circ$ represents a singularity in the sense that the flow remains laminar up to the trailing edge, while transition is observed in experiments at far lower Reynolds number at near zero incidence [50, 160]. From the perspective of numerical modeling, the extent to which the 2D flow model and zero inflow turbulence level influence the results should be considered.

4.4. CONCLUSION

Strong amplification of instability waves is linked to a separation bubble or separated shear layer on the pressure and/or the suction side. The reattachment point on both pressure and suction sides moves upstream with increasing Reynolds number. Therefore, the transition region, constituting the aft portion of the separation bubble, also moves upstream. This Reynolds-number dependence is weak compared to changes with angle of attack. With increasing angle of attack, the reattachment point on the suction

side shifts upstream. On the pressure side, the reattachment shifts further downstream in the case of a separation bubble, while the reverse flow region extends further into the wake in the case of a separated shear layer. These dependencies of the topology promote the division of the Reynolds-number and angle-of-attack domains into pressure- and suction-side-dominated regimes of tonal noise generation. They provide conditions for which either pressure- and/or suction-side instability waves are amplified sufficiently close to the trailing edge to induce the roll-up of spanwise coherent vortical structures, which then coherently convect past the latter and thus contribute to tonal noise generation. Suction-side events dominate tonal noise emission at low Reynolds number, while pressure-side events prevail at high Reynolds number. With increasing angle of attack the overlap region between the regimes becomes progressively smaller due to a larger sensitivity of the reattachment and transition location to Reynolds number. An overview of the regimes identified in the present study was given in figure 4.13 and indicated that the domain of tonal noise extends over a larger range of Reynolds number than typically indicated previously for the NACA 0012 airfoil.

Experiments with forced boundary layer transition have shown that interaction between events on the two sides, such as suggested by the secondary feedback [129] or hydrodynamic interaction [16], is not a necessary condition for the presence of side tones and a *ladder* structure. Nevertheless, such interaction has an influence on the details of the emitted tonal noise. Especially with regard to such interaction, assessment and quantification of the spanwise correlation length on the two sides may lead to further insight. In the present study, the side tone structure and modulation are most prominent in the suction-side-dominated regime. A fine *ladder* structure is not present near zero incidence, but indications of a *ladder* structure are observed at higher angle of attack. Previous reports suggest that the *ladder* structure is also evident in the pressure-side-dominated regime at higher Reynolds numbers.

5

AMPLITUDE MODULATION OF AMPLIFIED INSTABILITY WAVES

If amplitude modulation is present in the noise at a receiver, the noise is perceived as being more annoying than if the noise has no modulation. It can become impossible [to] ignore the noise which might otherwise be acceptable.

Dick Bowdler [206]

In this chapter, the temporal development of vortical structures in the vicinity of the trailing edge is discussed. Results of simultaneous time-resolved PIV measurements within the aeroacoustic source region and of acoustic measurements are presented in order to establish the correspondence between the flow evolution and the acoustic emissions.

Time-resolved analysis shows that downstream convecting vortical structures pass the trailing edge at a frequency equal to that of the primary tone. Non-stationary spectral analysis of the acoustic pressure and the velocity signals near the trailing edge show a similar periodic amplitude modulation, which is then related to the tones in the acoustic spectrum. The periodic amplitude modulation of the acoustic pressure and velocity fluctuations on the pressure side is also observed when transition is forced on the suction side, showing that pressure side events alone can be the cause.

Parts of this chapter have been published in the Journal of Fluid Mechanics 747 (2014) [50].

5.1. INTRODUCTORY REMARKS

AMPLITUDE MODULATION of the acoustic pressure signal¹ has been pointed out by Desquesnes *et al.* [129] to be associated to multiple tones in the acoustic spectrum. Their results support the earlier hypothesis that the dominant tone frequency is associated to boundary layer instabilities passing the trailing edge. At the trailing edge acoustic waves are scattered, sustaining a feedback mechanism with the susceptible part of the laminar boundary layer. A transient analysis based on the short-time Fourier transform of the acoustic signal showed that the tones in the acoustic power spectrum are associated to a near periodic amplitude modulation of the primary tone.

This modulation has been associated to the varying phase difference between aerodynamic fluctuations on the two sides of the airfoil near the trailing edge. It was conjectured that an interaction of events on the pressure and suction sides is necessary for the occurrence of multiple tones. However, no experimental evidence for this transient behavior of aerodynamic velocity fluctuations has been presented previously.

The periodic amplitude modulation resulting in multiple tones can be explained by mechanisms other than the secondary feedback loop discussed by Desquesnes *et al.* [129]. It is thus of interest whether the periodic amplitude modulation of acoustic pressure, observed in the numerical simulation by Desquesnes *et al.* [129], can also be observed experimentally. Further, it is investigated whether this amplitude modulation is also evident in the velocity field near the trailing edge and what its relevance is. Finally, the question whether multiple tones are also present if the boundary layer on one side is turbulent is addressed. For this purpose, three cases of the NACA 0012 profile at moderate Reynolds number (see chapter 4) are discussed in greater detail:

1. $u_\infty = 24\text{m/s}$, $\alpha_{geo} = 2^\circ$ with smooth airfoil
2. $u_\infty = 24\text{m/s}$, $\alpha_{geo} = 2^\circ$ with the suction side tripped
3. $u_\infty = 24\text{m/s}$, $\alpha_{geo} = 4^\circ$ with smooth airfoil

5.2. DESCRIPTION OF EXPERIMENTS

For a description of the NACA 0012 airfoil and facility (Vertical-Tunnel at Delft University of Technology) used to obtain the experimental results reported in this chapter, the reader is referred to section 4.2 or to Pröbsting *et al.* [50].

5.2.1. ACOUSTIC MEASUREMENTS

Two LinearX M51 microphones are positioned on opposite sides of the airfoil at a distance of 1.1m and perpendicular to the chord plane at the level of the trailing edge. Nominally, the microphones have a flat frequency response between 50Hz and 20kHz. The microphones are calibrated with a GRAS piston phone.

Measurements are taken at a sampling frequency of 40kHz for a period of 20s for statistical purposes. For processing the statistical data, the Coherent Output Power (COP) method [37], previously applied for the measurement of trailing edge noise by Brooks

¹see appendix F for a discussion

and Hodgson [36], filters the incoherent part of the signal under the assumption of uniform directivity. If not mentioned otherwise spectral estimates are computed using an average periodogram method [203], where a Hamming windowing function is applied to each segment of the acquired signal [207]. For the COP, the cross-spectral density is considered instead of the auto-spectra density. The number of samples per window is 16,384 and an overlap of 50% is applied, resulting in a frequency resolution of 2.44Hz. For transient analysis and correlation, data is acquired simultaneously with the PIV measurements. The wavelet transform of a single microphone signal is computed as described in appendix E [205].

5.2.2. FLOW FIELD MEASUREMENTS

The airflow is seeded with water-glycol based fog particles of mean diameter of $1\mu\text{m}$. Illumination is provided by a Litron Nd:YLF laser (dual cavity). The measurement domain (approximately $3.2 \times 1.6\text{cm}^2$) includes the flow upstream and downstream of the trailing edge on both sides of the airfoil (figure 4.2). Illumination through the trailing edge is affected by local refraction, causing a shadowed region where velocity field data is thus not available.

A Photron *FastCam* SA1.1 (1024×1024 pixels (px), 12bits, pixel pitch $20\mu\text{m}$) equipped with a Nikon Micro-Nikkor 200mm prime lens was used and operated at a focal ratio $f_{\#} = 4$. The optical magnification is $M = 0.65$ leading to a digital imaging resolution of 32px/mm. With this aperture, the diffraction limited particle image diameter is estimated to be less than 1px at the plane of focus (diffraction spot size $d_{diff} = 9\mu\text{m}$), which can lead to unresolved particle images and in turn a large bias error due to peak-locking. Therefore, the plane of focus is slightly shifted away from the illumination plane leading to defocused particle images encompassing approximately 2-3px, which eliminates peak-locking errors. The measurement system is controlled by a PC workstation, equipped with a LaVision Highspeed Controller that synchronizes illumination and imaging devices, and operated by the LaVision *DaVis* 8 software, which is also used for image pre-processing and interrogation. In double frame mode, the acquisition frequency for image pairs is $f_{acq} = 6\text{kHz}$. The pulse separation is adjusted such that the particle displacement in the free-stream is approximately equal to 0.47mm (15px in the image plane). Sequences are recorded for a duration of 1.16s, equivalent to 6,970 image pairs contained in each sequence. Table 5.1 summarizes the parameters of the PIV measurements. Assuming a random error of 0.1px on the localization of the correlation peak, which is typically reported for planar PIV experiments [167], the relative random error on the velocity can be estimated with $\sigma/u_{\infty} = 0.1/15 = 0.007$ in the free-stream.

Images are processed using an iterative multi-grid, multi-pass technique with window deformation and a final window size of 0.5mm in physical space (16px). The overlap factor is 75%, resulting in a vector spacing of approximately 0.125mm. To improve the spatial resolution in wall-normal direction, Gaussian window weighting (aspect ratio 2:1) is applied during the correlation process [208]. For the x - y coordinate system, the origin is defined at the trailing edge and the direction of the abscissa coincides with that of the chord line for an airfoil at zero angle of attack. Velocity components are denoted by u and v , respectively. The coordinates in the surface attached coordinate system on the two sides of the airfoil are denoted by x_t and x_n , where the abscissa is tangential

Table 5.1: Parameters related to planar PIV measurement.

Parameter	Symbol	Value
Lens focal length		200mm
Focal ratio	$f_{\#}$	4
Magnification	M	0.65
Field of view	FOV	$32 \times 16\text{mm}^2$
Acquisition frequency	f_{acq}	6kHz
Free-stream displacement	Δx	15px
Measurement time	T	1.16s
Number of samples	N	6,970
Window size	δ_x	0.5mm
Vector spacing		0.125mm
Vector grid		100×50

to the surface of the airfoil and the origin is located at the trailing edge. Here, velocity components are denoted by u_t and u_n , respectively.

5

5.3. RESULTS AND DISCUSSION

5.3.1. PERIODIC AMPLITUDE MODULATION OF ACOUSTIC PRESSURE

The presence of multiple tones in the acoustic spectrum has been associated to an amplitude modulation through a non-stationary signal analysis by Desquesnes *et al.* [129]. Making use of a windowed short-time Fourier transform method, they investigated the acoustic pressure in the far-field and observed that its amplitude modulates almost periodically. Indeed, the spectrum of a signal based on a carrier frequency $f_{n_{max}}$ (see section 2.3 for definitions) and an amplitude modulation at frequency Δf reproduces the discrete tonal features observed in the acoustic pressure spectra reported in chapter 4 (for an explanation of amplitude modulation see appendix E).

For case 1 ($u_{\infty} = 24\text{m/s}$, $\alpha_{geo} = 2^\circ$), the time series of the acoustic pressure is shown in the upper part of figure 5.1. The period of the high frequency oscillations in the signal is approximately 0.54ms, while the amplitude modulates periodically with a period of approximately $T = 7.4\text{ms}$. Introducing a normalized time reference $t^* = tu_{\infty}/c$ the above mentioned periods are equal to $\Delta t^* = 0.13$ and $\Delta T^* 1.78$.

A statistical estimate of both discrete frequency and its modulation is obtained by wavelet decomposition of the far-field acoustic pressure. The procedure follows the recommendations given by Torrence and Compo [205] and the Morlet wavelet is chosen for this type of frequency analysis (see appendix E). In figure 5.1 (bottom) contour lines of the square modulus of the continuous wavelet transform coefficients are shown. The axes represent time and pseudo-frequency, closely associated to the Fourier frequency through the choice of the wavelet scale. Maxima occur centered on a horizontal line close to the dominant tone frequency $f_{n_{max}}^* = 7.7$ (1,865Hz). The regular appearance and disappearance of the peaks confirms the presence and periodic nature of the amplitude modulation. Matching the observation of $\Delta T^* = 1.78$ in the time series, the first modulation frequency is $\Delta f^* = 0.56$ (135Hz), which is equal to the frequency separa-

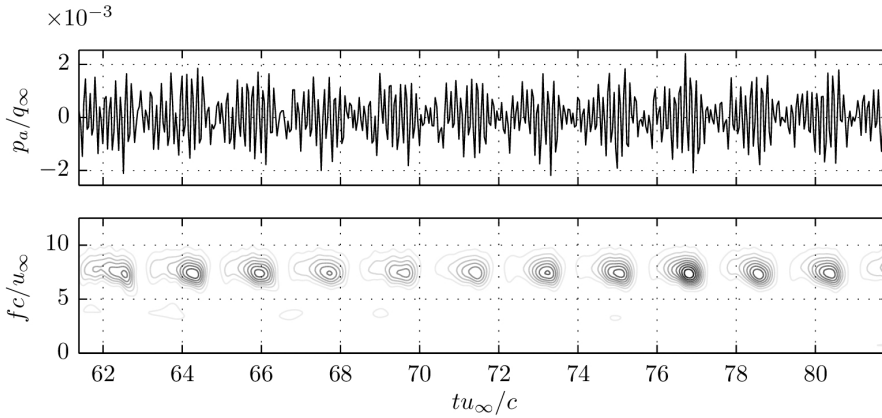


Figure 5.1: Time series (top) and normalized square magnitude of wavelet coefficients (bottom) of acoustic pressure signal, case 1.

tion Δf observed in the acoustic spectra. In principle, this amplitude modulation is not restricted to a frequency of Δf , but can also occur at multiples of this frequency $m\Delta f$, which leads to further side peaks in the acoustic spectrum, with $m = 1, 2, \dots$ (see discussion in appendix E).

Two additional features of the amplitude modulation can be observed. Firstly, the dominant tone frequency tends to slightly decrease during a single modulation cycle, which indicates that the dominant tone frequency is slightly altered along the emission cycle. Secondly, the growth of the amplitude of the oscillations before reaching the peak value appears to be less steep than the descending part.

For the case of forced transition on the suction side of the airfoil (24m/s, 2° , suction-side tripped, case 2), figure 5.2 shows the time series and wavelet decomposition of the acoustic pressure in the far-field. Compared to the case where no transition is forced (figure 5.1, case1) the amplitude variation, although less pronounced, is still present, while the maximum amplitude of the signal is about equal. The wavelet analysis reveals a temporal variation of the pressure through amplitude modulation. The frequency of the dominant tone $f_{n_{max}}^* = 6.6$ (1,585Hz) is slightly lower compared to case 1, in contrast to the modulation frequency $\Delta f^* = 0.67$ (160Hz). In this case the amplitude temporal variation is even more skewed than in the previous case: within the growth process a first peak or plateau region is observed, which results in a harmonic component at $f^* \approx 2\Delta f^*$. The maximum amplitude of this secondary peak is lower in amplitude compared to the primary peak.

At higher angle of attack (24m/s, 4° , case 3), the flow is turbulent on the suction side. In this case only weak tones are observed, which is corroborated by the time series and wavelet decomposition of the acoustic pressure in figure 5.3. Overall, the amplitude of the signal remains lower compared to the tonal case at lower angle of attack (figure 5.1) and most energy is contained in the spectrum below $f^* = 0.5$.

It can be concluded that the periodic amplitude modulation of the acoustic pres-

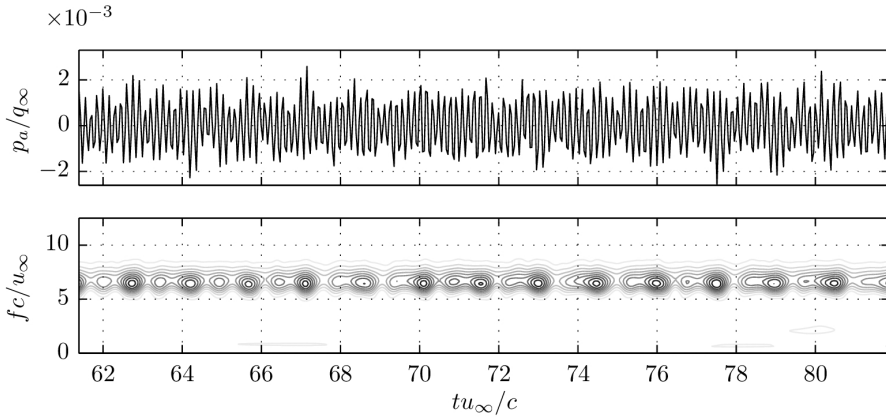


Figure 5.2: Time series (top) and normalized square magnitude of wavelet coefficients (bottom) of acoustic pressure signal, case 2 (forced transition on suction side boundary layer).

5

sure is reproduced by experiments, which confirms the observations of Desquesnes *et al.* [129] in their 2D DNS study with otherwise similar conditions and provides an explanation for the discrete tones in the spectrum. Desquesnes *et al.* [129] explained this modulation with a vortex wake pattern bifurcation, a phase variation between the pressure fluctuations on the two sides of the trailing edge. However, reasons for such an amplitude variation in the acoustic pressure can be manifold as noted by the same authors and recently by Plogmann *et al.* [119]. Since the periodic amplitude modulation is also observed for the case of forced transition, where the relative phase of the boundary layer velocity fluctuations on the two sides cannot be defined, it must be concluded that this variation in phase is not the only mechanism that can lead to an amplitude modulation of the acoustic pressure.

5.3.2. FLOW STRUCTURE AND TOPOLOGY

From the time-averaged statistics of the velocity field, its instability characteristics can be inferred. For case 1, the average velocity profile on the pressure side shows an inflection point throughout the measurement domain (figure 5.4a), a necessary condition for the presence of an inviscid-type instability [130]. The flow is separated close to the trailing edge and roll-up of coherent vortical structures can be observed. As noted by a number of researchers [16, 44, 129], this local flow separation is believed to be a necessary condition for tonal noise. The same authors denote this as a laminar separation bubble in cases where reattachment close to the trailing edge is observed. Here, the point of inflection of the mean velocity profile becomes further separated from the wall downstream, which is followed by an increase of the maximum reverse flow velocity. It is estimated that at the trailing edge the reverse flow attains approximately $0.1u_e$, where u_e is the local boundary layer edge velocity. Upstream, the time-averaged streamwise velocity fluctuations show evidence of two maxima which can be clearly distinguished at $x_t/c = -0.05$, where additionally a third peak in the upper part of the boundary layer

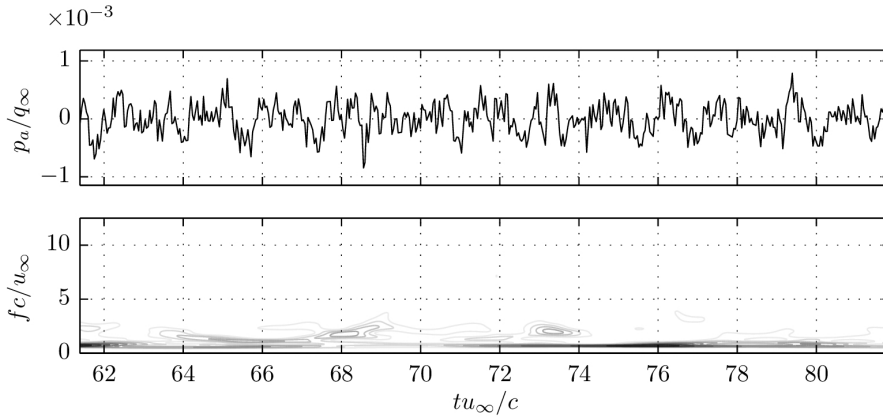


Figure 5.3: Time series (top) and normalized square magnitude of wavelet coefficients (bottom) of acoustic pressure signal, case 3.

is visible. This triple peak structure of the streamwise velocity fluctuations is one of the features often described for cases of tonal noise emission [16, 129]. Although the boundary layer evolves towards a turbulent state, the velocity profile at the trailing edge is still different from a turbulent boundary layer. The maximum value of the fluctuations attains 14% close to the trailing edge compared to approximately 3% at $x_t/c < -0.15$ due to the large growth rate in this region.

Desquesnes *et al.* [129] noted that no separation was present on the suction side in the tonal noise case, while a separation bubble was found between 18%-40% chord in the non-tonal case, which falls outside the current measurement domain and cannot be verified here. The mean velocity profiles appear to recover from an earlier separation (figure 5.4b) and a separation bubble is likely to be present upstream of the observed domain. An inflection point close to the wall is found at $x_t/c = -0.2$ and -0.15 but not further downstream, indicating that the flow is attached in the aft part of the airfoil. The profiles of velocity fluctuations reveal a double peak structure, also reported by Desquesnes *et al.* [129] and interpreted as evidence for the presence of a Rayleigh type instability. It is likely that the instability waves approach a saturated state before they convect past the trailing edge, which is supported by the relatively large amplitude ($u'_t/u_\infty = 0.3$) of the fluctuations at $x_t/c = -0.2$ and small variation along the wall-tangential coordinate.

When forcing transition on the suction side, the evolution of the mean velocity profiles on the pressure side is not seemingly altered (figure 5.5a), compare to figure 5.4a, showing a point of inflection and a region of reverse flow close to the wall. On the other hand, significant differences are present for the mean velocity fluctuations. The profiles at the first two stations in figure 5.5a show a single peak suggesting that no amplified instabilities are present. Further downstream at $x_t/c = -0.1$, where values of the reverse velocity have increased in magnitude, indications of a second maximum close to the wall are present. Even further downstream this second peak increases, reaching the magnitude of the first one at the trailing edge. No clear triple peak structure is evident for this

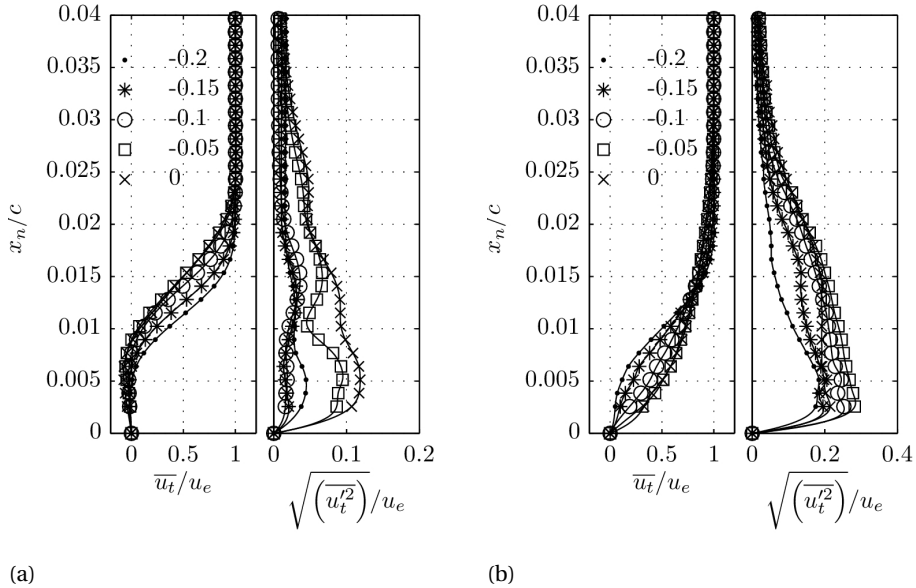


Figure 5.4: Mean (left) and root mean square fluctuations (right) of tangential velocity component on pressure side (a) and suction side (b) at different x_t/c (indicated in legend), case 1.

case upstream of the trailing edge. This suggests that a triple peak structure is not a necessary feature in the case of tonal emission as reported by Nash *et al.* [16].

In the absence of strong tones (case 3), the mean tangential velocity profiles on the pressure side (figure 5.5b) also reveal a region of reverse flow, yet with a slightly lower peak. A profound difference with respect to case 2 is found in terms of turbulence levels. With a maximum value below 3% up to the trailing edge the fluctuations in this case are relatively small due to the absence of larger amplitude vortical structures. The scenario here is that the boundary layer undergoes laminar separation close to the trailing edge and the growth of the instabilities is delayed with respect lower angles of attack (case 2, figure 5.6). This is consistent with a shift of the stagnation point towards the suction side on the airfoil nose and a shift downstream of the region of favorable pressure gradient (see discussion in section 4.3.4).

The instantaneous flow pattern for the cases presented here shows a number of distinctive features (figure 5.6), illustrated by velocity vectors overlaid on the contours of the spanwise vorticity component. For case 1, one can observe vortical structures connecting on the suction side and inducing a significant departure of the streamlines from a parallel pattern. Closer to the trailing edge, the vorticity pattern appears less coherent, which indicates three-dimensional breakdown to turbulence. On the pressure side the flow appears to be laminar up to 90% chord, where vortical structures develop due to a shear layer. For the case of forced transition (case 2), on the suction side no large coherent structures can be observed and the boundary layer is in a turbulent state. The pressure side however shows similar features when compared to case 1, with a roll-up of spanwise coherent vortices close to the trailing edge. At higher angle of attack (case

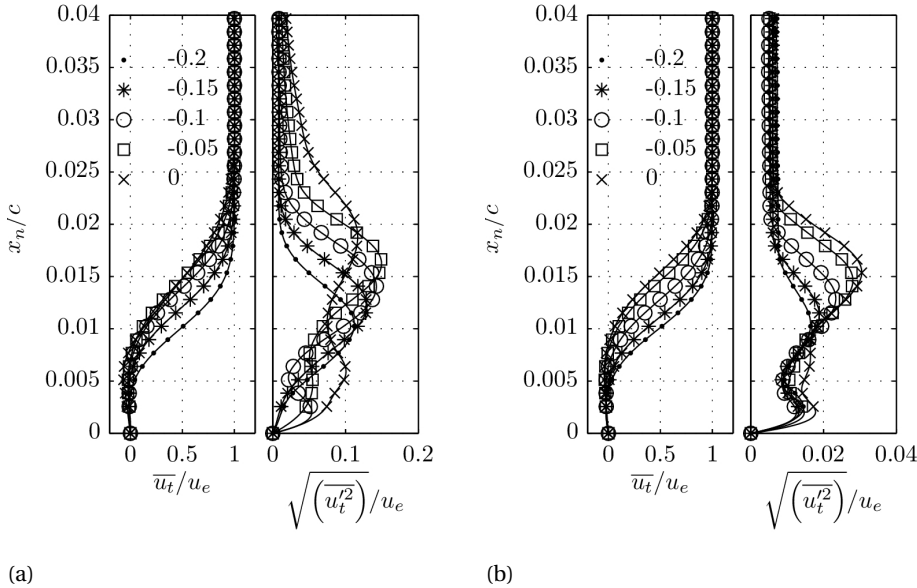


Figure 5.5: Mean (left) and root mean square fluctuations (right) of tangential velocity component on pressure side for case 2 (a) and case 3 (b) at different x_t/c (indicated in legend).

3) flow on the pressure side remains laminar almost up to the trailing edge, while the boundary layer on the suction side approaches a turbulent state with an indication of larger scale turbulent bulges. The instantaneous flow structure for a wider range of flow conditions was presented in figure 4.14.

5.3.3. AMPLIFICATION OF INSTABILITY WAVES

Arbey and Bataille [18] ascribed the narrowband contribution of the acoustic spectrum to the diffraction at the trailing edge of the pressure perturbations induced by growing instabilities, since they found by linear stability analysis that the unstable mode with the largest growth rate occurs at a frequency close to the broadband center frequency in the acoustic spectrum.

Thereafter, spatial linear stability analysis has been applied by a number of researchers [16, 44, 119, 125, 126, 129, 163] for identification of the most amplified modes and was already suggested by Tam [120]. In most cases this frequency is close to the dominant tone frequency, leading to the belief that one relates to the other [44, 129]. Moreover, Boutilier and Yarusevych [137] report that the maximum growth rate indicates the most amplified disturbances in the shear layer and thus to the roll-up frequency. This assumption has recently been challenged by Jones and Sandberg [125], who investigated the hydrodynamic instability based on a 2D DNS.

Based on the time-averaged velocity profiles (section 5.3.2), the growth rates for a range of frequencies have been obtained solving the Orr-Sommerfeld equation 5.1 [209]. The disturbances in the boundary layer can be described by a stream function $\Psi(y) =$

5

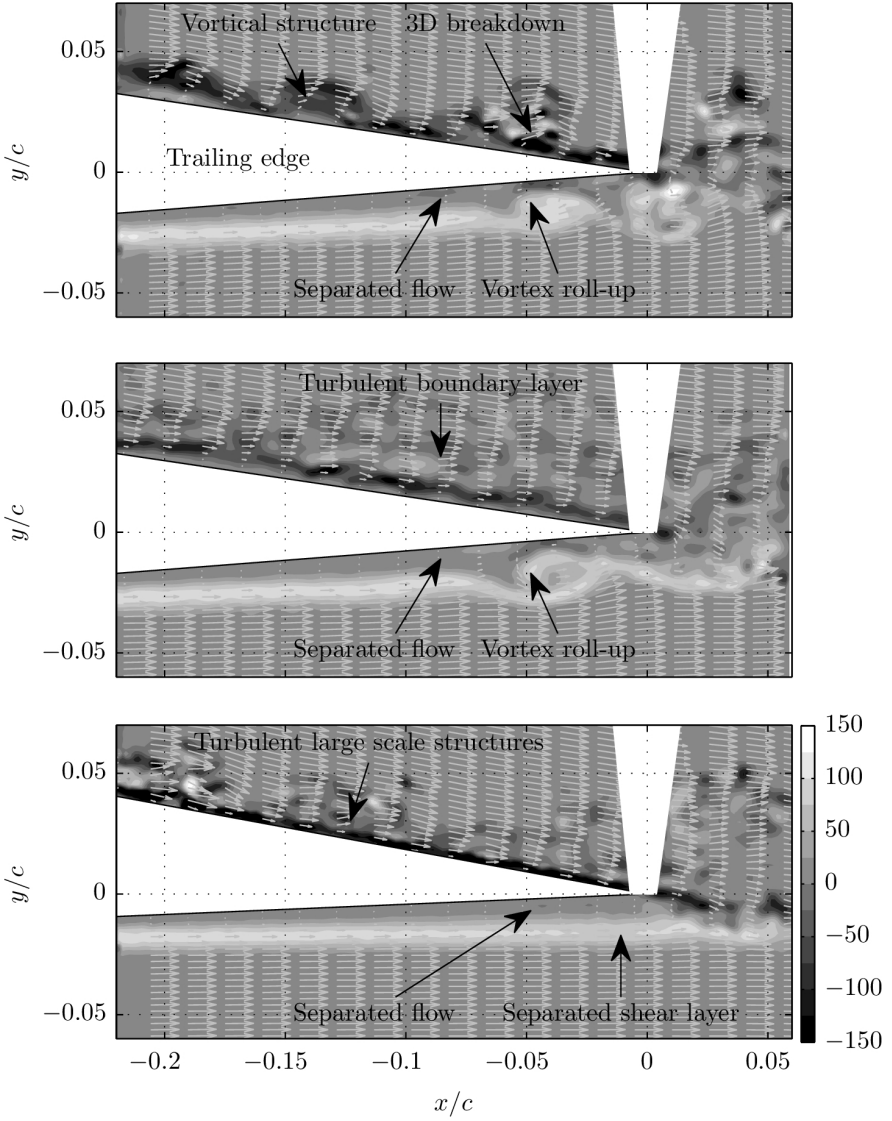


Figure 5.6: Contours of spanwise vorticity component $\omega_z c / u_\infty$ and velocity vectors for case 1 (top), case 2 (center), and case 3 (bottom).

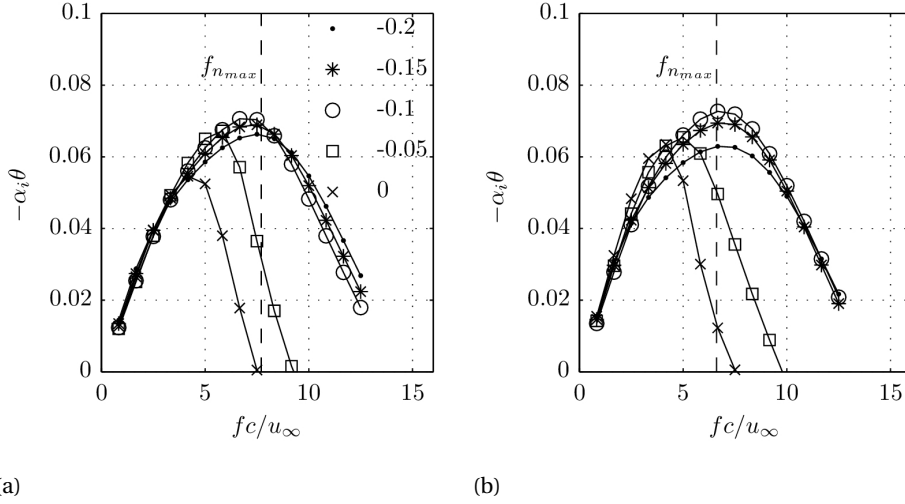


Figure 5.7: Spatial growth rate determined from linear stability analysis based on pressure side mean velocity profiles for case 1 (a) and case 2 (b) at different x_t/c (indicated in legend). Dashed line indicates the dominant tonal frequency observed in the acoustic spectra.

$\Phi(y) e^{i(\alpha x - \omega t)}$, where the eigenfunction $\Phi(y) = \alpha_0/2 + \sum_{n=1}^N \alpha_n T_n(y)$ can be expressed in a series of Chebychev polynomials $T_n(y)$ and $u(y)$ is the function describing the streamwise velocity component distribution as a function of the wall-normal coordinate:

$$\left[\left(\frac{d^2}{dy^2} - \alpha^2 \right)^2 - i Re(\alpha u - \omega) \left(\frac{d^2}{dy^2} - \alpha^2 \right) - \alpha u'' \right] \Phi = 0 \quad (5.1)$$

An estimation for $u(y)$ is based on the time average of the measured velocity fields. Fourfold integration over y with an appropriate choice of boundary conditions and expansion of the eigenfunction yields a system of equations that can be solved for α with given frequency ω and Reynolds number Re as a function of streamwise coordinate. Modes are unstable if the imaginary part of the wavenumber, referred to as growth rate, $Im\{\alpha\} < 0$.

For case 1, figure 5.7a shows the results for different locations along the chord on the pressure side. As observed in previous studies, the maxima indicate that the frequency associated to the largest growth rate is close to the frequency of the dominant tone (dashed line, $f_{n_{max}}^* = 7.7$).

For the case of forced transition on the suction side (case 2), figure 5.7b shows similar results. Away from the trailing edge ($x_t/c < -0.1$), the frequency associated to the maximum growth rate is close to that of the dominant tone observed in the spectrum of acoustic pressure (dashed line, $f_{n_{max}}^* = 6.6$). Closer to the trailing edge this frequency deviates more. It should be noted that the assumption of parallel flow and small disturbances with linear growth does not apply to the region where large vortices appear. This however is the case close to the trailing edge, in parts providing an explanation for the deviations.

It might be argued about the coupling of the flow and the importance of instabilities on the two sides of the airfoil. The answer for a symmetric profile such as the NACA 0012 depends on the angle of attack and Reynolds number under consideration as pointed out in chapter 4. At zero incidence and perfectly symmetric conditions, instabilities developed on the two sides of the airfoil must be equally significant for tonal noise generation. This is not the case with non-zero angle of attack, where the flow becomes asymmetric and separation tends to occur further upstream on the suction side than on the pressure side.

5.3.4. TEMPORAL EVOLUTION OF INSTABILITY WAVES

An effective way to visualize the properties of the vortical structures is by referring to the contours of the wall-normal velocity component, in this case approximated by the transverse velocity component. Figure 5.8a illustrates a sequence of contours for the airfoil at 2° incidence and 24m/s (case 1). The time separation between two consecutive images is about 167μs, equivalent to the measurement frequency of 6kHz. The spatial pattern of velocity fluctuations on the suction side predominantly convects downstream, while on the pressure side the amplitude grows over the aft 10mm and ultimately approaches that of the suction side near the trailing edge. The wavelength here is about half that of the suction side and the convective velocity is lower. The transverse velocity component shows only a small difference in phase at the trailing edge. As a result, the transverse fluctuations past the trailing edge appear further amplified. This constructive interference is not a stable situation and the phase difference varies over time, yielding the modulation effect of the dipolar emissions from the trailing edge as discussed by Desquesnes *et al.* [129].

When the transition on the suction side (figure 5.8b) is forced, the boundary layer does not undergo separation and develops along the airfoil in the turbulent regime. As a result, no coherently convecting vortical structures are visible. Due to the absence of these structures the relative phase of the velocity fluctuations on the two sides cannot be defined. This observation excludes that a periodic phase modulation of velocity fluctuations [129] can be the only reason for an amplitude modulation of the acoustic pressure, as also noted recently by Plogmann *et al.* [119]. Instead, a different explanation for the amplitude modulation must be sought for.

When the angle of attack is further increased to 4° (figure 5.8c) the separated flow on the suction side undergoes transition to turbulence before reaching the trailing edge. However, as commented on earlier, evidence of larger scale convecting turbulent bulges is present. On the pressure side the region of favorable pressure gradient moves further downstream and no convecting instabilities are visible upstream of the trailing edge. The overall comparison of the three cases presented here underlines the importance of pressure side boundary layer instabilities and their rapid growth for overall tonal noise emission at this Reynolds number.

The coherent structures visible in figure 5.8 convect downstream as demonstrated for case 1 by the space-time contours of the wall-normal velocity component sampled along a line parallel to the surface of the airfoil in figure 5.9. On the suction side, the amplitude of the signal remains comparatively constant over the measurement domain (figure 5.9a) when compared to the pressure side (figure 5.9b), but close to the trailing

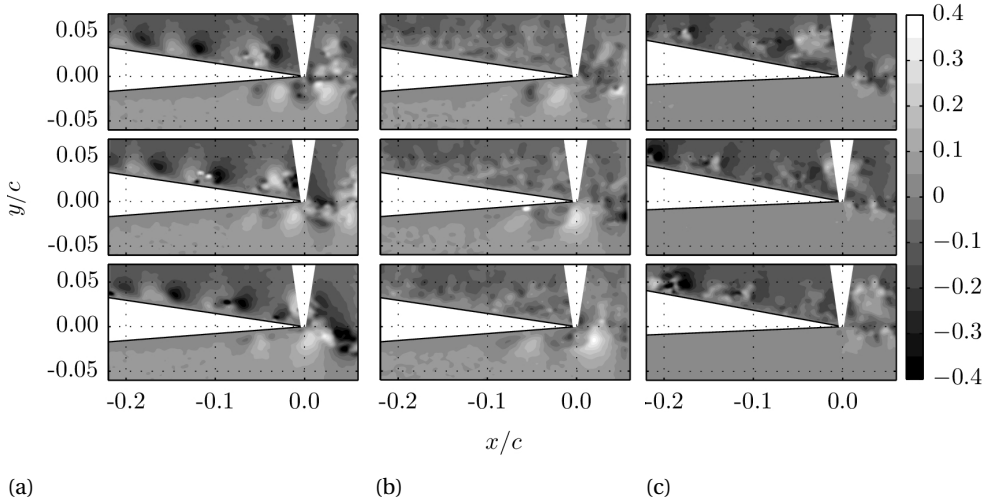


Figure 5.8: Sequences of three instantaneous velocity fields (6kHz): case 1 (a), case 2 with forced transition on the suction side (b), and case 3 (c). Contour levels for the transverse velocity component v/u_∞ are indicated.

edge the signal becomes less coherent due to breakdown of the large scale structures to turbulence. The convective velocity of the large scale structures is indicated by the slope of the dashed lines following the extrema in the diagram. On the suction side this convective velocity attains a value ($0.64u_\infty$, 15.4m/s) approximately twice that of the pressure side ($0.32u_\infty$, 7.7m/s). For free-stream velocities other than the one presented here, these ratios remain relatively constant. Case 2 shows a similar picture (figure 5.9c) and convective velocity on the pressure side ($0.31u_\infty$, 7.5m/s), but an earlier onset of transition.

Arcondoulis *et al.* [197] estimated the convective velocity by simultaneous hot-wire and acoustic measurements (NACA 0012, 67mm chord). Scanning the airfoil in increments of 1mm along the chord, the phase difference between the velocity and pressure signal provided an indication of the wavelength of the amplified instability waves or vortical structures and, therefore, an estimation of the convective velocity ($u_c = f\lambda$). In their experiments the hot-wire was positioned 1mm above the surface. Table 5.2 shows their results for comparison. At angle of attack 0° , their results showed an increase in convective velocity from $u_c/u_\infty = 0.32$ at $Re_c = 50,000$ to 0.42 at $Re_c = 150,000$. At angle of attack $\alpha_{eff} = 1.58$, Arcondoulis *et al.* [197] reported convection velocities between $u_c/u_\infty = 0.4$ and 0.46 on both suction and pressure side. However, the PIV results show a lower convective velocity at the center of the shear layer on the pressure side ($u_c/u_\infty \approx 0.35$). Although these values are similar ($u_c/u_\infty = 0.5 \pm 0.15$), the significant difference with respect to the present study may be attributed to the fixed wall-normal coordinate of the measurement location in both cases.

Figures 5.10a and 5.10b show a comparison of the auto-spectral density for the wall-normal velocity component at a point close to the trailing edge ($x_t = -1.1\text{mm}$, $x_n = 1.9\text{mm}$) for all three cases on the pressure and suction side, respectively. The average

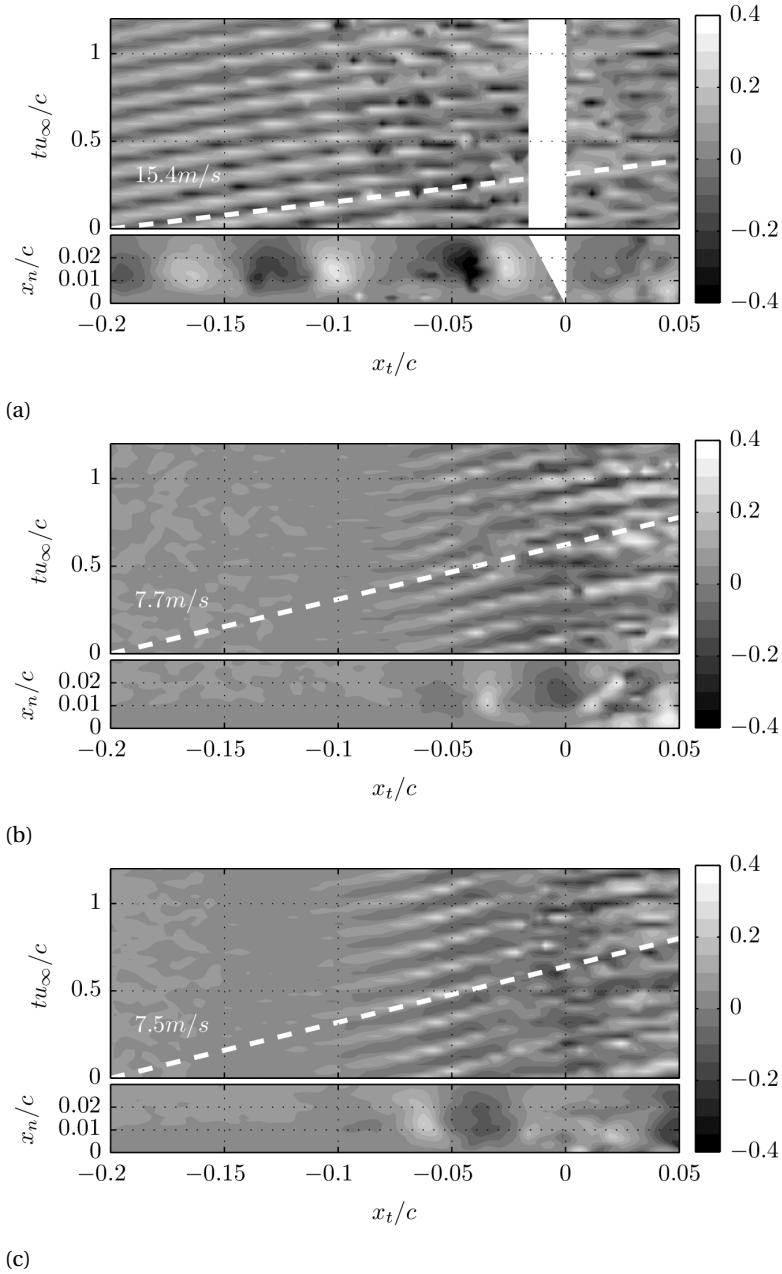


Figure 5.9: Contours of wall-normal velocity component on suction side (a) and pressure side (b) for case 1 and pressure side for case 2 (c) in space-time domain sampled along a line at $x_n = 1.3\text{ mm}$ (top) and in space at $t = 0$ (bottom). Dashed line indicates average convective velocity based on wavenumber-frequency analysis (figure 5.11).

Table 5.2: Convective disturbance velocity u_c/u_∞ . Experimental results of [197].

Re_c	0°	1.6° (1.58°)	
		pressure side	suction side
50,000	(0.32)	(0.46)	(0.46)
100,000	(0.38)	(0.46)	(0.46)
150,000	(0.42)	(0.40)	(0.40)

periodogram method [203] is computed to determine the auto-spectral density with segments of 512 samples and an overlap of 50%, where the Hamming window is applied to each segment [207]. This procedure results in a frequency resolution of 11.7Hz. For case 1, the most striking feature on the suction side (figure 5.10a) is the highest peak at $f_{n_{max}}^* = 7.7$ (1,865Hz) with symmetrically arranged side peaks. This will be elaborated on in the following section. On the pressure side (figure 5.10b), tones at similar frequencies and thus a side peak structure are present. When compared to the suction side, the peaks attain similar levels, while the broadband component is smaller by 2-5dB due to the earlier stage of transition. Forcing transition on the suction side of the airfoil (case 2) only leaves the indication of a peak at a lower frequency ($f_{n_{max}}^* = 6.6$, 1,585Hz). This matches the maximum peak on the pressure side, but the side peak structure is similar to case 1. This marked difference suggests that the remaining frequency peak on the suction side is due to the influence of the shedding from the pressure side. Note that the second largest peak close to $f^* = 12$ is due to aliasing. For the airfoil at larger angle of attack (case 3), the flow field at the sampling location on the pressure side does not show large amplitude fluctuations (figure 5.8c). The fluctuation levels are very low when compared to the fluctuations in the transitional cases (cases 1 and 2) and approach the experimental error associated to planar PIV. On the suction side indications of weaker peaks at frequencies similar to those of case 1 are found.

Representation of the wall-normal velocity fluctuations along a line parallel to the surface (figure 5.9) in the wavenumber-frequency space shows maxima (figure 5.11) at the same frequencies as the auto-spectral density (figure 5.10). The wavenumber-frequency decomposition is obtained following a similar approach as the average periodogram method for power spectra [203], but based on the two-dimensional Fourier transform over time and space with Hamming windows [207] applied over both dimensions. Energy content at positive wavenumbers indicates downstream propagating waves, while negative wavenumbers represent upstream propagation. For both suction (figure 5.11a) and pressure side (figure 5.11b) the maxima associated to the tonal noise are located in the first quadrant (positive wavenumbers). As anticipated, the convective velocity (grey solid line) on the suction side attains about twice the value on the pressure side under the assumption of constant convective velocity over the domain considered here. The wavelength relating this convective velocity to the tonal frequency indicates the length scale of the associated flow structures, in this case 8.3mm ($\lambda/c = 0.083$) and 4.1mm ($\lambda/c = 0.041$) on the suction and pressure side, respectively. These length scales match the wavelength of the wall-normal velocity fluctuations in figure 5.9 for case 1. Maxima in the fourth quadrant (negative wavenumbers) are due to aliasing and resemble spurious, upstream propagating waves.

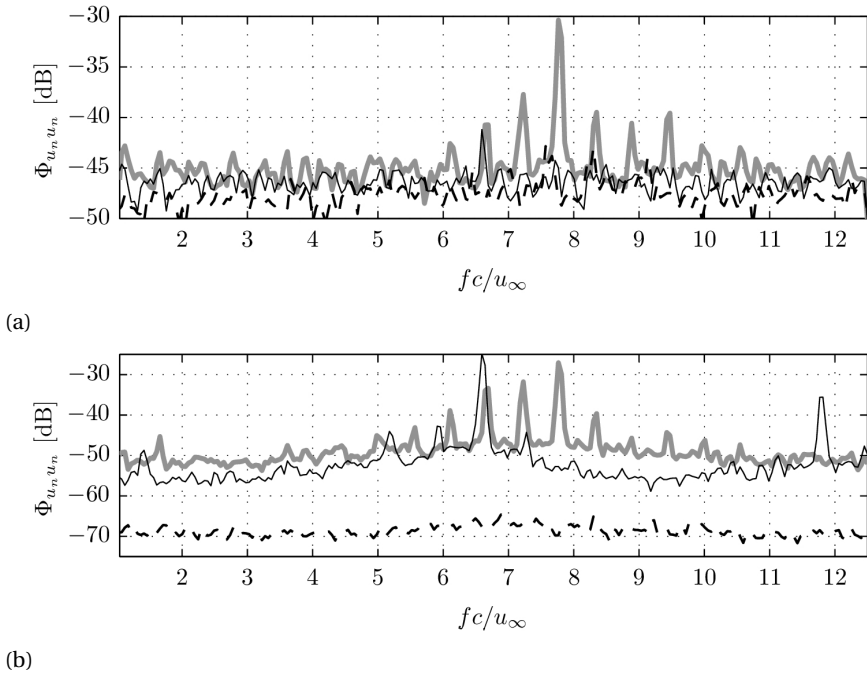
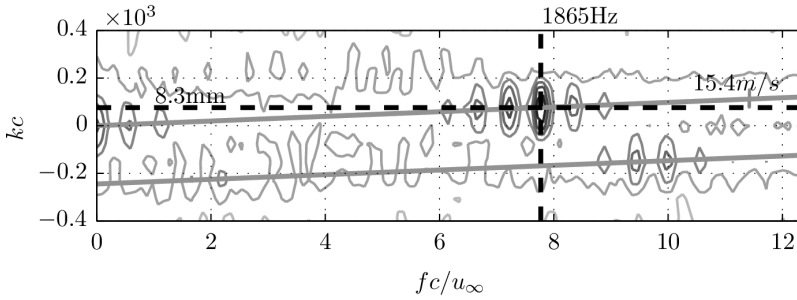
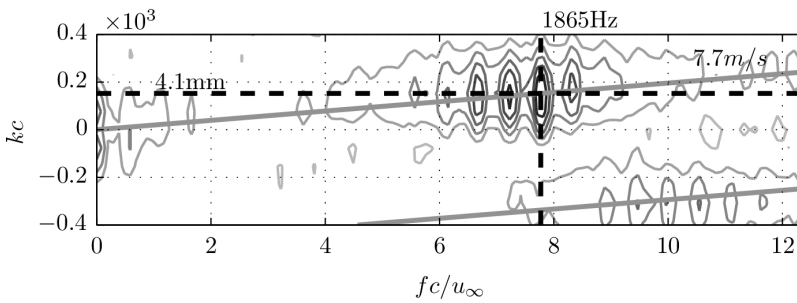


Figure 5.10: Spectra of wall-normal velocity component on suction side (a) and pressure side (b) at $x_t = -1.1\text{mm}$, $x_n = 1.9\text{mm}$ for case 1 (gray), case 2 (red), and case 3 (black dashed).



(a)



(b)

Figure 5.11: Wavenumber-frequency spectra of wall-normal velocity component (contour lines, grey to black) on suction side (a) and pressure side (b), $x_n = 1.2\text{mm}$, case 1. Further is indicated the convective velocity, dominant tone frequency and the corresponding wavelength.

5.3.5. PERIODIC AMPLITUDE MODULATION OF INSTABILITY WAVES

The presence of side peaks in the spectrum acoustic pressure for the case of forced transition (case 2) indicates that a variation in phase shift for the fluctuations on the two sides of the airfoil cannot be the only reason for periodic amplitude modulation. An alternative explanation is sought for by inspection of the spectral characteristics of the source field.

For the smooth airfoil case (case 1), the auto-spectral density of the acoustic pressure (figure 5.12, bottom) shows a primary tone at $f_{n_{max}}^* = 7.7$ (1,865Hz) and a frequency separation of $\Delta f^* = 0.56$ (135Hz) between the side tones. This structure implies a periodic amplitude modulation as cause for the occurrence of multiple tones (section 5.3.1). Comparing the velocity spectra (figure 5.12, top) to the acoustic spectrum similar features are found, including a slight asymmetry of the side peaks, which reflects a similar distribution of energy when compared to the acoustic spectrum. On the suction side the velocity spectra at all locations are very similar, confirming the convection of amplified instability waves or vortical structures without significant growth or decay. A different situation arises on the pressure side, where velocity fluctuations undergo amplification in the vicinity of the trailing edge. The similarity of these spectra suggests a similar modulation of the velocity amplitude in the source region, which in turn implies a modulation of the wall pressure. In view of diffraction theory [17], relating wall pressure fluctuations to the far-field acoustic pressure, a periodic amplitude modulation of the convecting, amplified instability waves and resulting vortical structures can provide an explanation for the appearance of multiple tones.

To investigate the time-dependent amplitude variation of the wall-normal velocity component at a point near the trailing edge, the signal is decomposed using wavelet analysis (appendix E). Figure 5.13 presents a time series of the wall-normal velocity component and its wavelet decomposition ($x_t/c = -0.05$, $x_n/c = 0.02$) for case 1 (24m/s, $\alpha = 2^\circ$) on the pressure side. The temporal diagram shows strong similarities to the acoustic pressure (figure 5.1) in terms of amplitude modulation and its period. The wavelet decomposition shows more clearly the energy contained at a crest centered at $f^* = 7.7$ (1,865Hz) with a modulation frequency of approximately $\Delta f^* = 0.56$ (135Hz). Closer examination reveals an incidentally occurring double peak structure at the same center frequency, which might be explained by a combination of higher harmonics of the base modulation frequency Δf^* . The presence of the almost periodic amplitude modulation strengthens the hypothesis regarding the important role of convecting instabilities on the noise generation process.

The velocity signal on the suction side does not follow the features of the acoustic signal as closely (figure 5.14). As became clear from the interpretation of the flow statistics in section 5.3.2, the mean square fluctuating velocity is slightly larger on the suction side and a similar but less coherent amplitude modulation is present in the time signal. The wavelet analysis confirms the presence of periodic amplitude modulation, but with the already mentioned double peak structure being far more pronounced on this side.

Considering contours of vorticity, there is a striking difference in the flow structure between the high and low amplitude phase of the noise generation process (figure 5.15). While in the high amplitude case distinct vortices are present in the boundary layer on both sides, in the situation with weak tones a separated shear layer is observed without

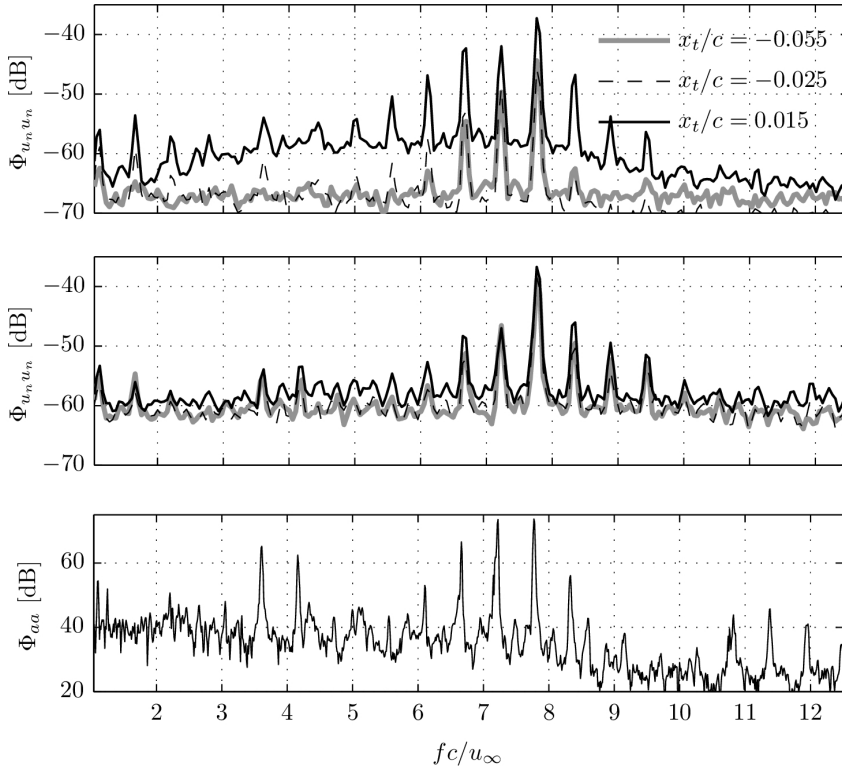


Figure 5.12: Spectra of wall-normal velocity component on pressure (top) and suction side (center) at $x_n/c = 0.038$ to spectrum of acoustic pressure (bottom), case 1.

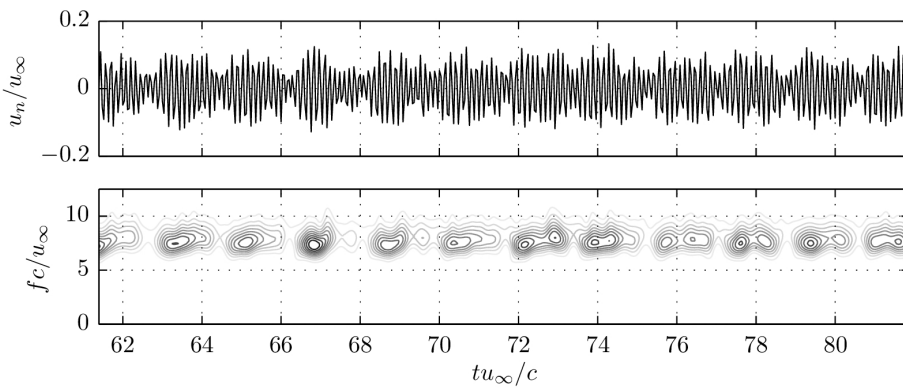


Figure 5.13: Time series (top) and normalized square magnitude of wavelet coefficients (bottom) of wall-normal velocity component on pressure side, $x_t/c = -0.05$, $x_n/c = 0.02$, case 1.

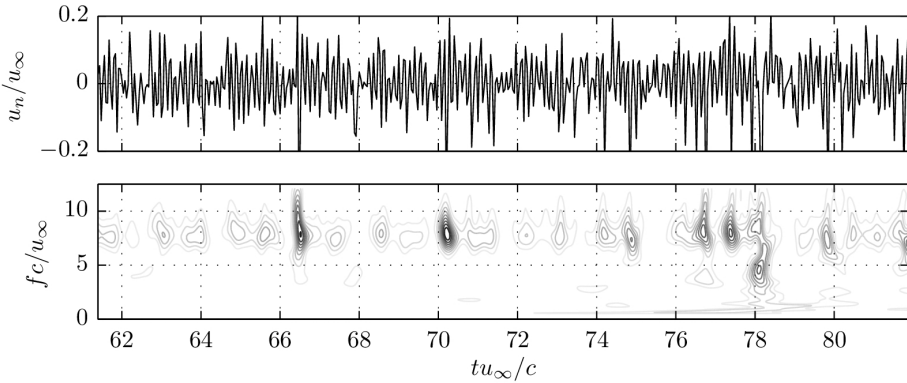


Figure 5.14: Time series (top) and normalised square magnitude of wavelet coefficients (bottom) of wall-normal velocity component on suction side, $x_t/c = -0.05$, $x_n/c = 0.02$, case 1.

5

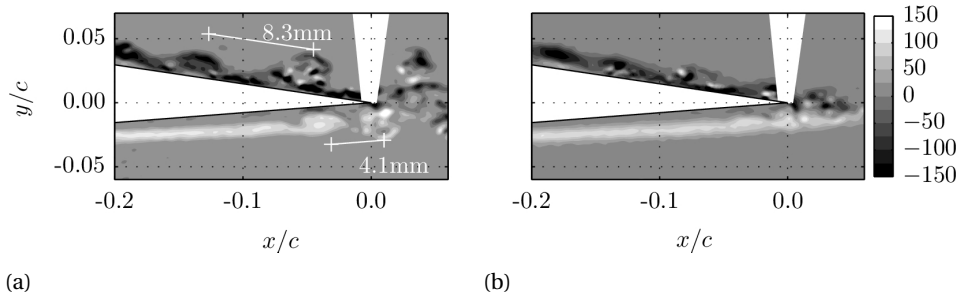


Figure 5.15: Contours of vorticity during the period of high amplitude (a) and low amplitude (b) noise emission, case 1. For the high amplitude case the characteristic wavelength determined based on the primary tone frequency and convective velocity (compare figure 5.11) is indicated.

large vortical structures on the pressure side.

Even with forced transition on the suction side multiple tones remain present (case 2). If the hypothesis holds true that this is due to a periodic amplitude modulation of the amplified instability waves, then this periodic amplitude modulation should also be present for the velocity components on the pressure side. The time series of the wall-normal velocity component confirms this amplitude modulation (figure 5.16), although less pronounced compared to the smooth airfoil configuration (case 1, figure 5.13). The wavelet decomposition reveals the amplitude modulation of a carrier signal at a slightly lower frequency $f_{n_{max}}^* = 6.6$ (1,585Hz) with a modulation frequency of approximately $\Delta f^* = 0.67$ (160Hz), as observed in the acoustic signal (figure 5.2).

In summary, the results indicate that in both cases examined here a substantial, periodic amplitude modulation of the velocity fluctuations on the pressure side is present, which introduces frequencies matching those of the tones. This periodic amplitude

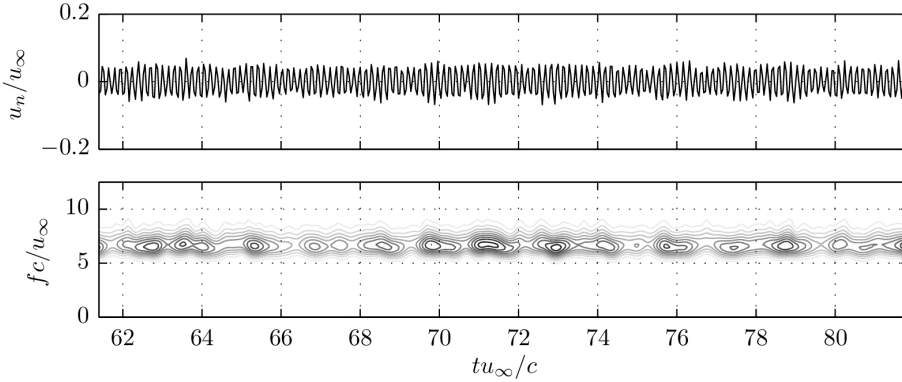


Figure 5.16: Time series (top) and normalized square magnitude of wavelet coefficients (bottom) of wall-normal velocity component on pressure side, $x_t/c = -0.05$, $x_n/c = 0.02$, case 2.

modulation of both the convecting hydrodynamic fluctuations and acoustic pressure leads to the tonal peaks present in the acoustic spectrum. Even in the case of a single-sided transitional boundary layer, the amplitude modulation induces a very similar effect and acoustic spectrum. However, a slight shift of the main frequency is observed which might be due to a change in the mean flow and therefore stability characteristics on the pressure side.

Figure 5.17a shows the cross-correlation coefficient of wall-normal velocity in the source field and acoustic pressure in the far-field (see appendix E). The data is shown for $\tau = 0$ (case 1), where the time shift has been corrected for the propagation time between the trailing edge and the location of the microphone. The result is similar to the one observed in the instantaneous velocity fields (figure 5.8a) with an alternating pattern of positive and negative values, also shown by Nakano *et al.* [47]. Since the acoustic pressure is dominated by the component at the primary tone frequency, the frequency at which the convecting vortical structures pass the trailing edge in the source field must be associated and equal to this primary tone frequency. It can be noted that the contours of correlation coefficient show comparatively high values even outside the domain typically defined as boundary layer. This result can be understood when considering the high circulation connected to strong vortices in the boundary layer, whose presence can also be felt in the free-stream, and the definition of the causality correlation, involving a normalization of the correlation function with the mean of the local velocity fluctuations (see equation E.11). The correlation coefficient is an indication for the ratio of the correlated part of the signal with respect to its overall energy and therefore its values in the free-stream can be high compared to the boundary layer, where the correlation coefficient can deteriorate due to 3D vortex breakdown and the presence of turbulence.

With a time shift $\tau = 1/(2\Delta f)$, equal to half the modulation period, the correlation coefficient shows the same structure and frequency but substantially lower magnitudes. This indicates that both quantities show a modulation at similar frequency,

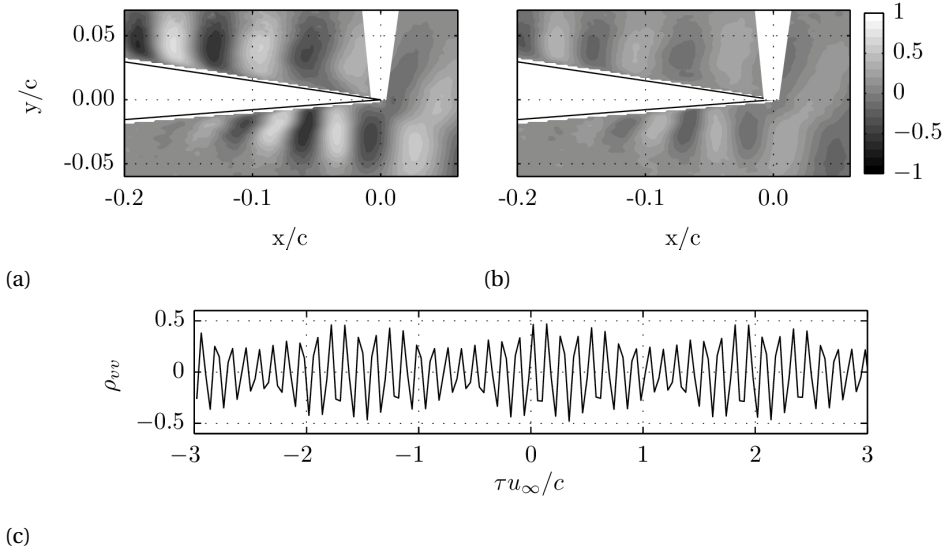


Figure 5.17: Contours of correlation coefficient (equation E.11) between transverse velocity component and acoustic pressure signal for $\tau = 0$ (a) and $\tau = 1/2\Delta f$ (b), case 1. Time series of correlation coefficient between transverse velocity sampled at point $x/c = -0.02$, $y/c = 0.04$ and acoustic pressure signal.

also confirmed by the periodically modulated nature of the correlation coefficient at point $x/c = -0.02$, $y/c = 0.04$ as a function of time separation τ (figure 5.17c). The periodic modulation of the correlation coefficient indicates that it is not only pure amplitude modulation of the convecting instabilities, but that other effects like breakdown to turbulence accentuate this effect, effectively reducing the correlation coefficient. Thus causality correlation supports the hypothesis that the periodically modulated convecting instabilities observed in the flow field on both sides of the airfoil upstream of the trailing edge are related to the noise generation.

Desquesnes *et al.* [129] suggested a phase modulation between the velocity fluctuations on the two sides of the airfoil, including a secondary feedback loop on the suction side, as possible cause and as a result a varying intensity of the scattered acoustic waves. The results of the transient analysis suggest (figure 5.13) a periodic amplitude modulation of the convecting, amplified instability waves as an alternative explanation. The periodic amplitude modulation of the acoustic waves explains the presence of multiple tones in the spectrum, but the question with respect to its physical cause and the frequency selection mechanism remains. In view of the feedback loop hypothesis, which has been proclaimed by a number of researchers in the past [18, 129] and recently demonstrated in an experimental study by Plogmann *et al.* [119], the mechanism behind the periodic amplitude modulation of the velocity fluctuations described in the present study might be as follows:

1. Wall pressure fluctuations in the boundary layer induced by the presence of vortical structures scatter at the trailing edge in the form of acoustic waves.

2. Acoustic waves propagate upstream and influence the initial amplitude of perturbations in the receptivity region, causing a periodic modulation.
3. Amplification of the modulated perturbations and convection of vortical structures towards the trailing edge.

5.4. CONCLUSION

Combined high-speed PIV and acoustic measurements have been performed to investigate the tonal noise generation and the underlying aeroacoustic source mechanism on a NACA 0012 airfoil at low Reynolds numbers.

For the cases presented here and with respect to the nature of tones in the spectrum, temporal and spectral analysis of the experimentally acquired data confirm the presence of a periodic amplitude modulation for the acoustic pressure, previously observed by Desquesnes *et al.* [129] in a DNS study. Wavelet decomposition of the signal reveals modulation frequencies of $m\Delta f$ with $m = 1, 2, \dots$, related to the occurrence of side peaks in the spectra with frequency separation $2m\Delta f$.

It is demonstrated by spatio-temporal analysis of the PIV data and causality correlation with the acoustic pressure that the dominant tone frequency $f_{n_{max}}$ is equal to the frequency at which vortical structures pass the trailing edge. Similar to the findings of previous studies, this frequency is found by linear stability analysis to be close to the frequency of the most amplified waves. For the parameter and boundary conditions of the present experiment and based on this direct observation and correlation.

Moreover, in the context of laminar boundary layer instability noise, periodic amplitude modulation is observed also for the velocity fluctuations near the trailing edge. This leads to the conclusion that multiple tones can arise not only from a phase modulation of fluctuations on pressure and suction side as proposed by Desquesnes *et al.* [129], but also from a periodic modulation of the fluctuation amplitude. The presence of a periodic amplitude modulation on the pressure side, even for the case of forced transition on the suction side, confirms that a two-sided feedback loop is not a necessary condition for the presence of multiple tones.

In view of feedback loop hypotheses that have been proclaimed by a number of researchers [18, 119, 129], it might be conjectured that through scattering of pressure fluctuations at the trailing edge, induced by periodically modulated convecting and amplified instabilities, acoustic waves propagate upstream, modulating the perturbations in the receptivity region and thereby sustaining a periodically modulating feedback loop as frequency selection mechanism for the discrete tones in the acoustic spectrum.

6

EFFECT OF TONAL NOISE ON SEPARATION BUBBLE DYNAMICS

*You jest about what you suppose to be a triviality,
in asking whether the hen came first from an egg
or the egg from a hen,
but the point should be regarded as one of importance -
one worthy of discussion and careful discussion at that.*

Macrobius Ambrosius Theodosius, *The Saturnalia* [210]

This chapter investigates the feedback effects due to tonal noise emission in a laminar separation bubble formed on the suction side of an airfoil in low Reynolds number flows. Simultaneous time-resolved, two-component PIV measurements, unsteady surface pressure and far-field acoustic pressure measurements were employed to characterize flow development and acoustic emissions.

Acoustic feedback between the trailing edge noise source and the upstream separation bubble narrows the frequency band of amplified disturbances, effectively locking onto a particular frequency. Tonal excitation further results in notable changes to the overall separation bubble characteristics. Roll-up vortices forming on the pressure side, where the bubble is located closer to the trailing edge, are shown to define the characteristic frequency of pressure fluctuations, thereby affecting the disturbance spectrum on the suction side. When the bubble on the pressure side is suppressed via boundary layer tripping, a weaker feedback effect is observed on the suction side.

Parts of this chapter have been published in the *Journal of Fluid Mechanics* (2015) [68].

6.1. INTRODUCTORY REMARKS

FORMATION of shear layer roll-up vortices can lead to undesirable unsteady loading and tonal noise emission. Strong tones are commonly observed on airfoils operating in the same domain of low Reynolds numbers where laminar separation bubbles are observed [18, 35, 50, 119]. In most cases, multiple tones at frequencies f_n , where the positive integer subscript n identifies the tone, have been observed [18, 117]. The dominating or primary tone, associated with the largest fluctuations in acoustic pressure, is identified by n_{max} at frequency $f_{n_{max}}$. These tones have been ascribed to the scattering of instability waves or resulting roll-up vortices, originating upstream and amplified through the separated shear layer, at the trailing edge [18]. Nash *et al.* [16] pointed out that a separation bubble or separated shear layer sufficiently close to the trailing edge is a necessary condition for the occurrence of tones. Due to the change in separation location, tonal noise emission at low Reynolds numbers is related to events on the suction side, while emission at high Reynolds numbers is dominated by pressure side events [50, 156].

The effect of tonal excitation may also be significant for experimental studies focused on separation bubble dynamics due to the well-documented sensitivity of laminar separation bubbles to test section environment [211, 212]. Previous works show variation of the shedding peak frequency f_{sh} from separation bubbles with u_∞^m , where the exponents m are in the range $m = 0.9$ to 1.92 [146]. This range remarkably resembles the variation of f_n and $f_{n_{max}}$ found in studies on laminar boundary layer instability noise discussed above. Several studies that investigated flow control over airfoils at low Reynolds numbers with acoustic excitation suggest that acoustic forcing can produce significant changes in separated shear layer development, specifically on the suction side [213–216]. Thus, it is possible that tonal emissions can have a notable upstream effect on flow development on the suction side of an airfoil in low Reynolds number flows, which may lead to substantial changes in separation bubble dynamics and, consequently, airfoil performance.

This chapter investigates the upstream influence of tonal noise, generated by the scattering of vortical structures at the trailing edge, on the laminar separation bubble development on the suction side of an airfoil. By systematically altering the characteristics of trailing edge noise emission, a significant upstream effect on flow development is observed for a range of low Reynolds numbers. An assessment of this effect is carried out using a combination of time-resolved PIV, unsteady surface pressure measurements, and far-field acoustic measurements.

6.2. DESCRIPTION OF EXPERIMENTS

Experiments were performed at Delft University of Technology in the low-speed vertical wind tunnel facility (V-Tunnel). This closed-loop wind tunnel has an open, circular test section 0.6m in diameter. The operating velocity range is between 5 and 45m/s. The free-stream velocity was set using a Pitot-static tube installed in the test section, with the associated uncertainty estimated to be less than 2%.

A NACA 0012 airfoil model is manufactured from acrylic glass and has a chord length of $c = 200\text{mm}$. The airfoil was installed approximately 0.15m downstream of the test

section nozzle (figure 6.1) between two circular end plates spaced by two chord lengths, complying with the recommendations for end-plate spacing of Boutillier and Yarusevych [217]. The model was positioned at geometric angle of attack $\alpha = 2^\circ$ with the associated uncertainty of approximately 0.1° . For a lift-generating airfoil placed in an open jet of given width H , the effective angle of attack α_{eff} is generally lower than the geometric angle of attack α due to deflection of the jet flow [204]. For the flow conditions investigated here, the effective angle of attack has been estimated to be $\alpha_{eff} \approx 1.2^\circ$.

The model was equipped with five microphones installed below pinholes (0.2mm diameter) on the suction side. The embedded microphones were used to characterize the development of dominant disturbances in the separated shear layer, as discussed by Gerakopoulos and Yarusevych [191]. The output of the microphones was equalized using an external acoustic reference signal. To characterize trailing edge emissions, a LinearX M51 microphone was positioned outside the flow in the mid-span plane at a distance of approximately 1m from the trailing edge. The microphone was calibrated using a GRAS piston phone. All acoustic signals were sampled at 100kHz and low-pass filtered at 20kHz. Acoustic data were acquired simultaneously with PIV measurements to enable comparative analysis. Separately, longer duration signals were recorded for spectral analysis. The auto-spectral density for microphone signals was computed using an ensemble averaging method [203], with a 50% overlap of consecutive signal windows. The resulting frequency resolution of the microphone spectra is approximately $\delta_f = 6\text{Hz}$, sufficient for resolving the dominant instability frequencies in the flow, which vary between approximately 100Hz and 1.5kHz.

In addition, dedicated acoustic measurements were performed in a separate experiment. The microphone was positioned in the same location as in the PIV experiments. Acoustic measurements were performed for a range of velocities between 5 and 35m/s in steps of 1m/s. For each free-stream velocity considered, data were acquired at an acquisition frequency of 51.2kHz for a measurement period of 30s. Spectral analysis resulted in a frequency resolution of $\delta_f = 10\text{Hz}$. In the discussion of the results, the auto-spectral density of acoustic pressure is denoted by $\Phi_{aa}(f)$ and the narrowband sound pressure levels (SPL) are denoted by $\delta_f \Phi_{aa}(f)$ and presented in dB (reference $20\mu\text{Pa}$).

Time-resolved, two-component PIV was employed to characterize spatio-temporal flow development. The flow was seeded with water-glycol-based fog particles with a mean diameter of approximately $1\mu\text{m}$. The particles were illuminated using a Quantronix *Darwin Duo* Nd:YLF laser, with a laser sheet positioned such that flow development over the suction side and around the trailing edge could be investigated (figure 6.1). Two high-speed cameras, a LaVision *Imager Pro* HS (4Mpx, $11\mu\text{m}$ pixel pitch) and a Photron *FastCam* SA 1.1 (1Mpx, $20\mu\text{m}$ pixel pitch) were used to capture double-frame particle images. The synchronization of image acquisition and flow illumination was performed using a LaVision *Highspeed Controller* and *DaVis* 8 software. The same software was employed for image analysis. The *Imager Pro* camera was equipped with a Nikon *Micro-Nikkor* 150mm lens and was used for imaging the boundary layer upstream of the trailing edge. It captured a field of view of $90 \times 19\text{mm}$ ($2,016 \times 428\text{px}$), covering the flow region of interest over the suction side. Double-frame image sequences were captured at 3kHz, with 6,000 image pairs acquired per sequence. The second camera, equipped with Nikon *Micro-Nikkor* 200mm lens, was used to capture a field of view of $23 \times 23\text{mm}$

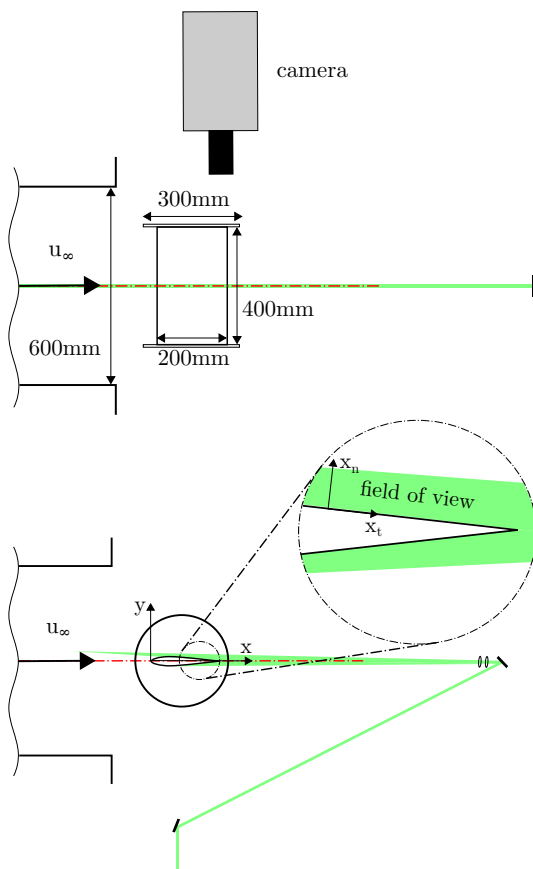


Figure 6.1: Experimental set-up for PIV measurements. Some elements are not drawn to scale. Note: the wall tangential (x_t) and normal (x_n) coordinates are defined in a surface attached coordinate system, and the origin for both the x and x_t coordinates is located at the leading edge.

Table 6.1: Parameters for PIV experiments.

Parameter	Symbol	Boundary layer	Trailing edge
Camera		Imager Pro HS	FastCam SA 1.1
Lens focal length		150mm	200mm
Magnification	M	0.25	0.89
Field of view	FOV	$90 \times 19\text{mm}^2$	$23 \times 23\text{mm}^2$
Acquisition frequency	f_{acq}	3kHz	1.5kHz
Free-stream displacement	Δx	15px	15px
		0.7mm	0.34mm
Number of samples	N	6,000	2,728
Interrogation window size		$16 \times 16\text{px}$	$16 \times 16\text{px}$
		$0.72 \times 0.72\text{mm}^2$	$0.36 \times 0.36\text{mm}^2$
Vector spacing		4px	4px
		0.18mm	0.09mm

($1,024 \times 1,024\text{px}$) around the trailing edge. In this arrangement, the sequences of double-frame images were acquired at 1.5kHz, with 2,728 image pairs per sequence. In both experiments, the laser pulse separation was adjusted to achieve displacements of approximately 15px in the image plane. The position of the focus plane was adjusted to obtain particle images of approximately 2 – 3px and avoid peak locking effects.

An iterative multi-grid, multi-pass technique with window deformation was used for image processing. For the final pass, a $16 \times 16\text{px}$ window and overlap factor of 75% were used. A Gaussian window weighting, with an aspect ratio of 2:1, was applied during the correlation process to reduce processing errors arising due to the local surface curvature and/or velocity gradients [208]. The resulting vector pitch was approximately 0.18mm and 0.09mm for the first and second camera arrangement, respectively. Based on a typical random error of 0.1px reported for two-component, planar PIV [167], the random error in velocity measurements is estimated to be less than 0.7% of the edge velocity, consistent with statistical variations in velocity data measured within the outer flow. Table 6.1 provides an overview of the parameters for the PIV experiments.

6.3. RESULTS AND DISCUSSION

6.3.1. OVERVIEW OF FLOW DEVELOPMENT AND TONE GENERATION

All results presented in this section pertain to a range of Reynolds numbers $0.65 \times 10^5 \leq \text{Re}_c \leq 4.5 \times 10^5$ and a fixed angle of attack $\alpha = 2^\circ$. These conditions were selected as they produce distinct tonal noise emissions in presence of laminar boundary layer separation, typical of airfoil operation in low Reynolds number flows. To illustrate key elements of flow development and the associated tonal noise production, figure 6.2 depicts a sequence of instantaneous vorticity fields around the trailing edge for $\text{Re}_c = 1.3 \times 10^5$. The coordinate system is chosen such that the x -axis aligns with the chord line of the airfoil and is measured from the leading edge, while the y -axis has the origin at the trailing edge (figure 6.1). The results show separated shear layers rolling up into vortices on both the suction and pressure side of the airfoil. On the suction side, the roll-up occurs

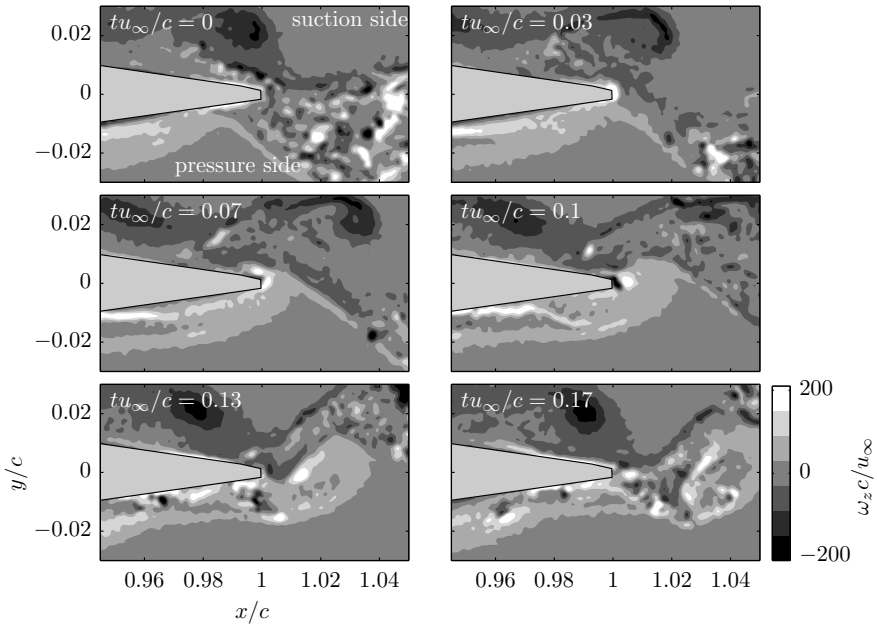


Figure 6.2: Spanwise vorticity field ω_z around the trailing edge for $Re_c = 1.3 \times 10^5$.

in the aft portion of a separation bubble upstream of the field of view. The roll-up on the pressure side occurs further downstream, just upstream of the trailing edge. The sequence shows approximately one shedding cycle, with shedding periods on the suction and pressure side closely matching. The depicted unsteady flow development around the trailing edge is accompanied by pronounced tonal noise emissions.

Figure 6.3 shows such tonal noise in the spectrum of acoustic pressure, namely a strong tone at $f_{n_{max}} = 295\text{Hz}$ ($f_{n_{max}} c/u_\infty = 5.9$) and its upper harmonics. Also presented in figure 6.3 are the spectra of vertical velocity fluctuations measured in separated shear layers on the suction and pressure sides, and the spectrum of surface pressure fluctuations from an embedded microphone on the suction side, with all the corresponding measurements acquired at the locations where shear layer roll-up vortices are observed. Comparison shows that velocity fluctuations on both sides of the airfoil are associated with the roll-up vortices, which occur at the same frequency as the tonal noise. This implies that tonal noise is produced due to the passage of the roll-up vortices over the trailing edge, agreeing with the results of Pröbsting *et al.* [50]. Moreover, the results suggest that vortices originating from the suction and pressure side lock on the same frequency. Considering notable differences in flow development on the two sides of the airfoil, such close agreement between the dominant frequencies indicates a likely upstream influence of the tonal noise on the separated shear layer development.

To investigate the nature of tonal emissions and their interaction with separated shear layer development, measurements were conducted in the following four configurations:

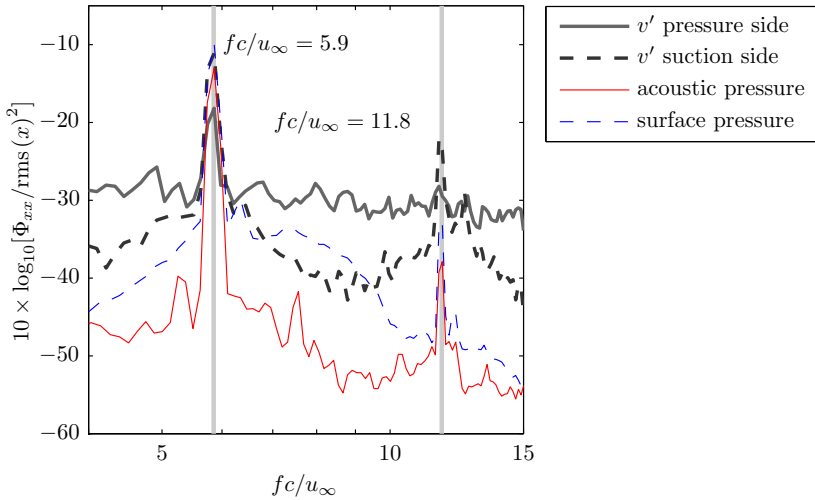


Figure 6.3: Comparison of auto-spectral density of transverse velocity fluctuations v' on pressure and suction side with acoustic and surface pressure fluctuations, $Re_c = 1.3 \times 10^5$.

- i) *smooth airfoil*
- ii) *tripped boundary layer on the pressure side*
- iii) *tripped boundary layer on the suction side*
- iv) *tripped boundary layer on both sides*

For boundary layer tripping, a 1cm wide strip of randomly distributed roughness elements (carborundum, nominal grain size 0.58mm) was placed upstream of the location of laminar boundary layer separation. The effectiveness of the trip was assessed via microphone measurements and PIV measurements around the trailing edge. Tripping the boundary layer on the pressure side (case ii) eliminates laminar separation and, consequently, shear layer roll-up on this side. Vice versa, tripping the boundary layer on the suction side (case iii) eliminates shear layer roll-up on that side. A similar methodology has been used to control boundary layer development in previous experimental studies [35, 50, 119, 156].

Figure 6.4 shows the variation of the spectral energy content of acoustic pressure fluctuations with free-stream velocity for the four configurations studied. For the smooth airfoil (case i), multiple tones (distinguished by index n) with continuously increasing frequency f_n are present. Over the entire range of velocities, sudden changes of the primary tone frequency $f_{n_{max}}$ (change in n_{max}) occur, and a *ladder* structure similar to that reported in previous studies on trailing edge noise emerges (e.g. Paterson *et al.* [35]).

In contrast, when the boundary layer on both sides of the airfoil is tripped, tonal noise is suppressed except for the free-stream velocities below approximately 7m/s, where

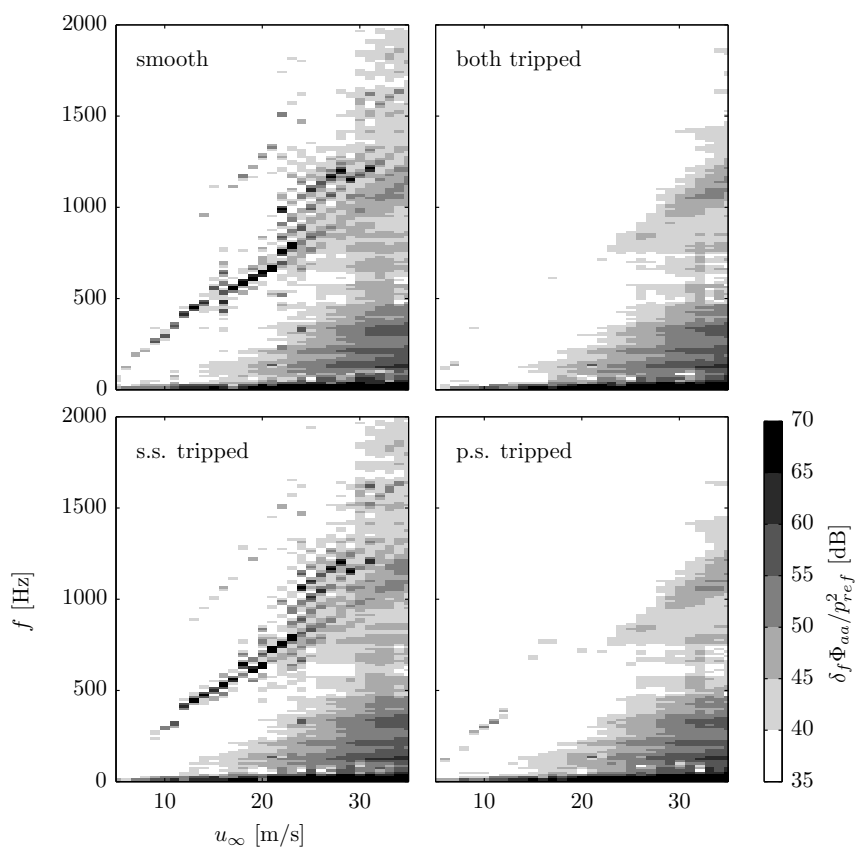


Figure 6.4: Narrowband Sound Pressure Level $\delta_f \Phi_{aa}$ in dB (reference pressure $20\mu\text{Pa}$) for airfoil in smooth and tripped configurations.

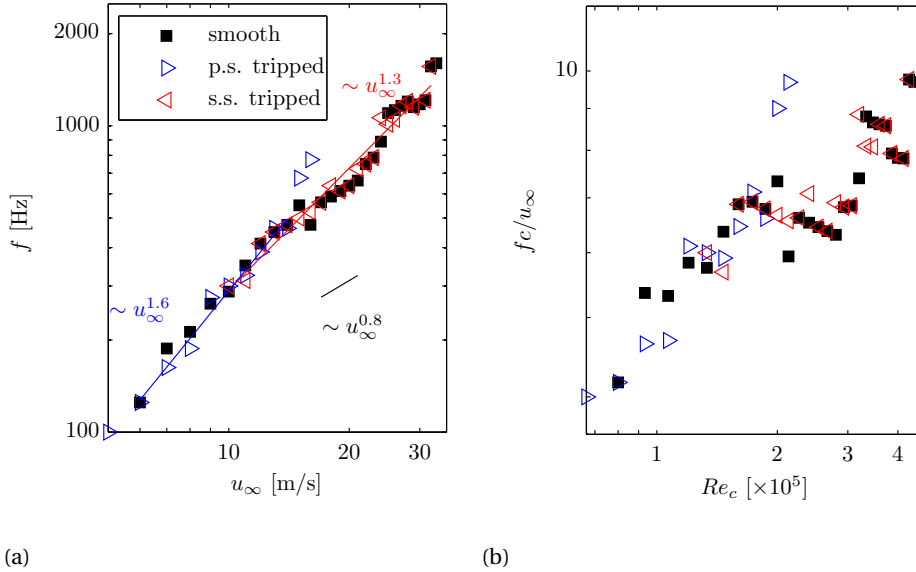


Figure 6.5: Variation of primary tone frequency $f_{n_{max}}$ with free-stream velocity (a) and non-dimensional representation (b).

the boundary layer trip eventually fails to suppress separation. A comparison of the results pertaining to the tripped pressure side (case ii) and tripped suction side (case iii) with those for the smooth airfoil (case i) suggests that the separated shear layer development on the pressure side dominates the overall tone generation, particularly at higher velocities. The onset of tonal noise generation on the pressure side (case iii) occurs at approximately 10m/s. The shedding of shear layer vortices on the suction side (case ii) can sustain tonal noise generation at speeds below approximately 15m/s and contributes to the overall emission produced on the smooth airfoil only within that velocity range. From their onset at 10m/s, shear layer vortices on the pressure side are the dominant contributors. These trends agree with those reported for acoustic measurements in an anechoic wind tunnel on a half-scale NACA 0012 model at the same angle of attack [52].

A comparison of the primary tone frequency variation for the configurations discussed is shown in figure 6.5a. At free-stream velocities below 10m/s, $f_{n_{max}}$ for the smooth airfoil (case i) agrees with the one for the tripped pressure side (case ii) and thus is probably due to suction side events. At these velocities, the primary tone frequency follows a power law relation $f_{n_{max}} \sim u_\infty^{1.6}$. For $u_\infty \geq 10$ m/s, the close agreement between $f_{n_{max}}$ for the smooth airfoil (case i) and that for the tripped suction side (case iii) demonstrates that the tone generation is governed by the development of separated shear layer vortices on the pressure side. Within this range, the trend of the primary tone frequency follows a power law relation $f_{n_{max}} \sim u_\infty^{1.3}$ for cases (i) and (iii). A significant change is encountered when the pressure side is tripped for $u_\infty > 10$ m/s (case ii). In this case, $f_{n_{max}}$ changes significantly to higher frequency. For the smooth airfoil (case i), the overall trend

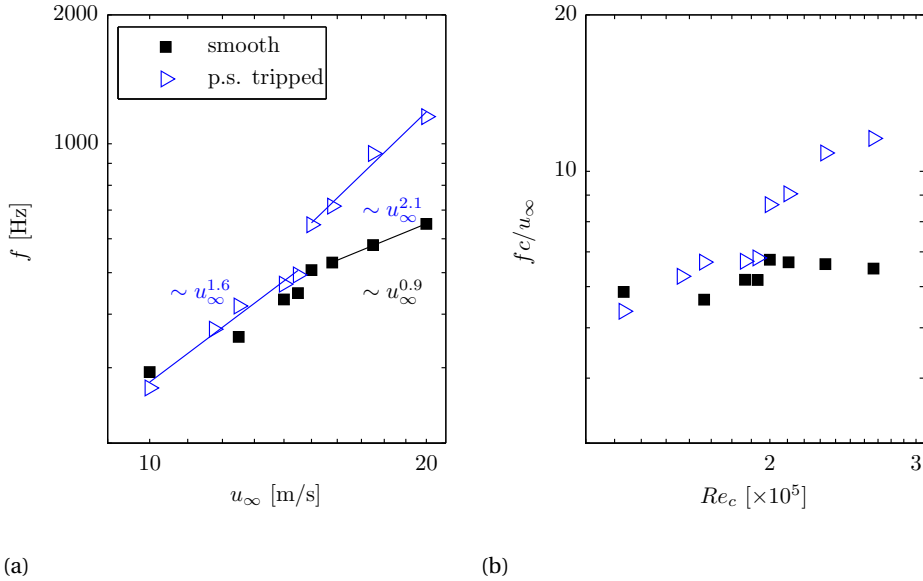


Figure 6.6: Variation of shedding frequency f_{sh} on the suction side with free-stream velocity (a) and non-dimensional representation (b).

6

of the primary tone frequency variation with velocity is close to $f_{n_{max}} \sim u_\infty^{1.5}$. In contrast, the variation of the frequency of the individual tones f_n follows a power law relation with a different exponent, close to $f_n \sim u_\infty^{0.8}$ (figure 6.5a). Both trends have been reported in and are in agreement with previous studies (e.g. Arbey and Bataille [18], Paterson *et al.* [35], Chong and Joseph [117]).

The results presented thus far illustrate that tonal noise emissions are due to the periodic shedding of shear layer roll-up vortices over the trailing edge. When present, such shedding on the pressure side dominates tonal noise generation at higher Reynolds numbers. Under such conditions, boundary layer separation on the pressure side occurs closer to the trailing edge compared to that on the suction side. As a result, shear layer vortices forming on the pressure side maintain higher strength and correlation across the span as they pass over the trailing edge [52], a condition for which classical edge noise theory predicts stronger noise emission [17]. At low velocity, when shear layer separation on the pressure side does not occur upstream of the trailing edge, weaker tonal emissions can also be produced by roll-up vortices forming on the suction side. It is of interest to examine how the tonal noise emissions affect the frequency of the roll-up vortices on the suction side. To achieve this, embedded microphone measurements were conducted on a smooth airfoil (case i) and with tripped pressure side (case ii). The measured surface pressure fluctuations were verified to reflect the passage of shear layer vortices using PIV data. Similar embedded arrays were used to study unsteady separated shear layer development in previous studies [137, 191].

Figure 6.6 presents the shedding frequency f_{sh} of shear layer vortices on the suc-

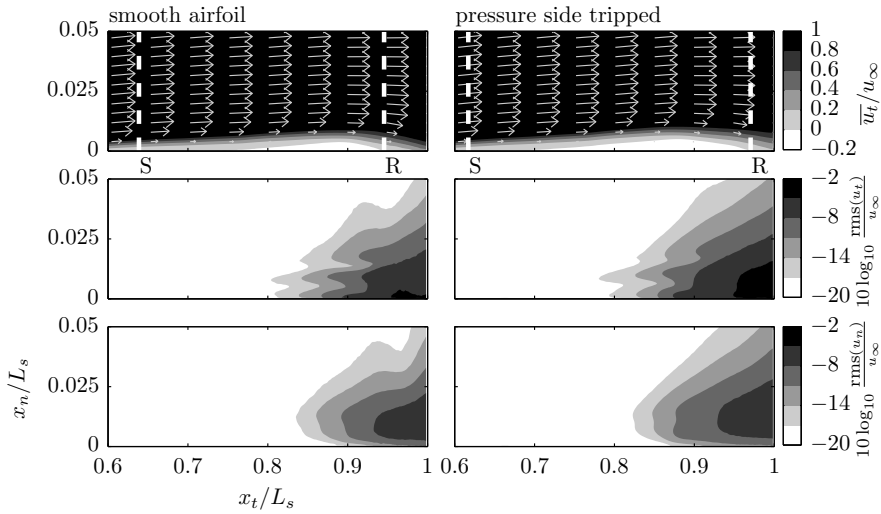
tion side for cases (i) and (ii). The frequency was identified as that corresponding to the maximum auto-spectral density of the unsteady surface pressure, which was obtained through the suction side embedded microphone measurements. Comparing the data for the smooth airfoil (case i) and that with tripped pressure side (case ii) shows notable differences in f_{sh} , which implies that strong tonal emissions present for case (i) affect the dominant separated shear layer frequency on the suction side via a global instability mechanism [15, 125]. For the smooth airfoil (case i), the shedding frequency f_{sh} on the suction side follows a similar ladder-type structure and closely matches the corresponding tonal frequency $f_{n_{max}}$ (figure 6.5). With the pressure side tripped (case ii), the shedding frequency f_{sh} also follows a power law relation, but with an exponent significantly higher than that for the smooth airfoil (case i, figure 6.6), and no particular ladder structure can be identified. For $Re_c < 2 \times 10^5$, the shedding frequency follows $f_{sh} \sim u_\infty^{1.6}$, similar to the trend of the primary tone frequency $f_{n_{max}}$ due to suction side shedding at lower Reynolds number (figure 6.6). The trend changes markedly at about $Re_c = 2 \times 10^5$, where the shedding frequency experiences a large increase to values $f_{sh} c / u_\infty \approx 10$.

The sudden change in the shear layer shedding frequency observed in the present study is attributed to changes in the separated shear layer development on the suction side due to acoustic excitation that can be explained as follows. As expected from previous investigations on low Reynolds number airfoils [134, 137], the separation point and roll-up location move upstream with increasing Reynolds number. Thus, at lower Reynolds numbers, coherent vortices periodically pass the trailing edge on the suction side, generating tones. The scattered acoustic pressure waves propagate upstream and excite instability waves, which are amplified in the separated shear layer and lead to vortex shedding. Thus, a feedback loop is established, which influences the frequency selection mechanism [18] and can be viewed as a global instability [15, 125]. Increasing the Reynolds number eventually disrupts this feedback loop due to a loss in coherence of the convecting vortical structures and lower amplitude of the scattered acoustic waves. As a result, a sudden change in shedding frequency is observed, and the frequency selection follows that expected for the natural transition process in the separated shear layer, which can be viewed as a local convective instability mechanism.

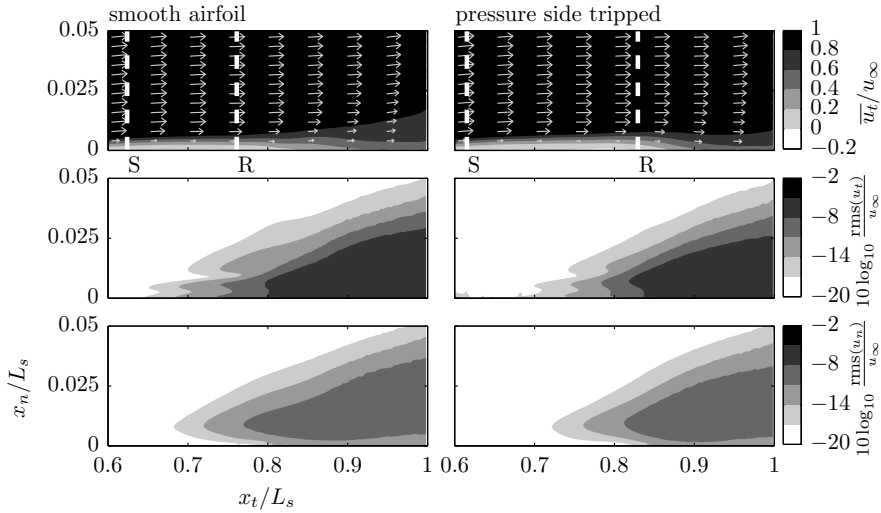
6.3.2. EFFECT OF ACOUSTIC EXCITATION ON SEPARATION BUBBLE

Following up on the analysis of the results in figure 6.3, it is of interest to examine in more detail the upstream effect of tonal noise on the separation bubble development on the suction side. This is achieved by a comparative analysis of PIV measurements pertaining to the smooth airfoil (case i) and tripped pressure side (case ii) configurations at two different Reynolds numbers, $Re_c = 1.3 \times 10^5$ and $Re_c = 2.05 \times 10^5$. The results in this section are presented in a surface-attached, curvilinear coordinate system. Here x_t denotes the wall-tangential and x_n the wall-normal coordinate direction, while the arc length L_s over one side of the airfoil is used for normalization. The origin is located at the leading edge.

The time-averaged wall-tangential velocity component $\overline{u_t}$ and root-mean-square (rms) fluctuations of both velocity components, $\text{rms}(u_t)$ and $\text{rms}(u_n)$, are compared in figure 6.7. Figures 6.7a and 6.7b show the results for $Re_c = 1.3 \times 10^5$ and $Re_c = 2.05 \times 10^5$, respectively. The data for the smooth airfoil (case i) in the left column are contrasted with



(a) Smooth airfoil (left) and with pressure side tripped (right). $Re_c = 1.3 \times 10^5$



(b) Smooth airfoil (left) and with pressure side tripped (right). $Re_c = 2.05 \times 10^5$

Figure 6.7: Time-averaged \overline{u}_t and root-mean-square of velocity components $\text{rms}(u_t)$, $\text{rms}(u_n)$ on the suction side. Smooth airfoil (left) and with pressure side tripped (right).

those for the pressure side tripped case (case ii) in the right column. Additionally, the estimated separation (S) and reattachment point (R) locations are indicated. For the same cases, figure 6.8 shows the time-averaged boundary layer parameters: boundary layer thickness δ_{99} based on 99% of the edge velocity u_e , displacement thickness δ^* , and the pressure coefficient based on the edge velocity velocity $c_p = (p_e - p_\infty)/q_\infty$, where $p_e = p_\infty - 1/2\rho u_e^2$, $q_\infty = 1/2\rho u_\infty^2$, and p_∞ is the static pressure in the free-stream.

At the lower Reynolds number (figure 6.7a), where tonal emissions are produced in both configurations, the position of the separation bubble and its extent do not change significantly between the two cases. The boundary layer separates at $x_t/L_s = 0.64$ (case i) and 0.62 (case ii). Reattachment occurs just upstream of the trailing edge at $x_r/L_s = 0.95$ (case i) and 0.97 (case ii). In agreement with these results, Arcondoulis *et al.* [197] found separation to occur at 65% chord for a NACA 0012 airfoil and similar flow conditions ($\alpha_{eff} = 1.58^\circ$, $Re_c = 1.5 \times 10^5$). Similarly to the separation bubble location, the pressure coefficient (figure 6.8a) is virtually identical over approximately 80% of the separation bubble length. These similarities indicate that acoustic excitation has a similar effect for both cases on the locations of separation and transition. A steep increase in velocity fluctuations is found near $x_t/L_s = 0.85$. This point is located at about two-thirds of the path length between separation and reattachment. Minor changes in the growth of disturbance amplitude can be deduced from the root-mean-square fluctuations and are attributed primarily to the slight reduction in the sound pressure level of acoustic excitation for case (ii) (figure 6.4).

In contrast, significant changes are observed in the results for the higher Reynolds number case, $Re_c = 2.05 \times 10^5$ (figure 6.7b). The boundary layer separates near $x_t/L_s = 0.62$ (cases i and ii), but reattaches at $x_r/L_s = 0.76$ for the smooth case (case i) and significantly further downstream ($x_r/L_s = 0.83$) if the pressure side is tripped (case ii). Thus, with respect to the lower Reynolds number case (figure 6.7a), the overall separation bubble shrinks significantly, a trend that is reported in previous studies [137]. The extent of the separation bubble increases significantly with the pressure side tripped (case ii). This is attributed to an earlier onset of transition, marked by a steep increase of the amplitude of velocity fluctuations near $x_t/L_s = 0.7$ (case i) and $x_t/L_s = 0.75$ (case ii), which indicates that transition occurs further downstream with the pressure side tripped (case ii). Figure 6.4 showed that tripping the pressure side boundary layer (case ii) effectively eliminates strong tonal noise at this Reynolds number ($Re_c = 2.05 \times 10^5$). The absence of acoustic excitation delays transition and consequently reattachment in case (ii) (figure 6.7b), causing the significant increase in the shedding frequency f_{sh} of the roll-up vortices on the suction side (figure 6.6). The difference in the structure of the separation bubble is supported by the boundary layer parameters presented in figure 6.8b, which shows that pressure recovery is delayed and the pressure gradient remains moderate farther downstream with the tripping device applied (case ii). In summary, the results illustrate that the acoustic excitation induces notable changes to the time-averaged parameters of the separation bubble. The effect of the natural tonal excitation observed here is similar to that seen in experiments involving control of flow development on an airfoil in low Reynolds number flows with acoustic forcing [216].

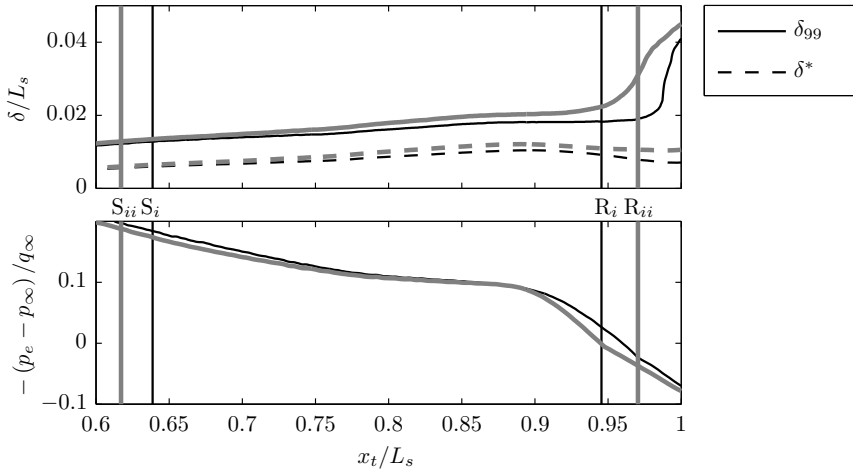
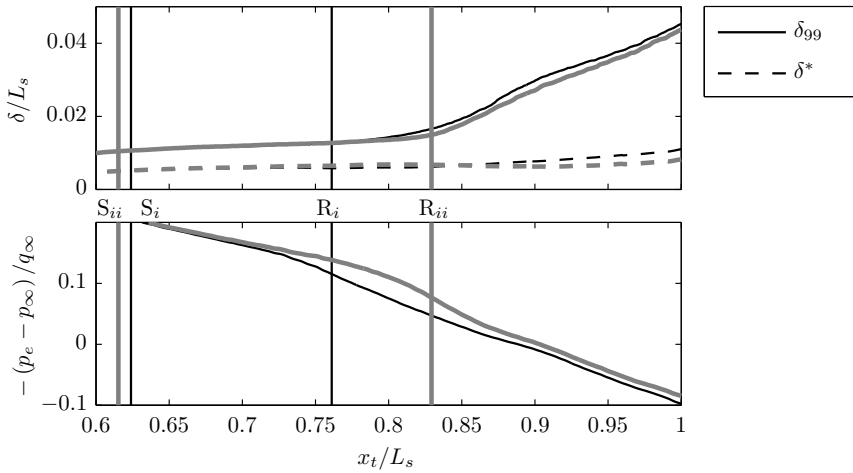
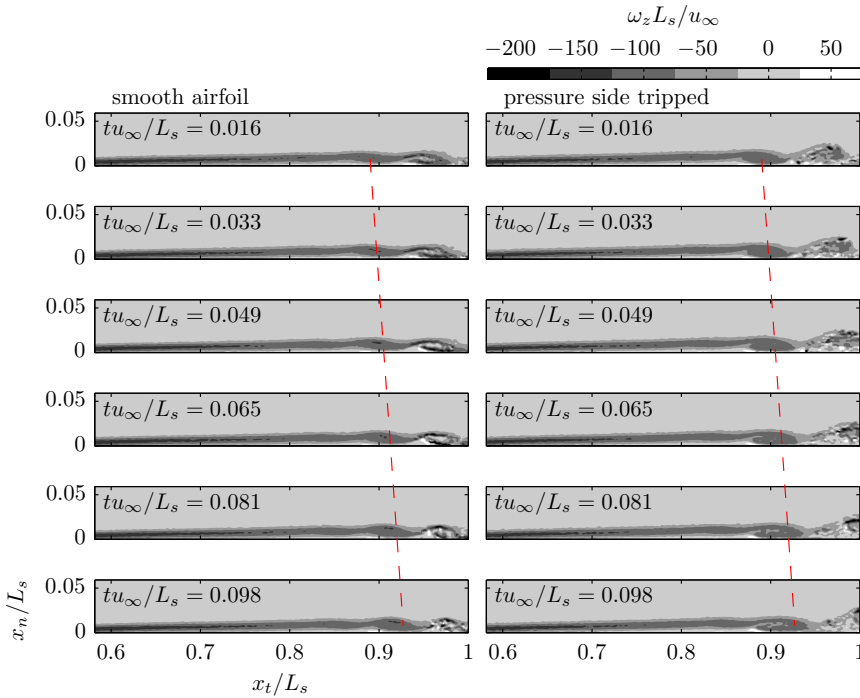
(a) $Re_c = 1.3 \times 10^5$ (b) $Re_c = 2.05 \times 10^5$

Figure 6.8: Boundary layer parameters and pressure coefficient based on edge velocity u_e for the suction side for a) $Re_c = 1.3 \times 10^5$ and b) $Re_c = 2.05 \times 10^5$.



(a) Smooth airfoil (left) and with pressure side tripped (right). $Re_c = 1.3 \times 10^5$

(b) Smooth airfoil (left) and with pressure side tripped (right). $Re_c = 2.05 \times 10^5$

Figure 6.9: Time sequences of spanwise vorticity fields ω_z on the suction side. The temporal separation between two consecutive images is 0.33ms.

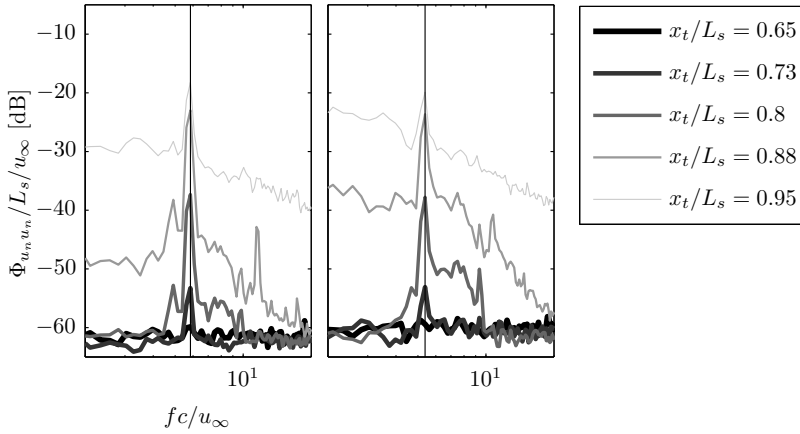
6.3.3. TEMPORAL EVOLUTION OF UNSTABLE DISTURBANCES

Figure 6.9 shows time sequences of spanwise vorticity fields $\omega_z L_s / u_\infty$, depicting the temporal evolution, amplification, and turbulent breakdown of the roll-up vortices in the aft portion of the separation bubble. Figures 6.9a and 6.9b show the data for the low ($Re_c = 1.3 \times 10^5$) and high ($Re_c = 2.05 \times 10^5$) Reynolds number cases, respectively. Roll-up of the shear layer becomes clearly visible in figure 6.9 at the respective location of steep increase in velocity fluctuations seen in figure 6.7. The dashed lines indicate locations of constant phase of the fluctuations induced by the convecting vortical structures. Their slopes thus give an indication of the convective velocity u_c .

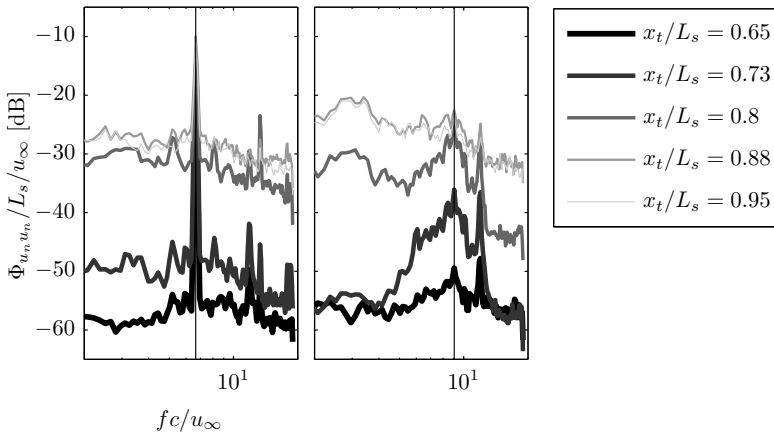
For $Re_c = 1.3 \times 10^5$ (figure 6.9a), the roll-up occurs at approximately $x_t / L_s = 0.85$. Due to the close agreement between the shedding frequencies f_{sh} (figure 6.6) and similar convective velocity for the two cases at this Reynolds number, the characteristic size of these structures is similar. While an earlier break-up of the roll-up vortices is observed when the pressure side boundary layer is tripped (case ii), coherent vortical structures are swept periodically past the trailing edge in both cases, leading to tonal noise emissions.

As anticipated from the time-averaged results, more significant changes are observed for $Re_c = 2.05 \times 10^5$ (figure 6.9b). The presence of strong tonal excitation for the smooth airfoil (case i) leads to earlier shear layer roll-up. The characteristic wavelength of the structures is notably larger for the smooth airfoil (case i) compared to the tripped case (case ii). This condition complies with the frequency of the structures for case (i) being lower than that attained with the pressure side boundary layer tripped (figure 6.6), given similar convective velocities for the two cases (figure 6.9). Roll-up vortices become less coherent upstream of the trailing edge than those for the lower Reynolds number, which is a manifestation of three-dimensional turbulent break-up and supported by positive vorticity ω_z within vortex cores for $x_t / L_s > 0.85$. As a result of this process, in both cases, only weakly coherent structures convect past the trailing edge on the suction side. Therefore, suction side events have negligible influence on tonal noise generation at this Reynolds number, as seen in acoustic measurements for the corresponding cases presented in figure 6.4.

Figure 6.10 depicts the auto-spectral density of the wall-normal velocity component sampled along the line described by the maximum fluctuations of the wall-tangential velocity component $rms(u_t)$ in the separated shear layer. For $Re_c = 1.3 \times 10^5$ (figure 6.10a), the spectra show clearly defined peaks at frequency $f_{sh} c / u_\infty = 5.9$ and $f_{sh} c / u_\infty = 5.4$ (indicated by vertical lines) for the smooth and tripped cases (cases i and ii), respectively. In both cases, the auto-spectral density at the shedding frequency increases towards the trailing edge due to amplification of disturbances within the separated shear layer. The spectral energy content becomes distributed over a broader range of frequencies downstream of the shear layer roll-up location ($x_t / L_s > 0.85$, figure 6.9a), which signifies later stages of transition to turbulence. For the smooth airfoil (case i), the growth of instabilities in the separated shear layer is associated with a narrower frequency band centered on the shedding frequency f_{sh} . This indicates a stronger upstream influence due to acoustic excitation (figure 6.9a). Nevertheless, since the differences in the amplitude of tonal emissions are not substantial for this Reynolds number (figure 6.4), the shedding frequency does not vary substantially between the two cases. The relatively minor



(a) Smooth airfoil (left) and with pressure side tripped (right). $Re_c = 1.3 \times 10^5$



(b) Smooth airfoil (left) and with pressure side tripped (right). $Re_c = 2.05 \times 10^5$

Figure 6.10: Auto-spectral density of wall-normal velocity component $\Phi_{u_n u_n}$ on the suction side. Smooth airfoil (left) and with pressure side tripped (right).

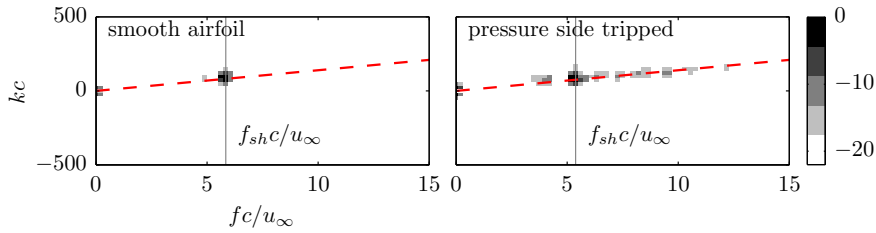
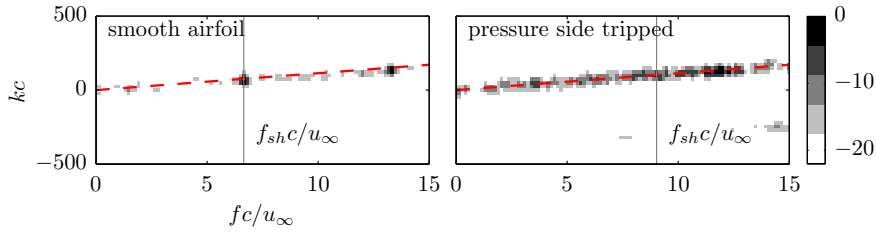
(a) $Re_c = 1.3 \times 10^5$ (b) $Re_c = 2.05 \times 10^5$

Figure 6.11: Wavenumber-frequency spectra of wall-normal velocity component u_n on the suction side (dB scale with respect to maximum value) along the line of maximum $rms(u_t)$ on the suction side. Smooth airfoil (left) and with pressure side tripped (right).

6

changes in the shedding frequency are attributed to the minor changes in the feedback loop characteristics as well as the effect of mean flow deformation on the stability characteristics of the separated shear layers discussed by Marxen and Rist [148] and Marxen *et al.* [218].

Consistent with the previously discussed results, the spectra pertaining to $Re_c = 2.05 \times 10^5$ (figure 6.10b) show a significant difference in the development of the shear layer disturbances. For the smooth airfoil (case i), the presence of the strong tone causes the growth of shear layer disturbances to lock onto a narrow frequency band centered at the tone frequency ($f_{sh}c/u_\infty = 6.7$). In contrast, when acoustic excitation due to shedding from the pressure side is suppressed (case ii), shear layer transition is associated with a significantly broader frequency range centered at a higher frequency ($f_{sh}c/u_\infty = 9.1$). The marked difference in the spectra are reminiscent of those encountered in experiments with forced and unforced transition [138], where disturbances lock onto the forcing frequency rather than occurring within a broader wave packet. Thus, unlike the lower Reynolds number case, the suppression of tonal noise production (case ii) leads to significant differences in shear layer transition for this Reynolds number, and, hence, significantly changes bubble characteristics on the suction side.

The dominant velocity perturbations along the center of the shear layer (maximum $rms(u_t)$) are induced by the convection of amplified disturbances in the shear layer (figure 6.9). Figures 6.11a and 6.11b show the wavenumber-frequency spectrum of the wall-normal velocity component along the line of maximum $rms(u_t)$ for $Re_c = 1.3 \times 10^5$ and

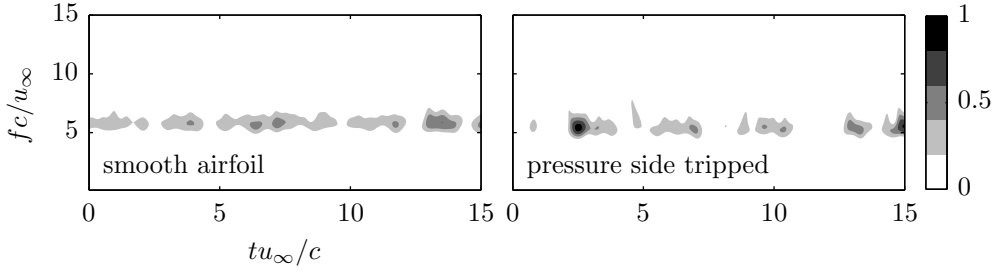
Table 6.2: Characteristics of shear layer vortices.

case	Re_c	$f_{sh}c/u_\infty$	u_c/u_∞	λ_{sh}/c	$k_{sh}c$
i)	1.3×10^5	5.9	0.45 ± 0.03	0.075	83.8
ii)	1.3×10^5	5.4	0.45 ± 0.03	0.085	74.9
i)	2.05×10^5	6.7	0.55 ± 0.03	0.082	76.6
ii)	2.05×10^5	9.1	0.55 ± 0.03	0.060	104.7

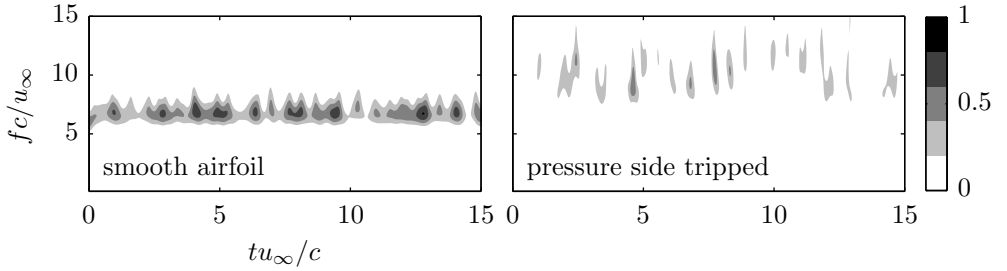
$Re_c = 2.05 \times 10^5$, respectively. The wavenumber-frequency spectrum was computed by averaging the square modulus of the windowed two-dimensional Fast Fourier Transform (FFT). In all cases, the energy is concentrated along a line, commonly referred to as the convective ridge [106] (indicated by the dashed line in figure 6.11). The convective velocity is related to the slope of the convective ridge as $u_c = 2\pi f/k$. Then, the wavenumber and wavelength associated with the vortical structures shed at f_{sh} (see figure 6.10, marked by the solid line in figure 6.11) are found as $k_{sh} = 2\pi f_{sh}/u_c$ (at the intersection of the dashed and solid lines in figure 6.11) and $\lambda_{sh} = 2\pi/k_{sh}$, respectively. Table 6.2 summarizes the convective velocity, frequency, wavelength, and wavenumber related to the roll-up vortices. For similar flow conditions ($\alpha_{eff} = 1.58^\circ, Re_c = 1.5 \times 10^5$), Arcondoulis *et al.* [197] report a convective velocity of $u_c/u_\infty = 0.4$ and similar values were found in other studies [144, 146].

For the high Reynolds number case ($Re_c = 2.05 \times 10^5$), a significant change in wavelength was observed with acoustic excitation (figure 6.9b). The data in table 6.2 confirm that the change in wavelength is due to the difference in frequency only, while the convective velocity remains constant. It should be noted that a second convective ridge associated with negative wavenumbers in figure 6.9b is due to temporal aliasing.

A wavelet analysis employing the Morlet wavelet is used to investigate temporal variations in the energy content and frequency of fluctuations in the shear layer [205]. Here, the analysis is applied to the wall-normal velocity fluctuations u_n along the line of maximum wall-tangent velocity fluctuations $rms(u_t)$ (i.e. the same data as used for wavenumber-frequency analysis, figure 6.11). The modulus of the normalized wavelet coefficients is depicted in figures 6.12a and 6.12b for $Re_c = 1.3 \times 10^5$ and $Re_c = 2.05 \times 10^5$, respectively. At the lower Reynolds number (figure 6.12a), the frequency and energy content associated with the roll-up vortices exhibit comparatively small temporal variations. Larger variations in both of these characteristics are observed when the boundary layer on the pressure side is tripped (case ii). A similar trend is observed for $Re_c = 2.05 \times 10^5$ (figure 6.12b). However, while the variations in frequency for the smooth airfoil (case i) are comparable to those observed for the lower Reynolds number (figure 6.12a), the absence of acoustic excitation (case ii) leads to significantly larger variations in both the frequency and energy content associated with the dominant flow structures on the suction side. This is consistent with the broader spectral peaks observed in figure 6.10b for this case, implying that the strength and frequency of the roll-up vortices undergo significantly more substantial temporal variations in the absence of tonal emissions.



(a) $\text{Re}_c = 1.3 \times 10^5$



(b) $\text{Re}_c = 2.05 \times 10^5$

Figure 6.12: Temporal variation of the modulus of wavelet coefficients for the wall-normal velocity component u_n (normalized with respect to maximum) along the line of maximum $\text{rms}(u_t)$ on the suction side. Smooth airfoil (left) and with pressure side tripped (right).

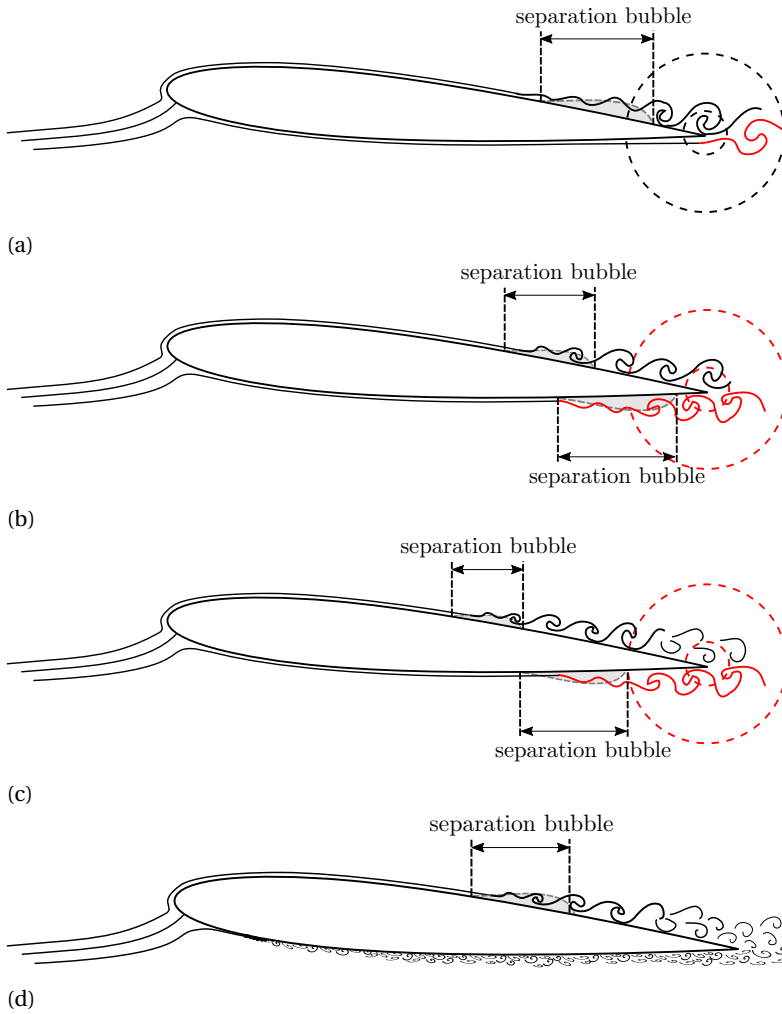


Figure 6.13: Schematics of flow regimes related to separation bubble development on the suction side: a) suction-side dominated trailing edge tone, b) pressure-side dominated trailing edge tone, with contribution from the suction side feedback loop, c) pressure-side dominated trailing edge tone, d) suction side separation bubble in the absence of significant tonal emissions. Note, some elements are not drawn to scale.

6.3.4. SUMMARY OF FEEDBACK EFFECT

The presented results and analysis indicate that strong mutual interaction can occur between separation bubble development on an airfoil at low Reynolds numbers and trailing edge tonal noise emissions. When a separation bubble is located sufficiently close to the trailing edge, shear layer roll-up vortices can retain sufficient strength and coherence at the trailing edge. Periodic passage of these structures over the trailing edge induces tonal noise emission. The resulting acoustic pressure waves travel upstream and promote separated shear layer transition. As a consequence, the transition process locks onto a narrow frequency band, and a feedback loop is established between the separation bubble and the tonal emissions produced by the shear layer vortices at the trailing edge.

The distinct types of flow development identified in the present study are summarized schematically in figure 6.13. At lower Reynolds numbers, when the separation bubble does not form on the pressure side, a separation bubble on the suction side is located relatively close to the trailing edge (figure 6.13a). The produced shear layer vortices retain sufficient strength and coherence at the trailing edge, generating tonal emission. Upstream propagation of the acoustic pressure waves establishes a feedback loop with the separation bubble. As the Reynolds number is increased, the separation bubble moves upstream. The trend for the shedding frequency on the suction side follows approximately $f_{sh} \sim u_{\infty}^{1.6}$, which matches $f_{n_{max}}$. A similar regime can be obtained, and extended to higher Reynolds numbers, by tripping the boundary layer on the pressure side. With the boundary layer being turbulent on the pressure side, only suction side events can cause tonal noise emission.

In the absence of the boundary layer trip, an increase of the Reynolds number eventually leads to separation bubble formation and shear layer roll-up on the pressure side (figure 6.13b). Being formed closer to the trailing edge, more coherent roll-up vortices reach the trailing edge on the pressure side. As a result, separated shear layer development on the pressure side takes over tonal noise generation and dominates the frequency selection. Here, a feedback loop is established between the pressure side separation bubble and tonal emission. Moreover, the tonal noise emission also affects the separation bubble development on the suction side, locking the amplification of disturbances and, hence, the shedding frequency f_{sh} to that of the primary tone $f_{n_{max}}$. When the separation bubble on the suction side is located sufficiently close to the trailing edge, a second feedback loop is established, as the suction side rollers continue to contribute to the tone generation.

Further increase in Reynolds number causes the separation bubbles to move upstream and shrink further (figure 6.13c). The second feedback loop with the suction side separation bubble eventually breaks up, as the suction side roll-up vortices experience turbulent breakdown upstream of the trailing edge and their contribution to tonal noise generation becomes negligible. However, the upstream propagation of acoustic pressure waves, induced by pressure side events, continues to govern the frequency selection for the dominant shear layer disturbances on the suction side. The trend for the shedding frequency on the suction side follows approximately $f_{sh} \sim u_{\infty}^{1.3}$, with minor deviations from that observed for the regime depicted in figure 6.13b.

However, if at high Reynolds numbers tonal noise emission is suppressed by the ap-

plication of a tripping device on the pressure side, flow development on the suction side changes markedly (figure 6.13d). Specifically, the shear layer transition process now involves amplification of disturbances in a significantly broader range of frequencies, as expected for unforced transition (figure 6.10b). The size of the separation bubble and the shedding frequency increase compared to that in the presence of the tone. The shedding frequency increases with increasing free-stream velocity as $f_{sh} \sim u_{\infty}^{2.1}$ (figure 6.6), with the value of the exponent being significantly higher than that observed in the presence of pressure side (figures 6.13b to 6.13c) or suction side (figure 6.13a) acoustic feedback.

The transition between the regimes depicted in figure 6.13 is probably accompanied by transients. In particular, the analysis of the present results suggests the presence of transient flow development between suction and pressure side dominated regimes (figures 6.13a and 6.13b) and when the feedback loop breaks on the suction side (figures 6.13b to 6.13c).

It should be noted that the distinct flow regimes depicted in figure 6.13 and, more importantly, the progression from one regime to another are defined based on the data obtained in the present investigation specific to a given airfoil model and angle of attack. While some variations in flow development can be expected for different airfoil profiles and angles of incidence, the fundamental physical mechanisms and the associated types of flow development depicted in figure 6.13 are certainly not unique to the present investigation. The suction side dominated regime (figure 6.13a) is expected to occur at relatively low angles of attack, as it requires the formation of a separation bubble close to the trailing edge, which is known to move upstream with increasing angle of attack [137]. This is supported by recent acoustic measurements conducted in an anechoic facility by Pröbsting and Scarano [52]. Finally, the development of a separation bubble on the suction side, which was of particular interest in the present investigation, has been shown to be influenced significantly by tonal emissions. The observed effect of the trailing edge tone on separation bubble development is similar to that reported in flow control investigations involving periodic forcing [213–216], and is thus expected to manifest whenever significant tonal emissions are produced.

The presence of periodic acoustic excitation has been shown to have a significant effect on separation bubble development. Specifically, the tonal forcing of the separated shear layer locks the band of amplified disturbances to the forcing frequency. Similar to external forcing, this promotes transition and leads to the reduction in the size of the separation bubble. The induced changes to the mean flow further cause the separation bubble to move upstream. The trend of the shedding frequency follows $f_{sh} \sim Re_c^m$, with exponents ranging between $m = 0.8$ and $m = 2.1$, depending on the considered flow regime and Reynolds number range. This range of exponents is similar to that reported for experimental studies of separation bubble dynamics for various profiles by Yarusevych *et al.* [146]. Thus, the possible effect of acoustic feedback on separation bubble development should be considered when conducting experimental studies focused on separation bubble dynamics and comparing data from different investigations.

6.4. CONCLUSION

An acoustic feedback due to tonal noise emission on amplified disturbances in a laminar separation bubble formed on the suction side of an airfoil in low Reynolds num-

ber flows was investigated experimentally. The experiments were performed on a NACA 0012 airfoil for a range of chord Reynolds numbers $0.65 \times 10^5 \leq Re_c \leq 4.5 \times 10^5$ and at effective angle of attack $\alpha_{eff} \approx 1.2^\circ$. Time-resolved, two-component PIV measurements were performed simultaneously with surface and far-field microphone measurements to characterize flow development.

For the selected range of experimental conditions, laminar boundary layer separation occurred on both sides of the airfoil. The amplification of disturbances in separated shear layers on either the suction or pressure side (or both) leads to shear layer roll-up and shedding of vortices from separation bubbles. When these structures form sufficiently close to the trailing edge and retain sufficient strength and coherence, their passage over the trailing edge leads to strongly periodic pressure fluctuations. Feedback of acoustic pressure waves, in turn, affects the amplification of unstable disturbances in the separated shear layer. Through the feedback between the acoustic pressure waves and the shear layer transition process, the frequency band of amplified disturbances narrows significantly and the shedding frequency locks to the frequency of the tone. As a result, the transition process is promoted and, consequently, overall separation bubble characteristics are altered. The effect is similar to that due to external periodic forcing observed in previous studies.

At higher Reynolds numbers, when separated shear layer roll-up occurs on both the suction and pressure side, the unsteady flow development on the pressure side defines the characteristic frequency of pressure fluctuations, thereby affecting the disturbance spectrum on the suction side. This is due to the closer proximity of the pressure side separation bubble to the trailing edge, leading to the passage of more coherent vortices over the trailing edge. Under such conditions, the shedding frequency on the suction side locks onto the frequency of the tone, which is imposed by the shedding frequency of pressure side events.

At lower Reynolds numbers, when a separation bubble does not form on the pressure side and roll-up does not occur upstream of the trailing edge, or when it is suppressed by tripping the boundary layer, tonal emissions can be produced due to suction side separated shear layer vortices. In this case, a strong feedback effect is also established between the tonal emissions and the shear layer transition on the suction side. At the intermediate range of Reynolds numbers, when the roll-up occurs on the pressure side and the suction side bubble is located sufficiently close to the trailing edge, strong shedding occurs over the trailing edge from both the suction and pressure side. In this regime, the tone production is influenced by the events on both sides of the airfoil and by their interaction.

The results illustrate that the formation of periodic, coherent structures in the aft portion of a separation bubble not only plays a critical role in the transition process but can also establish acoustic feedback. This is shown to affect the selection of the dominant frequency of the shear layer disturbances and separation bubble characteristics. While the observed effect is expected to occur only at relatively low angles of attack, it can have a profound influence on flow development and, thus, must be considered in studies on low Reynolds number airfoils, in general, and those focused on separation bubble dynamics, in particular.

II

TURBULENT BOUNDARY LAYER TRAILING EDGE INTERACTION

7

PRESSURE RECONSTRUCTION IN A TURBULENT BOUNDARY LAYER

*With increasing distance, our knowledge fades, and fades rapidly.
Eventually, we reach the dim boundary - the utmost limits of our telescopes.
There, we measure shadows, and we search among ghostly errors of measurement
for landmarks that are scarcely more substantial.
The search will continue. Not until the empirical resources are exhausted,
need we pass on to the dreamy realms of speculation.*

Edwin Powell Hubble, *The Realm of the Nebulae*

This chapter focuses on the applicability of tomographic PIV to estimate the correlation of pressure fluctuations. The latter is required for estimation of aeroacoustic noise radiation of the turbulent boundary layer trailing edge interaction. Three-dimensional time-resolved velocity field measurements are obtained using high-speed tomographic PIV on a fully developed flat plate turbulent boundary layer for the estimation of wall pressure fluctuations.

The pressure field is obtained by solving the Poisson equation for incompressible flows, where the source terms are obtained from time-resolved velocity field measurements. The experimental results are compared to those of a Direct Numerical Simulation (DNS) at similar Reynolds number. Computed surface pressure fluctuations are further validated by means of simultaneous measurements by a pinhole microphone and compared to semi-empirical models available in literature. Finally, the coherence of surface pressure fluctuations and the resulting span- and streamwise coherence lengths are estimated and compared to semi-empirical models and DNS results.

Parts of this chapter have been published in *Experiments in Fluids* **54** (2013) [183].

7.1. INTRODUCTORY REMARKS

SPANWISE CORRELATION of pressure fluctuations at the wall under a turbulent boundary layer is of importance in aeroacoustics, for instance for the estimation of trailing edge noise and in vibro-structural problems. The estimation of trailing edge noise emission through surface pressure statistics was discussed in section 2.2.4.

Nevertheless, measurements of the space-time correlation of the pressure field require complex instrumentation involving several surface pressure transducers or microphones, installed inside the model or flush mounted on the model's surface. Moreover, transducer based measurements close to the trailing edge prove to be difficult due to the intrusiveness of the methods and the difficulty of fitting a large number of sensors within thin geometries, such as sharp trailing edges.

In recent years, the development of high-speed PIV techniques opened new possibilities for the investigation and understanding of complex flows including turbulent flow phenomena and aeroacoustic sources. Under the assumption of incompressible flow, the momentum equation provides a relation between the velocity field and the gradient of the hydrodynamic pressure. Within the limitations of this assumption and the measurement data, reconstruction of the pressure field becomes possible with time-resolved PIV (section 3.3). This procedure provides a non-intrusive alternative for the determination of flow field pressure fluctuations within the flow, which does not require model instrumentation.

The estimation of the correlation function and correlation length requires the evaluation of the wall pressure auto- and cross-spectral densities. For a given choice of the measurement volume, restrictions due to the imaging resolution of the camera sensor pose a limit on the attainable measurement resolution. Further limitation on the maximum size of the measurement volume is due to the available energy per pulse provided by the illumination system, which is particularly severe for high-speed systems. Due to these restrictions, the measurement volume cannot be extended to include the entire boundary layer. Despite of this limitation, Ghaemi *et al.* [181] have demonstrated that uniform and constant boundary conditions can be applied in the outer part of the boundary layer, preserving the magnitude pressure fluctuations over a large range of frequencies.

Therefore, a configuration with a thin volume parallel to the wall, but extending to the outer part of the boundary layer, is suggested to respond to the requirements of a measurement domain of sufficient stream- and spanwise extent. This measurement configuration is not new, for instance Schröder *et al.* [179] applied it to fully developed boundary layers, and Atkinson *et al.* [219] assessed the inner region of the boundary layer in a similar way. High-speed experiments have not been carried out in this configuration, but are required for the purpose of the present study.

The study described in this chapter aims at determining the feasibility of an experimental approach, based on volumetric time-resolved velocity field data from tomographic PIV, to obtain unsteady surface pressure spatio-temporal characteristics. In particular, an estimation of the unsteady surface pressure correlation and correlation length is desired. The assessment of this approach is corroborated with a DNS at similar conditions as in the experiment. Moreover, simultaneous unsteady surface pressure measurements are used to compare to the pressure reconstructed from PIV.

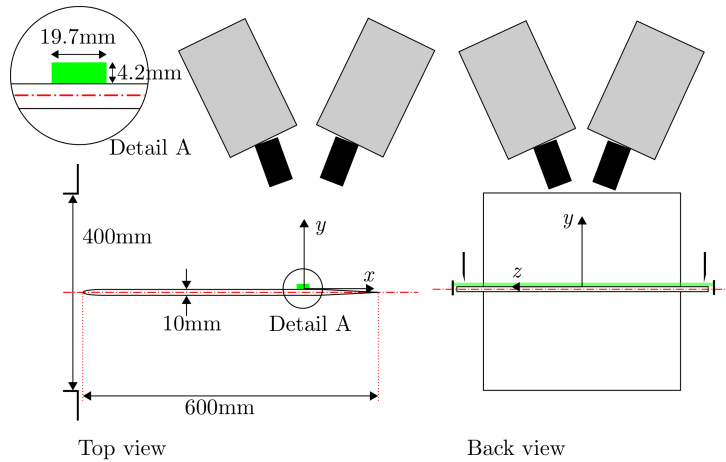


Figure 7.1: Schematic of tomographic PIV experiment. Note that some elements are not drawn to scale.

7.2. DESCRIPTION OF EXPERIMENTS

Planar and time-resolved tomographic PIV experiments were performed on a flat plate of 600mm chord, 400mm wetted span, and 10mm maximum thickness in the low speed wind tunnel facility (W-Tunnel) at Delft University of Technology. The plate possesses an elliptical leading edge and terminates in a sharp trailing edge at an enclosed angle of 4.8° . The boundary layer was tripped 100mm downstream of the leading edge by a 5mm wide tripping device of 3D roughness elements with a nominal grain size of 0.84mm.

The measurement volume is located at center span, 435mm downstream of the leading edge, on the flat section of the plate. At a free stream velocity of $u_\infty = 10\text{m/s}$, the Reynolds number based on the local boundary layer thickness ($\delta = 9.4\text{mm}$) is $Re_\delta \approx 6,240$ and that based on the momentum thickness is $Re_\theta \approx 730$.

7.2.1. PLANAR FLOW FIELD MEASUREMENTS

For the characterization of the boundary layer planar PIV was used. A Photron *Fast-Cam SA1.1* CMOS camera ($1,024 \times 1,024\text{px}$, 12bit, pixel pitch $20\mu\text{m}$), equipped with a Nikon *Micro-Nikkor* 105mm prime lens, recorded images over a field of view (FOV) of $58 \times 58\text{mm}^2$. The numerical aperture was set to $f_\# = 2.8$ to maximize the amount of light collected. At such value of the numerical aperture, the particle image diameter is smaller than 1px on the sensor, which would result in large bias errors. Therefore, the plane of focus was slightly shifted away from the illumination plane, resulting in defocused particle images encompassing approximately 2px. Illumination was provided by a Quantronix *Darwin Duo* Nd:YLF laser ($2 \times 25\text{mJ/pulse}$ at 1kHz). The boundary layer was illuminated from a downstream location with the propagation direction of the light parallel to the chord, which strongly reduces light reflections from the wall. A light sheet of approximately 2mm thickness was thus formed. Water-glycol based tracer particles with mean diameter $1\mu\text{m}$ were used for seeding the flow.

At magnification $M = 0.37$ one pixel is equivalent to $54\mu\text{m}$ in the object plane. The

Table 7.1: Parameters for planar PIV experiment

Parameter	Symbol	Value
Field of view	FOV/δ	6.2×6.2
	FOV/δ_v	$1,990 \times 1,990$
Magnification	M	0.37
Interrogation window size	ws/δ	0.16×0.04
	ws/δ_v	53×13
Pulse separation	dt	$80\mu s$
Acquisition frequency	f_{acq}	125Hz
Number of samples		4,500

recording comprises 4,500 image pairs at 125Hz with a pulse separation of $dt = 80\mu s$, corresponding to a displacement of approximately 0.8mm (15px) in the free stream. The illumination and imaging systems were synchronized with a LaVision *High-Speed-Synchronizer* and controlled by the *DaVis 8* software. The latter was also used for the image pre-processing and interrogation.

An iterative, multi-grid correlation with window deformation procedure (window size 16×16 px, 75% overlap) results in velocity vectors on a grid with a vector spacing of 0.16mm (4px). For the correlation procedure, the wall region is masked and weighted windows with an aspect ratio of 4:1 are used, equivalent to a rectangular window size of approximately $1.5 \times 0.37\text{mm}^2$ (28×7 px). Effects of weighting functions have been investigated and reported by Astarita [220]. The main advantage of Gaussian compared to top-hat weighting is the reduction of random errors due to signal truncation at the edges. Table 7.1 provides an overview of the parameters for the planar PIV experiment.

7

7.2.2. VOLUMETRIC FLOW FIELD MEASUREMENTS

Four Photron *FastCam SA1.1* CMOS cameras, equipped with Nikon *Micro-Nikkor* 105mm prime lenses, were arranged such that their optical axes deviates from the surface normal by an angle of approximately 25° in the y - z plane and 15° in the x - y plane (figure 7.1). The numerical aperture was adjusted to $f_\# = 11$ for the tomographic experiments. Scheimpflug adapters were used to adjust the lens plane such that the measurement median plane was parallel to the focal plane. To maximize the scattered light intensity, a multi-pass light amplification system consisting of an arrangement of two mirrors and knife-edges was used [179, 180] and illumination was provided by a Quantronix *Darwin Duo* Nd:YLF laser. Figure 7.1 shows a schematic of the experimental set-up.

At an average magnification of $M = 0.45$, the voxel size in the object space is $42.3\mu m$. The image sequence was recorded at acquisition frequency $f_{acq} = 10\text{kHz}$. The resulting particle displacement in the free stream is approximately $u_\infty/f_{acq} \approx 1\text{mm}$ (24 voxels, vx). The region of interest (ROI) of the CMOS cameras is halved at this framing rate and thus the active sensor size is $512 \times 1,024\text{px}^2$. On average, the particle image diameter is $d_\tau = 1.8\text{px}$ (standard deviation 0.4px) and the seeding density was 0.07ppp (particles per pixel).

LaVision *DaVis 8* was used for volume self-calibration [221] and the MART algorithm

Table 7.2: Parameters for tomographic PIV experiment

Parameter	Symbol	Value
Reconstructed volume	V/δ	$2.1 \times 0.45 \times 4.4$
	V/δ_v	$668 \times 146 \times 1,430$
Magnification	M	0.45
Interrogation volume size	v/δ	$0.14 \times 0.07 \times 0.14$
	v/δ_v	$45 \times 23 \times 45$
Acquisition frequency	f_{acq}	10kHz
Number of samples		1,500

was applied for iterative reconstruction [175] over a domain of $19.3 \times 4.2 \times 41.3\text{mm}^3$. To obtain the vector field, the sequence of objects were analysed with a volume deformation iterative multi-grid technique with a final interrogation volume size of $32 \times 16 \times 32\text{vxl}$ at 75% overlap, resulting in vector spacing of 0.16mm along the wall-normal and 0.33mm in the other coordinate directions. The high-speed acquisition allows to strengthen the correlation signal by a short-time sliding-average correlation technique, whereby the interrogation kernel encompasses four subsequent objects (three object pairs), and has recently been compared to other approaches for multi-frame interrogation [172]. The no-slip condition at the wall is imposed by setting to zero the velocity vectors at or below the position of the surface during the iterative correlation process. This condition has been shown to stabilize the interrogation and reduces the number of spurious vectors [222]. The normalized time step and measurement frequency are $\Delta t u_\infty / \delta = 0.011$ and $f_{acq} \delta / u_\infty = 9.4$ ($\omega_s \delta^* / u_\infty = 9.4$), respectively. Table 7.2 gives an overview of the parameters for the tomographic PIV experiment.

Based on the tomographic PIV data, the pressure field at the surface was reconstructed following the methodology described in section 3.3.

7.2.3. SURFACE PRESSURE FLUCTUATIONS

The fluctuating pressure at the surface of the plate was measured within the measurement volume using a Sonion 8010T condenser microphone. Sensitivity charts provided by the manufacturer specify the response of this microphone to be constant between 300Hz and 7kHz with equivalent noise levels of about 15dB SPL (equivalent to $p_{rms} \approx 100\mu\text{Pa}$). The sensor was installed in a cavity below a pinhole with a diameter of $200\mu\text{m}$. For further details, the reader is referred to section 3.4 and the study of Ghaemi *et al.* [181].

The microphone measurement was performed simultaneously with tomographic PIV at a frequency of 30kHz, where the acquisition sequence was triggered through the PIV synchronisation system. A sequence of 30s duration was recorded.

7.2.4. DIRECT NUMERICAL SIMULATION

A compressible DNS of a turbulent boundary layer was performed at Reynolds number $\text{Re}_\theta = 1,000$ and Mach number $M_0 = 0.3$. The numerical algorithm has been described by Pirozzoli and Bernardini [223, 224]. Reference length and velocity scales are

Table 7.3: Comparison of vector spacing and extension of domain.¹

Symbol	PIV	DNS
$\Delta x/\delta$	0.036	0.033
$\Delta y/\delta$	0.018	0.004 – 0.1
$\Delta z/\delta$	0.036	0.030
L_x/δ	2.1	45.00
L_y/δ	0.45	2.25
L_z/δ	4.4	4.50

Table 7.4: Characterization of boundary layer in experiments.

Parameter	Symbol	Value
Boundary layer thickness	δ	9.4mm
Displacement thickness	δ^*	1.5mm
Momentum thickness	θ	1.1mm
Wall shear velocity	u_τ	0.52m/s

the boundary layer thickness at the center of the computational domain and the free stream velocity, respectively. Data was sampled on a domain extending over $L_x/\delta = 45$ in streamwise, $L_y/\delta = 2.25$ in wall-normal, and $L_z/\delta = 4.5$ in spanwise direction. The data was sub-sampled by a factor two in each coordinate direction, resulting in a temporal sampling of $\Delta t u_\infty/\delta = 0.045$ ($\omega_s \delta^*/u_\infty = 25.4$) and a vector spacing of $\Delta x/\delta = 0.033$ and $\Delta z/\delta = 0.030$ in streamwise and spanwise direction, respectively. In wall-normal direction the sampling resolution ranges from $\Delta y/\delta = 0.004$ near the wall to $\Delta y/\delta = 0.1$ in the free stream. A set of 3,000 samples, equivalent to a non-dimensional time interval of $T u_\infty/\delta = 137$, is considered.

7.3. RESULTS AND DISCUSSION

7.3.1. CHARACTERIZATION OF BOUNDARY LAYER

Outer scales are determined by trapezoidal integration over the time-averaged velocity fields obtained from planar PIV and the solution of the DNS. For the simulation, the friction velocity u_τ/u_∞ is determined based on a linear fit in the inner region of the boundary layer. Instead, for the experiment, where this information is not accessible, the friction velocity is determined based on a curve fit over the logarithmic region [225] with constants $\kappa = 0.4$ and $B = 4.0$ [226], which apply at low Reynolds number ($\text{Re}_\theta = 730$). Figure 7.2 shows the mean velocity data scaled with the parameters determined using the procedures outlined above. Table 7.4 lists the parameters of the turbulent boundary layer at the measurement location and table 7.5 provides a comparison of the dimensionless parameters relevant to both experiment and simulation.

For the experiment, a shape factor of $H = \delta^*/\theta = 1.45$ confirms the presence of a fully

¹the vector spacing for PIV is one quarter the interrogation element size (overlap factor 75%)

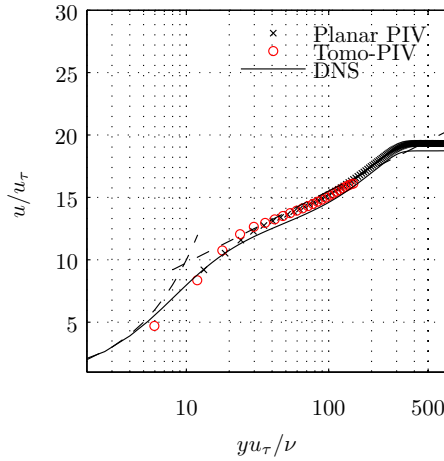


Figure 7.2: Mean velocity profiles scaled based on inner boundary layer scales.

Table 7.5: Comparison of boundary layer parameters from experiment and simulation.

Parameters	Symbol	PIV	DNS
Displacement thickness	δ^*/δ	0.16	0.18
Momentum thickness	θ/δ	0.12	0.12
Wall shear velocity	u_τ/u_∞	0.052	0.053
Shape factor	H	1.45	1.50
Reynolds number	Re_δ	6,240	8,185
	Re_θ	730	1,000
	Re_τ	436	325
Time scale ratio	Re_T	16.8	23.3

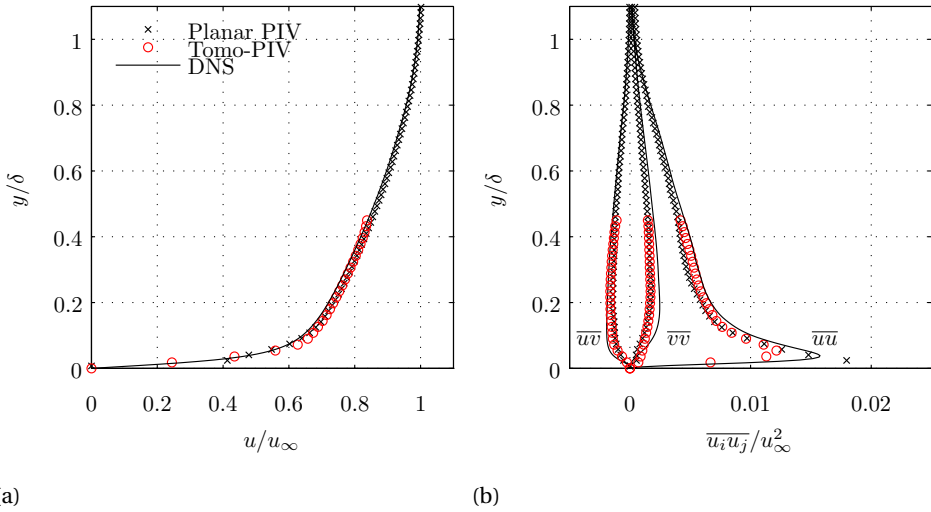


Figure 7.3: Mean velocity (a) and Reynolds stress profiles (b) for planar, tomographic PIV and DNS normalized with outer boundary layer parameters.

developed turbulent boundary layer. Average velocity profiles and components of the Reynolds stress tensor for experimental data and simulation are shown in figure 7.3 and are in good agreement. For the given choice of the measurement domain, tomographic PIV data is only available in the lower half of the boundary layer.

The mean velocity profile obtained from tomographic PIV exhibit slight deviations within 3% of the free stream velocity (figure 7.3a). The distributions of the normal components of the Reynolds stress tensor (figure 7.3b) show good agreement between measurement and DNS data in the outer region. Approaching the wall, the streamwise velocity fluctuations measured with planar PIV exceed the maximum found in the DNS solution. Instead, the tomographic data shows a lower value of the peak, which is ascribed to the averaging effect of the interrogation volume.

As an indication for the outer time scale, the eddy turn-over time is estimated with $\delta^*/u_\infty \approx 150\mu\text{s}$ or a non-dimensional frequency of $\omega\delta^*/u_\infty = 1$. The inner time scale corresponds to $\delta_v/u_\tau = 56\mu\text{s}$ or non-dimensional frequency $\omega\delta^*/u_\infty = 16.8$. The acquisition frequency of 10kHz therefore appears to be sufficient for resolution of the outer time scale, but not for the inner one. The ratio of inner and outer time scale, $\text{Re}_T = 16.8$, is required as parameter in the model of Goody [109] for the wall pressure spectrum. In the remainder of this study δ^*/u_∞ and δ^* are used as outer time and length scale, respectively, while δ_v/u_τ and $\delta_v = \nu/u_\tau$ are used as inner scales.

As outlined in section 3.3, the turbulent fluctuations in the turbulent boundary layer are profoundly linked to pressure fluctuations through the Poisson equation. The spatial organization of the turbulent boundary layer in experiment and simulation is compared qualitatively by means of snapshot visualization (figure 7.4). The features of the turbulent boundary layer are represented by means of the streamwise velocity component

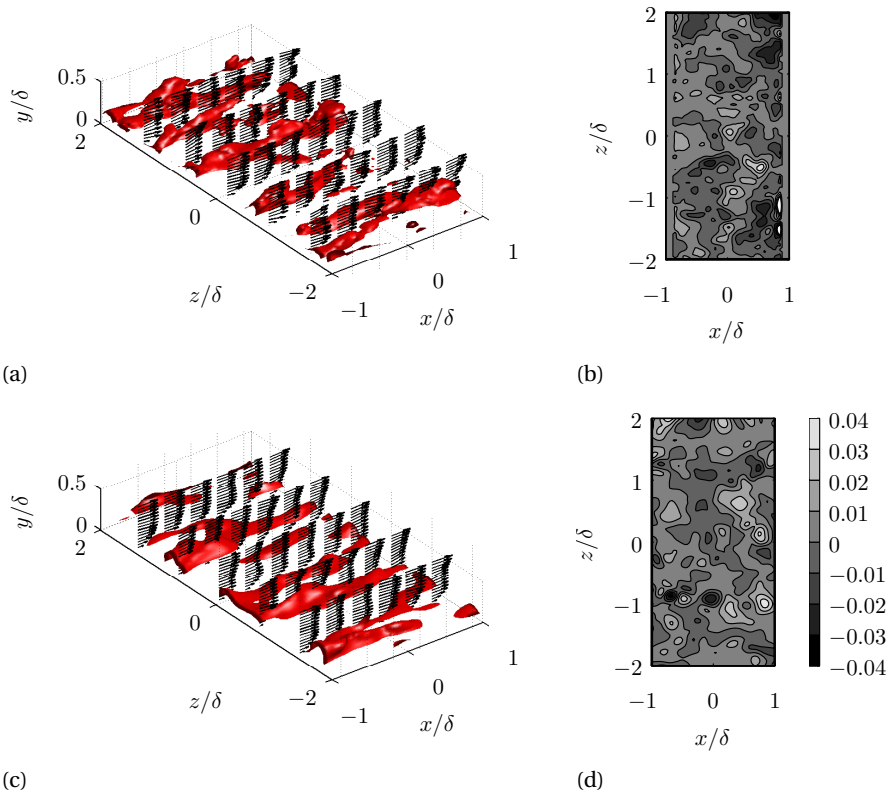


Figure 7.4: Visualization of streamwise velocity iso-contours ($0.6u_\infty$) and velocity vectors for PIV (a) and DNS (c). Instantaneous reconstruction of unsteady surface pressure field (b) and DNS solution (d) visualized by contours of p'/ρ_∞ .

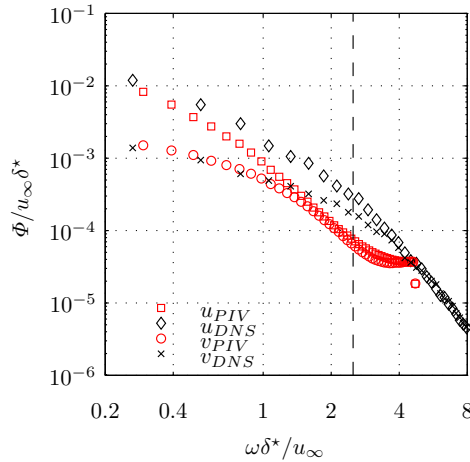


Figure 7.5: Normalised auto-spectral density of streamwise and wall-normal velocity components. Comparison of tomographic PIV and DNS data at $y/\delta = 0.1$.

iso-surface ($u/u_\infty = 0.6$) that return the organization of the flow into streamwise aligned low and high speed regions (figures 7.4a and 7.4c). The spacing between low and high speed velocity regions in the inner region of the boundary layer, about half the spanwise distance between two velocity iso-surfaces, is on the order of 100 viscous lengths $\delta_v = \nu/u_\tau \approx 2.9\text{mm}$, typical for Reynolds numbers $Re_\theta \leq 6,000$ [227]. Pirozzoli [228] investigated the size of the energy-containing eddies in the outer turbulent wall layer and found a typical integral length scale of 0.3δ for the streamwise velocity fluctuations. Examination of the instantaneous pressure coefficient in a plane parallel to the wall shows slightly spanwise elongated patches of low and high pressure on the same order of magnitude for simulation and experiment 7.4b and 7.4d.

7.3.2. TURBULENCE CHARACTERISTICS

First, the spectral energy distribution and the coherence are examined for the streamwise and wall-normal velocity components. For this comparison, data was sampled in a plane parallel to the surface at $y/\delta = 0.1$. Figure 7.5 depicts the average auto-spectral density of the velocity fluctuations. Note that streamwise velocity fluctuations show a higher energy content at lower frequency, likely caused by streamwise coherent regions of low speed fluid protruding from the viscous sublayer into the upper regions of the boundary layer. On the other hand, wall-normal velocity fluctuations are associated with ejection and sweep events of smaller extent [227]. For both velocity components, the spectra start to level off at $\omega \delta^* / u_\infty = 2.5$ and converge to a plateau at approximately $\Phi u_\infty / \delta^* = 3 \times 10^{-5}$ for higher frequency, indicating a threshold for the random measurement error. Assuming the random error to be uniformly distributed over the frequency range, this level is equivalent to fluctuations of 0.1m/s or a standard error of roughly 0.2vxl .

This difference between streamwise and wall-normal velocity components is em-

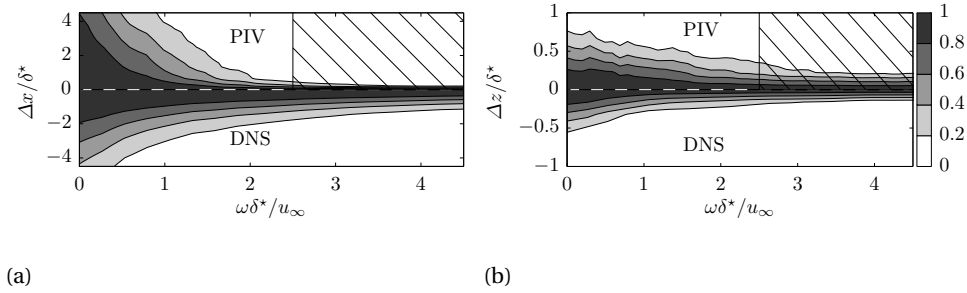


Figure 7.6: Streamwise coherence $\gamma_u^2(\omega, \Delta x)$ (a) and spanwise coherence $\gamma_u^2(\omega, \Delta z)$ (b) of streamwise velocity fluctuations at $y/\delta = 0.1$.

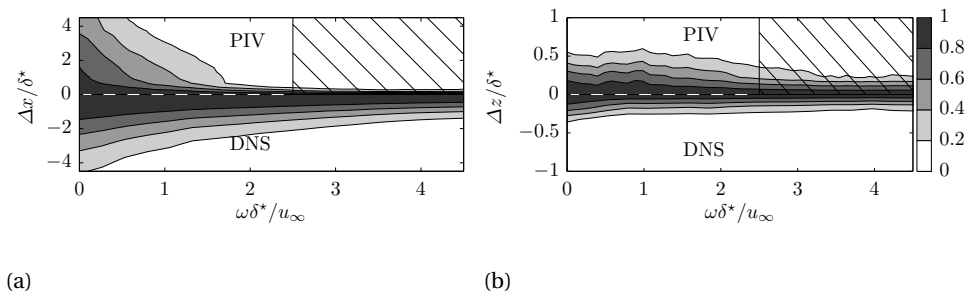


Figure 7.7: Streamwise coherence $\gamma_v^2(\omega, \Delta x)$ (a) spanwise coherence $\gamma_v^2(\omega, \Delta z)$ (b) of wall-normal velocity fluctuations at $y/\delta = 0.1$.

phasized when examining the coherence of the streamwise and wall-normal fluctuating velocity components in figures 7.6 and 7.7, respectively: the streamwise velocity component exhibits a larger streamwise coherence at low frequencies when compared to the wall-normal component in figures 7.6a and 7.7a. For frequencies $\omega\delta^*/u_\infty \lesssim 1.5$, the streamwise coherence of the streamwise velocity component compares well for experimental data and the DNS solution, while the comparison for the wall-normal component is less favourable. The more pronounced loss in coherence of the latter may be explained with the arrangement of the measurement volume, which implies an unfavourable condition for the measurement of the wall-normal (out-of-plane) velocity component and therefore a larger random error. The hatched area indicates the frequency range exceeding 2.5kHz which was identified in figure 7.5 as dominated by measurement noise.

Note the difference in the length scale between streamwise and spanwise velocity fluctuations. For separations equal to the displacement thickness δ^* and frequencies $\omega\delta^*/u_\infty \lesssim 1$, both velocity components show a streamwise coherence larger than 0.4. The spanwise coherence falls below this value within approximately half of the distance, which approaches the resolution of the PIV measurement in this case. Thus, velocity dynamic range (noise floor) and spatial resolution can be considered as limiting param-

eters for correlation estimates and values provided in this section can be considered as upper bounds of these limits.

7.3.3. UNSTEADY SURFACE PRESSURE

The pressure in the measurement domain is reconstructed following the methodology presented section 3.3 and compared to the fluctuating wall pressure measured by the pinhole microphone. Note that an artificial interface for the reconstruction process is located at $y/\delta = 0.07$ above the wall. Under the assumption of small pressure gradient normal to the wall, the values obtained at the interface are regarded as approximation for the unsteady surface pressure. The auto-spectral density based on the PIV data is estimated with a window averaging procedure with segments of 96 samples and an overlap of 50% and applying the Hamming window function to each segment (section E). The same procedure is applied to the DNS data (segments of 192 samples) and for the microphone signal (288 samples).

Measurement noise influences the estimation of the auto-spectral density and correlation to a certain extent as discussed in section 3.2.1. For reduction of the random noise component, a larger number of time steps can be considered in the reconstruction of the particle path and evaluation of the material derivative (section 3.3.5). Figure 7.8 shows the influence of this parameter on the spectral estimate and the microphone measurement for comparison. For small stencils $N = 5$ ($4\Delta t$), random noise leads to an overestimation of the auto-spectral density over almost the entire resolved frequency range. With increasing stencil size $N = 7$ ($6\Delta t$) and $N = 9$ ($8\Delta t$), the spectral estimate converges to the results obtained by the direct measurements with a dynamic range extending over two decades.

Since no single scaling rule leads to collapse of boundary layer pressure spectra over the entire frequency range, two scaling rules based on inner and outer flow variables are adopted following previous works (section 2.2.2). In general, scaling based on outer variables is expected to yield a satisfactory collapse in the low frequency range, the opposite is true for high frequency.

Figure 7.9a shows a comparison of the pressure spectra scaled based on outer flow variables. The data obtained using the PIV approach ($N = 9$), microphone measurements, and the DNS solution are displayed together with the data of Schewe [110]. The thin solid line indicates an estimation of the auto-spectral density provided by the model of Goody [109] for the present data, while the dashed line indicates the modelled spectrum for the data of Schewe [110]. For the present experiment, the measured and reconstructed spectra show a good agreement for frequencies between $0.8 \leq \omega\delta^*/u_\infty \leq 2.5$. Over this frequency range also the DNS data at $y/\delta = 0.05$ agrees well with the data at the surface. For higher and lower frequencies the reconstructed and directly data agrees within approximately 3dB. At low frequencies the PIV based spectra tend to overestimate the levels provided by the microphone. An underestimation is observed at higher frequency up to the range where noise starts to dominate the spectrum. The underestimation is likely due to the filtering property of the multi-step image interrogation algorithm and large stencil in the estimation of the material derivative. A plateau corresponding to the random noise level is encountered for frequencies exceeding $\omega\delta^*/u_\infty \approx 3.5$ at a level of $\Phi u_\infty/q_\infty^2 \delta^* = 3 \times 10^{-7}$. An estimate of the noise level for the fluctuating pressure is

$\tilde{p}/q_\infty = 10^{-3}$, obtained by assuming a uniform noise level over the frequency range.

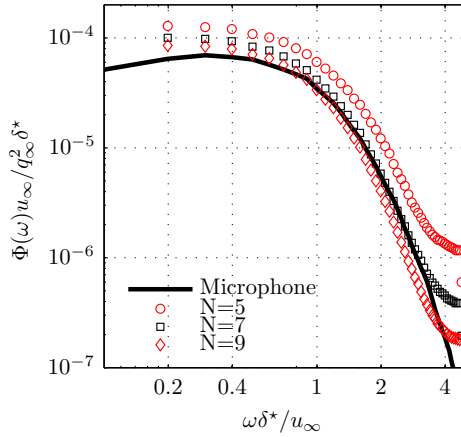


Figure 7.8: Comparison of pressure spectrum scaled with outer variables for different number of steps N considered for the estimation of the material derivative.

As expected, in this outer scaling representation the collected data collapses well at low frequency up to $\omega\delta^*/u_\infty \approx 1$. Due to the lower value for the ratio of outer and inner time scales in the experiments Re_T , the spectrum starts to fall off at lower frequencies when compared to the DNS and reference data at higher Reynolds number, in line with the model.

The pressure spectrum scaled on inner flow variables in figure 7.9b is consistent with previous works as the data shows an improved collapse for higher frequencies and a constant slope of ω^{-5} is retrieved in the high frequency range. The indicated slope of ω^{-1} is characteristic for the overlap range, which however becomes narrow for low Reynolds numbers [109]. The model of Goody [109] was calibrated based on the data of Schewe [110] for low Reynolds numbers and thus the perfect agreement for this case should not be surprising.

For the computation of the correlation coefficient, both signals are band-pass filtered for $0.3 \leq \omega\delta^*/u_\infty \leq 3$ ($300\text{Hz} \leq f \leq 3\text{kHz}$) and the microphone signal is sub-sampled to match the sampling frequency of the tomographic PIV system. Figure 7.10a shows a comparison of the time signals for a subset of the data. The cross-correlation coefficient reaches a maximum close to 0.6 (figure 7.10b).

With regard to the spatial structure of the pressure fluctuations, the averaged spatial correlation of the pressure field shows slightly spanwise elongated iso-contours (figure 7.11). For both experiment and simulation the correlation decreases to 0.1 within about twice the displacement thickness for the streamwise coordinate, and negative values for larger separations. These features resemble closely the generic shape of the unsteady surface pressure correlation function reported by Bull [229]. In his later review, Bull [107] comments that small scale structures contribute to circular contours, while large-scale fluctuations primarily contribute to spanwise elongated, oval contours as observed for

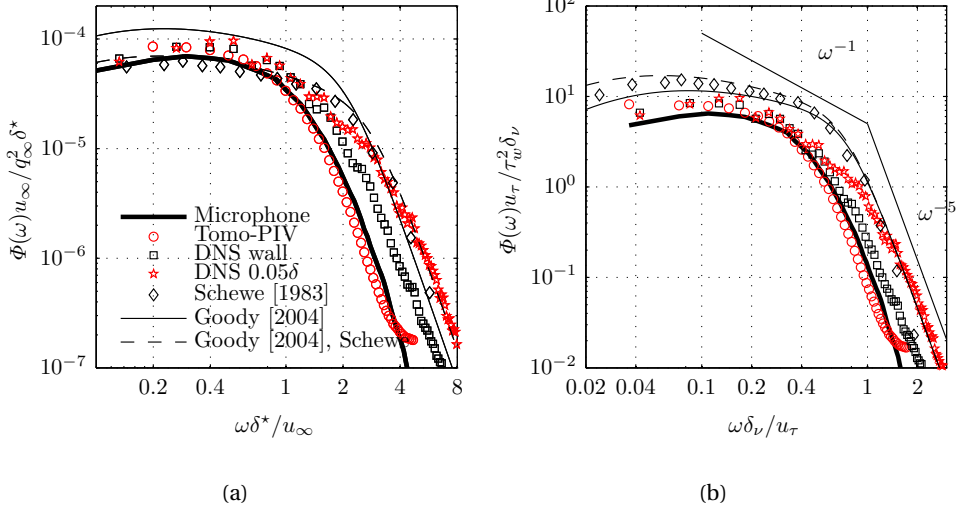


Figure 7.9: Pressure spectrum scaled with outer (a) and inner (b) variables, $N = 9$.

7

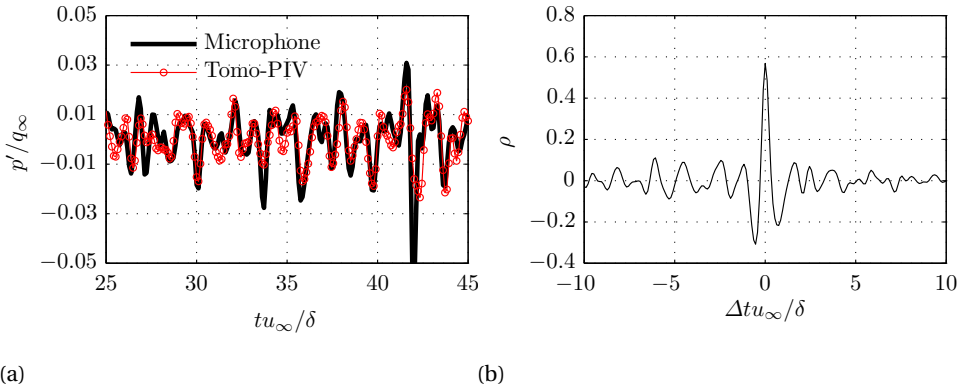


Figure 7.10: Comparison of pressure time series (a) and cross-correlation coefficient (b) between microphone signal and reconstruction from PIV data, $N = 9$.

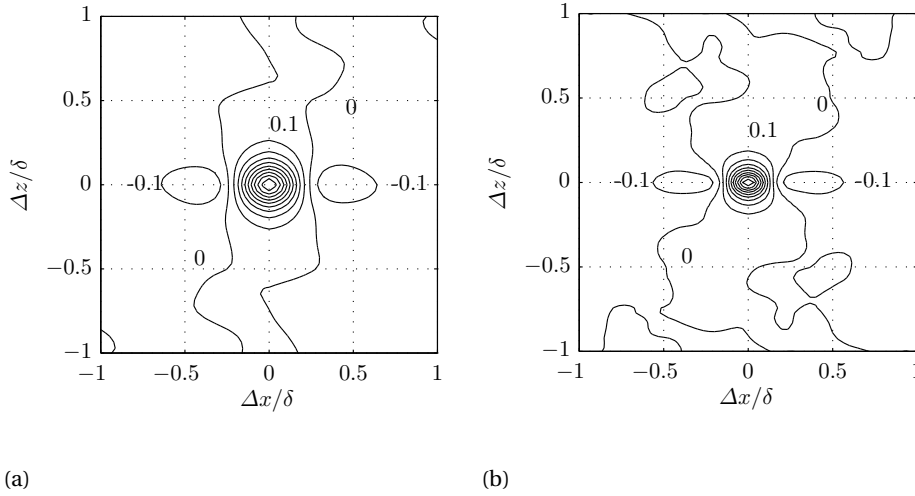


Figure 7.11: Time-averaged spatial correlation of pressure fluctuations based on PIV (a) and DNS (b) data filtered between $0.3 < \omega\delta/u_\infty < 3$, $N = 9$.

the instantaneous snapshots in figures 7.4b and 7.4d..

Based on the reconstructed pressure fields, the coherence defined in equation E.20 is evaluated by estimating cross- and auto-spectral densities. Denoting the spatial separation along the spanwise coordinate direction by Δz , the spanwise coherence function is $\gamma_p(\omega, \Delta z)$. Similarly, varying the streamwise separation results in the streamwise coherence function $\gamma_p(\omega, \Delta y)$.

For the coherence in streamwise direction a clear difference can be observed for stencils of different length ($N = 5, 7$, and 9) as demonstrated by the contour plots in figures 7.12a through 7.12c, also showing comparison to the DNS. The size of the interrogation window used during the correlation procedure is indicated for reference (dashed line, black) and the hatched area indicates the frequency range not regarded to be well measured (compare figure 7.5).

In general, the coherence along the streamwise direction attains higher values at low frequency and decays below the resolvable scales at higher frequencies $\omega\delta^*/u_\infty > 2.5$. For larger stencils, results show better comparison better with the reference. Thus, measurement noise likely causes underestimation of the coherence function for $N = 5$. The results for larger stencils appear to converge, as also observed for the auto-spectral density in figure 7.8, and show good agreement with the reference over the frequency range $0.5 < \omega\delta^*/u_\infty < 2.5$.

The spanwise coherence (figure 7.12d) shows larger discrepancy by overestimating the coherence when compared to the DNS data. Moreover, clear frequency dependence is not visible with only a small decay at high frequency. Considering the decay of the magnitude square coherence below levels of 0.2 over the width of one interrogation volume, it is suggested that the overestimation stems from limits imposed by the spatial res-

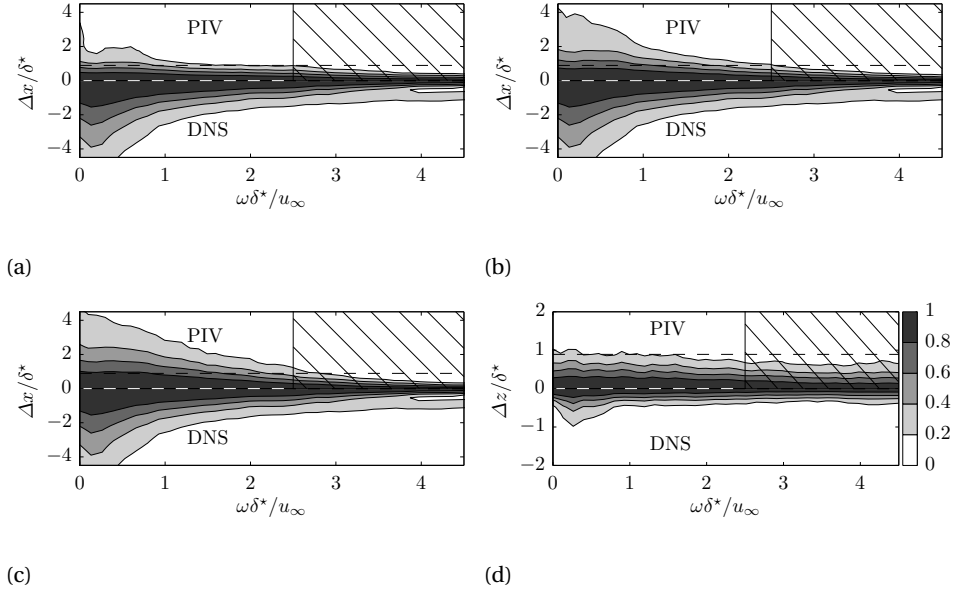


Figure 7.12: Contour plot of streamwise coherence $\gamma_p^2(\omega, \Delta x)$ with $N = 5$ (a), 7 (b), and 9 (c), and spanwise coherence $\gamma_p^2(\omega, \Delta z)$ with $N = 9$ (b) of pressure fluctuations (dashed line indicates size of interrogation window).

7

olution of the tomographic PIV measurements and correlation of the velocity field data over the interrogation window. Comparison to the coherence of the wall-normal velocity component in figure 7.7 reveals similar tendency. Overall, the coherence of pressure fluctuations over the span shows substantially faster decay compared to the streamwise direction, indicating the measurement resolution in this dimension to be a critical design parameter for similar experiments. The data displayed in figures 7.12c and 7.12d provides the basis for curve fits to estimate the correlation lengths.

7.3.4. ESTIMATION OF CORRELATION LENGTH

The estimation of the correlation length in equation 2.11 involves an integration of the coherence function over its spatial coordinate. Direct integration is prone to convergence issues, since limitations in the total number of samples prevent the coherence function to converge to zero. An exponential fit (equation 3.1) significantly improves the robustness of the estimation. Note, the limited resolution and overlap between neighbouring interrogation volumes in PIV provides a lower limit for the coherence and correlation length, since velocity vectors are correlated over this scale.

Figure 7.13a demonstrates the exponential fit, resulting in the streamwise correlation length for two frequencies ($\omega\delta^*/u_\infty = 0.73$ and 1.47) for the PIV data. The fitting procedure has been applied to the first 20 data points. Similarly, figure 7.13b demonstrates the exponential fit for the spanwise coherence.

Based on this fitting procedure the correlation length is determined at each frequency,

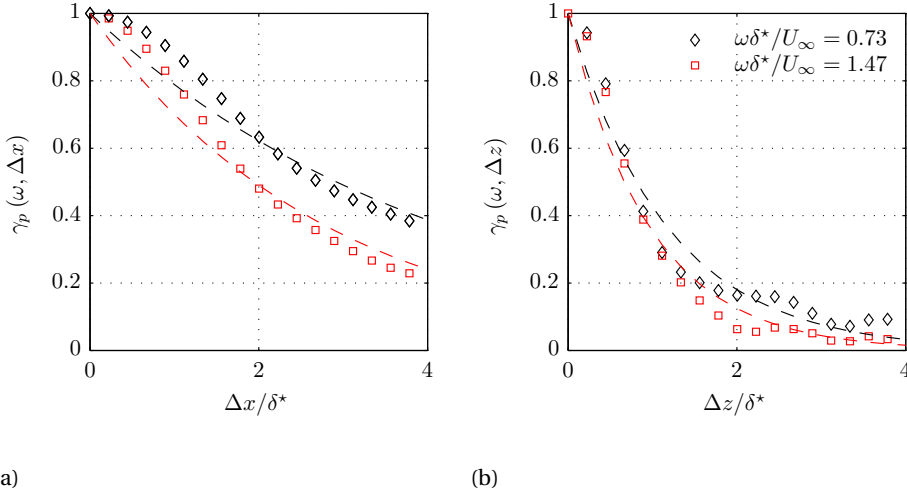


Figure 7.13: Exponential fit to streamwise (a) and spanwise (b) coherence data at $\omega\delta^*/u_\infty = 0.73$ and 1.47 , $N = 9$.

shown in figures 7.14a and 7.14b. The streamwise correlation length assumes substantially larger values than its spanwise counterpart for lower frequency. Estimates for the correlation length based on the semi-empirical models of Corcos [113] (equation 2.19) and Efimtsov [114] (equation 2.21) are added for comparison. The constants used in the model equations are $\alpha_1 = 0.1$, $\alpha_1 = 72.8$, and $\alpha_3 = 1.54$ for the streamwise coordinate direction and $\alpha_1 = 0.77$, $\alpha_2 = 548$, and $\alpha_3 = 13.5$ for the spanwise coordinate direction [111]. The horizontal line at $0.87\delta^*$ indicates the measurement resolution of the PIV measurements.

Figure 7.14a shows estimates for the streamwise correlation length based on measurements, simulation, and semi-empirical models. Consistently, the results show decaying value of l_x for increasing frequency. Results obtained using the semi-empirical models coincide for frequency exceeding about $\omega\delta^*/u_\infty = 1.5$. Qualitatively, PIV and DNS results show similar trends with almost identical slope for $0.8 \leq \omega\delta^*/u_\infty \leq 2$, but with values of the correlation length significantly lower than predicted by the models ($l_x/\delta^* =$ between 1 and 4). Note that both models rely on empirical constants, which have been established for considerably higher Reynolds numbers. Also, the values found for the semi-empirical parameters in the model equations show a significant scatter between experiments (section 2.2.2). Interestingly, at low frequency, the PIV results suggest a constant or decaying value for l_x , consistent with the extended model of Efimtsov [114]. Instead, the DNS simulation indicates an increase to substantially larger values of l_x . These discrepancies are not fully understood and require further scrutiny.

Comparison with figure 7.14b shows that the spanwise correlation length in the turbulent boundary layer is comparatively small ($1 - 1.5\delta^*$), and in particular smaller than the measurement resolution for $\omega\delta^*/u_\infty > 0.8$. Estimates are thus more challenging in the spanwise direction. Both semi-empirical models start collapsing at $\omega\delta^*/u_\infty > 1$. At

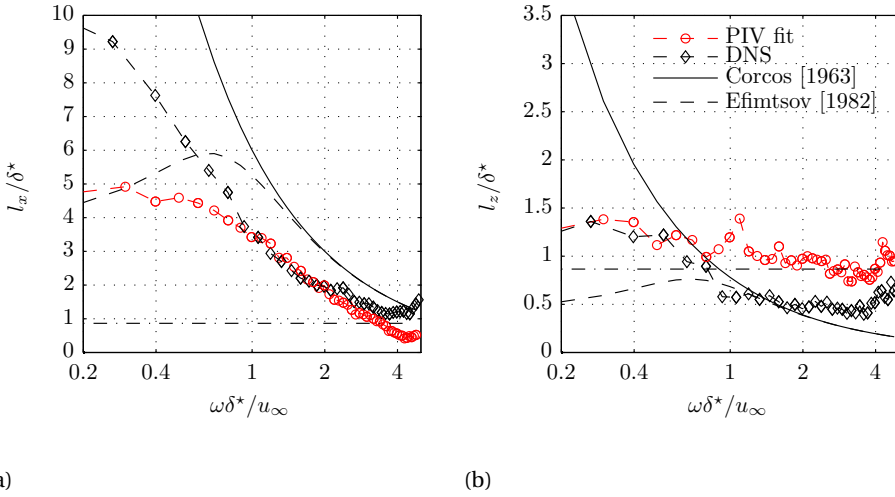


Figure 7.14: Streamwise (a) and spanwise (b) correlation length estimated from PIV and DNS data. Estimates based on model equations 2.19 (—) and 2.21 (---) for comparison and resolution of tomographic PIV in a plane parallel to the wall (—), $N = 9$.

such frequency, the estimate of l_z is only a fraction of δ^* , which implies very small structures. Estimates from PIV and DNS appear to agree with the model predictions over a limited range ($\omega\delta^*/u_\infty < 0.7$). The spatial resolution and measurement dynamic range are considered as the main limiting factors, since the value of the estimated correlation length tends to converge to the value of the window size.

7.4. CONCLUSION

Information on the spatio-temporal structure of the pressure field below a turbulent boundary layer at low Reynolds numbers has been obtained using volumetric velocity fields measured by tomographic high-speed PIV. Results have been compared to semi-empirical models, pinhole microphone measurements, and a DNS solution of a zero pressure gradient boundary layer at similar Reynolds number.

Estimates of the unsteady surface pressure auto-spectral density and coherence function depend on an appropriate choice of the scheme and stencil size used to estimate the material derivative. Small stencils do not attenuate measurement noise, which results in an underestimation of the coherence function and correlation length. Similar conclusion likely applies to the correlation method used for image interrogation, but this has not been investigated explicitly.

The auto-spectral density of the unsteady surface pressure, obtained using tomographic PIV, compares well to the direct measurement, obtained using pinhole microphones. Compared to the DNS solution and data available from literature, good collapse of the data is demonstrated. This collapse is obtained for higher frequencies when scaled on inner and for lower frequencies when scaled on outer flow variables. Measurement

noise causes substantial deviation from the measured unsteady surface pressure auto-spectral density for $\omega\delta^*/u_\infty > 3$, but also a lower frequency and in particular for small stencil size ($N = 3$).

In the case of streamwise coherence PIV based results are in good agreement with reference data from the DNS simulation over an extended range of frequencies $0.5 < \omega\delta^*/u_\infty < 2.5$. In contrast, the spanwise resolution of the coherence function is limited by the small spanwise correlation length relative to the measurement resolution and a consistent overestimation of the coherence function is observed.

For estimating the stream- and spanwise correlation length an exponential fit is applied. The streamwise correlation length results compare well to the DNS solution for a frequency range $0.8 \leq \omega\delta^*/u_\infty \leq 2.5$. PIV and DNS results follow similar trends when compared to the models of Corcos [113] and Efimtsov [114]. At frequencies exceeding $\omega\delta^*/u_\infty = 2.5$, the estimate of the correlation length is questionable due to limits on the spatial and temporal resolution available in the experiment. These limits must be taken into account when designing future experiments for assessing the spatio-temporal structure of turbulent flows based on tomographic PIV and, in particular, the unsteady surface pressure field of a turbulent boundary layer.

8

PIV BASED ESTIMATION OF TRAILING EDGE NOISE

*There is nothing new to be discovered in physics now.
All that remains is more and more precise measurement.*

attributed to William Thomson, Baron Kelvin and Scottish physicist

The feasibility of estimating broadband trailing edge noise with high-speed tomographic Particle Image Velocimetry (PIV) measurements is studied. A thin plate terminating in a sharp trailing edge provides a generic test case for turbulent boundary layer trailing edge interaction noise. Far-field noise is linked to the wavenumber-frequency spectrum of the surface pressure fluctuations in proximity of the trailing edge through diffraction theory. High-speed tomographic PIV measurements return volumetric and time-resolved information about all velocity components for the resolved spatio-temporal scales and can therefore provide the required statistical quantities. For the turbulent boundary layer interacting with the trailing edge, these statistics include the auto-spectral density, spanwise correlation length, and convective velocity of the unsteady surface pressure, which are thus estimated.

Acoustic phased array measurements in an anechoic environment provide a reference for comparison. Over the resolved frequency band, PIV based noise estimation results compare favorably with the reference measurements. Especially at lower frequencies, where existing, empirical models for the unsteady surface pressure spectrum are not accounted for, tomographic PIV can offer an alternative approach to complex and intrusive model instrumentation for assessing the relevant statistical quantities.

Parts of this chapter have been published in the Journal of Sound and Vibration **346** (2015) [66].

8.1. INTRODUCTORY REMARKS

TRAILING EDGE NOISE has received ample attention in recent years due to its relevance in wind turbine applications and has become increasingly important for aircraft design due to the reduction of other, primary noise sources [5, 230]. Therefore, new methods for the assessment and characterization of the aeroacoustic source are of interest. Theory suggests that a complete description of the source for the turbulent boundary layer trailing edge interaction problem requires volumetric and time-resolved information [17, 72, 79, 86]. To this end, Morris [12] recently highlighted the use of advanced Particle Image Velocimetry (PIV) methods as a complementary tool for aeroacoustic research.

With the development of tomographic PIV and high-power diode-pumped high-speed lasers and CMOS cameras, PIV has the potential to provide volumetric and time-resolved information about the flow field. In the past, PIV systems have been employed in studies relating to aeroacoustics by a number of researchers. For instance, Shannon and Morris [46] investigated the noise generation process due to periodic vortex shedding at a beveled trailing edge by phase-locked PIV. Based on planar high-speed PIV Lorenzoni *et al.* [62] estimated the noise due to vortex-structure interaction for a cylinder-airfoil problem and found that the tonal component associated to coherent shedding from the cylinder showed good agreement when compared to acoustic measurements. However, an estimation of the broadband component showed reasonable agreement only after the spanwise correlation length of the velocity fluctuations was accounted for, which required a complementary planar PIV experiment in a plane including the spanwise direction. Therefore, deviations were ascribed to the influence of the spanwise correlation of the velocity field, which cannot be estimated from a single planar PIV experiment. Similar observations were reported by Koschatzky *et al.* [60] for the case of cavity noise, who likewise observed good agreement for the tonal component and attributed deviations in the broadband component to the absence of information about the spanwise coherence. In agreement with theory, these observations suggest that for a full source description in broadband type turbulent boundary layer trailing edge interaction noise problems time-resolved and volumetric measurements are required.

The objective of this chapter is to assess and demonstrate the feasibility of broadband noise prediction for the case of a sharp trailing edge by means of time-resolved tomographic PIV. The interaction of a developed turbulent boundary layer over a flat plate with a sharp trailing edge is considered. The chapter describes the experimental procedure to estimate broadband noise. Underlying aspect of aeroacoustic theory are discussed in section 2.1.3. The relevant statistical quantities of the unsteady surface pressure field, which is deduced using the methodology described in section 3.3, are assessed. Finally, noise predictions based on PIV are compared to phased array measurements.

8.2. DESCRIPTION OF EXPERIMENTS

Acoustic phased array and tomographic PIV measurements are conducted. Acoustic measurements are performed in the NLR's small anechoic tunnel (KAT), while the tomographic PIV experiments are carried out at a low speed wind tunnel at Delft University of

Technology.

For the experiments a flat plate (chord length $c = 600\text{mm}$) with elliptical leading edge and wedge shaped, sharp trailing edge was selected. The maximum thickness of the plate is 10mm and its surfaces include an angle of 4.8° at the trailing edge. The plate is mounted vertically between end-plates at zero angle of attack.

Transition of the boundary layers on both sides of the plate is forced by 3D roughness elements (carborundum, grain size 0.84mm) distributed randomly over a 10mm wide band, located 100mm downstream of the leading edge and covering the entire span. In addition to the use of a tripping device, the chord based Reynolds numbers $Re_c \geq 400,000$ (for $u_\infty \geq 10\text{m/s}$) are within the turbulent regime.

8.2.1. ACOUSTIC MEASUREMENTS

The small anechoic tunnel at NLR (KAT) is an open circuit, open jet wind tunnel. A room of dimensions $5 \times 5 \times 3\text{m}^3$ surrounds the test section. Its walls are covered with foam wedges (depth 0.5m), resulting in absorption higher than 99% above 500Hz. Two horizontal end-plates on the upper and lower side of the rectangular $0.38 \times 0.51\text{m}^2$ nozzle form a semi-open test section for airfoil self-noise measurements. To suppress reflections, the end-plates are acoustically lined with a layer of sound absorbing foam (depth 55mm) covered by a 5% open perforated plate. Despite the anechoic environment, the measurement of boundary layer trailing edge interaction noise remains challenging and requires the use of a phased array to distinguish the trailing edge noise source from parasitic noise sources.

A microphone array, consisting of 48 LinearX *M51* 1/2-inch microphones (aperture $0.8 \times 0.6\text{m}^2$), is mounted in an open grid. It is placed at a distance of 0.6m from the tunnel axis (figure 8.1) with its center in the mid-span plane. The small distance is chosen to account for the low signal-to-noise ratio expected for turbulent boundary layer trailing edge interaction noise. The flow velocity varied in the range from $u_\infty = 15\text{m/s}$ to 75m/s .

The layout of the microphones is designed for maximum side-lobe suppression between 1kHz and 20kHz (figure 8.2). All but two closely spaced microphones at the center of the array are equipped with windscreens and calibrated using a piston phone. The calibration was corrected based on frequency dependent calibration curves available for each individual microphone and the is additionally confirmed using a calibration source at a known position. No corrections are applied for microphone directivity and corresponding effects amounts to less than 2dB for angles up to 45° and frequency up to 15kHz. Acoustic data from the array microphones is synchronously measured using the VIPER data-acquisition system [231]. The data acquisition system implements a 500Hz analogue high-pass and 15.36kHz analogue low-pass filter. Data is sampled at a frequency of 30.72kHz for a measurement time of 30s.

The array data is processed using the SOLACAN software [232]. The beamforming is based on the conventional beamforming technique [233], where elements of the main diagonal in the cross-power matrix are disregarded. It follows the common approach of representing the acoustic source by a distribution of point sources. Further, non-uniform microphone spacing, coherence loss effects, and shear layer refraction are accounted for and are elaborated on below. For the present experiment, the beamforming is performed in the chord plane ($y = 0$). Source maps with the 1/3-octave band source

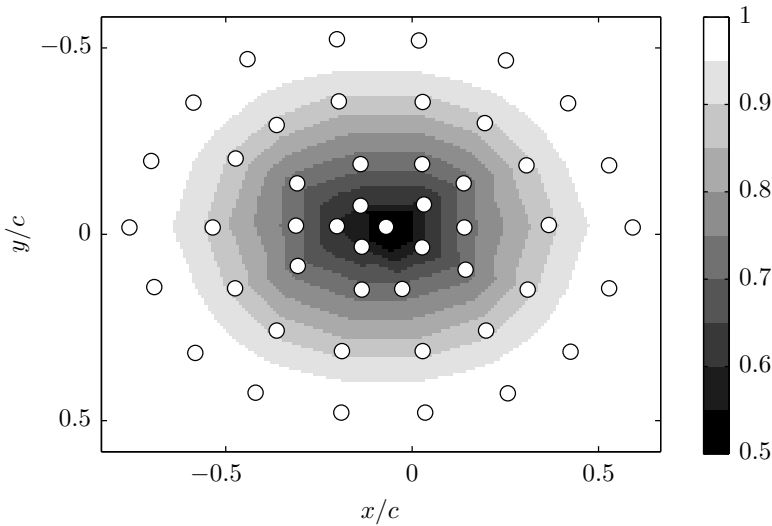


Figure 8.2: Phased array layout with microphone positions (circles) and contour levels of associated weighting factors, inversely proportional to local density of microphone distribution.

represents the response to a point source. Depending on the width of the point spread function, the fixed integration region does not contain the entire power associated to a source at the trailing edge. Furthermore, sources from the portion of the span located outside of the integration region contribute to the integral. These effects are commonly denoted as *spectral leakage*. To account for spectral leakage, an incoherent line source covering the entire span is simulated. The assumption of incoherent sources is justified due to the small correlation length compared to the spatial resolution of the array [235]. The beamforming algorithm and integration procedure is then applied to the simulated signals at the location of the array microphones and a correction factor accounting for the difference between measured and actual source power is derived. The correction ranges from -6.3dB at 0.63kHz to 0.3dB at 12.5kHz . For details on this line source correction procedure and the determination of absolute levels from phased array measurements, the reader is referred to Oerlemans and Sijtsma [235]. The corrected results then provide the SWL for 100mm of span.

Despite the use of source integration around the trailing edge, the measured SWL can be influenced by background noise from the wind tunnel. This background noise contribution was quantified by performing acoustic measurements without model at all velocities. If the difference between measured levels with and without the plate installed was larger than 3dB , the background noise level was subtracted. Results for frequencies where the difference was less than 3dB are not included in the spectra presented in this study.

The interpretation of the array measurements is not trivial and requires further explanation: the integrated SWL measured by the array represents the SWL of an *equivalent point source* (monopole) required to produce the average sound pressure level (SPL),

reference pressure $p_{ref} = 20\mu Pa$) over the locations of the array microphones [235]. The SPL induced by this equivalent point source at an observer distance $r_O = \sqrt{x_O^2 + y_O^2 + z_O^2}$ can then be obtained through application of equation 8.1).

$$SPL = SWL + 10\log_{10} \left(\frac{\rho c_0}{4\pi r_O^2} \frac{P_{ref}}{P_{ref}^2} \right) \quad (8.1)$$

The equivalent SWL measured by the array is influenced by the directivity of noise emission and distribution of microphones. For comparison of the predicted SWL based on tomographic PIV with the values measured by the array, the equivalent SWL for 0.1 m span needs to be obtained for the predicted results. First, the 1/3-octave band equivalent SWL for a point source at center span is computed at microphone location \mathbf{x}_m through equation 8.2, where $\Phi_{aa}(\omega, \mathbf{x}_m)$ is given by equation 2.35 and integration in the frequency domain is performed over 1/3-octave bands with center frequency f_c .

$$SWL_m(f_c) = 10\log_{10} \left(\frac{4\pi r_O^2}{\rho c_0} \frac{1}{P_{ref}} \int_{\sqrt{2}\pi f_c}^{2^{3/2}\pi f_c} \Phi_{aa}(\omega, \mathbf{x}_m) d\omega \right) \quad (8.2)$$

The equivalent SWL for comparison to the array measurements is obtained through averaging the results of equation 8.2 over all microphone locations. As for the array measurements, the average SPL over the solid angle covered by the array aperture can be obtained through application of equation 8.1.

Hot-wire measurements were taken with a DANTEC StreamLine CTA system. A single wire probe (diameter $5\mu m$) is aligned parallel to the trailing edge for comparison with the PIV data. Wake profiles are measured 5mm downstream of the trailing edge ($x/c = 0.0083$) by traversing the hot-wire along the y -coordinate direction. The analogue signal is low-pass filtered (cut-off frequency 10kHz) and sampled at a rate of 18kHz for 10s. For the hot-wire spectra presented in the results section, the frequency band up to 6kHz are considered.

8.2.2. FLOW FIELD MEASUREMENTS

High-speed tomographic PIV experiments [176] were carried out in a $0.4 \times 0.4m^2$ open jet, open circuit tunnel at Delft University of Technology (W-Tunnel) at a free stream velocity of $u_\infty = 10m/s$.

Four Photron *Fastcam* SA1.1 CMOS cameras ($1,024 \times 1,024px$, 12 bits, $20\mu m$ pixel pitch) equipped with Nikon *Micro-Nikkor* 105mm prime objectives and Scheimpflug adapters were used for imaging, while illumination was provided by a Quantronix *Darwin Duo* Nd:YLF (25mJ per pulse at 1kHz) laser and a multi-pass light amplification system was used to increase the light intensity in the measurement volume [180]. The laser beam was cut by knife-edges aligned parallel to the surface of the plate, to form a measurement volume of size $17 \times 6.6 \times 32mm^3$ flush to the surface on one side of the trailing edge (figure 8.3). A numerical aperture of $f_\# = 11$ provided a depth of field sufficient to maintain illuminated particles within focus. After an initial target calibration, volume self-calibration [221] was used to correct the calibration function. A sequence of images

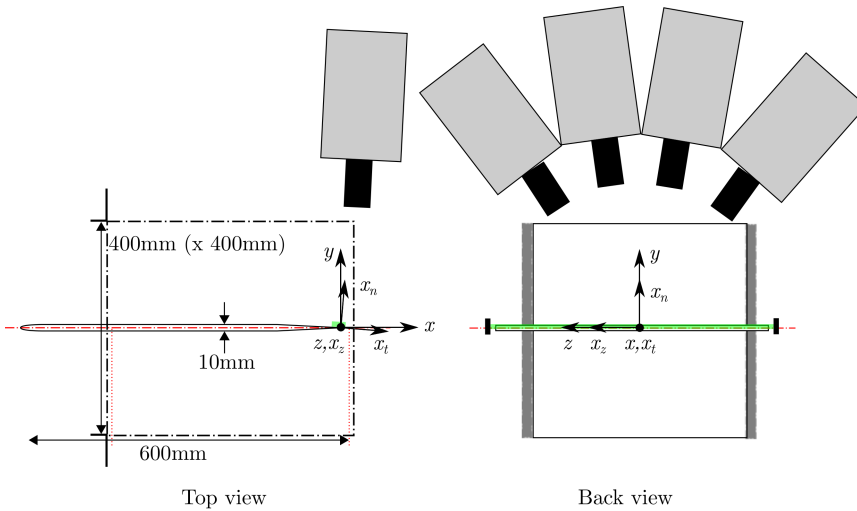


Figure 8.3: Schematic of set-up for tomographic PIV measurements.

was recorded at acquisition frequency $f_{acq} = 10\text{kHz}$ for about 0.4s. The particle displacement between consecutive images in the free stream is approximately 1mm (28 voxels) and the particle image density is estimated to be 0.06 *ppp* (particles per pixel).

LaVision *DaVis* 8 was used for self-calibration and reconstruction with the MART algorithm, resulting in objects containing the 3D distribution of intensity. The vector field sequence was obtained analyzing the reconstructed objects with the Fluid Trajectory Correlation method [173], final interrogation volume size of $28 \times 16 \times 28\text{vxl}$ ($1 \times 0.58 \times 1\text{mm}^3$), and spatial overlap of 75%. The analysis is based on a short sequence of 7 subsequent objects and the motion of the fluid parcel along the trajectory is approximated locally by a second order polynomial. This procedure results in a vector spacing of 0.15mm along the wall-normal and 0.25mm along the other coordinate directions. Due to the strong shear rate close to the wall, the iterative analysis is stabilized by setting any velocity vector at or below the wall to zero. Table 8.1 gives an overview of the parameters related to the tomographic PIV experiment.

Error estimation was described in section 3.3.5. Considering equation 3.14 with a digital image resolution of $S = 28\text{vxl}/\text{mm}$ the random measurement error on the velocity field is $\epsilon_{u,rand} = 0.071\text{m/s}$. With an average particle acceleration within the inner layer of about $\|\mathbf{D}\mathbf{u}_p/Dt\| \approx 1,000\text{m/s}^2$ (estimated from measurements) the systematic error on the velocity field is estimated as $\epsilon_{u,sys} = 0.025\text{m/s}$ (equation 3.15).

With the same estimate for the particle acceleration and an approximation of the gradient based on the mean velocity field in the inner layer $|\nabla \cdot \mathbf{u}| = 1,000/\text{s}$ (estimated from measurements), the truncation error (equation 3.20) on the material derivative estimate for a stencil $N = 5$ is $\epsilon_{Lag,trunc} = 100\text{m/s}^2$ or 10% when compared to the average value. The random error on the material derivative due to the random measurement error of the velocity field (equation 3.21) is about 360m/s^2 for $N = 5$ and decreases with increasing stencil size N . The contribution to the error due to the systematic measurement error

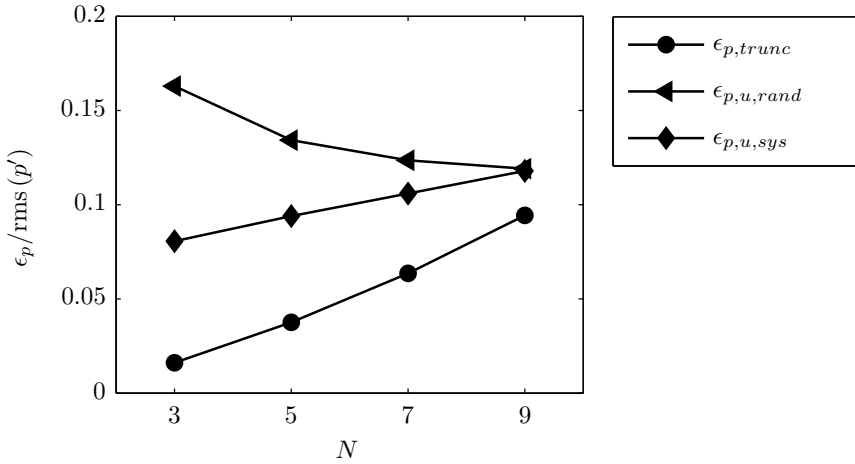


Figure 8.4: Estimated errors of reconstructed wall pressure field relative to root-mean-square rms(p').

on the velocity field is estimated with equation 3.22 to be $\epsilon_{Lag, u, sys} = 250 \text{m/s}^2$.

The corresponding error estimates on the pressure fluctuations are obtained from equation 3.23 with $h = 0.25 \text{mm}$. Figure 8.4 shows the final error estimates with respect to the measured rms(p') of the wall pressure fluctuations as a function of stencil size. On one hand, this error analysis (figure 8.4) indicates that the random error decreases by 5% for a stencil of $N = 9$ compared to $N = 3$. On the other hand, systematic error become dominant for large stencils. Note that these error levels are in good agreement with the values given by Ghaemi *et al.* [181] and Pröbsting *et al.* [183].

8

Complementary planar PIV provide a larger field of view of $52 \times 52 \text{mm}^2$ encompassing a region centered on the trailing edge in the mid span plane. A single Photron *Fastcam* SA 1.1 was used to capture the image sequence. The Quantronix *Darwin* Duo and light sheet optics were located downstream of the test section, providing simultaneous illumination on both sides of the plate. A series of 1,500 double frame images were acquired at 125Hz with a pulse separation of $80 \mu\text{s}$, corresponding to a free stream displacement of approximately 16px. LaVision *DaVis* 8 was used for interrogation with a final window size of $0.81 \times 0.81 \text{mm}^2$ (16×16 pixels) and 75% overlap. This procedure results in vector fields with a vector spacing of about 0.2mm. Table 8.2 gives an overview of the PIV related parameters for this configuration.

The unsteady surface pressure is reconstructed following the methodology described in 3.3. To evaluated the spanwise correlation length $l_z(\omega)$, the normalized cross-spectral density $\gamma(\omega, \Delta z) = \Phi_{pp}(\omega, \Delta z) / \Phi_{pp}(\omega)$ is required. Thus, the unsteady surface pressure cross-spectral density $\Phi_{pp}(\omega, \Delta z)$ is evaluated using a modified periodogram method [203]. A Hamming window is applied to the segments consisting of 128 samples and the data is processed with 50% overlap. Additionally, the average over the homogeneous direction along the span is considered. This procedure provides a suitable estimator

Table 8.1: Parameters for tomographic PIV experiment.

Parameter	Symbol	Value
Measurement domain	$L_x \times L_y \times L_z$	$17 \times 6.6 \times 32 \text{mm}^3$
Magnification	M	0.55
Imaging resolution	S	28vxl/mm
Interrogation volume size		$28 \times 16 \times 28 \text{vxl}$
	$\delta_x \times \delta_y \times \delta_z$	$1 \times 0.58 \times 1 \text{mm}^3$ $0.08 \times 0.05 \times 0.08 \delta_{99}^3$
Pulse separation	dt	$100 \mu\text{s}$
Acquisition frequency	f_{acq}	10kHz
	$f_{acq} \delta_{99} / u_\infty$	12.6
Number of samples		4,096

Table 8.2: Parameters for planar PIV experiment.

Parameter	Symbol	Value
Field of view		$52 \times 52 \text{mm}^2$
Magnification	M	0.39
Imaging resolution	S	19.6vxl/mm
Interrogation window size		$16 \times 16 \text{px}$
	$\delta_x \times \delta_y$	$0.81 \times 0.81 \text{mm}^2$ $0.06 \times 0.06 \delta_{99}^2$
Pulse separation	dt	$80 \mu\text{s}$
Acquisition frequency	f_{acq}	125Hz
	$f \delta_{99} / u_\infty$	0.16
Number of samples	N	1,500

Table 8.3: Boundary layer parameters determined from planar PIV measurements at $x_t/c = -0.025$, $u_\infty = 10\text{m/s}$.

Parameter	Symbol	Value
Displacement thickness	δ^*	2.5mm
Momentum thickness	θ	1.7mm
Boundary layer thickness	δ_{99}	$13.1 \pm 0.4\text{mm}$
	δ_{95}	$10.3 \pm 0.4\text{mm}$
Viscous length scale (estimated)	δ_ν	$32\mu\text{m}$
Reynolds number	Re_{δ^*}	1,660
	Re_θ	1,150
	$Re_{\delta_{99}}$	8,830
Shape factor	$H = \delta^*/\theta$	1.45

[236, 237]. A similar procedure is applied to estimate the auto-spectral density and coherence of the velocity field.

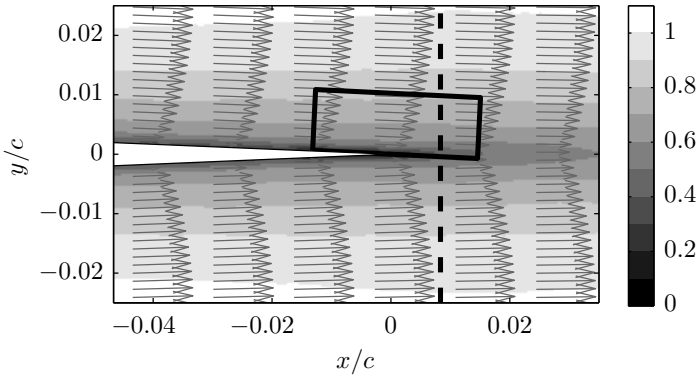
8.3. RESULTS AND DISCUSSION

8.3.1. FLOW CHARACTERISTICS

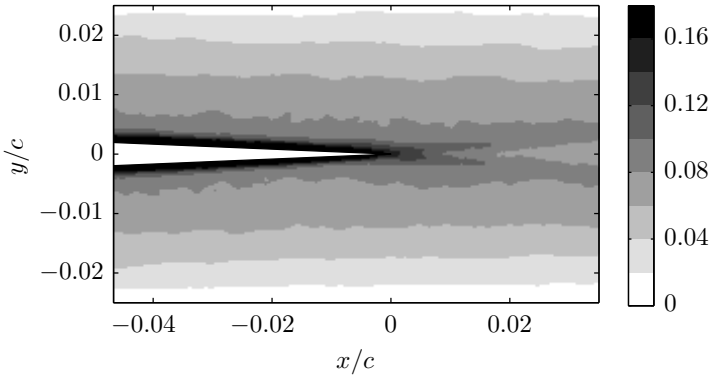
Comparison of the noise spectra acquired at different Reynolds numbers requires knowledge of the scaling parameters for the flow around the trailing edge. The latter are obtained from planar PIV measurements. Figure 8.5 shows the average velocity magnitude (figure 8.5a) and turbulence intensity (figure 8.5b) around the sharp trailing edge. The box in figure 8.5a indicates the dimensions of the measurement volume for tomographic PIV and the dashed line the sampling location for the hot-wire measurements. The small variation in wake thickness close to the trailing edge (figure 8.5a) and the double peak structure of the turbulent fluctuations in the near wake (figure 8.5b) are consistent with the merging of turbulent boundary layers from opposite sides of the plate. The absence of vortex shedding confirms that the sharp edge geometry can be considered as a test case for the turbulent boundary layer trailing edge interaction noise.

Visualization of the volumetric tomographic PIV velocity field data with iso-surfaces of the Q-criterion for vortex identification [238] and contour levels of spanwise vorticity ($\omega_z = \partial v/\partial x - \partial u/\partial y$) reveals the instantaneous flow structure (figure 8.6) with coherent vortex filaments. The existence of coherent vortex filaments in turbulent boundary layers is well established and has often been discussed in literature [227]. These filaments, inclined by 45° , often resembling the characteristic shape of a hairpin legs. The typical scale of these vortex filaments is typically larger than the interrogation volume size ($\delta^*/\delta_y \approx 4.4$). It should be noted that due to the measurement volume does not extend to the free stream. Therefore, the heads of the hairpin vortices are not always captured.

The boundary layer parameters for a location upstream of the trailing edge ($x_t = -15\text{mm}$) based on the planar PIV measurements are tabulated here for reference (table 8.3). For a definition of the integral quantities and inner boundary layer parameters the reader is referred to White [127]). δ_{95} and δ_{99} denote the boundary layer thickness



(a) Average of velocity magnitude $\overline{|\mathbf{u}|}/u_\infty$ and velocity vectors. Cross-section of tomographic PIV measurement volume (box) and hot-wire measurement position (dashed line).



(b) Root-mean-square of velocity magnitude $\text{rms}(|\mathbf{u}|)/u_\infty$.

Figure 8.5: Time-averaged velocity distribution (a) and turbulent fluctuations (b) from planar PIV measurements.

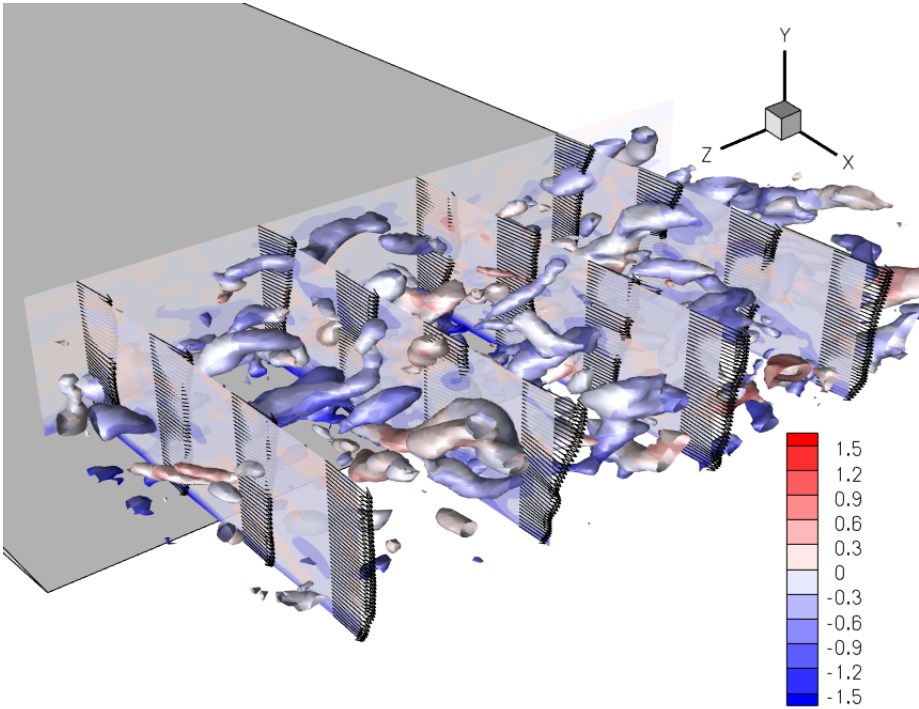


Figure 8.6: Visualization of coherent structures by iso-surfaces of Q and velocity vectors in planes along the span. The color levels indicate the value of the spanwise vorticity component $\omega_z \delta^* / u_\infty = (\partial v / \partial x - \partial u / \partial y) \delta^* / u_\infty$.

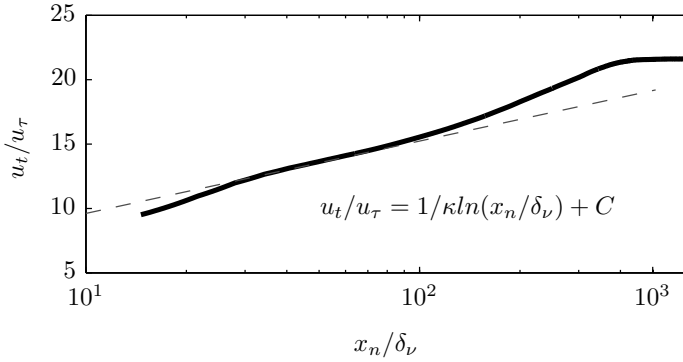


Figure 8.7: Boundary layer profile of average velocity component u_t obtained from planar PIV measurements, $x_t/c = -0.025$. Inner boundary layer scales are estimated based on a Clauser fit [225].

based on 95% and 99% edge velocity, respectively. Inner scales are estimated based on a Clauser plot [225] with $\kappa = 0.41$ and $C = 4$ (figure 8.7), which results in a shear velocity of $u_\tau = 0.47 \pm 0.02 \text{ m/s}$, with the uncertainty value given due to the finite resolution of the measurement. The corresponding viscous length scale is $\delta_\nu = \mu / (\rho u_\tau) = 32 \mu\text{m}$. A shape factor of $H = \delta^*/\theta = 1.45$ confirms the presence of a turbulent boundary layer [127]. Pröbsting *et al.* [183] presented a characterization of the boundary layer on the same plate upstream of the tapered trailing edge part and found comparable values for the boundary layer parameters. Apart from the higher Reynolds number at the trailing edge, differences can be attributed to the slight adverse pressure gradient over the wedge and transition to the wake.

A meaningful comparison between the acoustic and flow field measurements requires that the flow conditions in the two facilities match and further that the experimental results can be scaled. For this purpose the velocity profiles in the wake measured during the PIV and acoustic experiments (hot-wire measurements) are compared and scaling parameters determined. Figure 8.8 shows a comparison of the in-plane average and *rms* (root-mean-square) velocity magnitude along the y -coordinate direction in the near wake at $x = 5 \text{ mm}$ ($x/c = 0.0083$) behind the trailing edge (figure 8.5, indicated by dashed line). The average velocity in figure 8.8a measured by hot-wire data (symbols) and PIV measurements (lines) in the two experiments agrees within 2% of the free stream velocity. The maximum turbulence intensity (figure 8.8b) is found near $y/\delta_w^* 0.1$. Compared to the average velocity magnitude, the fluctuation level shows a stronger tendency to decrease with Reynolds number near the center of the wake, which is attributed to Reynolds number dependence of the wake flow and the fixed measurement location. Fluctuation levels measured in the PIV experiments are slightly lower than those measured by hot-wire anemometry (about 5%). The levels measured by the hot-wire probe in the free-stream indicates that a higher noise component adds to the root-mean-square value shown in figure 8.5b, which might cause such deviation.

The definitions of boundary layer integral quantities are extended to the wake by integrating over the measured wake profile (see texts, e.g. [127]). Table 8.4 lists the wake

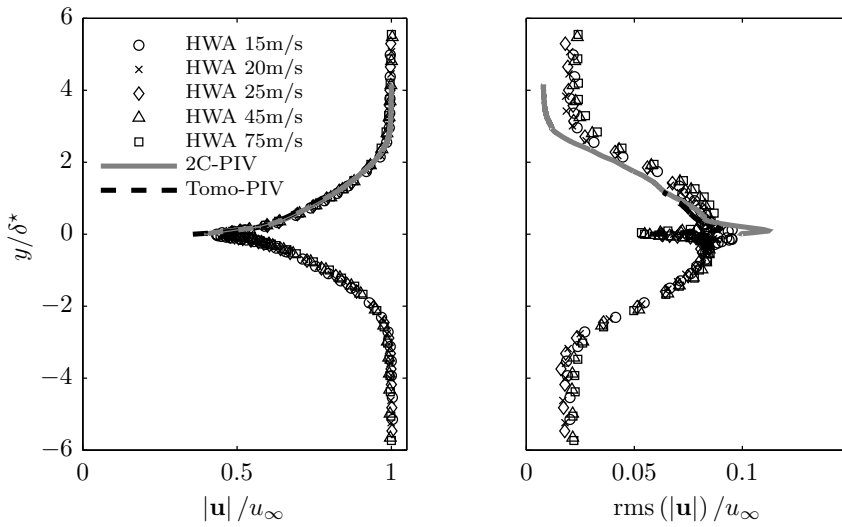
(a) Average of velocity magnitude $\overline{|\mathbf{u}|}$.(b) Root-mean-square of velocity magnitude $\text{rms}(|\mathbf{u}|)$.

Figure 8.8: Comparison of flow field statistics in the near wake measured with PIV (lines) and hot-wire anemometry (markers) during the acoustic measurement campaign (markers) at $x/c = 0.0083$. For PIV the 2-component velocity magnitude $|\mathbf{u}| = \sqrt{u^2 + v^2}$ is considered.

Table 8.4: Wake thickness parameters for PIV and acoustic measurements.

		PIV		Acoustic measurements			
[3pt] Ref. velocity	u_∞ [m/s]	10	15	20	25	45	75
Displacement thickness	δ_w^* [mm]	5.0	4.9	4.8	4.6	4.5	4.4
Momentum thickness	θ_w [mm]	3.5	3.5	3.4	3.3	3.2	3.2
Wake thickness	δ_{95_w} [mm]	21.0	19.7	19.5	19.4	18.9	18.9

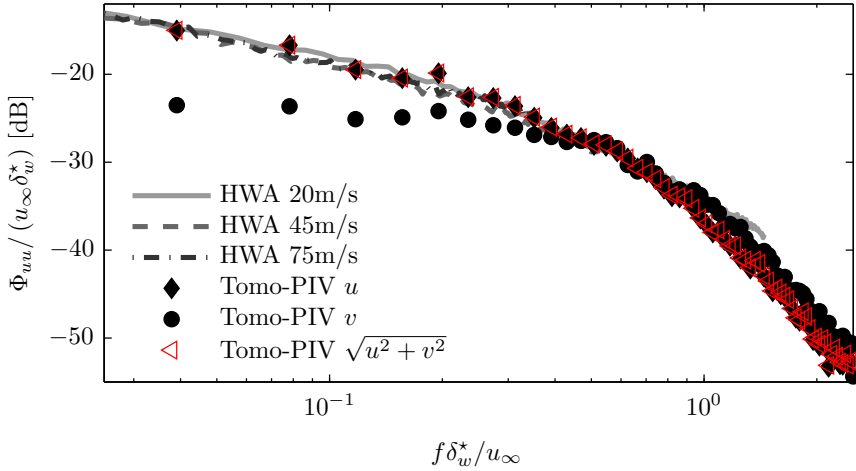


Figure 8.9: Comparison of velocity auto-spectral density measured by tomographic PIV (markers) and hot-wire anemometry (lines) during the acoustic measurement campaign ($x/c = 0.0083$, $y/c = 0.005$). For hot-wire measurements, the measured velocity magnitude fluctuations are considered. For PIV, spectra for the individual velocity components (u , v) and 2-component velocity magnitude ($|\mathbf{u}| = \sqrt{u^2 + v^2}$) are shown.

parameters. To distinguish the latter from boundary layer parameters the subscript w is introduced. Comparison of the displacement thickness in the wake and boundary layer reveals a ratio $\delta_w^*/\delta^* \approx 2$ as expected for a sharp trailing edge in the near wake.

The distribution of scales present in the turbulent near wake results in a broadband type spectrum for the velocity components at $x/c = 0.0083$, $y/c = 0.005$ (figure 8.9). While the spectra of the u - and v -velocity components at lower frequency show differences of up to 10dB, the fluctuations attain a more isotropic character at higher frequency. The differences at low frequency are ascribed to the presence of low speed streaks in the turbulent boundary layer, which introduce larger fluctuations in the streamwise component in this range. Comparison with hot-wire measurements shows a good agreement for frequencies $f \delta_w^*/u_\infty < 1$ (2kHz).

As discussed in section 2.2.2, the spanwise correlation length of the unsteady surface pressure is an important modeling parameter. The latter will be examined first for velocity fluctuations and later for the more relevant pressure fluctuations. Figure 8.10 shows

the spanwise coherence magnitude $\sqrt{\gamma^2(\omega, \Delta z)}$ of the tangential and wall-normal velocity fluctuations at $x_t/c = 0$ and $x_n/c = 0.005$. By definition, the coherence has a unit value at $\Delta z/\delta^* = 0$. With increasing separation, the coherence generally decreases to values below 0.2, before reaching a second maximum at about $\Delta z/\delta^* = 2.3$ for the streamwise component and $\Delta z/\delta^* = 1.5$ for the wall-normal component. The exact separation associated to this second maximum is a function of frequency. Corresponding scales in terms of boundary layer displacement thickness $\Delta z/\delta_v = 100$ are on the order of the spacing between low speed streaks [227]. The larger spacing for the streamwise velocity component might be related to the spacing of low speed streaks, while the shorter spacing for the wall-normal velocity component is related to the streamwise vortices responsible for their production. For high frequencies and separation Δz smaller than the interrogation window size (figure 8.10, dashed line), the coherence magnitude is bound by a minimum value due to correlation of the measured velocity vectors in this domain [183]. The correlation length in the high frequency range is therefore expected to be overestimated.

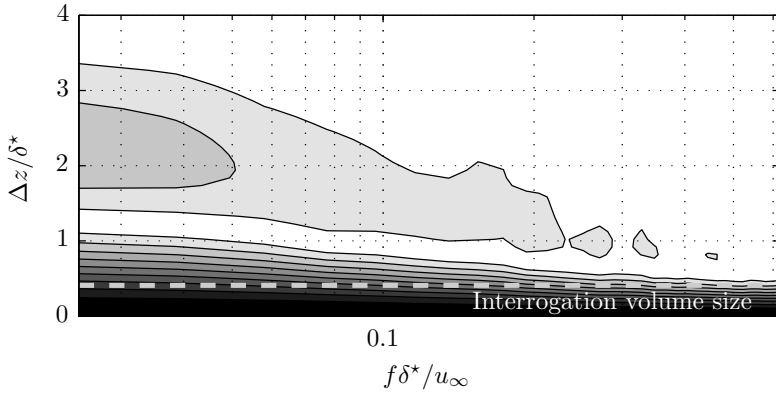
Due to the presence of the secondary maxima for both velocity components (figure 8.10), an exponential fit is not suitable for an estimation of the correlation length of velocity components in a turbulent boundary layer. Therefore, the correlation length is estimated by evaluation of the integral expression over Δz . The results obtained through numerical integration indicate a decrease by a factor of 2 between $f\delta^*/u_\infty = 0.04$ and 0.4 (figure 8.11).

8.3.2. NOISE EMISSION

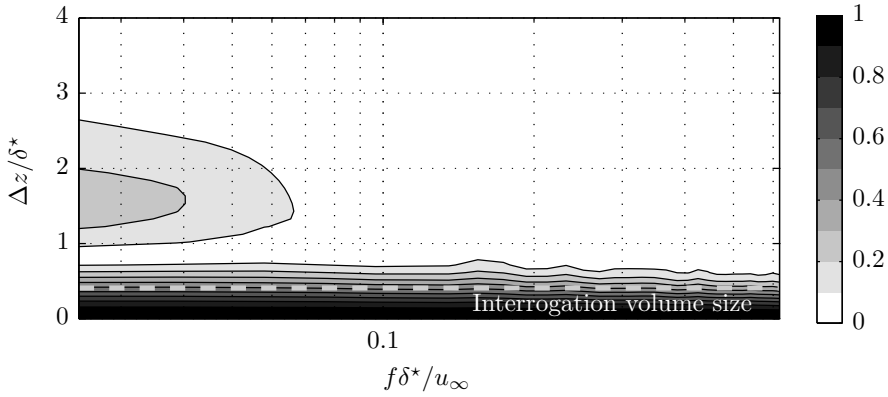
To isolate trailing edge noise from other noise sources, source maps are generated through the procedure detailed in section 8.2.1. Figure 8.12 shows results obtained at free stream velocity of 75m/s with the frequency varying between 1.5kHz ($f\delta_w^*/u_\infty = 0.09$) and 10kHz ($f\delta_w^*/u_\infty = 0.59$). For all frequencies the noise source is centered on the trailing edge. With increasing frequency and decreasing acoustic wavelength the resolution of the measurement improves. As described in section 8.2.1, the 1/3-octave band sound power levels $SWL_{1/3}$ for an equivalent point source at center span are obtained using a source power integration method.

Figure 8.13a) shows the integrated 1/3-octave band source power levels $SWL_{1/3}$ to increase with free stream velocity u_∞ . For a semi-infinite half plane Ffowcs Williams and Hall [72] showed that the intensity in the far-field due to a single eddy of length scale δ passing near the discontinuity scales with $u_\infty^3 M_0^2 \delta^2$. Howe [239] obtained similar results: considering the implications of the Corcos model [113] for the characteristics of the pressure spectrum he suggests a scaling with $u_\infty^4 M_0 \delta$. In all cases the authors suggest a frequency spectrum he scaling with the local turbulence length scale δ , which in the case of a turbulent boundary layer can be any outer layer length scale, and the reference velocity u_∞ . For a number of experiments it is reported that a scaling with $u_\infty^{4.5}$ leads to a better collapse than the aforementioned scaling rules [230]. Frequencies are expected to scale with the reference velocity and a length scale characteristic for the turbulence near the trailing edge, requiring the definition of a Strouhal number.

In the present case, the best collapse for the acoustic data is found when scaled with $u_\infty^{4.5} \delta$ (figure 8.13b), considering the free stream velocity u_∞ and the wake displacement thickness δ_w^* (table 8.4) as reference scales. Over the entire range of Strouhal numbers,



(a) Wall-tangential velocity component u_t .



(b) Wall-normal velocity component u_n .

Figure 8.10: Magnitude of spanwise coherence $\sqrt{\gamma^2(\omega, \Delta z)}$ for $x_t/c = 0$, $x_n/c = 0.005$. The dashed line indicates the spanwise extension of the interrogation volume δ_z .

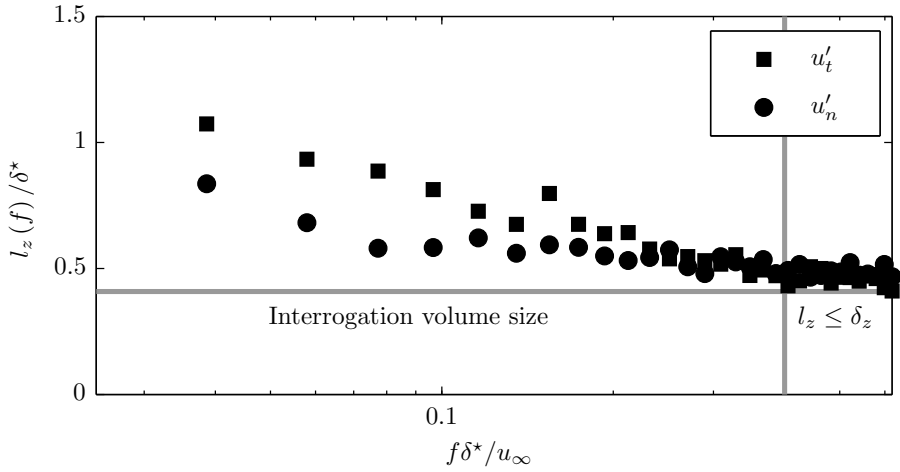


Figure 8.11: Spanwise correlation length l_z of wall-tangential and wall-normal velocity fluctuations, u_n and u_t respectively, at $x_t/c = 0$ and $x_n/c = 0.005$.

scaled results collapse with a remaining scatter of 1-2.5dB. Deviations at high frequency can be related to the Reynolds number dependence of the turbulent wall pressure spectrum [108].

Tuinstra *et al.* [240] investigated repeatability, effect of tripping, and signal to noise ratio for the phased array measurements presented here. They further provided a comparison with single microphone measurements for a case where the signal to noise ratio was considered to be good and found agreement within 1dB.

8

8.3.3. SURFACE PRESSURE FLUCTUATIONS

The statistics of the unsteady surface pressure field (equation 2.14) contain the relevant fluid dynamic properties of the turbulent boundary layer for the estimation of noise under the assumption of convection past the trailing edge. The incompressible pressure field in the tomographic measurement volume is reconstructed using the methodology described in section 3.3.

The auto-spectral density for the different stencils (figure 8.14) is computed from sampled unsteady surface pressure data at the trailing edge. Modified periodograms [203] are computed and averaged for windows of 128 samples with an overlap of 75% and over the span, resulting in a bandwidth of about 78.1Hz. At frequencies $f\delta^*/u_\infty < 0.1$ (400Hz) the scatter of the data remains within 1dB. Hwang *et al.* [108] summarized the characteristics of turbulent boundary layer surface pressure spectrum and in particular pointed out the slopes over the different frequency ranges (solid lines). Figure 8.14 shows further a comparison with the model proposed by Amiet [17] (equation 2.16). The comparison clearly shows that the model is not sufficient for an accurate estimation of the surface pressure fluctuations in this case. Note that the differences between the results

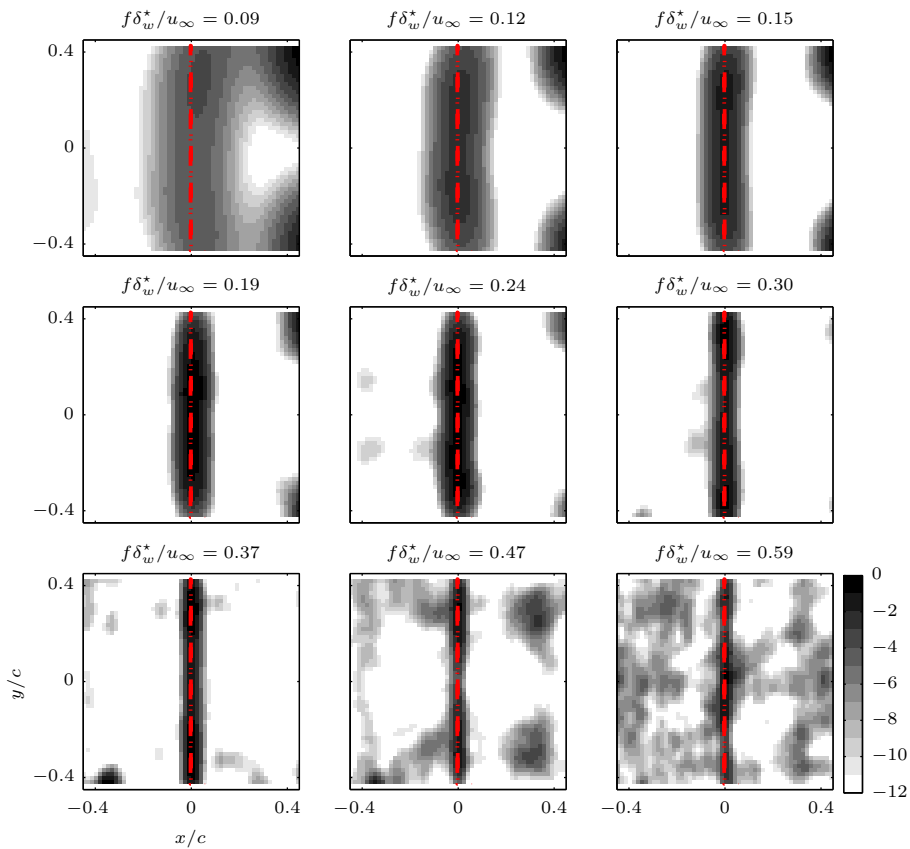
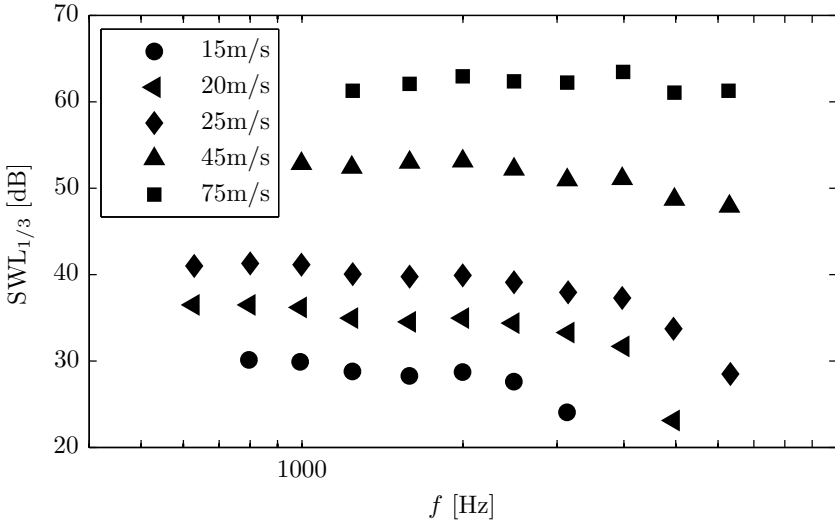
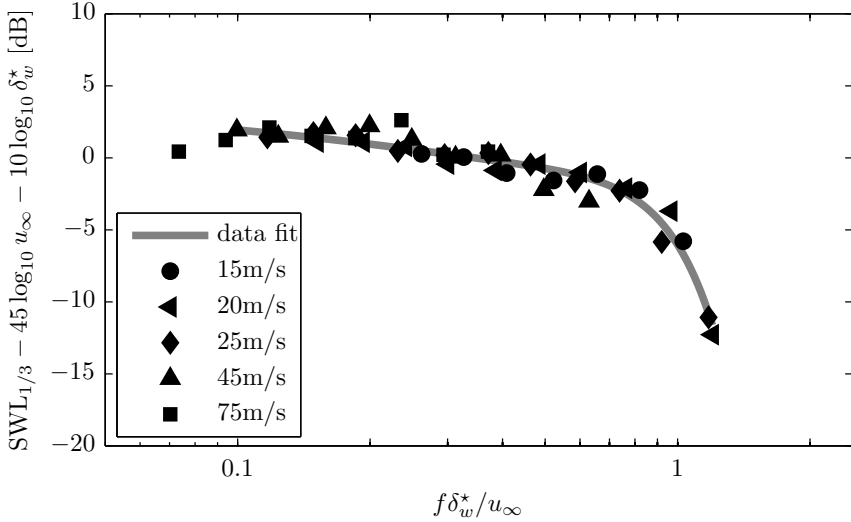


Figure 8.12: Source power maps of point source distribution obtained from conventional beamforming (dB with reference to maximum). The contour color scale is adjusted for each map separately with the range restricted to -12 dB with respect to the maximum. Line indicates the location of the trailing edge at $x/c = 0$. The source maps are shown for $u_\infty = 75$ m/s.



(a) 1/3-octave band source power level.



(b) 1/3-octave band source power level $SWL_{1/3}$ scaled with free stream velocity u_{∞} and wake displacement thickness parameter δ_w^* . Solid line indicates curve fit.

Figure 8.13: 1/3-octave band source power level measured by phased array for a range of reference velocities between 15 and 75 m/s.

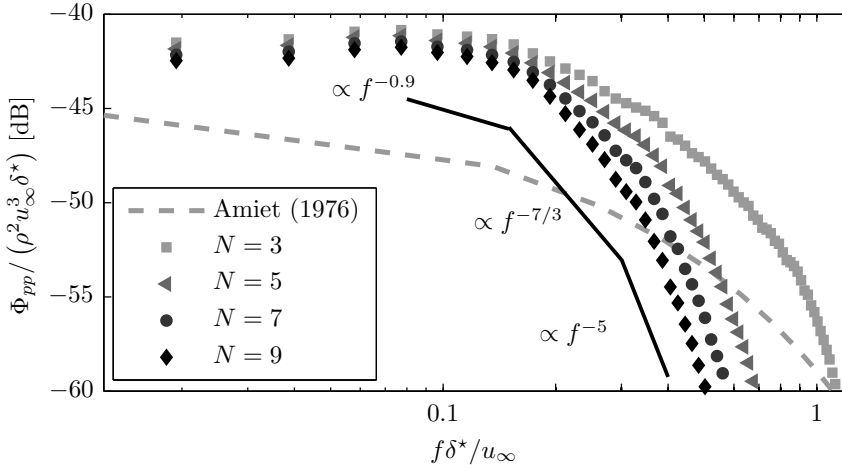


Figure 8.14: Auto-spectral density of unsteady surface pressure fluctuations at the location of the trailing edge for estimation of the material derivative with stencil $N = 3, 5, 7$, and 9 . Also indicated are the characteristic slopes of a turbulent boundary layer pressure spectrum [108] (solid lines) and the model solution following equation 2.16 (dashed line).

for the different stencils are due to the combined effect of an increase in truncation error and reduction in random error or noise. Systematic truncation error lead to an underestimation of the auto-spectral density, while random measurement errors result in an overestimation. Error analysis (figure 8.4) indicates that the random error is dominant for $N = 3$, while systematic error become dominant for larger stencils.

For the estimation of the coherence function the reconstructed unsteady surface pressure is sampled at the location of the trailing edge. Additionally, averages over the span for same spanwise separations Δz are considered. Figure 8.15 shows the resulting spanwise coherence, which is similar to that of the velocity fluctuations for small Δz (figure 8.10b), but shows marked differences at increasing separation: secondary maxima, which are present in the coherence functions of both in-plane velocity components (figures 8.10), are not found for the pressure.

Roger and Moreau [86] introduced the corrected correlation length, taking into account the spanwise wavenumber k_z (equation 2.13). In the present study, the term $kz_0\Delta z/S_0$ arising in the evaluation of equation 2.13 for the large aspect ratio approximation ($k_z = kz_0\Delta z/S_0$, equation 2.35), is small such that $\cos(kz_0\Delta z/S_0) > 0.9$ even for an observer at the edge of the array aperture ($\mathbf{x}_0 = [0\text{m}, 0.3\text{m}, 0.6\text{m}]$, see figure 8.16). This holds for the considered observer positions \mathbf{x}_0 , maximum spanwise separation represented in the measurement volume, and frequencies $f < 2\text{kHz}$ ($f\delta^*/u_\infty < 0.5$). Therefore, the spanwise correlation length $l_z(\omega) = l_z(\omega, 0)$ is considered in the following ($\cos(kz_0\Delta z/S_0) = 1$).

The correlation length is estimated by the two alternative exponential curve-fitting approaches in equation 3.1 and 3.2. Figure 8.17 demonstrates the fits for two frequen-

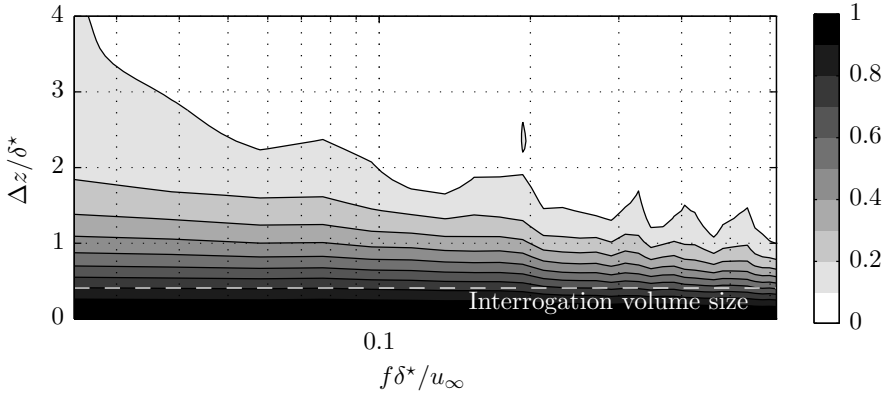


Figure 8.15: Magnitude of spanwise coherence $\sqrt{\gamma^2(\omega, \Delta z)}$ of unsteady surface pressure fluctuations at the location of the trailing edge, $N = 5$.

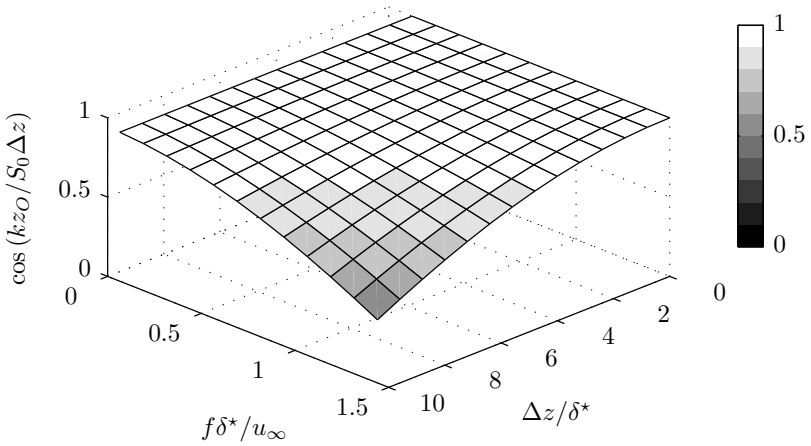


Figure 8.16: Influence of spanwise wavenumber $k_z = k_{zO}/S_0$ on corrected correlation length (equation 2.13) through $\cos(k_z \Delta z)$ term for the ranges of spanwise separation Δz and frequency f of interest in PIV measurements. Data shown for $\mathbf{x}_O = [0\text{m}, 0.3\text{m}, 0.6\text{m}]$.

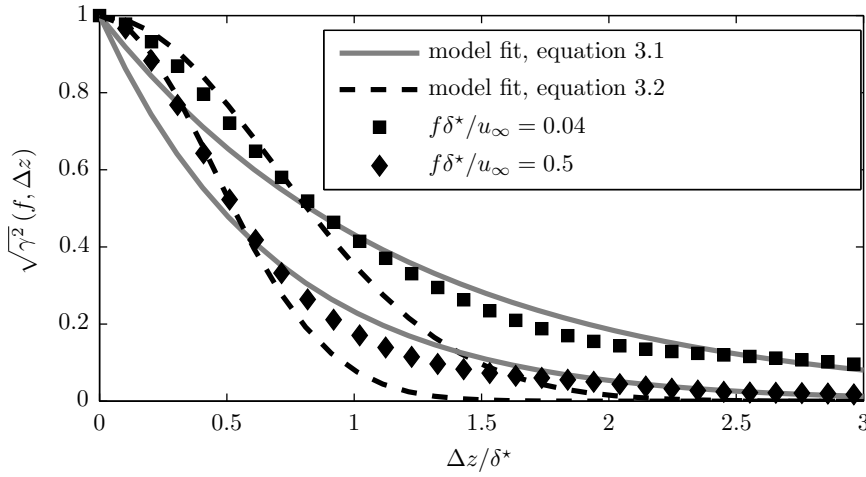


Figure 8.17: Spanwise coherence $\sqrt{\gamma^2}(f, \Delta z)$ of unsteady surface pressure for $f\delta^*/u_\infty = 0.04$ and 0.5. Additionally, the curve fits based on equations 3.1 (solid lines) and 3.2 (dashed lines) are shown. Data shown for stencil size $N = 5$.

cies, 0.16kHz ($f\delta^*/u_\infty = 0.04$) and 2kHz (0.5). At small separation Δz the exponential fit (equation 3.1) shows larger deviation since it does not respect the physical condition of zero derivative at $\Delta z/\delta^* = 0$. In contrast, the fit based on the Gaussian function (equation 3.2) provides a good estimation for small separation, but tends to zero fast at larger separation. Examination of the mean square deviation of the fit from the data points indicates that equation 3.1 provides a better estimate for the frequencies of interest (< 2 kHz).

The correlation length estimated using the two approaches (figure 8.18) exhibits a maximum difference of 20% at $f\delta^*/u_\infty = 0.01$. In view of the observations regarding the goodness of the fits, equation 3.1 is likely to provide a better estimate of the correlation length for the frequency range below $f\delta^*/u_\infty = 0.5$ and is thus selected for noise estimation. Here, also the size of stencil has only a minor effect on the correlation length, amounting to a deviation of about 10%. At high frequencies, exceeding $f\delta^*/u_\infty = 0.5$ (2kHz) the estimated correlation length based on equation 3.2 converges to the limit posed by the size of the correlation volume due to the finite spatial resolution of the PIV experiments [183]. For the frequency range of primary interest in the present study ($0.1 \leq f\delta^*/u_\infty \leq 0.4$) a good agreement with both the Corcos and Efimtsov model is found. Note that the correlation length at low frequencies is subject to debate as the deviation between the models shows. For different Reynolds and Mach number and for a one-sided turbulent boundary layer, Sandberg and Sandham [104] found in their DNS simulations a correlation length following the trend given by the Corcos model at low frequencies (equation 2.19), while the experimental results here indicate a substantially lower correlation length. It should be noted however, that the experimental results are

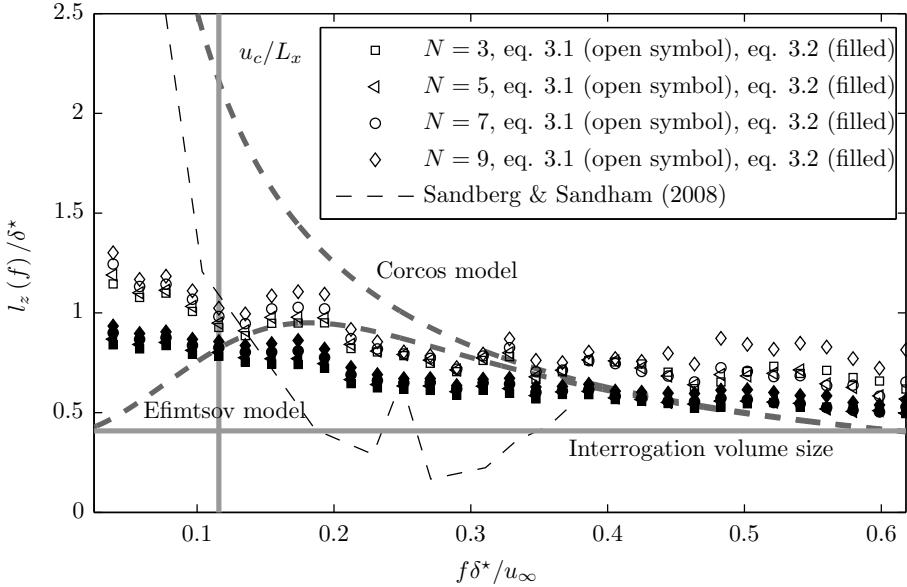
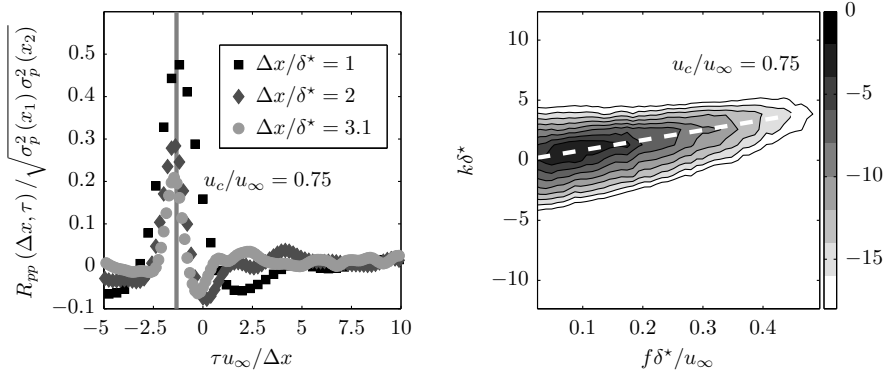


Figure 8.18: Fit of spanwise correlation length of unsteady surface pressure for $N = 3, 5, 7,$ and 9 with equation 3.1 (open symbols) and 3.2 (filled). Correlation volume size (horizontal line) and frequency corresponding to convection of turbulent pressure fluctuations u_c/L_x (vertical line). Correlation length given by semi-empirical models of Corcos [113] and Efimtsov [114] (dashed lines).

likely to underestimate the correlation length for $f < u_c/L_x$ (figure 8.18, vertical line) due to application of the approximate boundary conditions (equation 3.13).

The last parameter required for the description of the surface pressure field characteristics is the integral convection velocity u_c . An estimation of the convection velocity is obtained through cross-correlation analysis of the pressure signal at two points separated by a distance Δx . The two points are chosen symmetrically with respect to the trailing edge with $\Delta x/\delta^* = 1, 2,$ and 3.1 and results are averaged over the span (figure 8.19a). The maximum correlation coefficient at time separation τ_{max} decreases with increasing separation Δx . The normalized time separation $\tau_{max}u_\infty/\Delta x$ for the three cases compares well and yields an average estimate of the convection velocity with $u_c/u_\infty = \Delta x/|u_\infty\tau_{max}| = 0.75$ (solid line).

Figure 8.19b shows the wavenumber-frequency spectrum of the unsteady surface pressure fluctuations. A curve connecting the maxima in the wavenumber-frequency spectrum is commonly denoted as *convective ridge*. The product of wavelength and frequency at each point of the convective ridge indicates the predominant convection velocity of perturbations at that respective frequency [106, 107]. The dashed line in figure 8.19b shows the integral convection velocity found by cross-correlation analysis (figure 8.19a). Its proximity to the convective ridge agrees with previous reports of the convection velocity being a weakly dependent on frequency only. Therefore, for the purpose of noise estimation in the following section, the convection velocity is assumed to be con-



(a) Normalised cross-correlation function of unsteady surface pressure R_{pp} as function of time delay τ for two points separated by a streamwise distance $\Delta x = x_2 - x_1$.

(b) Wavenumber-frequency spectrum (dB with respect to maximum) for a spatial domain of $0.016c$. The solid line indicates the convective velocity $u_c / u_\infty = 0.75$.

Figure 8.19: Time-correlation (a) and wavenumber-frequency spectrum (b) of unsteady surface pressure fluctuations for estimation of convection velocity u_c . Results are shown for stencil $N = 7$.

stant $u_c / u_\infty = 0.75$. This value is close to the typical range of convection velocities for turbulent boundary layers reported by Howe [106] among others.

8.3.4. APPLICATION OF DIFFRACTION THEORY

Application of equation 2.35 with the surface pressure statistics presented in section 8.3.3 obtained from tomographic PIV provides the auto-spectral density of acoustic pressure in the far-field. For comparison with the array measurements, the equivalent source power level (equation 8.2) is computed. Since the measurement volume is restricted to a single side of the plate, the analysis implicitly contains the assumption that the boundary layer on the opposite side represents an uncorrelated source region of equal strength (+3dB). Results consider a span of $L = 100\text{mm}$.

The product of chord and acoustic wavenumber kc (Helmholtz number) determines the compactness of the plate at the given frequency and therefore has an influence on the directivity of the overall noise emission (figure 8.20). For $kc \ll 1$, that is cases where the acoustic wavelength exceeds the chord, the plate is compact and the directivity assumes a dipolar pattern [86]. In contrast, if $kc \gg 1$ the plate can be considered as semi-infinite. At these frequencies the directivity pattern assumes a cardioid pattern. This is almost exclusively the case for the frequencies of interest here ($> 400\text{Hz}$). However, for kc approaching unity leading edge back-scattering becomes important as pointed out by Roger & Moreau [86, 87] and usually requires inclusion of the correction term \mathcal{I}_2 (figure 8.20a).

In the present case, the acoustic reference data is obtained through a power integration procedure (section 8.2.1) considering only the trailing edge as noise source. There-

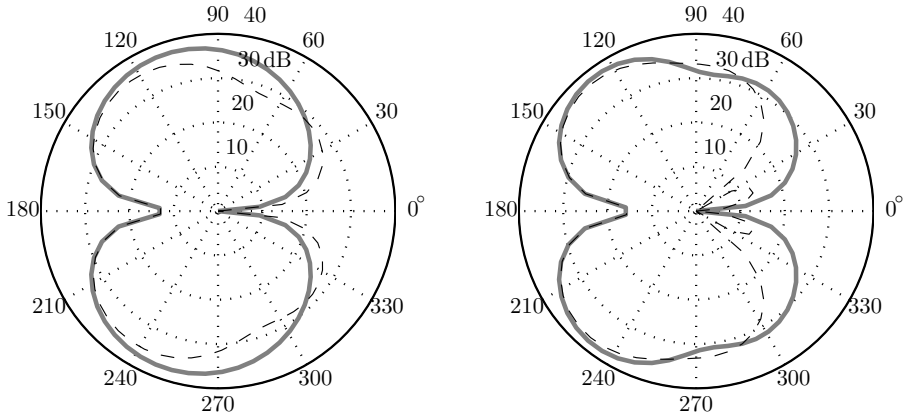
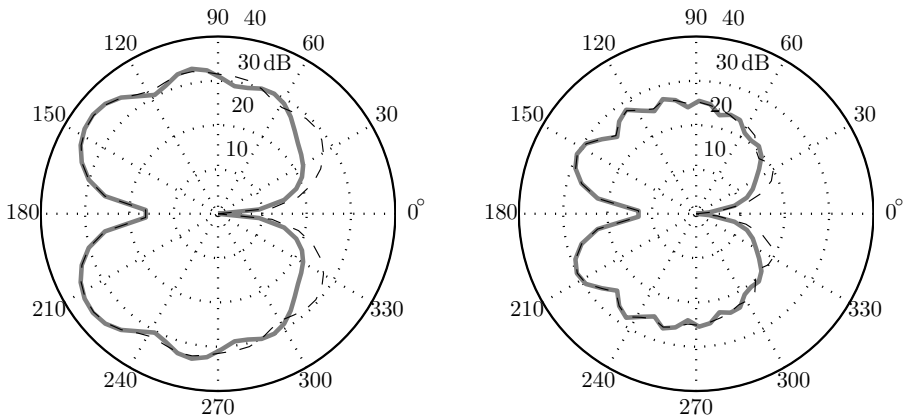
(a) $kc = 2.6$.(b) $kc = 5.1$.(c) $kc = 10.3$.(d) $kc = 19.7$.

Figure 8.20: Directivity patterns ($4\pi r_{Of}^2 \Phi_{aa} / p_{ref}^2$, dB) based on tomographic PIV data (equation 2.35) for frequencies $kc = 2.6$ (0.23kHz), 5.1 (0.47kHz), 10.3 (0.94kHz), and 19.7 (1.8kHz). Solution with scattering term only (\mathcal{S}_1 , solid line) and including leading edge back-scattering term ($\mathcal{S}_1 + \mathcal{S}_2$, dashed), $N = 5$.

fore, at high frequencies the direct scattering term (\mathcal{S}_1) should be considered for comparison.

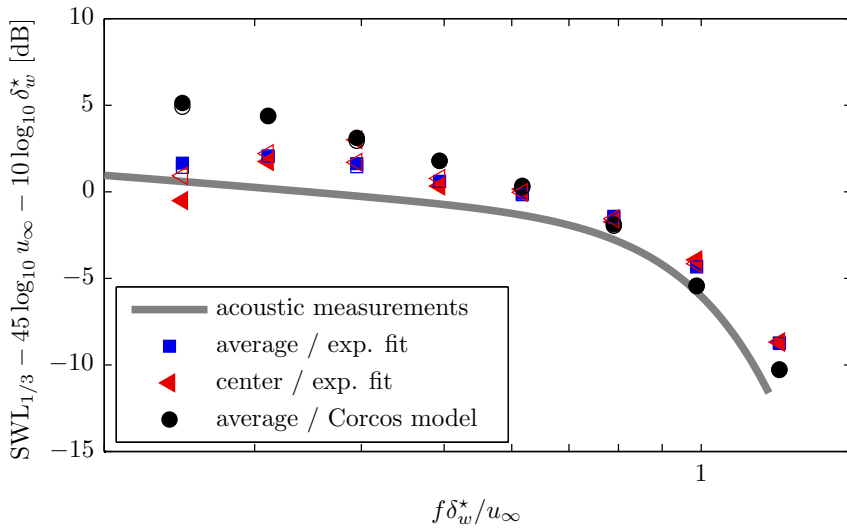
The directivity plots in figure 8.20 show that there are directivity effects due to the position of the array microphones with respect to the trailing edge. Figure 8.21a compares the acoustic measurements to the average equivalent SWL over the positions of the microphones (equation 8.2) and the equivalent SWL at the center of the array for $N = 5$. For the average SWL these variations due to these directivity effects are small due to spatial averaging over the aperture of the array. For the frequencies investigated here, the maximum deviation of the average SWL with respect to that at the center position is approximately 1dB at low frequency. Considering leading edge back-scattering (open symbols) results in a smaller deviation between the center location and even less for the average result.

Further, figure 8.21a shows a comparison between estimates, where the correlation length is determined from PIV measurements and a case where the correlation length is estimated by the model in equation 2.19. At higher frequencies ($f\delta_w^*/u_\infty > 0.6$) results based on the model compare well to the reference acoustic measurements. Due to the limitations posed by spatial resolution of the PIV measurement, the model potentially even provides a better estimation of the correlation length at high frequencies if the empirical constants known. However, at lower frequencies the Corcos model for the correlation length is known to overestimate the actual correlation length and consequently results in an overestimation of up to 5dB. It should be noted that, for the specific case of a turbulent boundary layer, models for the correlation length taking into account the peel-off at low frequencies are available [114]. Yet, these models are not generally applicable to other trailing edge flows, involving for instance trailing edge bluntness and vortex shedding. Moreover, these models rely on empirical constant which need to be determined in different experiments.

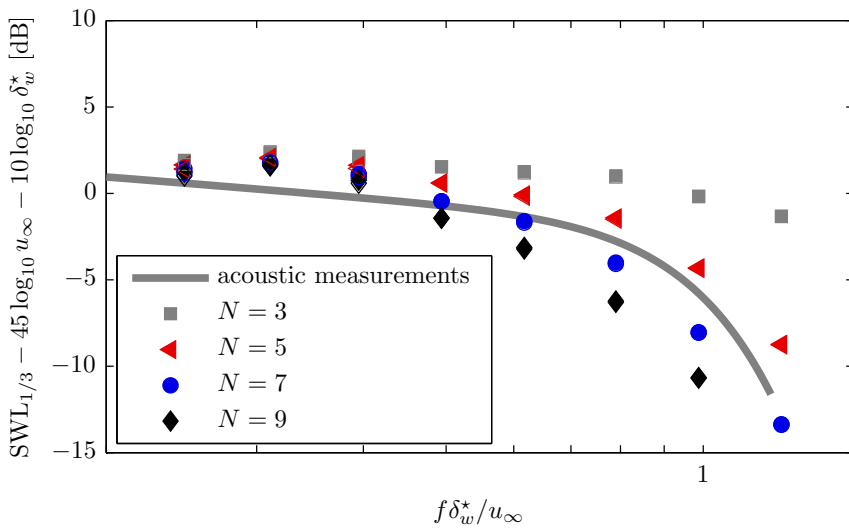
A comparison of the averaged results obtained for the different stencils N used in the estimation of the material derivative shows a collapse within 1dB at lower frequencies ($f\delta_w^*/u_\infty < 0.4$, 800Hz). Below $f\delta_w^*/u_\infty < 0.5$ the estimates show a collapse within the scatter of the acoustic measurements (3dB). The deviation at larger frequencies is mostly due to the effect of the stencil size on the estimation of the material derivative and the resulting auto-spectral density (figure 8.14). As indicated in the discussion of the surface pressure spectrum in figure 8.14, the noise component of the spectrum for a smaller stencil size ($N < 5$) leads to a significant overestimation of the pressure fluctuations when $f\delta_w^*/u_\infty > 0.4$, while the truncation error becomes dominant for larger stencils ($N \geq 7$). In view of this error analysis it appears plausible that the stencils $N = 5$ and $N = 7$ provide show the smallest deviation with respect to the reference. The scatter of results at high frequencies also shows that further investigation into the properties and behavior of PIV correlation and material derivative estimation is required in order to provide optimum estimates.

8.4. CONCLUSION

High-speed tomographic PIV measurement techniques have been performed around a sharp trailing edge with the purpose of PIV based trailing edge noise estimation. Diffraction theory links the trailing edge noise perceived in the far-field to the characteristics of



(a) Comparison of average $SWL_{1/3}$ over microphone locations and $SWL_{1/3}$ at array center. Comparison of Corcos model (equation 2.19) and exponential fit for correlation length (equation 3.1), $N=5$.



(b) Influence of stencil size ($N=3,5,7,9$) for estimation of material derivative.

Figure 8.21: Comparison of estimated 1/3-octave band source power spectra (equation 8.2) with acoustic measurements (line, compare figure 8.13b). Solution including first order scattering from the trailing edge (\mathcal{S}_1 , filled symbols) and effect of leading edge back-scattering term ($\mathcal{S}_1 + \mathcal{S}_2$, open symbols).

the unsteady surface pressure field at the trailing edge. Models for the unsteady surface pressure characteristics are only available for a small number of canonical flow conditions and thus alternative approaches are required. In the present study, the required statistics of the unsteady surface pressure field have been evaluated from the tomographic PIV measurements.

Following previous works, the unsteady surface pressure auto-spectral density has been obtained. Over a restricted frequency range ($0.1 \leq f\delta^*/u_\infty \leq 0.4$), the estimates of the correlation length show a favorable comparison with classical models. At higher frequency the correlation length is overestimated due to the finite window size. The convection velocity of unsteady surface pressure fluctuations has been found to be 75% of the free-stream velocity in agreement with the range typically found for zero pressure gradient boundary layers.

Acoustic reference measurements are acquired using a phased microphone array measurement technique and provide the equivalent SWL over the aperture of the array. Normalization with $u_\infty^{4.5}\delta_w^*$ results in a collapse of the experimental data within about 2dB. Estimates of the acoustic emission based on application of diffraction theory show a good agreement with the acoustic reference measurements over the given frequency range ($0.2 \leq f\delta_w^*/u_\infty \leq 0.8$), but are sensitive to the estimation of the material derivative at high frequencies. Further research with regard to the characteristics of the PIV correlation and material derivative estimation schemes is required in order to extend applicability towards higher frequency. At low frequency, the limited measurement volume size in tomographic PIV poses the main limitation.

III

TRAILING EDGE BLUNTNES NOISE

9

PREDICTION OF TRAILING EDGE BLUNTNES NOISE

*There are two possible outcomes:
If the result confirms the hypothesis,
then you've made a measurement.
If the result is contrary to the hypothesis,
then you've made a discovery.*

attributed to Enrico Fermi

Vortex shedding at blunt and beveled trailing edges generates tonal noise, which is usually undesired. The flow field around a beveled trailing edge is characterized and a statistical description is obtained by means of planar high-speed two-component and stereoscopic Particle Image Velocimetry (PIV) measurements. The development of the shear layers and vortex roll-up is described.

Noise emission due to vortex shedding is predicted from an analytic solution, derived from diffraction theory and the reversed Sears' problem, and compared to acoustic phased array measurements. This approach was shown to provide accurate results for sharply truncated edges, but questions with regard to the applicability with different trailing edge geometries remain open. The prediction requires the auto-spectral density, correlation length, and convective velocity of the upwash velocity component in the vortex formation region. Direct application with data obtained from PIV measurements shows an overestimation of about 15 to 20dB the acoustic measurements.

Parts of this chapter are considered for publication in the International Journal of Aeroacoustics.

9.1. INTRODUCTORY REMARKS

TRAILING EDGE BLUNTNES large in comparison to the boundary layer thickness generates vortex shedding in the wake, which in turn results in a narrowband or even tonal noise component, also referred to as *singing* [19]. The characteristics of such blunt and semi-blunt trailing edges with regards to flow induced noise generation continue to be of interest for current and future design aspects of lifting surfaces on wind turbines, aircraft, and submarines.

Blake [19] stated that a trailing edge can be considered as sharp if a bluntness parameter $T/\delta^* < 3.3$, where T is the thickness of the truncated trailing edge and δ^* the displacement thickness of the boundary layer at the trailing edge. For larger values of the bluntness parameter, vortex shedding linked to tonal noise is likely to occur. Compared to broadband noise, tonal components are often perceived as rather disturbing. Thus, good understanding of noise generation at trailing edges is required to effectively avoid such situations.

Roger *et al.* [105] argued that noise generation due to vortex shedding can be modeled by a reverse Sears' problem, where vorticity is shed at the trailing edge, instead of encountering the leading edge as described by Amiet [115]. For cases involving vortex shedding, following this approach the data required for noise estimation can be reduced to statistics of the upwash velocity in the near wake [87, 105], i.e. its auto-spectral density, spanwise correlation length, and convective velocity. Roger *et al.* [105] applied this approach to the case of a sharply truncated plate with $\delta^*/T \ll 1$. Comparison of the predictions with acoustic measurements showed excellent agreement, confirming thus the applicability of this approach.

However, as commented by Roger *et al.* [105] and Roger and Moreau [87], assumptions intrinsic to this particular use of diffraction theory and the wake model render the equation only strictly applicable if vortex formation occurs immediately at the edge. This is a questionable assumption when the edge is beveled and applicability of the approach in such cases is still not clear. Blake [19] emphasized the importance of the vortex formation length l_f for noise generation and proposed an analytic model, showing that mean-square fluctuations of the unsteady surface pressure near the trailing edge are proportional to y_f/l_f . He then pointed out that this also has implications for noise emission.

The feasibility to predict acoustic emission based on PIV in combination with diffraction theory has recently been demonstrated by Pröbsting *et al.* [66] for the case of a turbulent boundary layer interacting with a sharp trailing edge. Bilka *et al.* [95] predicted noise emission from a series of beveled trailing edges following the methodology of Roger *et al.* [105]. The authors indirectly estimated the auto-spectral density of the upwash velocity in the wake from uncorrelated PIV measurements by invoking Taylor's hypothesis, i.e. by assuming pure convection of the frozen turbulence pattern. A correlation length estimate was obtained from unsteady surface pressure measurements near the trailing edge. The result was compared to data available from acoustic measurements and good agreement was found between the predicted and measured noise spectra. This agreement was in contradiction with the assessment and considerations of noise generation at rounded or beveled trailing edges of Blake [19] and Roger *et al.* [105].

The discussion in this chapter revisits this point of controversy and assesses the validity of the model, proposed by Roger *et al.* [105], to estimate the noise emission at a

beveled trailing edge. Reference acoustic results are obtained by acoustic phased array measurements and beamforming. Using high-speed PIV, the auto-spectral density, spanwise correlation length, and convective velocity of the upwash velocity component in the near wake are assessed. Based on these results, tonal noise emission is estimated and compared to the acoustic measurements. In particular, the results are compared to those of Bilka *et al.* [95] in order to clarify questions regarding the applicability of the methodology for cases involving vortex shedding and rounded trailing edges.

9.2. DESCRIPTION OF EXPERIMENTS

Flow field and acoustic measurements were conducted at the vertical low turbulence wind tunnel facility at Delft University of Technology, an open-jet wind tunnel with a test section of $0.4 \times 0.4\text{m}^2$. The turbulence intensity at the nozzle exit is approximately 0.1%.

A flat plate with an elliptical leading edge and an asymmetric beveled trailing edge was investigated. The plate had a chord length of $c = 360\text{mm}$, a thickness of $T = 20\text{mm}$, and a span of $L = 400\text{mm}$. The beveled trailing edge was defined by a radius of curvature $R/T = 2.5$ and an enclosed angle $\theta = 45^\circ$ (figure 2.5). 2D mean flow was ensured by the presence of side plates. x , y , and z denote the streamwise, transverse, and spanwise coordinate directions, respectively. The origin of the coordinate system is placed at the trailing edge (figure 2.13).

The boundary layer was tripped at the quarter chord position ($x = -3c/4$) on both sides of the plate using 3D roughness elements. The roughness elements were carborundum grains with a nominal size of 0.84mm, randomly distributed over strips of 10mm width.

9.2.1. ACOUSTIC MEASUREMENTS

The acoustic array consisted of 64 PUIAUDIO 665-POM-2735P-R omni-directional electret-condenser microphones with a sensitivity of $-35 \pm 2\text{dB}$ (ref. 1V/Pa) over a frequency range of 0.2 – 25kHz. The microphones were mounted on a metal grid (grid spacing $3 \times 3\text{cm}$) and arranged in a multi-arm logarithmic spiral configuration [39] as shown in figure 9.1. The array was placed in a plane parallel to the chord plane at $y = 1.03\text{m}$. Its center was located at $x = -50\text{mm}$, upstream of the trailing edge, and at mid-span ($z = 0\text{m}$). Acoustic measurements were performed for the range of free stream velocities between $u_\infty = 25\text{m/s}$ and 40m/s. At each velocity, signals were acquired for a duration of 60s.

The analogue signals were amplified, band-pass filtered, and sampled at an acquisition frequency of $f_s = 50\text{kHz}$. For calibration, a transfer function was applied to the signals in the frequency domain during post-processing. Auto- and cross-spectral density of the signals were computed using an average periodogram method for windows of 2,048 samples and an overlap of 75% [203], resulting in a frequency resolution of 24.4Hz.

The array microphones (denoted by $n = 1 \dots 64$) returned signals of acoustic pressure $\mathbf{p}(t) = [p_1(t) \dots p_{64}(t)]^T$, where \cdot^T is the transpose. For frequency domain beamforming, the amplitude at frequency f is written as $\mathbf{p}(f) = [p_1(f) \dots p_N(f)]$. To derive the source powers over the region of interest, the signals are analyzed using the conventional beam-

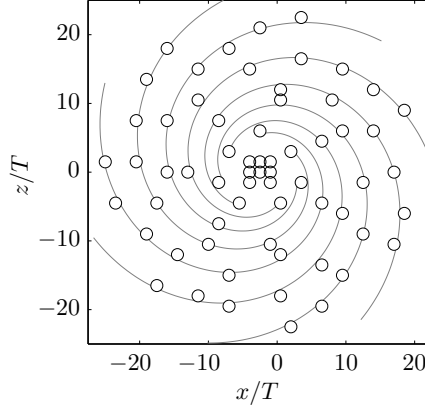


Figure 9.1: Arrangement of microphones in multi-arm logarithmic spiral configuration.

forming technique and a distribution of simple point sources is assumed to model the source region. The so-called *steering vector* describes the influence of a point source at location ξ on the sensor location \mathbf{x}_n , where $\mathbf{M}_0 = \mathbf{u}_\infty/c_0$, $\beta^2 = 1 - \|\mathbf{M}_0\|^2$, and $\|\cdot\|$ is the Euclidean norm [40]:

$$\mathbf{g}_n(f, \xi) = \frac{-e^{2\pi i f \Delta t_e(\mathbf{x}_n, \xi)}}{4\pi \sqrt{[\mathbf{M}_0 \cdot (\mathbf{x}_n - \xi)]^2 + \beta^2 \|\mathbf{x}_n - \xi\|^2}} \quad (9.1)$$

and Δt_e describes the emission time delay:

$$\Delta t_e = [-\mathbf{M}_0 \cdot (\mathbf{x}_n - \xi) + \sqrt{(\mathbf{M}_0 \cdot (\mathbf{x}_n - \xi))^2 + \beta^2 \|\mathbf{x}_n - \xi\|^2}] / c_0 \beta^2 \quad (9.2)$$

The source auto-powers associated to a given source location ξ and frequency f are solved for using

$$A(f, \xi) = \frac{\mathbf{g}(f, \xi)^* \mathbf{C}_g(f, \xi)}{\|\mathbf{g}(f, \xi)\|^4} \quad (9.3)$$

where $C_{mn} = (p_m(f) p_n^*(f))/2$ is the cross-spectral matrix of the measured acoustic pressure signals.

The refraction of acoustic waves, occurring at the interface between quiescent air and open jet, was taken into account in the determination of the steering vector by considering the average Mach number over the transmission path [40]. As a result, the distribution of source power associated to the point source distribution over the region of interest is obtained. Consecutively, the source power is integrated over a rectangular region around the trailing edge. This integration region is centered on the trailing edge and covers the central 200mm of the span, while the streamwise extent is adapted to the beamwidth for a given frequency. Spectral leakage (i.e. energy lost as a result of the finite integration region) is taken into account and corrected for by application of an array calibration function Oerlemans and Sijtsma [235], normalizing the integrated source

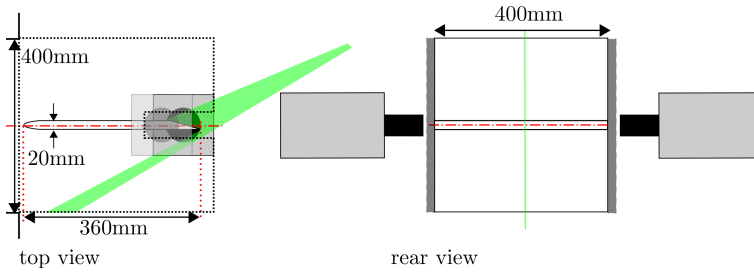


Figure 9.2: Schematic of the experimental set-up for the edge flow and near wake PIV measurements.

power by the equivalent for a point source at center span with unity source power. The resulting source power level represent an average over the aperture of the array [235]. A similar procedure was followed by Pröbsting *et al.* [66].

9.2.2. FLOW FIELD MEASUREMENTS

First, planar two-component PIV measurements were performed to assess the flow field around the trailing edge, its topology and the turbulent boundary layer parameters. Second, complementary planar stereoscopic (3-component) PIV measurement were conducted to assess the fluctuations of upwash velocity in the near wake behind the trailing edge.

In both experiments, the flow was seeded with water-glycol based fog fluid containing tracer particles of $1\mu\text{m}$ mean diameter. The particles were illuminated using a high repetition rate, diode pumped Quantronix *Darwin-Duo* dual cavity Nd:YLF laser. For imaging, two cameras of type Photron *Fastcam* SA1.1 with CMOS sensors ($1,024 \times 1,024\text{px}$, 12 bit $20\mu\text{m}$ pixel pitch) were used and equipped with Nikon *Micro-Nikkor* 105mm prime lenses. Synchronization of the PIV system was ensured by a LaVision *High-Speed controller* and for acquisition and correlation the LaVision *DaVis* 8 software package was used.

EDGE FLOW AND NEAR WAKE MEASUREMENTS

Laser and optical elements were arranged such that the light sheet illuminated a part of the mid-span plane around the trailing edge. The two cameras were located on opposite spanwise ends of the model and imaged the illuminated tracer particles through windows in the the side plates. Their optical axes were aligned with the spanwise (z -) coordinate direction and the aperture number was set to $f_{\#} = 8$. The field of view of each camera encompassed an area of about $45 \times 45\text{mm}$ (figure 9.2). 1,000 image pairs were recorded at a frequency of 125Hz and with a time separation equivalent to a particle displacement of approximately 15px in the free stream. Additionally, image sequences were recorded at a higher sampling rate of 2.7kHz. Measurement were performed for $u_{\infty} = 20\text{m/s}$, 30m/s , and 40m/s ($\text{Re} = 3.2, 3.8, \text{ and } 4.6 \times 10^4$).

An iterative multi-grid, multi-pass correlation technique was used for image interrogation with a final windows size of $16 \times 16\text{px}$ and 75% overlap between adjacent windows. This procedure results in a vector spacing of approximately 0.17mm. Table 9.1 provides an overview of the experimental parameters.

Table 9.1: Parameters for planar two-component, edge flow and near wake PIV measurements.

Parameter	Symbol	Value
combined field of view		$70 \times 35\text{mm}^2$
magnification	M	0.43
imaging resolution	S	22px/mm
interrogation window size		$16 \times 16\text{px}$
	$\delta_x \times \delta_y$	$0.7 \times 0.7\text{mm}^2$
		$0.034T \times 0.034T$
free stream displacement	dx	$\sim 0.7\text{mm}$
	dx/S	$\sim 15\text{px}$
acquisition frequency	f_s	125Hz / 2.7kHz
number of samples		1,000/2,700

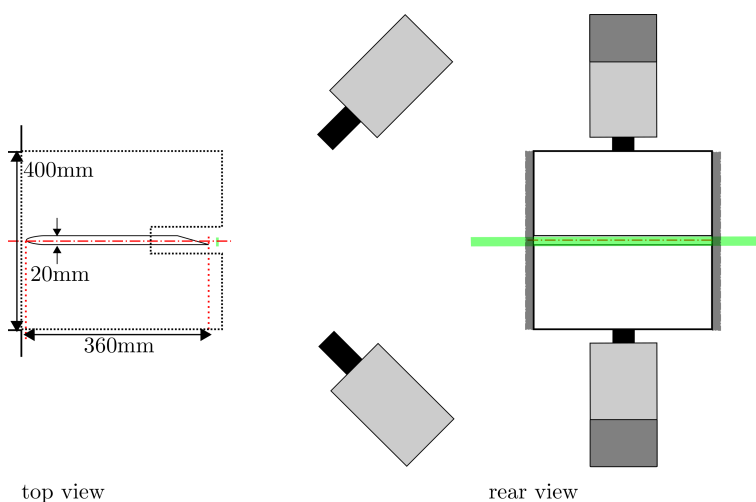


Figure 9.3: Schematic of experimental set-up for cross-flow stereoscopic PIV measurements.

9

CROSS-FLOW MEASUREMENTS

To assess the spanwise correlation length, stereoscopic PIV measurements were performed over a plane, orthogonal to the free stream flow direction, at $x/T = 1$ ($x = 20\text{mm}$) behind the trailing edge. The two cameras were positioned as shown in figure 9.3, with an angle of approximately 90° between their optical axes. To correct for the misalignment between focal plane and object plane, Scheimpflug adapters were used. The numerical aperture was set to $f_\# = 8$. 6,000 image pairs were recorded at a frequency of 6kHz and with a time separation equivalent to a particle displacement of approximately 0.5mm in the free stream (equivalent to approximately one quarter of the light sheet thickness). In this configuration, measurements were performed for $u_\infty = 20\text{m/s}$, 25m/s, 30m/s, and 35m/s.

An iterative multi-grid, multi-pass correlation technique was used for image interrogation with a final windows size of $16 \times 16\text{px}$ and 75% between adjacent windows. This

Table 9.2: Parameters for cross-flow plane, stereoscopic PIV measurements.

Parameter	Symbol	Value
field of view		$60 \times 25 \text{mm}^2$
magnification	M	0.48
imaging resolution	S	24px/mm
interrogation window size		$16 \times 16 \text{px}$
	$\delta_y \times \delta_z$	$0.65 \times 0.65 \text{mm}^2$
		$0.033T \times 0.033T$
free stream displacement	dx	$\sim 0.5 \text{mm}$
	dx/S	$\sim 12 \text{px}$
acquisition frequency	f_s	6kHz
number of samples		6,000

procedure results in a vector spacing of 0.16mm. Table 9.2 summarizes the experimental parameters. Auto- and cross-spectral densities of the velocity signals were computed using an average periodogram method for windows of 256 samples and an overlap of 75% [203], resulting in a frequency resolution of 23.4Hz.

9.3. RESULTS AND DISCUSSION

9.3.1. FLOW FIELD

BEVELED TRAILING EDGE FLOW CHARACTERISTICS

Figure 9.4 illustrates the flow field around the beveled trailing edge through a sequence of three instants (time separation $\Delta t u_\infty / T = 1.11$) with contours of the spanwise vorticity component $\omega_z T / u_\infty$ for $\text{Re} = 3.8 \times 10^4$. Two concentrated layers of vorticity from the upstream boundary layers can be identified. The first one separates from the curved, upper (suction) surface and contains small scale structures with primarily negative spanwise vorticity, indicating clockwise rotation. The second region separates at the tip of the trailing edge and shows primarily positive spanwise vorticity, indicating counter-clockwise rotation. Initially, the two regions remain separated from each other and the small scale vortical structures trail downstream before they start to interact at approximately $x/T = 0.5$. As noted by Shannon and Morris [46], the bulges of positive vorticity on the pressure side, rolling up into the reverse flow region, remain comparatively coherent while convecting downstream into the far wake.

The separated layers of positive and negative vorticity thus deform and roll-up into large scale vortical structures that trail downstream as shown by Shannon and Morris [46]. This large scale motion (wavelength approximately $1T$) is a principal characteristic of the blunt or beveled trailing edge and is commonly termed vortex shedding.

Over the Reynolds number range investigated in the present study, the flow field shows very similar principal characteristics. With increasing Reynolds number, the separation point on the suction side moves downstream (not shown here).

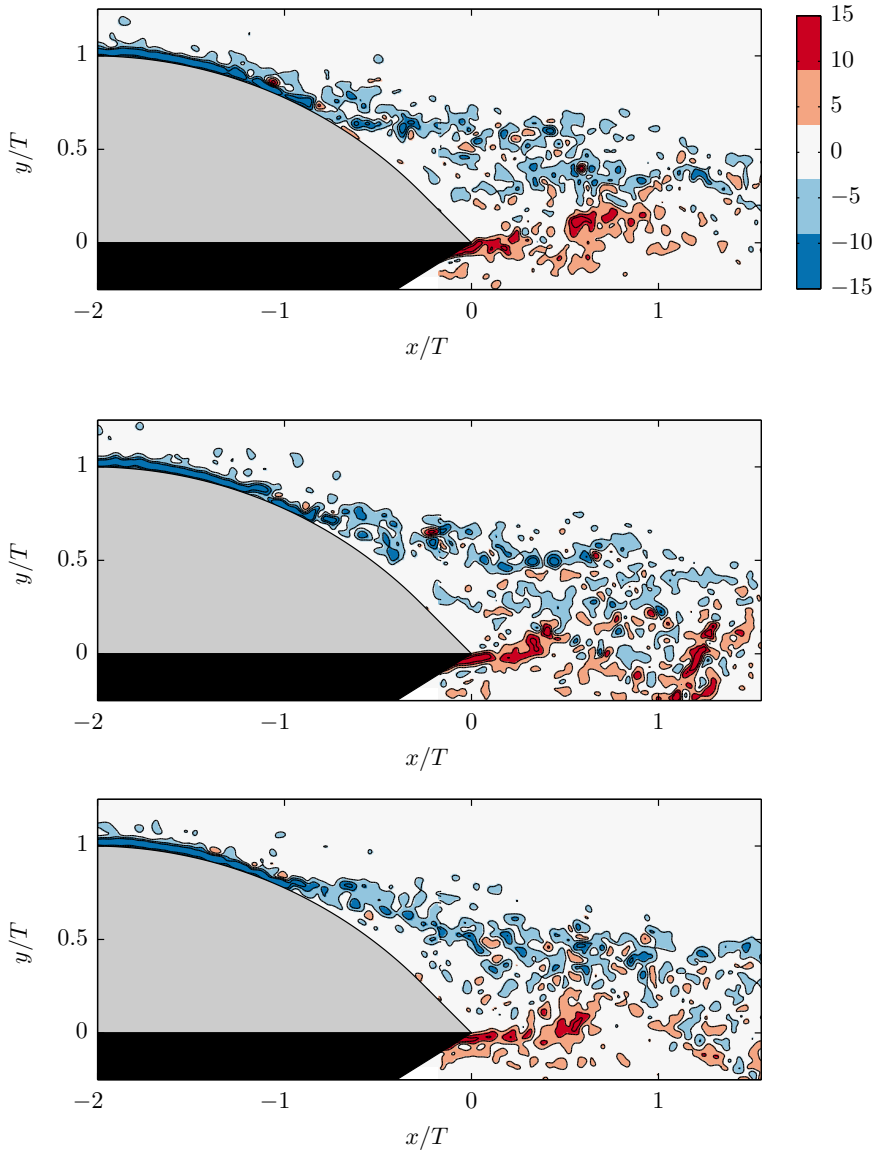


Figure 9.4: Contours of the spanwise vorticity component $\omega_z T / u_\infty$. Sequence of three snapshots (time separation $\Delta t u_\infty / T = 1.11$), $\text{Re} = 3.8 \times 10^4$.

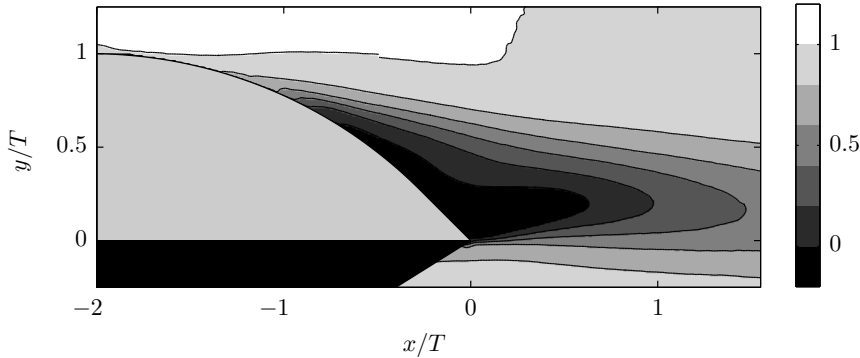


Figure 9.5: Time-averaged streamwise velocity component \bar{u}/u_∞ , $Re = 3.8 \times 10^4$.

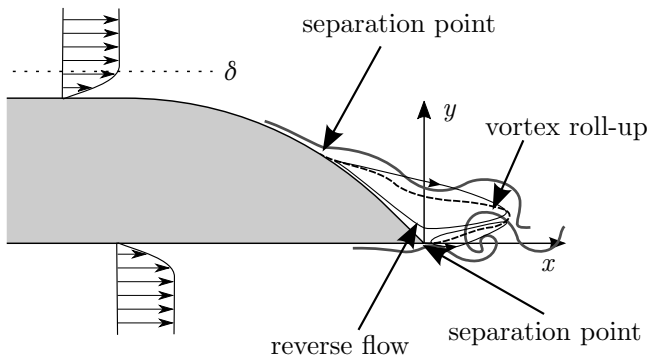


Figure 9.6: Principal features of flow around beveled trailing edge. The reverse flow region (bounded by dashed line), flow recirculation (thin lines), and roll-up of the shed vorticity (thick lines).

REVERSE FLOW AND SHEAR LAYER DEVELOPMENT

The mean streamwise velocity component (figure 9.5) reveals a large region of reverse flow (time-average streamwise velocity component $\bar{u} < 0$) at the aft portion of the beveled edge. This reverse flow region extends into the wake ($x/T > 0$) and connects to the model at a separation point on the curved upper surface (suction side) at about $x/T = -1$ and at the second separation point at $x/T = 0$. While the location of the upper separation point shifts downstream for increasing Reynolds number, the second separation point remains fixed at the sharp edge ($x/T = 0$). The shift of the upper separation point with Reynolds number thus also has an influence on the extent of the reverse flow region. Shannon and Morris [46] and Bilka *et al.* [95] presented statistics of the velocity field for a similar trailing edge, which agree with those shown here. Figure 9.6 summarizes the principal features of the blunt trailing edge flow.

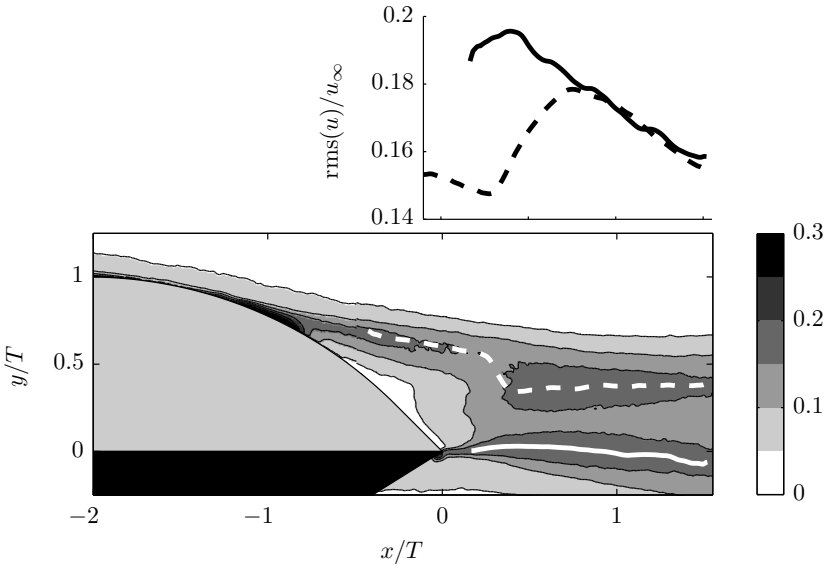
Fluctuations of streamwise velocity component $rms(u)$ (figure 9.7a) provide insight into the vortex shedding process. Maxima of $rms(u)$ originate at the two separation points and mark the lower and upper shear layers. After vortex roll-up, in a simple vortex convection model, the vertical distance between the two maxima can be inter-

preted as proportional to the size of the vortex core. Blake [19] defines the minimum distance at the end of the vortex formation zone as wake thickness parameter y_f and the corresponding distance to the trailing edge as vortex formation length scale l_f (figure 2.6). Figure 9.7b shows that fluctuations in the lower shear layer are about twice as strong as those in the upper shear layer. Between $0.5 < x/T < 1$, the maximum value $\text{rms}(v)/u_\infty > 0.2$, which is slightly lower than the values reported by Bilka *et al.* [95] ($\text{rms}(v)/u_\infty \approx 0.3$).

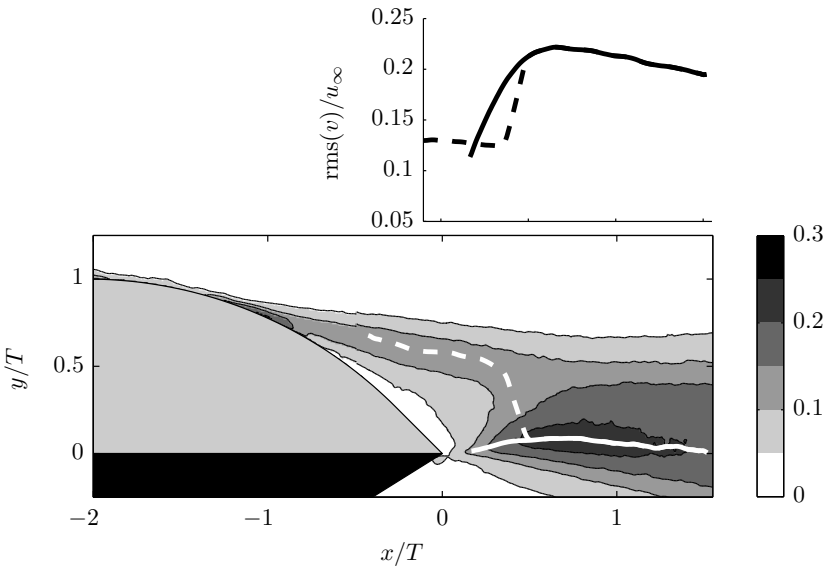
It should be noted that the definitions of the wake thickness and vortex formation length parameters given by Blake [19] leave room for interpretation of the term vortex formation zone. For instance, Shannon [92] considered only x/T outside of the reverse flow region, which does not necessarily coincide with the minimum separation between the maxima of $\text{rms}(u)$. It should further be noted that estimation of the vortex formation length l_f as defined by Blake [19] shows a large sensitivity due to the small inclination of the lines tracing the maximum $\text{rms}(u)$ location (figure 9.7a).

A more robust definition of the vortex formation length \tilde{l}_f is based on the upwash velocity component $\text{rms}(v)$ (figure 9.7b), namely the distance between trailing edge and the x -location of maximum $\text{rms}(v)$ in the near wake [241]. The maximum $\text{rms}(v)$ marks the end point of a sharp increase in the fluctuation level. It should be noted that this upwash velocity component is also directly related to the quantities required for noise prediction (equation 2.43). The maxima of $\text{rms}(v)$ are found further downstream than the location of minimum distance between the maxima of $\text{rms}(u)$. The corresponding vertical distance between the maxima in $\text{rms}(u)$ for the upper and lower shear layers is then defined as the alternative wake thickness parameter \tilde{y}_f . It should be noted that this definition is not new and it was found to often yield the same value as l_f [90]. However, in the past century fluctuations were often measured with single hot-wire probes, which in some cases, renders results not necessarily comparable when definitions are based on a single velocity component.

Table 9.3 lists the scaling parameters for the flow at different Reynolds numbers. The wake thickness ranges between $y_f/T = 0.24 - 0.36$ (high to low Reynolds number) and the vortex formation distance $l_f/T = 0.39 - 0.33$. The trend towards smaller wake thickness y_f , is consistent with the downstream movement of the suction side separation point and thus with the shrinking of the reverse flow region. With increasing Reynolds number, the vortex formation length (l_f) increases only slightly. For similar geometries, Blake [19] listed approximate values of $l_f/T = 1$ and $y_f/T = 0.5$, and thus $y_f/l_f = 0.5$. It should be noted that strict application of the definition given by Blake [19] in the present case results in a range of values $y_f/l_f \approx 0.6 - 1$. Interestingly, the alternative definition of the vortex formation length yields ratios significantly closer to that given by Blake [19], namely $\tilde{y}_f/\tilde{l}_f \approx 0.4 - 0.6$. It should further be noted that $x = \tilde{l}_f$ is also closer to the loca-



(a) Fluctuations of streamwise velocity component $rms(u)/u_\infty$.



(b) Fluctuations of upwash velocity component $rms(v)/u_\infty$.

Figure 9.7: rms of the velocity fluctuations around beveled trailing edge, $Re = 3.8 \times 10^4$. Lines indicate maxima in upper (dashed) and lower (solid) shear layer.

tion regarded by Shannon [92] as end of the vortex formation zone ($x/T = 1$).

Table 9.3: Characteristic length scales at different Reynolds numbers.

Parameter	Symbol			
free stream velocity	u_∞ [m/s]	20	30	40
Reynolds number	$Re = u_\infty T/\nu$ [$\times 10^4$]	2.5	3.8	5.1
bluntness parameter ¹	T/δ^*	14.3	13.2	12.4
wake thickness ²	y_f/T	0.36	0.28	0.24
wake thickness ³	\tilde{y}_f/T	0.42	0.36	0.33
vortex formation length ²	l_f/T	0.33	0.38	0.39
vortex formation length ³	\tilde{l}_f/T	0.71	0.67	0.78

¹ δ^* was measured using hot-wire measurements on suction side at $x/T = -2.5$ for $Re = 2.5 \times 10^4$ and extrapolated for higher Reynolds numbers

² definition based on minimum separation between maxima of $\text{rms}(u)$ [19]

³ definition based on maximum $\text{rms}(v)$

VORTEX SHEDDING

For prediction of noise emitted due to the large scale vortex shedding at the trailing edge by equation 2.43, statistics of the upwash velocity are required: the auto-spectral density $\Phi_{vv}(\omega)$, its spanwise correlation length $l_z(\omega)$, and the convective velocity in the wake u_c .

Results for $\Phi_{vv}(\omega)$ and $l_y(\omega)$ have been obtained from the high-speed cross-flow measurements at $x/T = 1$, which is located near the end of the vortex formation region indicated by $\tilde{l}_f/T \approx 0.7$ (compare table 9.3). It should be noted that the difference in $\text{rms}(v)$ between the two locations is small (figure 9.7b). Figure 9.8 shows the auto-spectral density of the v -velocity component. The non-dimensional spectra, obtained over a velocity ranging from $u_\infty = 20\text{m/s}$ to 35m/s , contain a maximum at the shedding frequency. The values collapse within 2dB at the shedding frequency and show even better agreement at higher frequency. Bilka *et al.* [95] reported an estimate of the auto-spectral density $\Phi_{vv}(\omega)$, obtained from uncorrelated PIV measurement by invoking the frozen turbulence assumption and imposing a convective velocity, about 20dB lower than the one in the present study. This substantial underestimation of the velocity fluctuations also lead to the unexpected agreement of the predicted vortex shedding noise with acoustic measurement results.

Figure 9.9 shows the corresponding spanwise coherence of the upwash velocity component (equation 2.47). A marked increase of the coherence at the shedding frequency and its harmonic is observed. This increase in coherence results in an increase of the correlation length (shown in figure 9.10), estimated by an exponential fit (equation 2.46) to the coherence data (figure 9.9) for each frequency band and velocity. Scaling based on the model thickness T and free stream velocity u_∞ (figure 9.10b) shows values between $0.7 \leq l_z(f_{sh})/T \leq 0.8$ with the exception of 25m/s . It is suspected that the increase at $u_\infty = 25\text{m/s}$ is due to the shedding frequency ($f_{sh} \approx 460\text{Hz}$) at this velocity being close to that of the first acoustic mode associated to the wind tunnel width ($c_0/0.8\text{m} \approx 430\text{Hz}$). Bilka *et al.* [95] considered the correlation length of surface pressure fluctuations on the

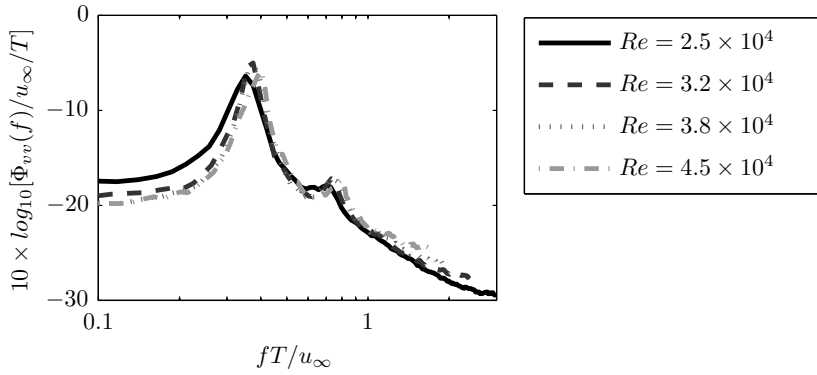


Figure 9.8: Spectra of upwash velocity at the end of vortex formation zone, $x/T = 1$.

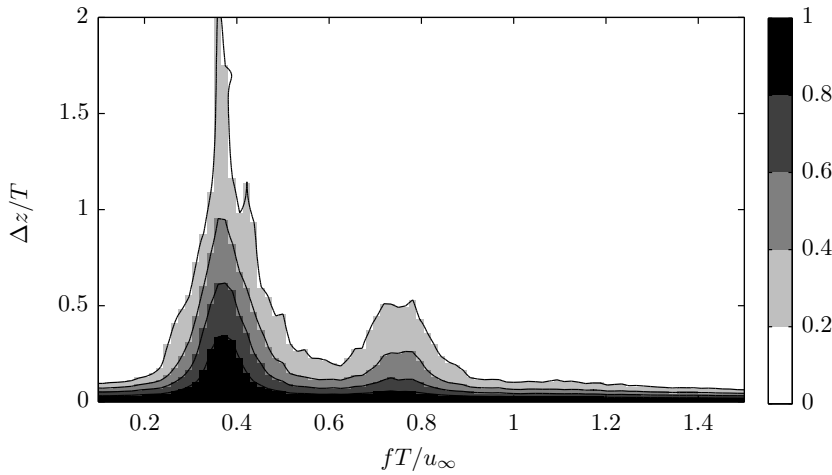


Figure 9.9: Coherence of upwash velocity $|\gamma(f, \Delta z)|$ (equation 2.47) along spanwise coordinate direction at the end of vortex formation zone, $x/T = 1$, $Re = 3.8 \times 10^4$.

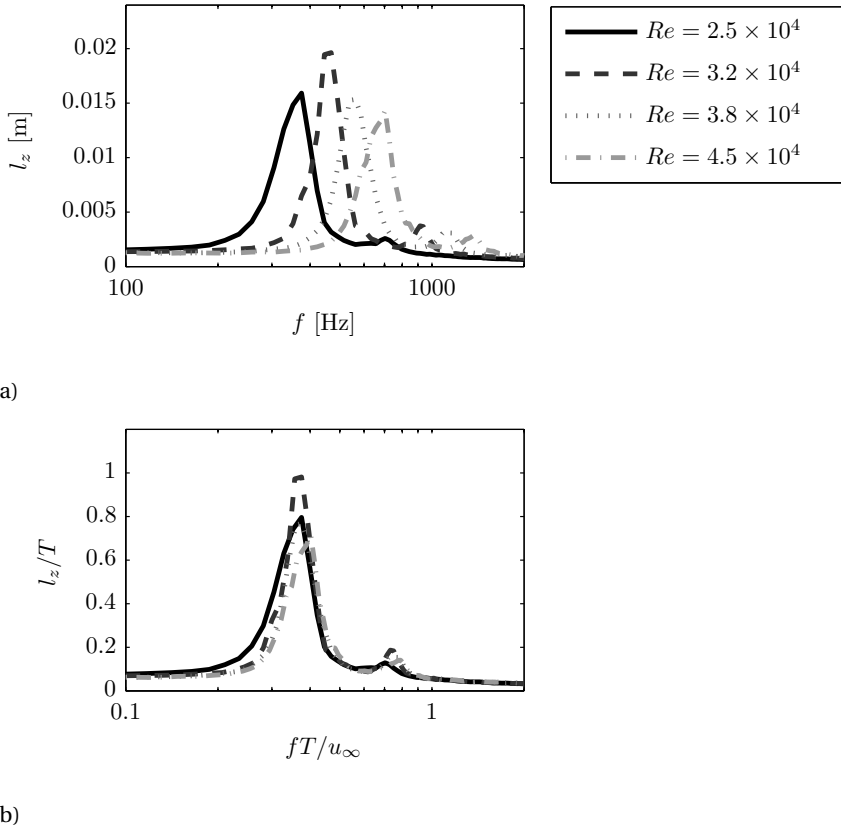


Figure 9.10: Correlation length of upwash velocity (a) and non-dimensional representation (b) (estimated using equation 2.46).

edge and reported a value of approximately $l_z/y_f \approx 2.5$ at the shedding frequency, which is thus similar to the correlation length of the upwash velocity measured in the present study ($l_z/y_f = 2.2 - 3.3$).

A last parameter in the vortex convection model (figure 2.6) and required for the evaluation of equation 2.43 is the convective velocity u_c , which is associated to the upwash velocity fluctuations at the shedding frequency. To determine u_c , the coherence function between the v -velocity component at each point in the field and the acoustic pressure signal recorded by a single microphone at the center of the array is considered. Figure 9.11 shows the relative phase of this coherence function at the shedding frequency f_{sh} and visualizes the associated wavelength λ_{sh} , which is represented by a phase difference of 2π in the streamwise coordinate direction. The product of f_{sh} and λ_{sh} then provides an estimation of the convective velocity u_c . The estimates for the different Reynolds numbers (table 9.4) show a value $u_c/u_\infty \approx 0.47$. This value is lower than the one reported by Roger *et al.* [105] for a sharply truncated trailing edge ($u_c/u_\infty \approx 0.6$).

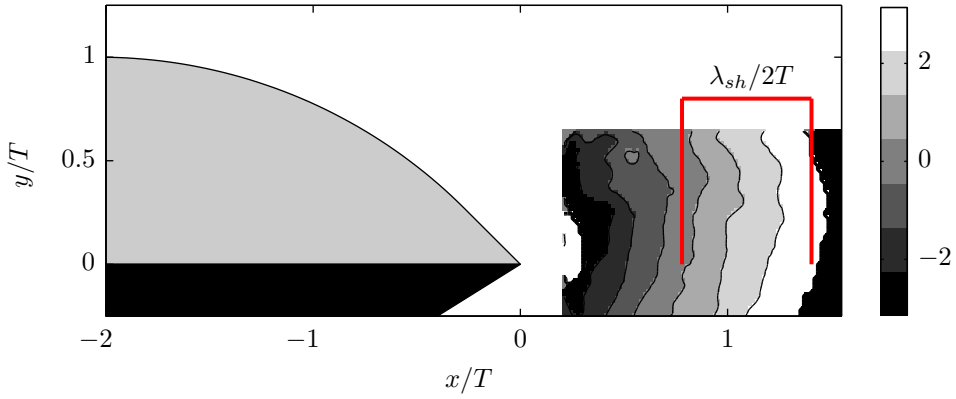


Figure 9.11: Relative angular phase of coherence function between local upwash velocity component v and acoustic pressure measured at center of microphone array, $Re = 3.8 \times 10^4$.

Table 9.4: Characteristic parameters related to vortex shedding at different Reynolds numbers.

Parameter	Symbol			
free stream velocity	u_∞ [m/s]	20	30	40
Reynolds number	$Re = u_\infty T / \nu [\times 10^4]$	3.2	3.8	4.6
wavelength	λ_{sh} / T	1.37	1.25	1.17
	λ_{sh} / y_f	3.8	4.5	4.9
	$\lambda_{sh} / \tilde{y}_f$	3.3	3.5	3.5
convective velocity	u_c / u_∞	0.48	0.46	0.47
shedding frequency	$f_{sh} T / u_\infty$	0.35	0.37	0.4
	$f_{sh} y_f / u_c$	0.26	0.22	0.20
	$f_{sh} \tilde{y}_f / u_c$	0.31	0.29	0.28

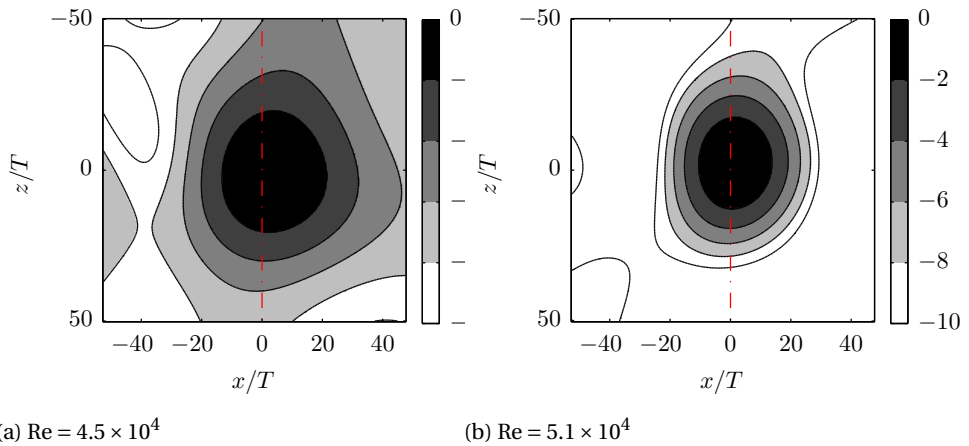


Figure 9.12: Acoustic source power map obtained from beamforming at shedding frequency. Dash-dotted line indicates location of trailing edge. Decibel scale with reference to maximum value.

9.3.2. ACOUSTIC EMISSION

ACOUSTIC MEASUREMENTS

To assess the validity of equation 2.43 for estimation of vortex shedding noise from beveled trailing edges, the latter is measured using an acoustic array as described in section 9.2.1. Figure 9.12 depicts source power maps at the shedding frequency, where the decibel scale is shown with respect to the maximum value. The dash-dotted line indicates the location of the trailing edge at $x/T = 0$.

Results of the integration procedure represent the average Sound Power Level (SWL) over the aperture of the array. The resulting SWL is then scaled to result in an estimate for the average auto-spectral density of the acoustic pressure Φ_{aa} assuming a point source at center span. A similar procedure was used by Pröbsting *et al.* [66]. Figure 9.13 shows the resulting estimate for Φ_{aa} , where the scaling for a compact dipole [20, 93] is used to render the auto-spectral density non-dimensional. In the energetic band around the shedding frequency, the results for different Reynolds numbers show good agreement.

For comparison, the results presented by Bilka *et al.* [95] are also shown in figure 9.13, which were obtained on models with identical geometry, $R/T = 2.5$ and $\theta = 45^\circ$. The reported bluntness parameter $T/\delta^* = 21.2$ is slightly higher compared to the one in the present study ($T/\delta^* = 12 - 14$). While the shedding frequency is slightly different, good agreement is found for the peak value near the shedding frequency 9.13 in particular at high Reynolds number. The slight difference is likely related to the different blockage ratio in the two experiments.

NOISE ESTIMATION

Figure 9.14 shows the predicted auto-spectral density of the acoustic pressure obtained through application of equation 2.43 with the statistics of the upwash velocity reported in section 9.3.1. For comparison with the array measurements, the estimated sound power is averaged over the locations of the microphones in the array. A similar pro-

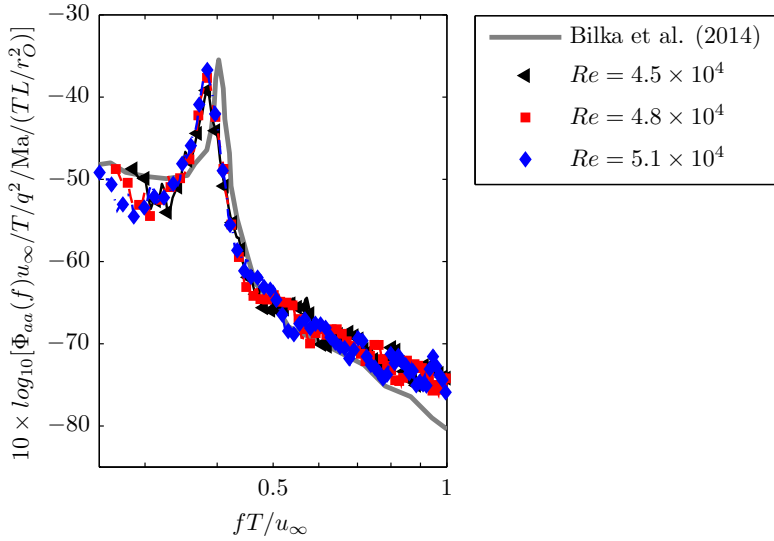


Figure 9.13: Non-dimensional auto-spectral density of acoustic pressure for different Reynolds numbers.

cedure was applied by Pröbsting *et al.* [66] for comparison of noise estimation with array measurements.

Strikingly, the auto-spectral density at the shedding frequency $f_{sh}T/u_\infty \approx 0.37$ is overestimated by almost 15 to 20dB. On one hand, this overestimation is in stark contrast to the reported match of predicted and measured spectra reported by Bilka *et al.* [95]. This disagreement can be explained by the erroneous estimate of the upwash velocity spectrum in the latter study. On the other hand, the tendency for overestimation is in line with the discussion of Blake [19] and Roger *et al.* [105]. Ffowcs Williams and Hall [72] analytically examined the case of a vortex near an infinite plate. They found that the sound intensity due to such a vortex to be inversely proportional to the cube of the distance to the trailing edge. The results presented in this section thus show that noise estimation based on the simplified wake model (equation 2.43) is not applicable for a beveled or rounded trailing edge in particular and thus also not in general. The results emphasize the importance of surface rounding and details of the flow for the trailing edge bluntness noise mechanism due to vortex shedding.

9.4. CONCLUSION

The flow around and in the near wake of a beveled trailing edge characterized by $\theta = 45^\circ$ and $R/T = 2.5$ was assessed. Its structure and general characteristics are in agreement with results presented in the past [19, 46, 95]. In particular, statistics of the upwash velocity at the end of the vortex formation zone have been obtained using a high-speed stereoscopic PIV set-up imaging the cross-flow plane. At this location, maximum fluctuations are $\text{rms}(v)/u_\infty \approx 0.23$ for the upwash component and its spanwise correlation

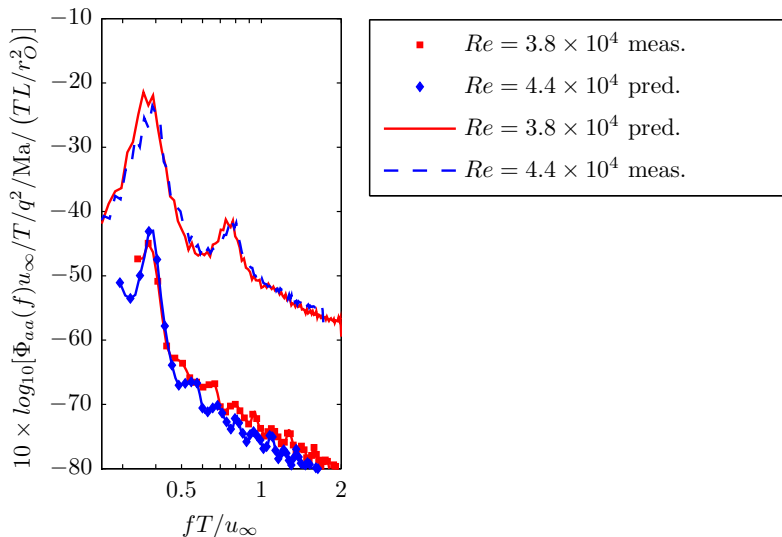


Figure 9.14: Comparison measured and predicted acoustic pressure auto-spectral density $\Phi_{aa}(f)$ for $Re = 3.8 \times 10^5$ ($u_\infty = 30\text{m/s}$) and $Re = 4.5 \times 10^5$ ($u_\infty = 35\text{m/s}$).

length scale at the shedding frequency $l_z(f_{sh})/T \approx 0.8$.

It was shown that straightforward application of equation 2.43 with the measured statistics for upwash velocity results in an overestimation of the auto-spectral density of acoustic pressure by about 15 to 20dB when compared to acoustic measurements. The trend for overestimation is in agreement with arguments of Blake [19] and Roger *et al.* [105] on the effect of the vortex formation distance.

The overestimation is likely due to the extent of the reverse flow region behind the trailing edge, removal of the upper shear layer from the edge, and delay of vortex roll-up to a location further downstream, which is quantified by the vortex formation length and wake thickness parameters. The values for these parameters were identified for the trailing edge geometry investigated in the present study and their ratio is similar to that of the values tabulated by Blake [19]. It was pointed out, however, that vortex formation length and wake thickness are not uniquely defined in the pertinent literature. For future investigation into the effect of these parameters on noise emission, their definition should be clarified. It was further pointed out that the unexpected agreement with acoustic results in the study of Bilka *et al.* [95] was related to an erroneous estimate of the upwash velocity spectrum.

The results presented here show that the simplified wake model in combination with diffraction theory is not applicable for arbitrary trailing edge geometries. The results further underline the importance of the details of the flow field and in particular flow separation for the noise emission at blunt and beveled trailing edges.

EPILOGUE

10

CONCLUSION

ADVANCED PIV methods have been applied for the study of aeroacoustic source mechanisms relevant for noise emission on wind turbine blades. In response to the research questions (see section 1.5), it was demonstrated how high-speed, stereoscopic, and tomographic PIV and pressure reconstruction techniques can be employed to obtain both qualitative and quantitative descriptions of the aeroacoustic source and underlying mechanisms. In particular, studies were presented demonstrating the potential of these methods to contribute to a better understanding of aeroacoustic source mechanisms (research question I) and to predict noise emission (II).

Using high-speed PIV and non-stationary signal analysis, the spatio-temporal structure of the aeroacoustic source for the case of laminar boundary layer instability noise was described in detail (*Part I*). A novel methodology was proposed to obtain a prediction of the broadband noise emitted at a trailing edge based on tomographic PIV and pressure reconstruction techniques (*Part II*). It was demonstrated that this method is capable of providing the information necessary for a sufficiently accurate description of the source, which was formerly unavailable in experimental research. Finally, it was demonstrated how quantities relevant for the description and prediction of the noise generated by vortex shedding on a blunt trailing edge can be measured by high-speed stereoscopic PIV (*Part III*).

The conclusions for each of part of this thesis are summarized below:

10.1. LAMINAR BOUNDARY LAYER INSTABILITY NOISE

Tonal noise emission for an airfoil at low to moderate Reynolds number was found to be related to events on pressure side, suction side, or to an interaction of the two (chapter 4). In general, events on one side can be relevant for tonal noise emission if a separation bubble or separated shear layer exists at a distance upstream of the trailing edge. The separated flow region must be located such that instability waves are amplified substantially with little loss of coherence by undergoing 3D breakdown and further transition to a turbulent state upstream of the trailing edge.

On the NACA 0012 airfoil and for a given non-zero angle of attack, this condition is met on the suction side at low Reynolds numbers and for the pressure side at higher Reynolds numbers. Due to this Reynolds number dependent difference in flow topology between the two sides of the airfoil, different regimes of tonal noise emission can be defined. At low Reynolds number suction-side events dominate tonal noise emission, while at high Reynolds number pressure-side events dominate tonal noise emission. Over an intermediate Reynolds numbers range, interaction or coupling between pressure- and suction-side events is important and can be of hydrodynamic and acoustic nature. Due to the symmetric condition at zero incidence for the NACA 0012, the interaction regime extends over the entire range of Reynolds numbers where tonal noise emission is observed. With increasing angle of attack, interaction is only of importance over a successively smaller range of Reynolds numbers.

The origin of multiple tones in the acoustic spectra for laminar boundary layer instability noise has been subject to debate for decades. It is typically associated to either an aeroacoustic feedback loop between tonal noise emission at the trailing edge and the receptivity region of the boundary layer or to hydrodynamic feedback. In chapter 5, multiple tones in the spectrum were shown to be related to a periodic amplitude modulation of the acoustic pressure signal. A similar amplitude modulation was observed for the velocity fluctuations associated to convecting vortical structures in the source region near the trailing edge. In the pressure- or suction-side-dominated regime, this periodic amplitude modulation can be self-sustained and as such does not require an interaction with a secondary acoustic feedback loop as suggested previously. The previously suggested concept of a secondary acoustic feedback loop, modulating the primary one, is only important for flow conditions within the interaction regime and may result in a shift of the frequencies associated to the tones in the spectrum (chapter 4). The question with regard to the precise mechanism for periodic amplitude modulation still awaits a definite answer and is subject to ongoing research efforts. From the results in the present study, it becomes evident that such research must differentiate between the different regimes of tonal noise generation, since they show fundamentally different behavior.

Thus, understanding of the aeroacoustic feedback loop has advanced. In chapter 6, excitation by tonal noise emission was found to have a strong influence on the transition process and leads to substantial changes in the structure and topology of the separation bubble. In particular, acoustic feedback results in a concentration of the energy associated to velocity fluctuations in the boundary layer over substantially narrower bands of frequencies. In absence of tonal noise, energy is spread over a broader range of frequencies. Tonal excitation can be self-induced if the spectrum is sufficiently narrowband at the trailing edge and vortical structures reach the latter in a coherent state. Alternatively, tonal noise excitation can be attributed to events on the opposite side of the trailing edge, resulting in changes to the flow development and mean flow topology. With tonal excitation present, the separation bubble is substantially shorter than it is the case without acoustic excitation. These effects of receptivity to acoustic waves may in parts explain the differences in vortex shedding from a separation bubble described in previous studies.

10.2. TURBULENT BOUNDARY LAYER TRAILING EDGE NOISE

Advanced (high-speed, tomographic) PIV measurements can be employed to obtain substantially more information on the spatio-temporal characteristics than conventional flow measurement techniques. In combination with pressure reconstruction techniques, it is possible to obtain estimates for the quantities relevant for broadband noise emission due to the interaction of the turbulent boundary layer with the trailing edge, e.g. spectra of fluctuations, correlation and convective velocity of the unsteady surface pressure field.

On one hand, the studies reported in chapters 7 and 8 on the boundary layer and trailing edge with comparison to surface and acoustic pressure measurements showed that satisfactory estimates can be obtained over a restricted band of frequencies. The experiments described in chapter 8 constitutes the first time that such a comprehensive approach has successfully been implemented for broadband noise estimation, combining state-of-the-art tomographic PIV and pressure reconstruction for application with diffraction theory. On the other hand, the spatial dynamic range of the measurement is limited by the hardware and requirements for the tomographic reconstruction. Available laser power poses a limit to the maximum extension of the measurement volume, while the finite resolution of the camera limits the maximum spatial dynamic range. This spatial dynamic range also restricts the range of resolvable frequencies, since higher frequencies are linked to smaller spatial scales. For pressure reconstruction in the turbulent boundary layer, the limitation of the spatial dynamic range is relevant, since a boundary condition for the pressure must nominally be imposed in the free stream, while still resolving small-scale turbulence.

Multi-frame approaches for image interrogation in PIV and pressure reconstruction based on fluid parcel tracking typically introduce temporal (and spatial) filtering effects. The resulting reduction in measurement noise comes at the expense of an increase in systematic (or truncation) error. Additionally, the relative magnitude of these errors is flow dependent. In order to obtain optimum and reliable estimates for spectral quantities relevant in aeroacoustics, especially in the high frequency range, an optimization approach is required. At present, the research on the frequency response of multi-frame interrogation schemes applied to different types of flows is in its infancy and the required optimization criteria are not available yet. For future application of pressure reconstruction methods from PIV data in aeroacoustics, it is thus recommend to further investigate wavenumber and frequency response characteristics, possibly with calibration approaches based on synthetic data sets.

10.3. TRAILING EDGE BLUNTNES NOISE

In chapter 9 the flow around and in the near wake of a beveled trailing edge was characterized. In particular, statistics of the upwash velocity at the end of the vortex formation zone have been obtained using a suitable, and for this purpose new high-speed stereoscopic PIV set-up imaging the cross-flow plane. In particular, it is possible to access the spanwise correlation length of the upwash velocity through this experimental arrangement.

A prediction model based on diffraction theory has been proposed in the past, which

requires the statistics of the upwash velocity after vortex formation. This method has been shown to provide accurate estimates of vortex shedding noise for sharply truncated trailing edges. However, its applicability for rounded or beveled trailing edges as well as airfoils remained controversial. Application of this prediction model in chapter 9 showed a large overestimation of the noise emission due to vortex shedding. It is suggested that the overestimation is in parts due to the extent of the reverse flow region behind the trailing edge, removal of the upper shear layer from the edge, and delay of vortex roll-up to a location further downstream. The prediction model is thus not applicable for application to arbitrary trailing edge geometries. Possibly, a correction to the model based on vortex formation length and wake thickness can be inferred from additional experimental data in the future.

REFERENCES

- [1] F. Howard, *Wilbur and Orville - A bibliography of the Wright Brothers*, dover ed. (Dover Publications, New York, 1998).
- [2] P. Gipe, *Wind Energy Comes of Age* (John Wiley & Sons, 1995).
- [3] M. J. Lighthill, *On sound generated aerodynamically. i. general theory*, Proceedings of the Royal Society of London A **211**, 564 (1952).
- [4] J. E. Ffowcs Williams, *Aeroacoustics*, Annual Review of Fluid Mechanics **9**, 447 (1977).
- [5] W. Dobrzynski, *Almost 40 years of airframe noise research: what did we achieve?* Journal of Aircraft **47**, 353 (2010).
- [6] C. J. Doolan, D. J. Moreau, and L. A. Brooks, *Wind turbine noise mechanisms and some concepts for its control*, Acoustics Australia **40**, 7 (2012).
- [7] F. van den Berg, *Wind turbine noise: an overview of acoustical performance and effects on residents*, in *Proceedings of ACOUSTICS 2013* (Australian Acoustical Society, Victor Harbor, Australia, 2013).
- [8] S. Wagner, R. Bareiß, and G. Guidati, *Wind turbine noise* (Springer-Verlag, 1996).
- [9] S. Oerlemans, M. Fisher, T. Maeder, and K. Kögler, *Reduction of wind turbine noise using optimized airfoils and trailing-edge serrations*, AIAA Journal **47**, 1470 (2009).
- [10] M. Herr and W. Dobrzynski, *Experimental Investigations in Low-Noise Trailing Edge Design*. AIAA Journal **43**, 1167 (2005).
- [11] R. Lerch, G. M. Sessler, and D. Wolf, *Technische Akustik*, 1st ed. (Springer-Verlag, Berlin, 2009).
- [12] S. C. Morris, *Shear-layer instabilities: Particle image velocimetry measurements and implications for acoustics*, Annual Review of Fluid Mechanics **43**, 529 (2011).
- [13] T. F. Brooks, D. S. Pope, and M. A. Marcolini, *Airfoil self-noise and prediction*, Tech. Rep. 1218 (NASA Reference Publication, 1989).
- [14] E. J. G. Arcondoulis, C. J. Doolan, A. C. Zander, and L. A. Brooks, *A review of trailing edge noise generated by airfoils at low to moderate Reynolds number*, Acoustics Australia **38**, 387 (2010).
- [15] M. F. de Pando, P. J. Schmid, and D. Sipp, *A global analysis of tonal noise in flows around aerofoils*, Journal of Fluid Mechanics **754**, 5 (2014).

- [16] E. C. Nash, M. V. Lowson, and A. McAlpine, *Boundary layer instability noise on airfoils*, *Journal of Fluid Mechanics* **382**, 27 (1999).
- [17] R. K. Amiet, *Noise due to turbulent flow past a trailing edge*, *Journal of Sound and Vibration* **47**, 387 (1976).
- [18] H. Arbey and J. Bataille, *Noise generated by airfoil profiles placed in a uniform laminar flow*, *Journal of Fluid Mechanics* **134**, 33 (1983).
- [19] W. K. Blake, *Mechanics of Flow-Induced Sound and Vibration* (Academic Press, 1986).
- [20] N. Curle, *The influence of solid boundaries upon aerodynamic sound*, *Proceedings of the Royal Society of London. Series A. Mathematical and Physical Sciences* **231**, 505 (1955).
- [21] J. C. Hardin and S. L. Lamkin, *Concepts for reduction of blade/vortex interaction noise*, *Journal of Aircraft* **24**, 120 (1987).
- [22] E. Pedersen and K. P. Waye, *Perception and annoyance due to wind turbine noise - a dose-response relationship*, *Journal of the Acoustical Society of America* **116**, 3460 (2004).
- [23] A. L. Marsden, M. Wang, J. E. Dennis, and P. Moin, *Trailing-edge noise reduction using derivative-free optimization and large-eddy simulation*, *Journal of Fluid Mechanics* **572**, 13 (2007).
- [24] T. Lutz, A. Herrig, W. Würz, M. Kamruzzaman, and E. Kramer, *Design and wind-tunnel verification of low-noise airfoils for wind turbines*, *AIAA Journal* **45**, 779 (2007).
- [25] M. S. Howe, *Aerodynamic noise of a serrated trailing edge*, *Journal of Sound and Vibration* **5**, 33 (1991).
- [26] M. S. Howe, *Noise produced by a sawtooth trailing edge*, *Journal of the Acoustical Society of America* **90** (1991).
- [27] R. R. Graham, *The silent flight of owls*, *Journal of the Royal Aeronautical Society* **38**, 837 (1934).
- [28] J. W. Jaworski and N. Peake, *Aerodynamic noise from a poroelastic edge with implications for the silent flight of owls*, *Journal of Fluid Mechanics* **723**, 456 (2013).
- [29] T. Dassen, R. Parchen, J. Bruggeman, and F. Hagg, *Results of a wind tunnel study on the reduction of airfoil self-noise by the application of serrated blade trailing edges*, *Tech. Rep. NLR-TP-96350* (NLR, 1996).
- [30] T. P. Chong, P. F. Joseph, and M. Gruber, *An experimental study of airfoil instability noise with trailing edge serrations*, in *Proceedings of the 16th AIAA/CEAS Aeroacoustic Conference*, AIAA 2010-3723 (AIAA, Stockholm, Sweden, 2010).

- [31] T. P. Chong and P. F. Joseph, *An experimental study of airfoil instability tonal noise with trailing edge serrations*, *Journal of Sound and Vibration* **332**, 6335 (2013).
- [32] C. Arce, D. Ragni, S. Pröbsting, and F. Scarano, *Flow field around a trailing edge at incidence*, in *Proceedings of the 33rd Wind Energy Symposium*, AIAA-2015-0991 (AIAA, Kissimmee, USA, 2015).
- [33] M. Wang, J. B. Freund, and S. K. Lele, *Computational prediction of flow-generated sound*, *Annual Review of Fluid Mechanics* **38**, 483 (2006).
- [34] C. J. Bahr, *An assessment of trailing edge noise measurement techniques*, Ph.D. thesis, University of Florida (2010).
- [35] R. W. Paterson, P. Vogt, M. R. Fink, and C. Munch, *Vortex noise of isolated airfoils*, *Journal of Aircraft* **10**, 296 (1973).
- [36] T. F. Brooks and T. H. Hodgson, *Trailing edge noise prediction from measured surface pressures*, *Journal of Sound and Vibration* **78**, 69 (1981).
- [37] F. V. Hucheson and T. F. Brooks, *Measurement of trailing edge noise using directional array and coherent output power methods*, in *Proceedings of the 8th AIAA/CEAS Aeroacoustics Conference*, AIAA-2002-2472 (AIAA, Breckenridge, Colorado, 2002).
- [38] R. H. Schlinker and R. K. Amiet, *Helicopter Rotor Trailing Edge Noise*, Tech. Rep. NAS1-15730 (NASA, 1981).
- [39] T. J. Mueller, ed., *Aeroacoustic Measurements* (Springer-Verlag, 2002).
- [40] P. Sijtsma, *Phased array beamforming applied to wind tunnel and fly-over tests*, Tech. Rep. NLR-TR-2010-549 (NLR, 2010).
- [41] S. Oerlemans and B. Méndez López, *Acoustic Array Measurements on a Full Scale Wind Turbine*, Tech. Rep. NLR-TP-2005-336 (NLR, 2005).
- [42] S. Buck, J. Roadman, P. Moriarty, and S. Palo, *Acoustic Array Development for Wind Turbine Noise Characterization*, Tech. Rep. NREL/TP-5000-60457 (National Renewable Energy Laboratory, 2013).
- [43] J. C. Yu and C. K. W. Tam, *Experimental investigation of the trailing edge noise mechanism*, *AIAA Journal* **16**, 1046 (1978).
- [44] A. McAlpine, E. C. Nash, and M. V. Lowson, *On the generation of discrete frequency tones by the flow around an aerofoil*, *Journal of Sound and Vibration* **222**, 753 (1999).
- [45] W. K. Blake, *A Statistical Description of Pressure and Velocity Fields at the Trailing Edges of a Flat Strut*, Tech. Rep. 4241 (David W. Taylor Naval Ship Research and Development Center, 1975).

- [46] D. W. Shannon and S. C. Morris, *Experimental investigation of a blunt trailing edge flow field with application to sound generation*, *Experiments in Fluids* **41**, 777 (2006).
- [47] T. Nakano, N. Fujisawa, and S. Lee, *Measurement of tonal-noise characteristics and periodic flow structure around NACA 0018 airfoil*, *Experiments in Fluids* **40**, 482 (2006).
- [48] S. Pröbsting, J. Serpieri, and F. Scarano, *High-speed PIV analysis of trailing edge aeroacoustics*, in *Proceedings of the 10th International Symposium on Particle Image Velocimetry* (Delft, The Netherlands, 2013).
- [49] S. Pröbsting, J. Serpieri, and F. Scarano, *Investigation of tonal noise generation on an airfoil with time-resolved PIV*, in *Proceedings of the 19th CEAS/AIAA Aeroacoustics Conference*, AIAA-2013-2110 (AIAA, Berlin, Germany, 2013).
- [50] S. Pröbsting, J. Serpieri, and F. Scarano, *Experimental investigation of aerofoil tonal noise generation*, *Journal of Fluid Mechanics* **747**, 656 (2014).
- [51] S. Pröbsting and S. Yarusevych, *Upstream effect of trailing edge tonal emissions on a laminar separation bubble*, in *Proceedings of the 32nd AIAA Applied Aerodynamics Conference*, AIAA-2014-2017 (AIAA, Atlanta, USA, 2014).
- [52] S. Pröbsting and F. Scarano, *Experimental investigation of isolated aerofoil noise*, in *Proceedings of the 21st International Congress on Sound and Vibration (ASC/IACAS, Beijing, China, 2014)*.
- [53] A. Henning, K. Kaepernick, K. Ehrenfried, L. Koop, and A. Dillmann, *Investigation of aeroacoustic noise generation by simultaneous particle image velocimetry and microphone measurements*, *Experiments in Fluids* **45**, 1073 (2008).
- [54] A. Henning, L. Koop, and K. Ehrenfried, *Simultaneous multiplane piv and microphone array measurements on a rod-airfoil configuration*, *AIAA Journal* **48**, 2263 (2010).
- [55] A. Henning, L. Koop, and K. Ehrenfried, *Causality correlation in aeroacoustics experiments by means of simultaneous PIV and microphone-array measurements*, in *Proceedings of the 3rd Berlin Beamforming Conference* (GFal, Berlin, Germany, 2010).
- [56] D. E. S. Breakey, J. A. Fitzpatrick, and C. Meskell, *Aeroacoustic source analysis using time-resolved PIV in a free jet*, *Experiments in Fluids* **54**, 1531 (2013).
- [57] A. Schröder, M. Herr, T. Lauke, and U. Dierksheide, *A study on trailing-edge-noise sources by means of time-resolved PIV*, in *New Results in Numerical and Experimental Fluid Mechanics V* (Springer-Verlag, 2006) pp. 373–380.
- [58] C. Haigermoser, F. Scarano, and M. Onorato, *Investigation of the flow in a circular cavity using stereo and tomographic Particle Image Velocimetry*, *Experiments in Fluids* **45**, 517 (2009).

- [59] A. T. de Jong, H. Bijl, and F. Scarano, *The aero-acoustic resonance behavior of partially covered slender cavities*, *Experiments in Fluids* **51**, 1353 (2011).
- [60] V. Koschatzky, P. D. Moore, J. Westerweel, F. Scarano, and B. J. Boersma, *High speed PIV applied to aerodynamic noise investigation*, *Experiments in Fluids* **50**, 863 (2011).
- [61] P. Moore, V. Lorenzoni, and F. Scarano, *Two techniques for piv-based aeroacoustic prediction and their application to a rod-airfoil experiment*, *Experiments in Fluids* **50**, 887 (2010).
- [62] V. Lorenzoni, M. Tuinstra, and F. Scarano, *On the use of time-resolved particle image velocimetry for the investigation of rod-airfoil aeroacoustics*, *Journal of Sound and Vibration* **331**, 5012 (2012).
- [63] C. Schram, A. Hirschberg, and R. Verzicco, *Sound produced by vortex pairing: prediction based on Particle Image Velocimetry*, *AIAA Journal* **42**, 2234 (2004).
- [64] D. Violato and F. Scarano, *Three-dimensional vortex analysis and aeroacoustic source characterization of jet core breakdown*, *Physics of Fluids* **25**, 015112 (2013).
- [65] M. Tuinstra, S. Pröbsting, and F. Scarano, *On the use of particle image velocimetry to predict trailing edge noise*, in *Proceedings of the 19th AIAA/CEAS Aeroacoustics Conference*, AIAA-2013-2252 (AIAA, Berlin, Germany, 2013).
- [66] S. Pröbsting, M. Tuinstra, and F. Scarano, *Trailing edge noise estimation by tomographic Particle Image Velocimetry*, *Journal of Sound and Vibration* **346**, 117 (2015).
- [67] AFDAR, <http://www.afdar.eu/>, .
- [68] S. Pröbsting and S. Yarusevych, *Effect of trailing edge tonal noise on laminar separation bubble dynamics*, *Journal of Fluid Mechanics* **in press** (2015).
- [69] S. Pröbsting, F. Scarano, and S. C. Morris, *Regimes of tonal noise on an airfoil at moderate Reynolds number*, *Journal of Fluid Mechanics* **in press** (2015).
- [70] M. S. Howe, *A review of the theory of trailing edge noise*, *Journal of Sound and Vibration* **61**, 437 (1978).
- [71] M. S. Howe, *Trailing edge noise at low Mach numbers, Part 2: Attached and separated edge flows*, *Journal of Sound and Vibration* **234**, 761 (2000).
- [72] J. E. Ffowcs Williams and L. H. Hall, *Aerodynamic sound generation by turbulent flow in the vicinity of a scattering half plane*, *Journal of Fluid Mechanics* **40**, 657 (1970).
- [73] A. Powell, *On the aerodynamic noise of a rigid flat plate moving at zero incidence*, *Journal of the Acoustical Society of America* **31**, 1649 (1949–1953).

- [74] D. G. Crighton and F. G. Leppington, *Scattering of aerodynamic noise by a semi-infinite compliant plate*, Journal of Fluid Mechanics **43**, 721 (1970).
- [75] D. G. Crighton, *Radiation from vortex filament motion near a half plane*, Journal of Fluid Mechanics **51**, 357 (1972).
- [76] M. S. Howe, *Contributions to the theory of aerodynamic sound, with application to excess jet noise and the theory of the flute*, Journal of Fluid Mechanics **71**, 625 (1975).
- [77] M. S. Howe, *The influence of vortex shedding on the generation of sound by convected turbulence*, Journal of Fluid Mechanics **76**, 711 (1976).
- [78] M. S. Howe, *The effect of forward flight on the diffraction radiation of a high speed jet*, Journal of Sound and Vibration **50**, 183 (1977).
- [79] D. M. Chase, *Sound radiated by turbulent flow off a rigid half-plane as obtained from a wavevector spectrum of hydrodynamic pressure*, Journal of the Acoustical Society of America **52** (1972).
- [80] D. M. Chase, *Noise radiated from an edge in a turbulent flow*, AIAA Journal **13**, 1041 (1975).
- [81] D. G. Crighton, *Radiation properties of a semi-infinite vortex sheet*, Proceedings of the Royal Society of London **A 330**, 185 (1972).
- [82] K. L. Chandiramani, *Diffraction of evanescent waves, with applications to aerodynamically scattered sound and radiation from un baffled plates*, Journal of the Acoustical Society of America , 19 (1973).
- [83] S. Moreau and M. Roger, *Back-scattering correction and further extensions of Amiet's trailing-edge noise model. part II: Application*, Journal of Sound and Vibration **323**, 397 (2009).
- [84] J. Christophe, *Application of Hybrid Methods to High Frequency Aeroacoustics*, Ph.D. thesis, Université libre de Bruxelles (2011).
- [85] M. S. Howe, *Edge-source acoustic Green's function for an airfoil of arbitrary chord, with application to trailing-edge noise*, The Quarterly Journal of Mechanics and Applied Mathematics **54**, 139 (2001).
- [86] M. Roger and S. Moreau, *Back-scattering correction and further extensions of Amiet's trailing-edge noise model, part 1: theory*, Journal of Sound and Vibration **286**, 477 (2005).
- [87] M. Roger and S. Moreau, *Extensions and limitations of analytical airfoil broadband noise models*, International Journal of Aeroacoustics **9**, 273 (2010).
- [88] W. K. Blake, *Trailing Edge Flow and Aerodynamic Sound*, Tech. Rep. (David W. Taylor Naval Ship Research and Development Center, 1984).

- [89] J. Gershfeld, W. K. Blake, and C. W. Knisely, *Trailing edge flows and aerodynamic sound*, in *Proceedings of the 1st AIAA Fluid Dynamics Conference*, 88-3826-CP (AIAA, Cincinnati, USA, 1988) pp. 2133–2140.
- [90] O. M. Griffin and S. E. Ramberg, *The vortex-street wakes of vibrating cylinders*, *Journal of Fluid Mechanics* **66**, 553 (1974).
- [91] M. S. Howe, *The influence of surface rounding on trailing edge noise*, *Journal of Sound and Vibration* **126**, 503 (1988).
- [92] D. W. Shannon, *Flow field and acoustic measurements of a blunt trailing edge*, Phd thesis, University of Notre Dame (2007).
- [93] D. W. Shannon and S. C. Morris, *Trailing edge noise measurements using a large aperture phased array*, *International Journal of Aeroacoustics* **7**, 147 (2008).
- [94] D. W. Shannon, S. C. Morris, and W. K. Blake, *Trailing edge noise from blunt and sharp edge geometries*, in *Proceedings of the ASME 2008 Noise Control and Acoustics Division Conference* (ASME, Dearborn, USA, 2008).
- [95] M. J. Bilka, S. C. Morris, C. Berntsen, J. C. Silver, and D. W. Shannon, *Flowfield and sound from a blunt trailing edge with varied thickness*, *AIAA Journal* **52**, 52 (2014).
- [96] M. Wang, *Towards numerical simulations of trailing-edge aeroacoustics*, in *Annual Research Briefs* (Center for Turbulence Research, 1996) pp. 133–142.
- [97] M. Wang, *Progress in large-eddy simulation of trailing-edge turbulence and aeroacoustics*, in *Annual Research Briefs* (Center for Turbulence Research, 1997) pp. 37–49.
- [98] M. Wang, *Computation of trailing-edge noise at low Mach number using LES and acoustic analogy*, in *Annual Research Briefs* (Center for Turbulence Research, 1998) pp. 91–106.
- [99] M. Wang and P. Moin, *Computation of trailing-edge flow and noise using Large-Eddy Simulation*, *AIAA Journal* **38**, 2201 (2000).
- [100] M. Wang, *Computation of trailing-edge aeroacoustics with vortex shedding*, in *Annual Research Briefs* (Center for Turbulence Research, 2005) pp. 379–388.
- [101] T. Colonius and S. K. Lele, *Computational aeroacoustics: progress on nonlinear problems of sound generation*, *Progress in Aerospace Sciences* **40**, 345 (2004).
- [102] H. M. Macdonald, *A class of diffraction problems*, *Proceedings of the London Mathematical Society*, 410 (1915).
- [103] K. Schwartzschild, *Die Beugung und Polarisation des Lichts durch einen Spalt - I*, *Mathematische Annalen* **55**, 177 (1902).

- [104] R. D. Sandberg and N. D. Sandham, *Direct Numerical Simulation of turbulent flow past a trailing edge and the associated noise generation*, Journal of Fluid Mechanics **596**, 353 (2008).
- [105] M. Roger, S. Moreau, and A. Guédel, *Vortex-shedding noise and potential-interaction noise modeling by a reversed Sears' problem*, in *Proceedings of the 12th AIAA/CEAS Aeroacoustics Conference*, AIAA-2006-2607 (AIAA, Cambridge, USA, 2006).
- [106] M. S. Howe, *Acoustics of fluid-structure interactions* (Cambridge University Press, New York, 1998).
- [107] M. K. Bull, *Wall-pressure fluctuations beneath turbulent boundary layers: Some reflections on forty years of research*, Journal of Sound and Vibration **190**, 299 (1996).
- [108] Y. F. Hwang, W. K. Bonness, and S. A. Hambric, *Comparison of semi-empirical models for the turbulent boundary layer wall pressure spectra*, Journal of Sound and Vibration **319**, 199 (2009).
- [109] M. C. Goody, *Empirical spectral model of surface pressure fluctuations*, AIAA Journal **42**, 1788 (2004).
- [110] G. Schewe, *On the structure and resolution of wall-pressure fluctuations associated with turbulent boundary-layer flow*, Journal of Fluid Mechanics **134**, 311 (1983).
- [111] W. Graham, *A comparison of models for the wavenumber-frequency spectrum of turbulent boundary layer pressures*, Journal of Sound and Vibration **206**, 541 (1997).
- [112] G. M. Corcos, *Resolution of pressure in turbulence*, Journal of the Acoustical Society of America **35**, 192 (1963).
- [113] G. M. Corcos, *The structure of the turbulent pressure field in boundary-layer flows*, Journal of Fluid Mechanics **18**, 353 (1964).
- [114] B. M. Efimtsov, *Characteristics of the field of turbulent wall pressure fluctuations at large Reynolds numbers*, Soviet Physics – Acoustics **28**, 289 (1982).
- [115] R. K. Amiet, *Acoustic radiation from an airfoil in a turbulent stream*, Journal of Sound and Vibration **41**, 407 (1975).
- [116] R. W. Paterson and R. K. Amiet, *Acoustic radiation and surface pressure characteristics of an airfoil due to incident turbulence*, Tech. Rep. CR-2733 (NASA, 1976).
- [117] T. P. Chong and P. E. Joseph, *"ladder" structure in tonal noise generated by laminar flow around an airfoil*, Journal of the Acoustical Society of America **131**, EL461 (2012).
- [118] H. Schlichting and K. Gersten, *Boundary-layer Theory*, 8th ed. (Springer-Verlag, 2000).

- [119] B. Plogmann, A. Herrig, and W. Würz, *Experimental investigations of a trailing edge noise feedback mechanism on a NACA 0012 airfoil*. *Experiments in Fluids* **54** (2013).
- [120] C. K. W. Tam, *Discrete tones of isolated airfoils*, *Journal of the Acoustical Society of America* **55**, 1173 (1974).
- [121] M. R. Fink, *Prediction of airfoil tone frequencies*, *Journal of Aircraft* **12**, 118 (1975).
- [122] S. E. Wright, *The acoustic spectrum of axial flow machines*, *Journal of Sound and Vibration* **45**, 165 (1976).
- [123] L. Aizin, *Sound generation by a tollmien-schlichting wave at the end of a plate in a flow*. *Journal of Applied Mechanical and Technical Physics* **3**, 50 (1992).
- [124] R. D. Sandberg, L. E. Jones, N. D. Sandham, and P. F. Joseph, *Direct numerical simulations of tonal noise generated by laminar flow past airfoils*, *Journal of Sound and Vibration* **320**, 838 (2009).
- [125] L. E. Jones and R. D. Sandberg, *Numerical analysis of tonal airfoil self-noise and acoustic feedback-loops*, *Journal of Sound and Vibration* **330**, 6137 (2011).
- [126] M. J. Kingan and J. R. Pearse, *Laminar boundary layer instability noise produced by an aerofoil*, *Journal of Sound and Vibration* **322**, 808 (2009).
- [127] F. M. White, *Viscous Fluid Flow*, 3rd ed. (McGraw-Hill, 2006).
- [128] M. Drela, *XFOIL: An analysis and design system for low Reynolds number airfoils*, in *Low Reynolds Number Aerodynamics*, Lecture Notes in Engineering, Vol. 54, edited by T. J. Mueller (Springer-Verlag, New York, 1989).
- [129] G. Desquesnes, M. Terracol, and P. Sagaut, *Numerical investigation of the tone noise mechanism over laminar airfoils*, *Journal of Fluid Mechanics* **591**, 155 (2007).
- [130] M. V. Lowson, S. P. Fiddes, and E. C. Nash, *Laminar boundary layer aeroacoustic instabilities*, AIAA Paper (1994).
- [131] M. V. Lowson, A. McAlpine, and E. C. Nash, *The generation of boundary layer instability noise on aerofoils*, AIAA Paper (1998).
- [132] E. C. Nash and M. V. Lowson, *Noise due to boundary layer instabilities*, in *Proceedings of the 1st CEAS/AIAA Aeroacoustics Conference* (AIAA, Munich, Germany, 1995) pp. 95–124.
- [133] E. C. Nash, *Boundary layer instability noise on aerofoils*, Phd thesis, University of Bristol (1996).
- [134] B. H. Carmichael, *Low Reynolds Number Airfoil Survey*, Tech. Rep. Contract Report No. 165803, Vol. I (NASA, 1981).

- [135] T. J. Mueller and J. D. DeLaurier, *Aerodynamics of small vehicles*, Annual Review of Fluid Mechanics **35**, 98 (2003).
- [136] P. B. S. Lissaman, *Low-Reynolds-Number airfoils*, Annual Review of Fluid Mechanics **15**, 223 (1983).
- [137] M. Boutilier and S. Yarusevych, *Parametric study of separation and transition characteristics over an airfoil at low Reynolds number*, Experiments in Fluids **52**, 1491 (2012).
- [138] A. Dovgal, V. Kozlov, and A. Michalke, *Laminar boundary layer separation: Instability and associated phenomena*, Progress in Aerospace Sciences **30**, 61 (1994).
- [139] S. Burgmann and W. Schröder, *Investigation of the vortex induced unsteadiness of a separation bubble via time-resolved and scanning PIV measurements*, Experiments in Fluids **45**, 675– (2008).
- [140] R. Hain, C. J. Kähler, and R. Radespiel, *Dynamics of laminar separation bubbles at low-Reynolds-number aerofoils*, Journal of Fluid Mechanics **630**, 129 (2009).
- [141] L. E. Jones, R. D. Sandberg, and N. D. Sandham, *Stability and receptivity characteristics of a laminar separation bubble on an aerofoil*, Journal of Fluid Mechanics **648**, 257 (2010).
- [142] J. R. Brinkerhoff and M. I. Yaras, *Interaction of viscous and inviscid instability modes in separation–bubble transition*, Physics of Fluids **23**, 124102 (2011).
- [143] O. Marxen and D. S. Henningson, *The effect of small-amplitude convective disturbances on the size and bursting of a laminar separation bubble*, Journal of Fluid Mechanics **671**, 1 (2011).
- [144] M. S. H. Boutilier and S. Yarusevych, *Separated shear layer transition over an airfoil at a low Reynolds number*, Physics of Fluids **24**, 084105 (2012).
- [145] J. H. Watmuff, *Evolution of a wave packet into vortex loops in a laminar separation bubble*, Journal of Fluid Mechanics **397**, 119 (1999).
- [146] S. Yarusevych, P. e. Sullivan, and J. G. Kawall, *On vortex shedding from an airfoil in low-Reynolds-number flows*, Journal of Fluid Mechanics **632**, 245 (2009).
- [147] L. E. Jones, R. D. Sandberg, and N. D. Sandham, *Direct Numerical Simulations of forced and unforced separation bubbles on an airfoil at incidence*, Journal of Fluid Mechanics **602**, 175 (2008).
- [148] O. Marxen and U. Rist, *Mean flow deformation in a laminar separation bubble: Separation and stability characteristics*, Journal of Fluid Mechanics **660**, 37 (2010).
- [149] M. Lang, U. Rist, and S. Wagner, *Investigations on controlled transition development in a laminar separation bubble by means of LDA and PIV*, Experiments in Fluids **36**, 43 (2004).

- [150] M. Alam and N. D. Sandham, *Direct Numerical Simulation of 'short' laminar separation bubbles with turbulent reattachment*, *Journal of Fluid Mechanics* **410**, 223 (2000).
- [151] S. Burgmann, C. Brücker, and W. Schröder, *Scanning PIV measurements of a laminar separation bubble*, *Experiments in Fluids* **41**, 319 (2006).
- [152] E. Wolf, C. J. Kähler, D. R. Troolin, C. Kykal, and W. Lai, *Time-resolved volumetric Particle Tracking Velocimetry of large-scale vortex structures from the reattachment region of a laminar separation bubble to the wake*, *Experiments in Fluids* **50**, 977 (2010).
- [153] O. Marxen, M. Lang, and U. Rist, *Vortex formation and vortex breakup in a laminar separation bubble*, *Journal of Fluid Mechanics* **728**, 58 (2013).
- [154] A. Lambert and S. Yarusevych, *Analyzing vortex dynamics in the laminar separation bubble via surface pressure measurements*, in *Proceedings of the AIAA Aviation 2015*, AIAA 2011-3928 (AIAA, Dallas, USA, 2015).
- [155] A. S. Hersh and R. E. Hayden, *Aerodynamic sound radiation from lifting surfaces with and without leading-edge serrations*, Tech. Rep. 114370 (NASA Contr. Rep., 1971).
- [156] A. Inasawa, T. Kamijo, and M. Asai, *Generation mechanism of trailing-edge noise of airfoil at low Reynolds numbers*, in *Proceedings of the 13th Asian Congress of Fluid Mechanics* (BSME, Dhaka, Bangladesh, 2010) pp. 125–128.
- [157] R. H. Ellsworth and T. J. Mueller, *Airfoil boundary layer measurements at low Re in an accelerating flow from a nonzero velocity*, *Experiments in Fluids* **11**, 386 (1991).
- [158] H. M. Atassi, *Feedback in separated flows over symmetric airfoils*, Tech. Rep. TM-83758 (AGARD, 1984).
- [159] S. Moreau and M. Henner, *Analysis of flow conditions in freejet experiments for studying airfoil self-noise*, *AIAA Journal* **41**, 1895 (2003).
- [160] E. J. G. Arcondoulis, C. J. Doolan, and A. C. Zander, *Airfoil noise measurements at various angles of attack and low Reynolds number*, in *Proceedings of ACOUSTICS 2009* (Australian Acoustical Society, Adelaide, Australia, 2009).
- [161] S. Takagi and Y. Konishi, *Frequency selection mechanism of airfoil trailing-edge noise*, *Journal of Aircraft* **47**, 1111 (2010).
- [162] C. K. W. Tam and H. Ju, *Aerofoil tones at moderate Reynolds number*. *Journal of Fluid Mechanics* **690**, 536 (2012).
- [163] T. Ikeda, T. Atobe, and S. Takagi, *Direct simulations of trailing-edge noise generation from two-dimensional airfoils at low Reynolds numbers*, *Journal of Sound and Vibration* **331**, 556 (2012).

- [164] V. V. Golubev, L. Nguyen, R. R. Mankbadi, M. Roger, and M. R. Visbal, *Acoustic feedback-loop interactions in transitional airfoils*, in *Proceedings of the 19th AIAA/CEAS Aeroacoustics Conference*, AIAA-2013-2111 (AIAA, Berlin, Germany, 2013).
- [165] J. E. Ffowcs Williams, *Hydrodynamic noise*, *Annual Review of Fluid Mechanics* **1**, 197 (1969).
- [166] J. Westerweel, *Fundamentals of digital particle image velocimetry*, *Measurement Science and Technology* **8** (1997).
- [167] M. Raffel, C. Willert, S. Wereley, and J. Kompenhans, *Particle Image Velocimetry*, 2nd ed. (Springer-Verlag, 2007).
- [168] R. Adrian and J. Westerweel, *Particle Image Velocimetry*, 1st ed. (Cambridge University Press, 2011).
- [169] F. Scarano and P. Moore, *An advection-based model to increase the temporal resolution of PIV time series*, *Experiments in Fluids* **52**, 919 (2010).
- [170] B. W. van Oudheusden, *PIV-based pressure measurement*, *Measurement Science and Technology* **24**, 032001 (2013).
- [171] A. Sciacchitano, *Uncertainty Quantification in Particle Image Velocimetry*, Phd thesis, Delft University of Technology (2014).
- [172] A. Sciacchitano, F. Scarano, and B. G. Wieneke, *Multi-frame pyramid correlation for time-resolved piv*, *Experiments in Fluids* **53**, 1087 (2012).
- [173] K. Lynch and F. Scarano, *A high-order time-accurate interrogation method for time-resolved PIV*, *Measurement Science and Technology* **24**, 035305 (2013).
- [174] K. Lynch, S. Pröbsting, and F. Scarano, *Temporal resolution of time-resolved tomographic PIV in turbulent boundary layers*, in *Proceedings of the 17th International Symposium on Applications of Laser Techniques to Fluid Mechanics* (Lisbon, Portugal, 2014).
- [175] G. E. Elsinga, F. Scarano, B. Wieneke, and B. W. van Oudheusden, *Tomographic Particle Image Velocimetry*, *Experiments in Fluids* **41**, 933 (2006).
- [176] F. Scarano, *Tomographic PIV: principles and practice*, *Measurement Science and Technology* **24** (2013).
- [177] K. Lynch and F. Scarano, *Experimental determination of tomographic PIV accuracy by a 12-camera system*, *Measurement Science and Technology* **25**, 084003 (2014).
- [178] S. Ghaemi, *Pressure fluctuations in the turbulent boundary layer*, Ph.D. thesis, Delft University of Technology (2013).

- [179] A. Schröder, R. Geisler, G. E. Elsinga, F. Scarano, and U. Direksheide, *Investigation of a turbulent spot and a tripped turbulent boundary layer flow using time-resolved tomographic PIV*, *Experiments in Fluids* **44**, 305 (2008).
- [180] S. Ghaemi and F. Scarano, *Multi-pass light amplification for tomographic particle image velocimetry applications*, *Measurement Science and Technology* **21** (2010).
- [181] S. Ghaemi, D. Ragni, and F. Scarano, *PIV-based pressure fluctuations in the turbulent boundary layer*, *Experiments in Fluids* **53**, 1823 (2012).
- [182] D. Palumbo, *Determining correlation and coherence lengths in turbulent boundary layer flight data*, *Journal of Sound and Vibration* **331**, 3721 (2012).
- [183] S. Pröbsting, F. Scarano, M. Bernardini, and S. Pirozzoli, *On the estimation of wall pressure coherence using time-resolved tomographic PIV*, *Experiments in Fluids* **54** (2013).
- [184] X. Liu and J. Katz, *Instantaneous pressure and material acceleration measurements using a four-exposure PIV system*, *Experiments in Fluids* **41**, 227 (2006).
- [185] J. J. Charonko, C. V. King, B. L. Smith, and P. P. Vlachos, *Assessment of pressure field calculations from particle image velocimetry measurements*, *Measurement Science and Technology* **21**, 105401 (2010).
- [186] R. de Kat and B. van Oudheusden, *Instantaneous planar pressure determination from piv in turbulent flow*, *Experiments in Fluids* **52**, 1089 (2012).
- [187] G. H. Golub and C. F. van Loan, *Matrix Computations* (Johns Hopkins University Press, Baltimore, Maryland, 1996).
- [188] D. Violato, P. Moore, and F. Scarano, *Lagrangian and eulerian pressure field evaluation of rod-airfoil flow from time-resolved tomographic PIV*, *Experiments in Fluids* **50**, 1057 (2011).
- [189] R. de Kat, *Instantaneous planar pressure determination from Particle Image Velocimetry*, Ph.D. thesis, Delft University of Technology (2012).
- [190] A. Boillot and A. K. Prasad, *Optimization procedure for pulse separation in cross-correlation PIV*, *Experiments in Fluids* **21**, 87 (1996).
- [191] R. Gerakopoulos and S. Yarusevych, *Novel time-resolved pressure measurements on an airfoil at a low Reynolds number*, *AIAA Journal* **50**, 1189 (2012).
- [192] B. Arguillat, D. Ricot, C. Bailly, and G. Robert, *Measured wavenumber: frequency spectrum associated with acoustic and aerodynamic wall pressure fluctuations*, *Journal of the Acoustical Society of America* **128**, 1647 (2010).
- [193] R. M. Lueptow, *Transducer resolution and the turbulent wall pressure spectrum*, *Journal of the Acoustical Society of America* **97**, 370 (1995).

- [194] Y. Tsuji, J. H. M. Fransson, P. H. Alfredsson, and A. V. Johansson, *Pressure statistics and their scaling in high-Reynolds-number turbulent boundary layers*, *Journal of Fluid Mechanics* **585**, 1 (2007).
- [195] R. Shaw, *Influence of hole dimensions on static pressure measurements*, *Journal of Fluid Mechanics* **7**, 550 (1960).
- [196] L. E. Kinsler, A. R. Frey, A. B. Coppens, and J. V. Sanders, *Fundamentals of Acoustics*, 4th ed. (John Wiley & Sons, New York, 2000).
- [197] E. J. G. Arcondoulis, C. J. Doolan, A. C. Zander, and L. A. Brooks, *An experimental investigation of airfoil tonal noise caused by an acoustic feedback loop*, in *Proceedings of ACOUSTICS 2013* (Australian Acoustical Society, Victor Harbor, Australia, 2013).
- [198] K. L. Schumacher, C. J. Doolan, and R. M. Kelso, *The effect of a cavity on airfoil tones*, *Journal of Sound and Vibration* **333**, 1913 (2014).
- [199] K. L. Schumacher, C. J. Doolan, and R. M. Kelso, *The effect of acoustic forcing on an airfoil tonal noise mechanism*, *Journal of the Acoustical Society of America* **136**, EL78 (2014).
- [200] T. Atobe, M. Tuinstra, and S. Takagi, *Airfoil tonal noise generation in resonant environments*, *Transactions of The Japan Society for Aeronautical and Space Sciences* **52**, 74 (2009).
- [201] V. V. Golubev, L. Nguyen, R. R. Mankbadi, M. Roger, and M. R. Visbal, *On flow-acoustic resonant interactions in transitional airfoils*, *International Journal of Aeroacoustics* **13**, 1 (2014).
- [202] T. J. Mueller, D. F. Scharpf, S. M. Batill, R. B. Strebinger, C. J. Sullivan, and S. Subramanian, *The design of a subsonic low-noise, low-turbulence wind tunnel for acoustic measurements*, in *Proceedings of the 17th AIAA Aerospace Ground Testing Conference*, AIAA-92-3883 (AIAA, Nashville, USA, 1992).
- [203] P. D. Welch, *The use of fast Fourier transform for the estimation of power spectra: a method based on time averaging over short, modified periodograms*, *IEEE Transactions on Audio and Electroacoustics* **15**, 70 (1967).
- [204] T. F. Brooks, M. A. Marcolini, and D. S. Pope, *Airfoil trailing-edge flow measurements*, *AIAA Journal* **24**, 1245 (1986).
- [205] C. Torrence and G. Compo, *A practical guide to wavelet analysis*, *Bulletin of the American Meteorological Society* (1998).
- [206] D. Bowdler, *Wind turbine syndrome - an alternative view*, *Acoustics Australia* **40**, 67 (2012).
- [207] F. J. Harris, *On the use of windows for harmonic analysis with the discrete Fourier transform*, *Proceedings of the IEEE* **66**, 51 (1978).

- [208] F. Scarano, *Theory of non-isotropic spatial resolution in PIV*, Experiments in Fluids **35**, 268 (2003).
- [209] J. van Ingen and M. Kotsonis, *A two-parameter method for e^N transition predictions*, in *Proceedings of the 6th AIAA Theoretical Fluid Mechanics Conference*, AIAA 2011-3928 (AIAA, Honolulu, USA, 2011).
- [210] Macrobius, *The Saturnalia*. *Trans. by Percival Vaughan Davies*. (Columbia University Press, New York, 1969).
- [211] T. J. Mueller, *Low Reynolds Number Vehicles*, Tech. Rep. Report 288 (AGARD, 1985).
- [212] M. V. Ol, B. R. McAuliffe, E. S. Hanff, U. Scholz, and C. J. Kähler, *Comparison of laminar separation bubble measurements on a low Reynolds number airfoil in three facilities*, in *Proceedings of the 35th AIAA Fluid Mechanics Conference and Exhibit*, AIAA-2005-51049 (AIAA, Toronto, Canada, 2005).
- [213] F. G. Collins and J. Zelenevitz, *Influence of sound upon separated flow over wings*, AIAA Journal **13**, 408 (1975).
- [214] M. Nishioka, M. Asai, and s. Yoshida, *Control of flow separation by acoustic excitation*, AIAA Journal **28**, 1909 (1990).
- [215] K. B. M. Q. Haman and D. J. McKinzie, *Control of laminar separation over airfoils by acoustic excitation*, AIAA Journal **29**, 1075 (1991).
- [216] S. Yarusevych, P. E. Sullivan, and J. G. Kawall, *Effect of acoustic excitation amplitude on airfoil boundary layer and wake development*, AIAA Journal **45**, 760 (2007).
- [217] M. S. H. Boutilier and S. Yarusevych, *Effects of end plates and blockage on low-Reynolds-number flows over airfoils*, AIAA Journal **50**, 1547 (2012).
- [218] O. Marxen, R. B. Kotapati, R. Mittal, and T. Zaki, *Stability analysis of separated shear flows subject to control by zero-net-mass-flux jet*, Physics of Fluids **27**, 024107 (2015).
- [219] C. Atkinson, S. Coudert, J.-M. Foucaut, M. Stanislas, and J. Soria, *The accuracy of tomographic Particle Image Velocimetry for measurements of a turbulent boundary layer*, Experiments in Fluids **50**, 1031 (2011).
- [220] T. Astarita, *Analysis of weighting windows for image deformation methods in PIV*, Experiments in Fluids **43**, 859 (2007).
- [221] B. Wieneke, *Volume self-calibration for 3D particle image velocimetry*, Experiments in Fluids **45**, 549 (2008).
- [222] R. Theunissen, F. Scarano, and M. L. Riethmuller, *On improvement of piv image interrogation near stationary interfaces*, Experiments in Fluids **45**, 557 (2008).
- [223] S. Pirozzoli, *Generalized conservative approximations of split convective derivative operators*, Journal of Computational Physics **229**, 7180 (2010).

- [224] M. Bernardini and S. Pirozzoli, *Wall pressure fluctuations beneath supersonic turbulent boundary layers*, *Physics of Fluids* **23**, 085102 (2011).
- [225] F. H. Clauser, *The turbulent boundary layer*, *Advances in Applied Mechanics* **4**, 1 (1956).
- [226] M. H. Buschmann and M. Gad-el-Hak, *Debate concerning the mean-velocity profile of a turbulent boundary layer*, *AIAA Journal* **41**, 565 (2003).
- [227] S. Robinson, *Coherent motions in the turbulent boundary layer*, *Annual Review Fluid Mechanics* **23**, 601 (1991).
- [228] S. Pirozzoli, *On the size of the energy-containing eddies in the outer turbulent wall layer*, *Journal of Fluid Mechanics* **702**, 521 (2012).
- [229] M. K. Bull, *Wall-pressure fluctuations associated with subsonic turbulent boundary layer flow*, *Journal of Fluid Mechanics* **28**, 719 (1967).
- [230] S. Oerlemans and P. Migliore, *Aeroacoustic wind tunnel tests of wind turbine airfoils*, in *Proceedings of the 10th AIAA/CEAS Aeroacoustics Conference*, AIAA-2004-3042 (AIAA, Manchester, Great Britain, 2004).
- [231] H. Holthusen and H. Smit, *A new data-acquisition system for microphone array measurements in wind tunnels*, in *Proceedings of the 7th AIAA/CEAS Aeroacoustics Conference*, AIAA-2001-2169 (AIAA, Maastricht, Netherlands, 2001).
- [232] P. Sijtsma, *Users guides of acoustic array data processing software – Extended issue*, Tech. Rep. NLR-TR-2009-528 (NLR, 2009).
- [233] P. Sijtsma, *Elements of acoustic array data processing*, Tech. Rep. NLR-TR-2014-003 (NLR, 2014).
- [234] R. K. Amiet, *Refraction of sound by a shear layer*, *Journal of Sound and Vibration* **58**, 467 (1978).
- [235] S. Oerlemans and P. Sijtsma, *Determination of absolute levels from phased array measurements using spatial source coherence*, Tech. Rep. NLR-TP-2002-226 (NLR, 2002).
- [236] A. Seybert and J. Hamilton, *Time delay bias errors in estimating frequency response and coherence functions*, *Journal of Sound and Vibration* **60** (1978).
- [237] J. S. Bendat and A. G. Piersol, *Random Data: Analysis and Measurement Procedures*, 4th ed. (John Wiley & Sons, 2010).
- [238] J. C. R. Hunt, A. A. Wray, and P. Moin, *Eddies, stream, and convergence zones in turbulent flows*, in *Proceedings of the Summer Program 1988* (CTR, 1988) pp. 193–208.
- [239] M. S. Howe, *Reference Manual on the Theory of Lifting Surface Noise at Low Mach Numbers*, Tech. Rep. AM-98-001 (Boston University, 1998).

- [240] M. Tuinstra, S. Oerlemans, and J. Gooden, *Trailing edge noise: A benchmark for PIV based noise prediction*, Tech. Rep. NLR-TP-2012-332 (NLR, 2012).
- [241] C. Tropea, A. L. Yarin, and J. F. Foss, eds., *Handbook of experimental fluid mechanics* (Springer-Verlag, 2007).
- [242] A. Henning, L. Koop, K. Ehrenfried, A. Lauterbach, and S. Kroeber, *Simultaneous multiplane PIV and microphone array measurements on a rod-airfoil configuration*, in *Proceedings of the 15th AIAA/CEAS Aeroacoustics Conference*, AIAA-2009-3184 (AIAA, Miami, USA, 2009).
- [243] M. J. Lighthill, *On sound generated aerodynamically. ii. turbulence as a source of sound*, *Proceedings of the Royal Society of London A* **222**, 1 (1954).
- [244] J. W. Cooley and J. W. Tukey, *An algorithm for the machine calculation of complex Fourier series*, *Mathematics of Computation* **19**, 297 (1965).

APPENDIX

A

FUNDAMENTAL DEFINITIONS OF ACOUSTICS

Comprehensive introductions to acoustics can be found in various textbooks, for instance in Kinsler *et al.* [196]. Here, a short summary of fundamental definitions is provided.

Sound waves constitute usually weak pressure p_a , velocity u_a , and density ρ_a fluctuations in a compressible fluid. Fluid particles oscillate forward and backward along the direction of propagation of the wave, thus constituting and propagating information in the form of longitudinal waves. If a convective mean flow is present, this acoustic particle motion may be superimposed. In the simplest case, for a quiescent fluid and perfect gas, the propagation of sound is described by a *wave propagation operator* for the acoustic pressure

$$\mathcal{L} = \frac{1}{c_0^2} \frac{\partial^2}{\partial t^2} - \nabla^2 \quad (\text{A.1})$$

, where $c_0 = (\gamma RT)^{1/2}$ is the speed of sound in the fluid with the ratio of specific heats γ ($\gamma \approx 1.4$ for air), the specific gas constant R (≈ 287 J/kgK for air), and the temperature T in units of K. In the absence of sources, the wave equation is written as

$$\mathcal{L} p_a = 0 \quad (\text{A.2})$$

The energy flux transmitted per unit area by the propagation of sound is characterized by the *instantaneous intensity* $I(t) = p_a u_a$ in units of W/m². The *intensity* I is the time average of $I(t)$.

$$I = \overline{I(t)} = \overline{p_a u_a} = \lim_{T \rightarrow \infty} \frac{1}{T} \int_0^T p_a u_a dt \quad (\text{A.3})$$

For plane waves, or in the far field of a source, the acoustic intensity is related to the pressure through the specific acoustic impedance of the propagation medium $\rho_0 c_0$

($\rho_0 c_0 \approx 415 \text{Pas/m}$ for air at 20°C). With the *effective amplitude* $p_e = (\overline{p_a^2})^{1/2} = \text{rms}(p_a)$, for a plane harmonic wave

$$I = \pm \frac{p_e^2}{\rho_0 c_0} \quad (\text{A.4})$$

, where the sign depends on the direction of propagation. The sound power P associated to a source is obtained by integration of I over a surface S with outward normal \mathbf{n} enclosing the source:

$$P = \int_S \mathbf{I} \cdot \mathbf{n} dS \quad (\text{A.5})$$

Due to the large range of possible values for p_e , ranging from $p_{ref} = 20 \mu\text{Pa}$ at the threshold of hearing to about 2kPa for a deafening sound, it is often quantified on a decibel scale through the *Sound Pressure Level*

$$\text{SPL} = 20 \log_{10} \left(\frac{p_e}{p_{ref}} \right) \quad (\text{A.6})$$

Similarly, the intensity level with $I_{ref} = 10^{-12} \text{W/m}^2$

$$\text{IL} = 10 \log_{10} \left(\frac{I}{I_{ref}} \right) \quad (\text{A.7})$$

and *Sound Power Level* with $P_{ref} = 10^{-12} \text{W}$

$$\text{SWL} = 10 \log_{10} \left(\frac{P}{P_{ref}} \right) \quad (\text{A.8})$$

B

SCHWARZSCHILD SOLUTION

The following formulation of the Schwarzschild solution [103] is reproduced from Roger and Moreau [86]. Let Φ be a 2D scalar field and solution of the Helmholtz equation

$$\frac{\partial^2 \Phi}{\partial x^2} + \frac{\partial^2 \Phi}{\partial y^2} + \mu^2 \Phi = 0$$

with boundary conditions

$$\begin{aligned} \Phi(x, 0) &= f(x) & x \geq 0 \\ \frac{\partial \Phi}{\partial y}(x, 0) &= 0 & x < 0 \end{aligned}$$

Then for any $x < 0$, the solution is given by

$$\Phi(x, 0) = \frac{1}{\pi} \int_0^{\infty} G(x, \xi, 0) f(\xi) d\xi$$

with

$$G(x, \xi, 0) = \sqrt{\frac{-x}{\xi}} \frac{e^{-i\mu(\xi-x)}}{\xi-x}$$

C

ACOUSTIC TRANSFER FUNCTION

Roger and Moreau [86] provided the acoustic transfer functions for the general case of a skewed gust. Here, the expressions from Roger and Moreau [87] are adapted to match the notations used in the present study.

For supercritical gusts, the direct scattering term \mathcal{S}_1 is given by

$$\mathcal{S}_1(k_x, k_z) = -\frac{e^{2iC}}{iC} \left\{ (1+i) e^{-2iC} \sqrt{\frac{B}{B-C}} E^* [2(B-C)] - (1+i) E^* [2B] + 1 \right\}$$

where

$$\begin{aligned} B &= \frac{k_x c}{2} + M_0 \frac{\mu c}{2} + \frac{\kappa c}{2} \\ C &= \frac{k_x c}{2} - \frac{\mu c}{2} \left(\frac{x_0}{S_0} - M_0 \right) \\ E(\xi) &= \int_0^\xi \frac{e^{it}}{\sqrt{2\pi t}} dt = C_2(\xi) + iS_2(\xi) \end{aligned}$$

where C_2 and S_2 are Fresnel integrals and

$$\begin{aligned} \beta^2 &= 1 - M_0^2 \\ \mu &= k/\beta^2 \\ \kappa^2 &= \mu^2 - k_z^2/\beta^2 \\ K_x &= \omega/u_c \end{aligned}$$

and the leading edge back-scattering term \mathcal{S}_2 is given by:

$$\frac{1}{H} \mathcal{S}_2(k_x, k_z) = \left\{ e^{2i\kappa c} [1 - (1+i) E^* (2\kappa c)] \right\}^c - e^{2iD} + i [D + k_0 c/2 + M_0 \mu c/2 - \kappa c/2] G$$

\cdot^c denotes multiplication of the imaginary part by $\epsilon = [1 + 1/(2\mu c)]^{-1/2}$.

$$\begin{aligned} H &= \frac{(1+i)e^{-2i\kappa c}(1-\Theta^2)}{2\sqrt{\pi}(u_\infty/u_c-1)k_0c\sqrt{B}/2} \\ D &= \kappa c/2 - \mu c x_O/(2S_O) \\ \Theta &= \sqrt{\frac{k_x + \mu M_0 + \kappa}{k_0 + \mu M_0 + \kappa}} \\ G &= (1+\epsilon)e^{i(\kappa c+D)}\frac{\sin(D-\kappa c)}{D-\kappa c} + (1-\epsilon)e^{i(-\kappa c+D)}\frac{\sin(D+\kappa c)}{D+\kappa c} \\ &\quad + \frac{(1+\epsilon)(1-i)}{2(D-\kappa c)}e^{2i\kappa c}E^*(2\kappa c) - \frac{(1-\epsilon)(1+i)}{2(D+\kappa c)}e^{-2i\kappa c}E(2\kappa c) \\ &\quad + \frac{e^{2iD}}{2}\sqrt{\frac{\kappa c}{D}}E^*(2D)\left[\frac{(1+i)(1-\epsilon)}{D+\kappa c} - \frac{(1-i)(1+\epsilon)}{D-\kappa c}\right] \end{aligned}$$

For subcritical gusts, the direct scattering term \mathcal{S}_1 is given by:

$$\begin{aligned} \mathcal{S}_1(k_x, k_z) &= -\frac{e^{-2iC}}{iC} \left\{ e^{-2iC} \sqrt{\frac{A'_x}{\mu c x_O/(2S_O) - i\kappa'c/2}} \Phi^\circ \left(\sqrt{2i \left(\frac{\mu c x_O}{2S_O} - i\kappa'c/2 \right)} \right) \right. \\ &\quad \left. - \Phi^\circ \left(\sqrt{2iA'_x} \right) + 1 \right\} \end{aligned}$$

and the leading edge back-scattering term \mathcal{S}_2 is given by:

$$\begin{aligned} \mathcal{S}_2(k_x, k_z) &= -\frac{e^{-2iB'}}{B'} H' \left\{ A' \left(e^{2iB'} \left[1 - \operatorname{erf} \left(\sqrt{2\kappa'c} \right) \right] - 1 \right) + \right. \\ &\quad \left. \sqrt{2\kappa'c} \left(k_0c/2 + \left(M_0 - \frac{x_O}{S_O} \right) \mu c/2 \right) \frac{\Phi^\circ \left(\sqrt{-2iB'} \right)}{\sqrt{-iB'}} \right\} \end{aligned}$$

Φ° denotes the complementary error function of complex argument and

$$\begin{aligned} H' &= \frac{(1+i)(1-\Theta'^2)}{2\sqrt{\pi}(\alpha-1)k_0c\sqrt{A'_x}/2} \\ A'_x &= k_x c/2 + M_0 \mu c/2 - i\kappa'c/2 \\ A' &= k_0 c/2 + M_0 \mu c/2 - i\kappa'c/2 \\ \Theta' &= \sqrt{A'_x/A'} \\ B' &= \frac{\mu c x_O}{2S_O} - i\kappa'c/2 \\ \kappa' &= \frac{c}{2} \sqrt{\frac{k_z^2}{\beta^2} - \mu^2} \end{aligned}$$

D

BASIC RELATIONS FOR APPLICATION OF PIV

Tracer particles used for seeding are characterized by their density ρ_p and mean diameter d_p . If ρ_f and μ are the density and dynamic viscosity of the fluid, respectively, the relaxation time τ_p (equation D.1) is a measure for the time response of the particle. In order for the particles to accurately represent the motion of the flow, the ratio of relaxation time and characteristic flow time scale should be small. This ratio is called the *Stokes number*.

$$\tau_p = \frac{(\rho_p - \rho_f) d_p^2}{18\mu} \quad (\text{D.1})$$

The diameter of the image of a tracer particle with diameter d_p is given by the geometric average of the diameter due to geometrical imaging Md_p , where M is the magnification, and the diameter due to diffraction limited imaging d_{diff} (equation D.2). The magnification is defined as the ratio of image and object size, and can be estimated by the ratio of object distance s_o and sensor distance s_i with respect to the effective lens plane $M = s_i / s_o$.

$$d_i = \sqrt{(Md_p)^2 + d_{diff}^2} \quad (\text{D.2})$$

The diameter due to diffraction limited imaging depends further on the aperture number (f-stop) $f_\#$ and the wavelength of the light λ as

$$d_{diff} = 2.44 f_\# \lambda (M + 1) \quad (\text{D.3})$$

A similar formula applies for the *depth of field* δ_z of the optical system:

$$\delta_z = 4.88 f_\#^2 \lambda \left(\frac{M + 1}{M} \right)^2 \quad (\text{D.4})$$

E

STATISTICAL DATA ANALYSIS

This appendix provides a short summary of definitions for statistical data analysis. For more details on statistical data processing, the reader is referred to Bendat and Piersol [237].

REYNOLDS DECOMPOSITION

For statistical analysis of boundary layer flows, a flow field variable u is often decomposed into a time average part, e.g. $\bar{u}(\mathbf{x})$, and a fluctuating part $u'(\mathbf{x}, t)$. This decomposition is called *Reynolds decomposition* (equation E.1).

$$u(\mathbf{x}, t) = \bar{u}(\mathbf{x}) + u'(\mathbf{x}, t) \quad (\text{E.1})$$

Similarly, for acoustic variables are often decomposed. For instance, in a mean (hydrodynamic) pressure $\bar{p}(\mathbf{x})$ and a small (acoustic) fluctuating part $p'(\mathbf{x}, t)$.

MEAN AND ENSEMBLE AVERAGE

For turbulence measurements, the time history of flow variables can be regarded as a random processes, which can be characterized by statistical moments. These statistical moments are defined in terms of the expected value $E[\cdot]$.

The first statistical moment is the *mean* value μ . Considering a random variable u , the mean value is defined by the integral expression in equation E.2, where $\mathcal{P}(u)$ is the probability density function of u :

$$\begin{aligned} \mu_u &= E[u] \\ &= \int_{-\infty}^{\infty} u \mathcal{P}(u) du \end{aligned} \quad (\text{E.2})$$

For a statistically *stationary* random process, the mean value μ_u of a flow field quantity μ_u only depends on the location in space \mathbf{x} and can be estimated by the time average $\bar{u}(\mathbf{x})$ of a recorded signal,

$$\begin{aligned}\mu_u &= \bar{u}(\mathbf{x}) \\ &= \lim_{T \rightarrow \infty} \frac{1}{T} \int_0^T u(\mathbf{x}, t) dt\end{aligned}\quad (\text{E.3})$$

Sampling a signal at finite time resolution (given by the *sampling frequency* f_{acq}) and over a finite period often does not provide sufficient information for exact evaluation of the integral in equation E.3. Instead, the time average is estimated through an ensemble average over the data collected in an experiment. Let $u(\mathbf{x}, t_i)$ be a discrete representation of the physical process $u(\mathbf{x}, t)$ at time instances t_i . The ensemble average (denoted by $\langle \cdot \rangle$) over time is represented by a sum over the recorded samples at time instances t_i :

$$\bar{u}(\mathbf{x}) \approx \langle u(\mathbf{x}, t) \rangle = \frac{1}{N} \sum_{i=1}^N u(\mathbf{x}, t_i) \quad (\text{E.4})$$

Similarly, if the statistical properties are *homogeneous* over a set of locations in space \mathbf{x}_i , the average over the locations of this set can be considered (equation E.5). This is often the case in boundary layer and wake flows, that are 2D in a time-averaged sense (statistically homogeneous over the span).

$$\mu_u \approx \langle u(\mathbf{x}, t) \rangle = \frac{1}{N} \sum_{i=1}^N u(\mathbf{x}_i, t) \quad (\text{E.5})$$

If the statistical process is both statistically stationary and homogeneous for a set of points in space, a combined ensemble average over space and time can be considered. For tomographic PIV measurements, where often comparatively few vector fields are available due to expensive data processing, additional averaging over space (e.g. across spanwise coordinate direction if homogeneous) can improve statistical convergence significantly.

VARIANCE AND COVARIANCE

Next to the mean value (*first statistical moment*), in the characterization of random processes often the *variance* (*second statistical moment*) is of interest. It provides an indication for the spread of the distribution about the mean μ_u . Similar to the mean value in the previous section, the variance is defined in terms of the expectation value $E[\cdot]$ as

$$\begin{aligned}\sigma_u^2 &= E[(u - \mu_u)^2] \\ &= \int_{-\infty}^{\infty} (u - \mu_u)^2 \mathcal{P}(u) du\end{aligned}\quad (\text{E.6})$$

The *standard deviation* σ_u is defined as the positive root of the variance. In practice, the standard deviation is estimated with the *root-mean-square* $\text{rms}(\cdot)$ estimator as

$$\begin{aligned}
\sigma_u^2 &\approx [\text{rms}(u(\mathbf{x}, t))]^2 \\
&= \frac{1}{N} \sum_{i=1}^N [u(\mathbf{x}, t_i) - \bar{u}(\mathbf{x})]^2 \\
&= \frac{1}{N} \sum_{i=1}^N [u'(\mathbf{x}, t_i)]^2
\end{aligned} \tag{E.7}$$

For two random variables $u(t)$ and $v(t)$, associated to statistically stationary processes, the covariance function is independent of time t and defined by

$$C_{uv}(\tau) = E[(u(t) - \mu_u)(v(t + \tau) - \mu_v)] \tag{E.8}$$

In the special case $v = u$, one recovers the expression for the variance (equation E.6) and $C_{uu} = \sigma_u^2$. The correlation function is related to the covariance function (equation E.8) through the product of the mean values:

$$R_{uv}(\tau) = E[u(t)v(t + \tau)] = C_{uv}(\tau) + \mu_u \mu_v \tag{E.9}$$

One says that two stationary processes are uncorrelated if $C_{uv}(\tau) = 0$ for all τ . Note that $C_{uv} = R_{uv}$ if one of the mean values, μ_u or μ_v , is zero. Equation E.9 is applied to an aeroacoustic source quantity (e.g. Lighthill stress tensor) in combination with a far field quantity (e.g. acoustic pressure) for causality correlation [53–55, 242].

If only the degree of linear dependence between the two signals is of interest for the analysis, the *correlation coefficient* $\rho_{uv}(\tau)$ is considered instead, and is bound by $-1 \leq \rho_{uv} \leq 1$,

$$\rho_{uv} = \frac{C_{uv}(\tau)}{\sigma_u \sigma_v} \tag{E.10}$$

Higher-order moments are sometimes considered and represent the symmetry of the signal about the mean value (skewness) and the presence of spikes (kurtosis).

CAUSALITY CORRELATION

A method for combining simultaneous PIV and acoustic measurements for the analysis of an aeroacoustics source has been applied by Henning *et al.* [53, 54, 55, 242] and is based on the cross-correlation between a near-field quantity $\vartheta(\mathbf{y}, t)$ measured by PIV at position \mathbf{y} and time t and the acoustic pressure $p'(\mathbf{x}, t)$ at the location of a receiver \mathbf{x} . The normalized cross-correlation function for a time shift τ is defined, where $\langle \cdot \rangle$ denotes an ensemble average over time:

$$R_{\vartheta, p'}(\mathbf{x}, \mathbf{y}, \tau) = \frac{\langle \vartheta(\mathbf{y}, t) p'(\mathbf{x}, t + \tau) \rangle}{\sqrt{\langle \vartheta^2(\mathbf{y}, t) \rangle \langle p'^2(\mathbf{x}, t) \rangle}} \tag{E.11}$$

Examples for choices of the near-field quantity include the stress tensor of Lighthill [3, 243] for a turbulent jet or the upwash velocity for a blunt trailing edge with vortex

shedding. However, care should be taken in the choice of an appropriate near-field quantity and interpretation of the results from causality correlation: correlation does not imply causation.

SPECTRAL DENSITY

The *two-sided cross-spectral density function* $S_{uv}(f)$ of two signals $u(\tau)$ and $v(\tau)$ can be defined as the Fourier transform of the correlation function (equation E.12), where f denotes the ordinary frequency and $\omega = 2\pi f$ the angular frequency.

$$S_{uv}(f) = \int_{-\infty}^{\infty} R_{uv}(\tau) e^{-2\pi f\tau i} d\tau \quad (\text{E.12})$$

Similarly, the auto-spectral density function S_{uu} is defined for the special case $v = u$. Since one is typically concerned with positive frequencies $f \geq 0$ and $S_{uv}(f) = S_{uv}(-f)$, one defines the *one-sided* cross-spectral density function (equation E.13).

$$\Phi_{uv}(f) = (f) \begin{cases} 2S_{uv}(f) & , f > 0 \\ S_{uv} & , f = 0 \\ 0 & , f < 0 \end{cases} \quad (\text{E.13})$$

Welch [203] described a procedure to obtain the spectral densities through Fourier analysis of the discrete time signals. This method is also called average modified periodogram method. The finite time Fourier transform of a sample record $u(t)$ sampled for a period $0 \leq t \leq T$ is defined in equation E.14.

$$U(f, T) = \int_0^T u(t) e^{-2\pi f t i} dt \quad (\text{E.14})$$

A consistent estimate of the spectral density requires an ensemble average over different realizations for a stationary random process. In practice, this ensemble average is obtained by dividing a recorded time sequence in segments (or windows). If U_K and V_K are the Fourier transforms for the realizations u_K and v_K of length T , the cross-spectral density function Φ_{uv} is obtained through equation E.15. Estimates for the auto-spectral density functions are obtained for the case $v = u$. The asterisk (\cdot^*) denotes the complex conjugate and the expectation value $E[\cdot]$ is evaluated over the realization K .

$$\Phi_{uv}(f) = 2 \lim_{T \rightarrow \infty} \frac{1}{T} E[U_K^*(f, T) V_K(f, T)] \quad (\text{E.15})$$

The realization K can be created by splitting a continuous time signal in segments. Especially for data intensive applications such as PIV, the segment period T and sampling frequency f_{acq} will always be finite and often limited by hardware considerations. For the discretely sampled data $u(t_k)$ with $t_k = k/f_{acq}$ and number of samples $N = f_{acq}T$ ($k = 0, 1, \dots, N-1$) the Fourier transform (equation E.14) is approximated through the *Discrete Fourier Transform* (DFT, equation E.16) scaled by the sampling frequency $1/f_{acq}$. Note that $f_n = n/NT$.

$$U_K(f_n, T) = \frac{1}{f_{acq}} \sum_{k=0}^{N-1} u(t_k) e^{-2\pi i n k / N} \quad (\text{E.16})$$

The DFT is often implemented through the *Fast Fourier Transform* (FFT) algorithm [244]. Windowing function are usually applied over each of the segments to reduce undesirable effects of spectral leakage. An in-depth discussion of the topic can be found in Harris [207].

The time related variables τ , T , and frequency f chosen for presentation in the this section can be replaced by their counterparts in space, for instance location x , segment length L , and wavenumber $\kappa = 1/\lambda$. In that case, the definitions presented here can be applied and equation E.17 provides an estimate of the wavenumber spectral density function.

$$\Phi_{uv}(\kappa) = 2 \lim_{L \rightarrow \infty} \frac{1}{L} E [U_k^*(\kappa, L) V_k(\kappa, L)] \quad (\text{E.17})$$

WAVENUMBER-FREQUENCY SPECTRAL DENSITY

If information on the spatio-temporal structure of a quantity is required, the wavenumber-frequency spectral density is considered. Consider the cross-spectral density $\Phi_{uu}(\Delta x, f) = \Phi_{u_1 u_2}(f)$ with u_1 sampled at x_1 and u_2 sampled at x_2 . If the random process considered is statistically homogeneous along the considered spatial dimension, the cross-spectrum is a function of separation $\Delta x = x_2 - x_1$ between two points only and its Fourier transform results in the wavenumber-frequency spectral density (equation E.18).

$$\Phi_{uu}(f, \kappa_x) = \lim_{L_x \rightarrow \infty} \int_{-L_x/2}^{L_x/2} \Phi_{uu}(f, \Delta x) e^{-2\pi \kappa_x \Delta x} d\Delta x \quad (\text{E.18})$$

The definition in equation E.18 represents the wavenumber-frequency spectrum for a single spatial dimension and time. This case is often encountered, when for instance the wavenumber-frequency decomposition of velocity fluctuations for streamwise wavenumbers only is of interest. In the 2D case, which represents for instance the decomposition of the unsteady surface pressure field in a streamwise gust component (k_x) and spanwise gust component (k_z), the definition can be extended (equation E.19)

$$\Phi_{uu}(f, \kappa_x, \kappa_z) = \lim_{L_x, L_z \rightarrow \infty} \int_{-L_x/2}^{L_x/2} \int_{-L_z/2}^{L_z/2} \Phi_{uu}(f, \Delta x, \Delta z) e^{-2\pi \kappa_x \Delta x} e^{-2\pi \kappa_z \Delta z} d\Delta z d\Delta x \quad (\text{E.19})$$

The measurements of the full wavenumber-frequency spectral density is complex and requires an array of sensors or field measurement techniques. An example for the measurement of unsteady surface pressure wavenumber-frequency spectral density is contained in the work of Arguillat *et al.* [192].

COHERENCE

The *coherence function* (also: *coherence squared function*) of two sample records $u(t)$ and $v(t)$ is defined in terms of cross- and auto-spectral density (equation E.20). $|\cdot|$ de-

notes the modulus and, thus, the coherence squared function is real valued and bounded $0 \leq \gamma_{uv}^2 \leq 1$ [237]. Similar to the correlation coefficient it indicates the degree of linear dependence between two signal components at frequency f .

$$\gamma_{uv}^2(f) = \frac{|\Phi_{uv}(f)|^2}{\Phi_{uu}(f)\Phi_{vv}(f)} \quad (\text{E.20})$$

The cross- and auto-spectral density required for the evaluation of equation E.20 can be estimated using the average modified periodogram procedure described in section E [236].

Assuming that there are no bias errors due to the finite bandwidth in the spectral estimation, an estimation of the relative convergence error on the coherence estimate ϵ_{γ^2} is given by equation E.21 [237], where n_d is the number of averages considered in the spectral estimation.

$$\epsilon_{\gamma^2} = \frac{\sqrt{2}(1-\gamma^2)}{\sqrt{\gamma^2}\sqrt{n_d}} \quad (\text{E.21})$$

WAVELET ANALYSIS

Torrence and Compo [205] provide an introduction to wavelet analysis. *Wavelet analysis* can be used to analyze non-stationary processes and in particular to estimate the power contained in a signal as a function of time. The continuous wavelet transform of the signal $u(t)$ is defined by convolution of the latter with a scaled and translated wavelet function Ψ , where s is the wavelet scale or *dilatation* factor:

$$\tilde{u}(s, t) = \int_{-\infty}^{\infty} u(t') \Psi^* \left(\frac{t-t'}{s} \right) dt' \quad (\text{E.22})$$

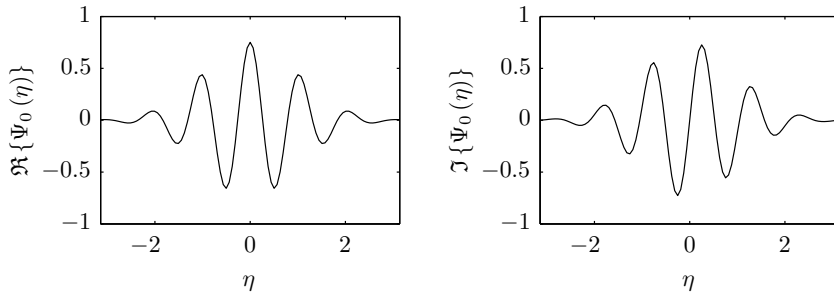
Given a signal $u(t_n)$, where $t_n = n/f_{acq}$ with $n = 0 \dots N-1$ and $\delta t = 1/f_{acq}$ the sampling frequency, a discrete version of the continuous wavelet transform (equation E.22) is written as

$$\tilde{U}(s, t_n) = \left(\frac{\delta t}{s} \right)^{1/2} \sum_{n'}^{N-1} u(t_{n'}) \Psi^* \left(\frac{(n'-n)\delta t}{s} \right) \quad (\text{E.23})$$

For spectral estimation, similar to Fourier analysis presented in the preceding section, the *Morlet wavelet* is frequently employed in the analysis (equation E.24), where ω_0 is the non-dimensional wavelet frequency [205].

$$\Psi(\eta) = \left(\frac{\delta t}{s} \right)^{1/2} \Psi_0(\eta) = \left(\frac{\delta t}{s} \right)^{1/2} \pi^{-1/4} e^{\omega_0 \eta i} e^{-\eta^2/2} \quad (\text{E.24})$$

In general, the wavelet coefficient obtained through equation E.23 are complex if the wavelet function is complex valued. The amplitude is then given by the modulus $|\tilde{U}|$ and the phase by $\tan^{-1}[\Im\{\tilde{U}\}/\Re\{\tilde{U}\}]$, where \Im and \Re indicated the imaginary and real parts, respectively. In analogy to the auto-spectral density, the wavelet power spectrum can be defined as $|\tilde{U}|^2$.



(a) Real part.

(b) Imaginary part.

Figure E.1: Morlet wavelet (equation E.24) function for $\omega_0 = 6$.

Through a relation between the wavelet dilatation s , frequency ω_0 , and Fourier period, a *pseudo frequency* f can be defined that is used to relate results from wavelet analysis to those of Fourier analysis. This relation is written as

$$f = \frac{\omega_0 + \sqrt{2 + \omega_0^2}}{4\pi s} \quad (\text{E.25})$$

F

AMPLITUDE MODULATION

Periodic amplitude modulation is often encountered in aeroacoustic applications, for instance in the superposition of sound originating from multiple sources. Here, two examples are provided.

Example 1: For two single frequency signals at similar frequency, the result of the superposition is a signal with periodic amplitude modulation, which is well known as *beat phenomenon*. Given the two frequencies $f_{c_1} = 0.2$ and $f_{c_2} = 0.18$, such that $f_{c_1} \approx f_{c_2}$. The signal $y(t)$ is given by

$$\begin{aligned} y(t) &= \frac{1}{2} [\cos(2\pi f_{c_1} t) + \cos(2\pi f_{c_2} t)] \\ &= \cos(\pi [f_{c_1} + f_{c_2}] t) \cos(\pi [f_{c_1} - f_{c_2}] t) \end{aligned} \quad (\text{E.1})$$

From the decomposition in equation E.1 it can be seen that the signal can be written as the product of a high frequency component $(f_{c_1} + f_{c_2})/2$ and a low frequency component $(f_{c_1} - f_{c_2})/2$. The latter is interpreted as a modulation frequency. Figure E.1 shows the signal in the time and in the frequency domain. The period of the modulation ($T = 50$) corresponds to the inverse of the modulation frequency $\Delta f = f_{c_1} - f_{c_2} = 0.02$, which is thus equal to the frequency separation of the two components in figure E.1.

Example 2: Periodic amplitude modulation is not only encountered for the superposition of acoustic waves originating from multiple sources. It is also a commonly encountered phenomenon in the aeroacoustic source region. An example for such a case are the instability waves encountered on aerofoils in transitional flow that generate laminar boundary layer instability noise (discussed in chapters 4 through 6). In some cases, the amplitude of the velocity fluctuations, induced by such instability waves, shows strong periodic amplitude modulation [50]. Such signal can be modeled by a carrier frequency f_c and modulation frequencies Δf , where Δf is the fundamental frequency of the periodic amplitude modulation (equation E.2).

$$y(t) = \frac{1}{2} [1 + \cos(2\pi \Delta f t)] \cos(2\pi f_c t) \quad (\text{E.2})$$

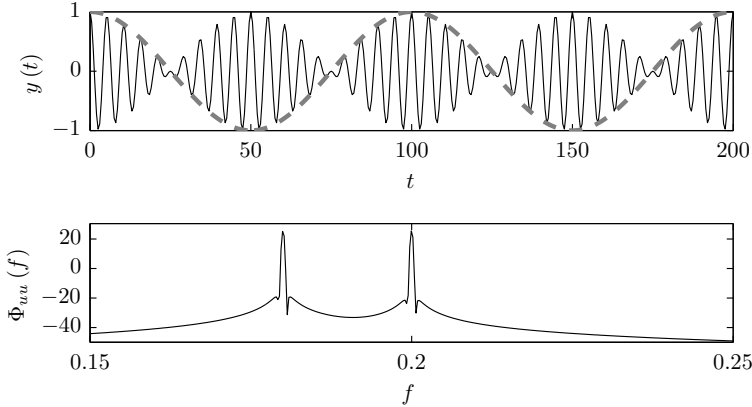


Figure E1: Beat phenomenon as a result of superposition of two single frequency signals with similar frequency (black). Low frequency envelope (grey). Time (top) and frequency domain (bottom).

Using equation E1, the product of the trigonometric functions in equation E2 can be interpreted as

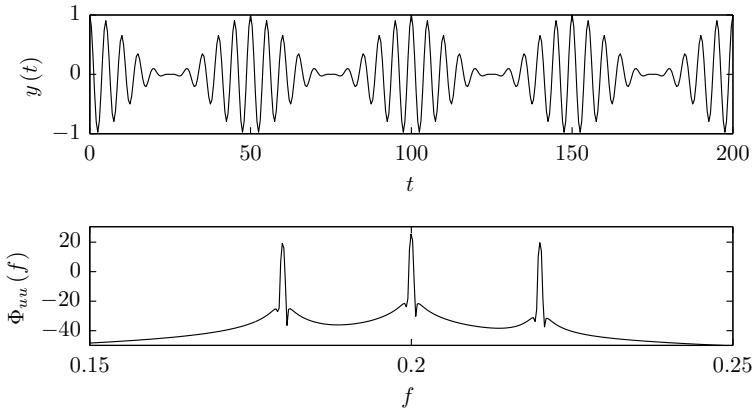
$$\cos(2\pi\Delta f t) \cos(2\pi f_c t) = \frac{1}{2} [\cos(2\pi [f_c + \Delta f] t) + \cos(2\pi [f_c - \Delta f] t)] \quad (\text{E3})$$

The resulting signal has discrete components at the carrier frequency f_c , at $f_c + \Delta f$, and $f_c - \Delta f$. Figure E2a shows the signal $y(t)$ in the time domain and the resulting auto-spectral density Φ_{yy} for $f_c = 0.2$ and $m\Delta f = 0.02$. Most energy is contained in the signal at the carrier frequency. The effect of the periodic amplitude modulation are two symmetrically arranged side peaks with a frequency separation of Δf with respect to the carrier frequency.

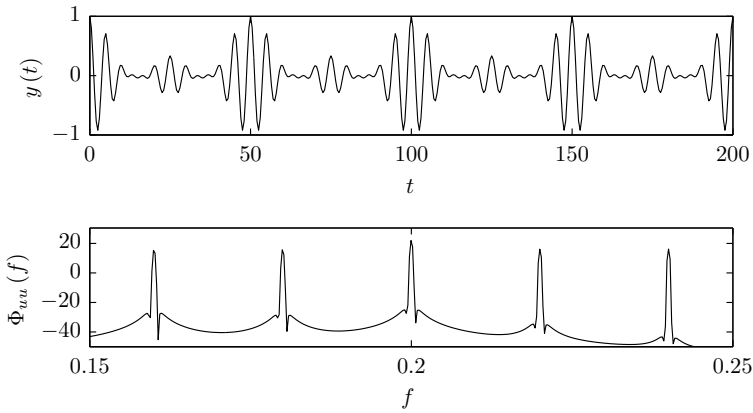
Example 3: The analysis can be extended to signals with further periodic amplitude modulation at upper harmonic frequency $m\Delta f$ of the fundamental modulation frequency Δf . An example including the fundamental ($m = 1$) and first harmonic ($m = 2$) is

$$y(t) = \frac{1}{3} \left[1 + \sum_{m=1}^2 \cos(2\pi m\Delta f t) \right] \cos(2\pi f_c t) \quad (\text{E4})$$

Figure E2 shows the signal $y(t)$ in the time domain and its auto-spectral density Φ_{yy} . Comparison to the figure E2a confirms that the periodic amplitude modulation at frequency $2\Delta f$ results in a second pair of side peaks with the equivalent frequency separation to the carrier frequency f_c .



(a) Periodic modulation at frequency Δf . Time (top) and frequency domain (bottom).



(b) Periodic modulation at frequencies Δf and $2\Delta f$. Time (top) and frequency domain (bottom).

Figure E2: Periodic amplitude modulation of single frequency signal.

CURRICULUM VITÆ

Non est ad astra mollis e terris via.

Seneca the Younger, *Hercules Furens*

STEFAN PRÖBSTING was born on September 20, 1985, in Kamp-Lintfort, Germany. He grew up in Kerken, a picturesque village located within the beautiful Lower Rhine area in the western part of the state of North Rhine-Westphalia. He obtained his matura at the Thomaëum in Kempen am Niederrhein before entering civilian service for a period of nine months. In 2006, he moved to the Netherlands to study aerospace engineering at Delft University of Technology.

In 2009, Stefan obtained his B.Sc. in Aerospace Engineering *cum laude*. He then went on to deepen his studies in the field of aerodynamics and followed the M.Sc. program in Delft together with an *honors program* on aeroacoustics. His thesis research was related to experimental aerodynamics and conducted under the guidance of Dr. S. Ghaemi and Prof. F. Scarano. The following year, he moved to Belgium to follow the Diploma Course at the Von Karman Institute for Fluid Dynamics in Brussels, conducting a research project in the area of computational fluid dynamics under the supervision of Prof. P. Rambaud and Prof. C. Schram. In summer 2011, he received his Diploma *cum laude* and was awarded the *Theodore von Karman Prize*. Only a few days later, he also received his M.Sc. in Aerospace Engineering *cum laude* at Delft University of Technology.

Having returned to Delft in fall 2011, Stefan has been working towards his Ph.D. within the experimental aerodynamics group of Prof. F. Scarano. His work is mainly concerned with the use and application of PIV for topics in aeroacoustics, in particular airfoil self-noise. In the course of his Ph.D. studies, Stefan spent a period as visiting research scholar within the experimental aeroacoustics group of Prof. S. C. Morris at the University of Notre Dame, USA.

During his studies, he was awarded the Huygens Scholarship by the Dutch Ministry of Education, Culture and Science. He is also alumnus of the German National Academic Foundation (Studienstiftung des deutschen Volkes).

LIST OF PUBLICATIONS

JOURNAL PUBLICATIONS

6. **S. Pröbsting**, S. Yarusevych, *Effect of Trailing Edge Tonal Noise on Laminar Separation Bubble Dynamics*, Journal of Fluid Mechanics **780**, pp. 167–191 (2015).
5. **S. Pröbsting**, F. Scarano, S. C. Morris, *Regimes of Tonal Noise on an Airfoil at Moderate Reynolds Number*, Journal of Fluid Mechanics **780**, pp. 407–438 (2015).
4. M. Kotsonis, R. K. Shukla, **S. Pröbsting**, *Control of Natural Tollmien-Schlichting Waves using Dielectric Barrier Discharge Plasma Actuators*, International Journal of Flow Control **7**, 1-2, pp. 37–54 (2015).
3. **S. Pröbsting**, M. Tuinstra, F. Scarano, *Trailing Edge Noise Estimation by Tomographic PIV*, Journal of Sound and Vibration **346**, pp. 117–138 (2015).
2. **S. Pröbsting**, J. Serpieri, F. Scarano, *Experimental Investigation of Aerofoil Tonal Noise Generation*, Journal of Fluid Mechanics **747**, pp. 656–687 (2014).
1. **S. Pröbsting**, F. Scarano, M. Bernardini, S. Pirozzoli, *On the Estimation of Wall Pressure Coherence using Time-Resolved Tomographic PIV*, Experiments in Fluids **54**, 7, 1567 (2013).

CONFERENCE PROCEEDINGS

15. W. C. P. van der Velden, **S. Pröbsting**, A. H. van Zuijlen, A. T. de Jong, Y. Guan, S. C. Morris *Numerical and Experimental Investigation of a Beveled Trailing Edge Flow and Noise Field*, 21st AIAA/CEAS Aeroacoustics Conference, Dallas, USA (2015).
14. J. Serpieri, M. Gupta, **S. Pröbsting**, F. Scarano, *Effect of Serrated Trailing Edge on Boundary Layer Instability Noise*, 21st AIAA/CEAS Aeroacoustics Conference, Dallas, USA (2015).
13. C. Arce, D. Ragni, **S. Pröbsting**, J. Madsen, *Experimental Comparison of Solid and Porous Trailing Edge Serrations*, Wind Turbine Noise, Glasgow, Scotland (2015).
12. C. Arce, D. Ragni, **S. Pröbsting**, F. Scarano, *Flow Field around a Serrated Trailing Edge at Incidence*, AIAA SciTech, Kissimmee, USA (2015).
11. **S. Pröbsting**, F. Scarano, *Experimental Investigation of Isolated Aerofoil Noise*, 21st International Congress on Sound and Vibration, Beijing, China (2014).
10. K. Lynch, **S. Pröbsting**, F. Scarano, *Temporal Resolution of Time-resolved Tomographic PIV in Turbulent Boundary Layers*, 17th International Symposium on Applications of Laser Techniques to Fluid Mechanics, Lisbon, Portugal (2014).
9. **S. Pröbsting**, A. Gupta, F. Scarano, Y. Guan, S. C. Morris, *Tomographic PIV for Beveled Trailing Edge Aeroacoustics*, 20th AIAA/CEAS Aeroacoustics Conference, Atlanta, USA (2014).

8. **S. Pröbsting**, S. Yarusevych, *Upstream Effect of Trailing Edge Tonal Emissions on a Laminar Separation Bubble*, 20th AIAA/CEAS Aeroacoustics Conference, Atlanta, USA (2014).
7. **S. Pröbsting**, J. Serpieri, F. Scarano, *High-speed PIV Analysis of Trailing Edge Aeroacoustics*, 10th International Symposium on Particle Image Velocimetry, Delft, The Netherlands (2013).
6. **S. Pröbsting**, J. Serpieri, F. Scarano, *Investigation of Tonal Noise Generation on an Airfoil with Time-resolved PIV*, 19th AIAA/CEAS Aeroacoustics Conference, Berlin, Germany (2013).
5. M. Tuinstra, **S. Pröbsting**, F. Scarano, *On the Use of Particle Image Velocimetry to predict Trailing Edge Noise*, 19th AIAA/CEAS Aeroacoustics Conference, Berlin, Germany (2013).
4. F. Scarano, S. Ghaemi, **S. Pröbsting**, *Data Reduction from Time-resolved Tomographic PIV for Unsteady Pressure Evaluation*, 51st AIAA Aerospace Sciences Meeting, Dallas, USA (2013).
3. **S. Pröbsting**, F. Scarano, M. Bernardini, S. Pirozzoli, *A Comparative Study of Turbulent Boundary Layer Wall Pressure Fluctuations obtained from High-speed Tomographic PIV and DNS*, 16th International Symposium on Application of Laser Techniques to Fluid Mechanics, Lisbon, Portugal (2012).
2. M. Debrouwere, L. Uyttersprot, J. Verwilligen, **S. Pröbsting**, D. G. Simons, F. Scarano, *Imaging of Rod-Airfoil Aeroacoustics using a Low-cost Acoustic Camera*, Berlin Beamforming Conference, Berlin, Germany (2012).
1. L. Koloszár, **S. Pröbsting**, N. Villedieu, P. Rambaud, J. Anthoine, *Simulation of Noise Propagation induced by two Co-rotative Vortices*, Open Source CFD International Conference, Barcelona, Spain (2009).